Evaluating strut-and-tie models for concrete elements by nonlinear finite element analysis

A. Sugianto

TU Delft

Evaluating strut-and-tie models for concrete elements by nonlinear finite element analysis

by

A. Sugianto

to obtain the degree of

Master of Science
in Structural Engineering

at the Delft University of Technology
to be defended publicly on Tuesday November 25, 2019 at 1:30 PM.

Student number:	4666836	
Project duration:	March 8, 2019 – November 25, 2019	
Thesis Committee:	Dr. ir. M. A. N. Hendriks	TU Delft, Chairman
	Y. Xia, MSc.	TU Delft, Daily supervisor
	Dr. ir. M. Lukovic	TU Delft, Supervisor

TU Delft

Preface

In this master thesis, I present the result of my research on evaluating the strut-and-tie models for concrete elements by nonlinear finite element analysis. This research was conducted from March 8th to November 25th of 2019 in order to obtain my Master's degree in Structural Engineering at Delft University of Technology. The research was the culmination of my academic experience at TU Delft and I am honored to have been presented with such an opportunity to contribute to the research on the topic of strut-and-tie modeling.

I would like to gratefully acknowledge the dedication of all members of my graduation committee. I would like to first express my gratitude toward the chairman of my graduation committee, Max Hendriks. I thank him for introducing me to the field of applied mechanics and giving me a chance to deal with this challenging subject. His generous advice and guidance motivated me to keep making positive improvements to my research work. In particular, I would also like to thank Yi Xia, my daily supervisor, for his active support and enthusiasm throughout my graduation project period. His invaluable remarks and feedback helped me to deliver an innovative concept to improve the strut-and-tie method evaluation process. Furthermore, I would also like to extend my gratitude to Mladena Lukovic for sharing her expertise and experience in concrete structures, as well as her critical suggestions for the development of the proposed technique.

Finally, I would like to thank my parents for the chance to explore and improve myself further in the Netherlands. And also many thanks to all my beloved friends that I made during my two years in TU Delft, without whom this thesis would not be possible. Special thanks to Radityo and Yasmin for their time and supports. Also to Jose, Maria, Knut, Anmol, David, Gigi, and Brigitte for their late companions in the thesis room, and for keeping me from getting fat by eating my snacks.

Andrew Sugianto
Delft, November 2019

Abstract

The strut-and-tie method (STM) has been acknowledged as one of the most reliable tools for designing discontinuity regions in structural concrete. It is capable of producing safe designs consistently since it was developed as an extension of the lower-bound theorem of plasticity theory. However, to aptly address a physical problem of a concrete element, STM often relies heavily on engineering experience and intuition. It is because the current STM has an inability to be transparent in informing the nonlinear consequences of choosing a certain ST model design, which make the method to be troublesome in more complicated design tasks.

In this thesis, a supplementary evaluation technique that employs nonlinear finite element analysis (NLFEA) is proposed as a solution. It is advantageous to incorporate NLFEA because it can provide nonlinear behavior of a structural concrete as objective insights for making a more informed decision in determining a suitable ST model. To incorporate NLFEA to STM, the concept of 'ties-as-extended-rebars' or TER model is introduced. A TER model is a numerical model used to assess the influence of a certain ST model design toward the nonlinear behavior of a concrete element. Through a TER model, an ST model is nonlinearly evaluated as a concrete element with embedded reinforcements. Additionally, to allow the TER model to generate a representative failure, the rebars in the TER model are extended with straight anchorage length. Then, the information generated by the model, i.e. failure mode and ultimate capacity, can be utilized as additional information to find a fitting ST model.

To assess its ability, the proposed technique was implemented on six ST models generated for two complex concrete beam elements. The implementation provided the TER model versions of the ST models. At the same time, the experimental results of the ST models were also validated using NLFEA. The validation attempt generated six numerical validation (NV) results, which were then compared with the TER model results. The result of the comparison indicated that five out of six TER models were able to suggest failure mode and ultimate capacity (R_{TER}) that are comparable with the failure mode and ultimate capacity (R_{NV}) from the NV results. In more detail, R_{NV} to R_{TER} ratio of models with similar failure mode has an average of 1.04 and a coefficient of variation of 11.1%, which suggests that the proposed technique can provide representative ultimate capacity value with relatively low variability.

Contents

List of Figures

List of Tables

List of Terminology

LD curve	*Load-displacement curve*
LEFEA	*Linear elastic finite element analysis*
LEFEM	*Linear elastic finite element method*
NLFEA	*Nonlinear finite element analysis*
NLFEM	*Nonlinear finite element method*
NV	*Numerical validation*
Rebar	*Reinforcement bar*
ST	*Strut-and-tie*
STM	*Strut-and-tie method*
TER model	*Ties-as-extended-rebars model*
TR model	*Ties-as-rebars model*
TO	*Topology optimization*
RC	*Reinforced concrete*

1 Introduction

1.1. General overview

After more than two decades since it was proposed by Schlaich, Schäfer, and Jennewein [25], strut-and-tie method (STM) is still acknowledged as one of the most reliable tools for engineers to design discontinuity regions in structural concrete. The method is consistent in producing safe designs because it was developed as an extension of the lower-bound theorem of plasticity theory. It allows an engineer to obtain a conservative solution by idealizing the flow of internal forces in a structure as a statically-admissible hypothetical truss model that transmits the imposed loads toward the supports. Due to its reliability, STM is currently recognized as a code-worthy design methodology and can generally be found in standard building codes for engineers to use.

Despite having a persevering capability in providing a conservative design, STM is still considered a troublesome method because of its iterative nature and lack of development [26]. Its design process that consists of truss modeling, truss analysis, and strut-and-tie (ST) dimensioning processes often have to be exercised repetitively before a suitable ST model can be obtained, as illustrated in Figure 1.1. Thus, STM can become a time-consuming process, especially in more complex design tasks. On top of that, there has been a shortage of studies that are dedicated to investigate and to improve the library of assumptions used in the method. Most provisions in its procedure are underdeveloped for dealing with complex cases. Consequently, the current STM evaluation framework often requires engineering experience and intuition for selecting an ST model that can aptly address a particular physical problem.

For tackling the time-consuming issue, many recent developments associated with STM are focused on implementing topology optimization method to automate the truss modeling process. The optimization method functions as a numerical algorithmic tool that iteratively redefine the original topology of a concrete structure until an optimal topology with a better performance in carrying the same load configuration is acquired. With the newly defined structural shape, engineers can deal with lesser number of possible truss configurations and can determine at a suitable ST model in a quicker manner. Most known algorithms that has been investigated for this purpose are ground truss method [30], evolutionary structural optimization (ESO) method [16], full homogenization method [13], solid isotropic material with penalty (SIMP) method [5].

While there has been an upsurge of attempts in automating the ST modeling process, there is still a lack of effort for improving STM evaluation procedure further to reduce its reliance on engineering experience and intuition. The problem with STM dependency is convoluted to solve because, in the

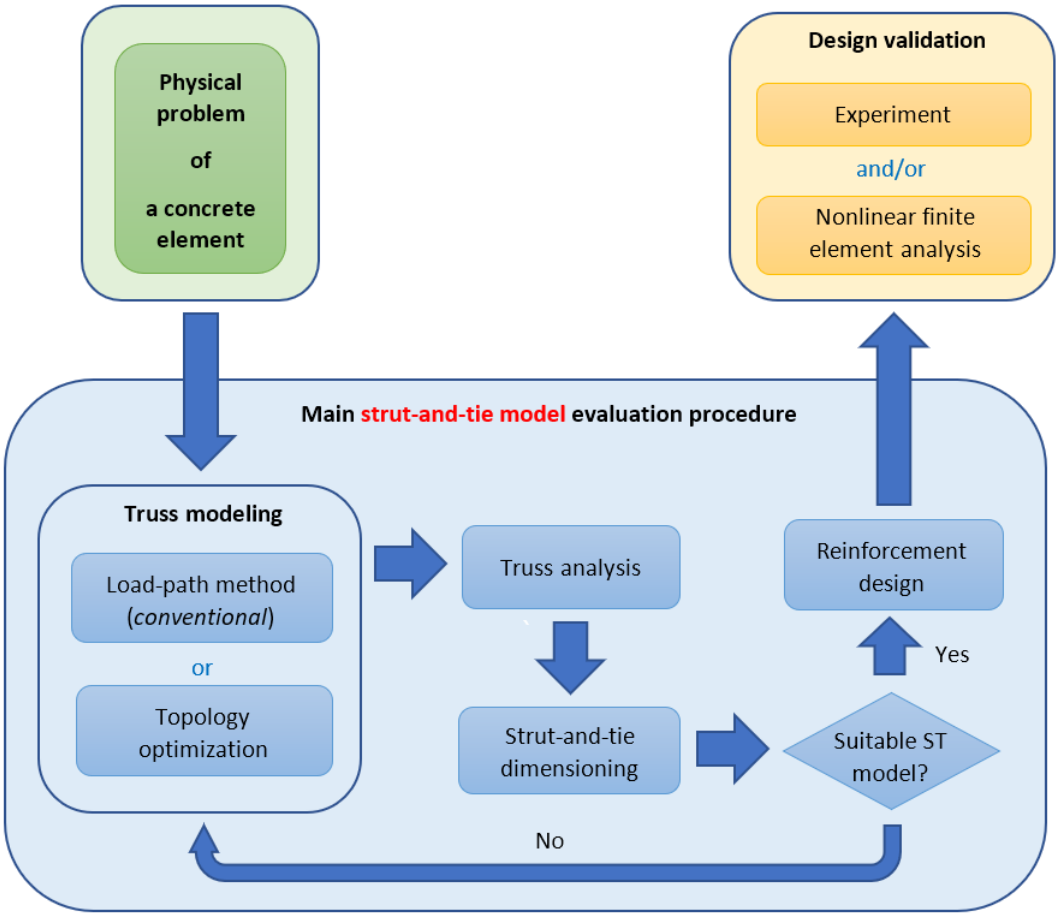

Figure 1.1: Current evaluation procedure of STM.

lower-bound analysis, a structure's behavior at its ultimate limit state is intended to be obscured. This difficulty results in challenges for determining the capacity of struts, defining the geometry of complex nodal zones, and estimating an accurate load-displacement response with STM [26].

This thesis is focused on addressing the latter issue in STM. A supplementary evaluation technique designated as a tool to promote STM to become a more data-driven method is proposed as a solution. The evaluation technique employs NLFEM to analyze an ST model as a concrete element with embedded reinforcements. It produces information regarding nonlinear behavior of the analyzed element, from which its users can make a more informed decision in determining a suitable ST model. To validate the proposed technique, six test cases from two independent STM-related experiments [3, 19] were utilized.

1.2. Aim of the research

The aim of this research is to improve the current STM-based evaluation framework to become a more data-driven design process. The improvement is sought through the implementation of NLFEA as one of the intermediate steps in the process of selecting a suitable ST model.

In order to achieve that goal, the following research questions are formulated:

Main research question

1. What evaluation technique can be supplemented into the current STM-based evaluation framework to turn it into a more data-driven ST modeling process?

Supporting research questions

2. How can the proposed technique be incorporated into the current ST modeling process?
3. How well does the proposed technique perform in suggesting a suitable strut-and-tie model?
4. What improvements can be brought to the current ST modeling process by incorporating the proposed technique?

1.3. Research methodology

The research work for this thesis consists of the formulation of the proposed evaluation technique, as well as its numerical testings and verification. The formulating process was an exploratory work that undertook an extensive literature review on the issue about STM reliance on engineering experience and intuition in determining a suitable ST model, and previously-researched techniques to solve it. The exploratory work established a baseline from which the author could start developing a prospective solution. The author determined that a fit solution to address the aforementioned issue is by developing an evaluation technique that employs NLFEA. Following that, a series of numerical testings were carried out in pursuit of discovering one approach that can incorporate NLFEA into the ST modeling process. The numerical trials utilized one experimental case which conducted a test on the performance of an ST model for a complex concrete beam element. After favorable results were obtained from the testings, the author attempted verification of the ability of the proposed technique. For the verification, the proposed technique was implemented on ST models from six test cases proposed in two independent STM-related experiments.

1.4. Scope of the research

As this thesis is designated to be completed in a stipulated amount of time, a few delimitation were set on the research. The following statements present the scope of this thesis:

- The main focus of this study is to discover a supplementary tool for STM that can promote it to become a more data-driven design method.
- Undisclosed information regarding material properties of the experimental specimens was analytically computed using formulas provided in EN 1992-1-1:2004 and fib Model code 2010.
- The proposed technique was only tested on six experimental size complex reinforced concrete beam elements due to the time limit.
- The numerical results in this study were generated using DIANA FEA 10.3 version.
- The numerical results in this study were generated with an established solution strategy provided in the Dutch guidelines for NLFEA of concrete structures [20].

- The numerical simulations in this study were not intended to investigate the correctness of the experimentation done in the literature.

1.5. Thesis outline

This thesis is structured such that the research questions are addressed in a logical manner. The thesis begins with *Chapter 1* that focuses on mainly introducing the motivation of the research and the research questions. *Chapter 2* presents a critical review of the current STM-based evaluation framework, as well as NLFEM which were utilized as a part of the proposed technique.

Following the latter chapter, two core parts of the thesis are presented. *Part 1* focuses on discussing the numerical validation of the experimental results of the test cases. The part consists of *Chapter 3* that describes the test cases and their experimental results, *Chapter 4* that presents the numerical validation process and its results, and *Chapter 5* that discuss the conclusion to the validation attempt.

Moreover, *Part 2* focuses on discussing the proposed technique. The part consists of *Chapter 6* that introduces the detail about the proposed technique, *Chapter 7* that focuses on presenting the results of implementing the technique on the ST models of the test cases, *Chapter 8* that presents the results of validating the implementation results using STM results, *Chapter 9* that presents the comparison between the implementation results and the numerical validation results of the test cases, *Chapter 10* that discuss the answers to the research questions, and *Chapter 11* that presents the recommendation for future researches in this topic.

2

Literature review

2.1. Strut-and-tie method

2.1.1. Concept

Strut-and-tie method (STM) is a methodology for designing structural concrete with discontinuities by idealizing the flow of internal forces in the structure as a statically-admissible hypothetical truss model that transmits the imposed loads to the supports. The method is an extension of the lower-bound theorem of plasticity theory, and therefore, it provides a solution that underestimates the actual ultimate load. Since STM is developed based on the equilibrium approach, there are two requirements that justify the safe solution: the equilibrium condition and the failure criteria. Despite having these two requirements, STM does not require its truss models to be kinematically stable. The geometry of an ST model is strictly related to a particular load configuration.

The concept of STM originated from the truss analogy presented by Ritter [21] and Mörsch [17] for shear design in B-region (short for Bernoulli or beam or continuity region) at which the Bernoulli hypothesis of plane strain distribution is assumed to be valid. The analogy was utilized to idealize the flow of the forces in a cracked concrete beam using a parallel chords truss model. It was then validated and further improved in the form of a full member or section design procedures, and later used as a basis for torsion-design methods by Collins and Mitchell [6].

Following that, Schlaich, Schäfer, and Jennewein [25] proposed a generalization of the truss analogy in order to apply it to every part of any structural concrete in the form of ST models. They suggested it as an alternative design method for treating structural concrete with discontinuities that has a more rational approach than the other design procedures that had bases on test results, rules of thumb, or past experience. This generalization was later matured into what is known as STM.

Currently, STM is recognized as one of the most reliable tools for designing D-region (short for discontinuity or disturbed or St. Venant region) in structural concrete. D-region can be defined as a section in a structure that has developed nonlinear strain distribution due to the presence of discontinuities. According to St. Venant principle, the width of a D-region spans for approximately one sectional depth of B-regions at either side of a discontinuity. A discontinuity in a structure can be prompted by a concentrated load (static discontinuity), an abrupt change of geometry (geometric discontinuity), or both, as illustrated in Figure 2.1.

For designing the topology of a truss model, STM assumes all principal stress fields to condense into compression and tension truss members which are joined by nodes. The compression and tension

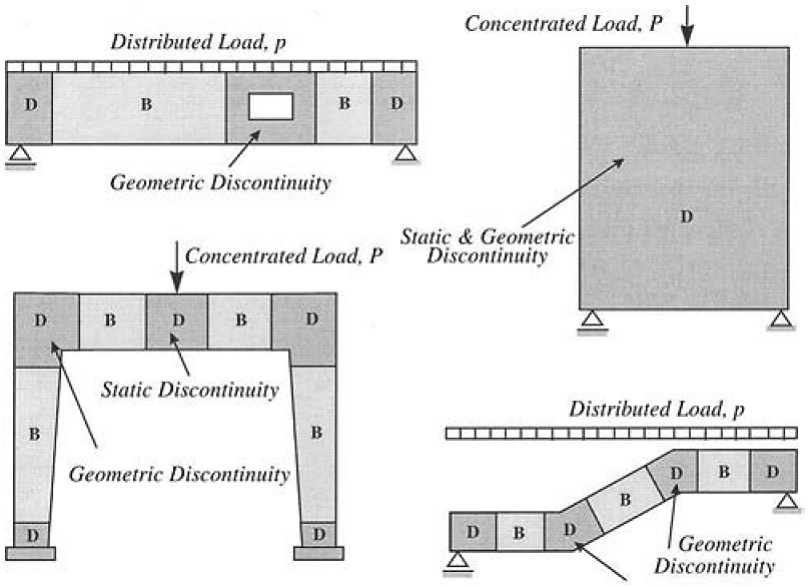

Figure 2.1: D-regions due to geometric discontinuity and/or static discontinuity [30].

truss members are named respectively as struts and ties. A strut represents a concentrated principal compressive stress field of concrete in the direction of a strut, while a tie can represent one or multiple sets of reinforcing bars, prestressing tendons, or prevailing principal tensile stress field of concrete in the direction of a tie. In the design process, a strut is often symbolized as a broken line and a tie as a solid line. The angle between a strut and a tie should not be smaller than 26.56 degrees, as it is the smallest angle that can occur between a strut and a tie at a shear span (a/d) of 2 where the tie is not influencing the strength of the strut.

Nodes, on the other hand, are analogous to joints at an actual truss and are the intersection points of three or more struts and/or ties. A node implies an abrupt change of direction of forces which in reality occurs over a specific area. Classification of nodes depends on the combination of forces acting on the node. Compression force acting on the node is usually denoted as 'C' and tension force is denoted as 'T'. There are essentially four types of nodes that are commonly used in STM: C-C-C, C-C-T, C-T-T, and T-T-T nodes, which are illustrated in Figure 2.2.

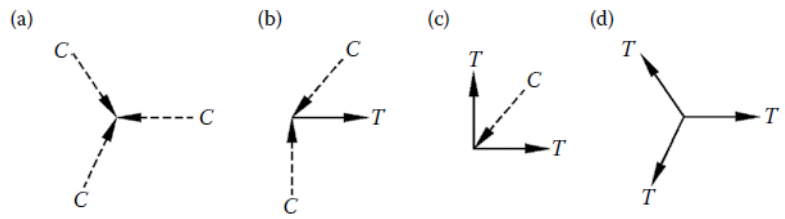

Figure 2.2: Nodes classification: (a) C-C-C node, (b) C-C-T node, (c) C-T-T node, and (d) T-T-T node [8].

Since concrete has a limited plastic deformation, STM fulfills this ductility requirement by adapting the struts and ties to the direction and size of the internal forces in highly stressed regions as they would be generated in accordance to the theory of elasticity. In a relatively lighter stressed region, the direction of drawn struts and ties may have a noticeable deviation from the elastic stress pattern without having a chance of exceeding a structural concrete's ductility requirement.

According to Tjhin and Kuchma [26], STM design process can be divided into five steps:

1. Defining the boundaries of the D-region and then evaluating the concentrated, distributed, and sectional forces that act on the boundaries of this region;
2. Sketching an ST model and solving for the truss member forces;
3. Selecting the reinforcing or prestressing steel that is necessary to provide the required tie capacity and ensuring that this reinforcement is properly anchored in the nodal zones (joints of the truss);
4. Evaluating the dimensions of the struts and nodes such that the capacity of these components is sufficient to carry the design force values; and
5. Providing distributed reinforcement to increase the ductility of the D-region.

STM can provide a structural analyst with some freedom in choosing the safest, the cheapest or even an optimized solution. Thus, designing with STM requires some design experience, as in selecting a representative overall statical system or a reasonable finite element mesh for the truss model. Examples of ST models applied on D-region of common structural elements can be observed in Figure 2.3.

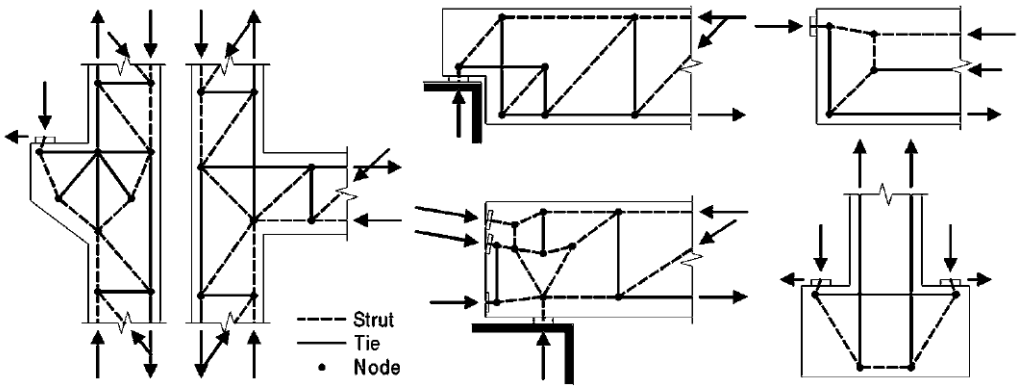

Figure 2.3: Example of ST models [26].

2.1.2. Typical ways for developing strut-and-tie models

Two typical ways for developing an ST model at D-regions are explained in this section. The first way is by using the conventional techniques which were developed by the originator of STM, Schlaich et al. [25]. They suggested the load path method, which can be combined with elastic stress analysis results and/or model optimization criterion, depending on the aim of the design. The second way is by applying topology optimization algorithms to assist the generation of an ST model. The detail of each process is explained in the following paragraphs.

2.1.2.1. Conventional way

2.1.2.1.1 Load path method

Load path method is the most basic method for developing an ST model in D-region. It systematically develops a truss model by manually tracing the flow of the forces in the structure. The tracing creates streamline of load paths from the applied loads to their equivalent reaction forces at the

supports, as shown in Figure 2.4b. The curvy load paths should then be replaced by polylines and later added with extra struts and ties to produce equilibrium at every node, as illustrated in Figure 2.4c. In a case where concentrated loads or stress resultants from a B-region are not completely balanced with the load path described, the load path of the remaining forces can be drawn entering the structure, but then leave it with a U-turn towards the applied load entry side, as illustrated in Figure 2.5.

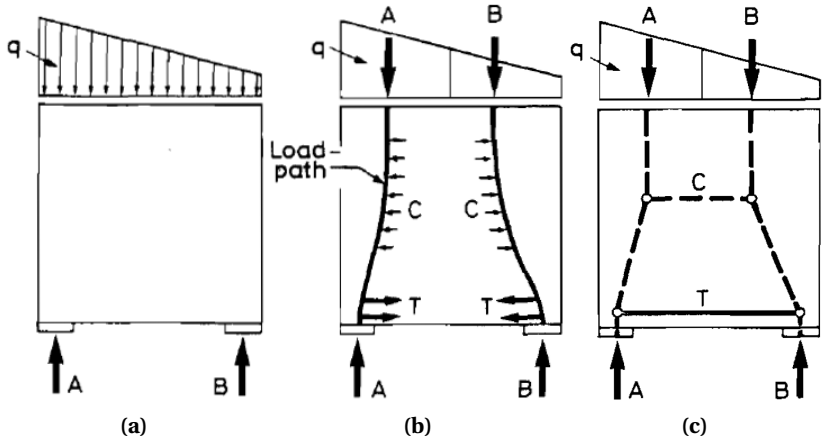

Figure 2.4: The load path method: (a) the structure and its loads; (b) the load paths through the structure; (c) the corresponding ST model [25]

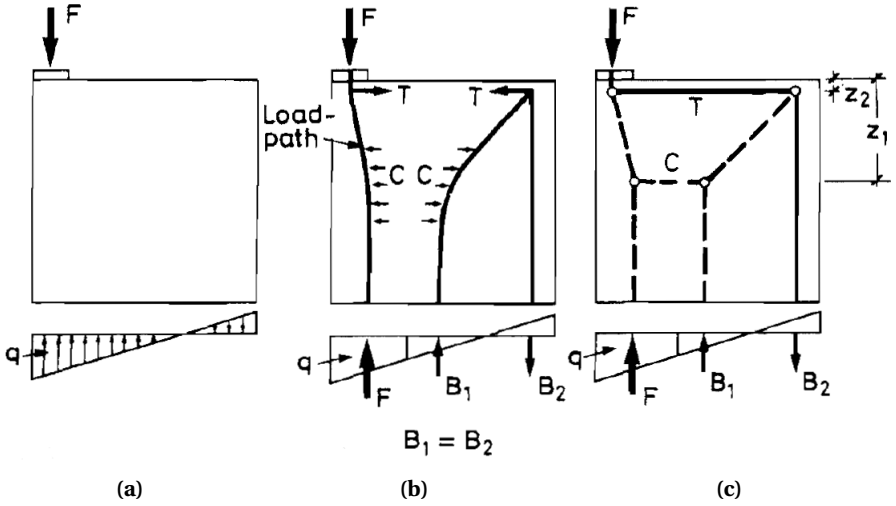

Figure 2.5: The load path method, including a 'U-turn': (a) the structure and its loads; (b) the load paths through the structure; (c) the corresponding ST model [25]

2.1.2.1.2 Elastic stress analysis

Developing a truss model for a D-region with load path method can be much simplified if the information about elastic stresses and principal stress trajectories is available from an elastic finite element analysis. With it, the location and the direction of struts and ties can immediately be determined and the truss members can be aligned at the center of their respective stress fields. Also, the position of the deviating force resultant can be positioned at the center of gravity of the elastic stress

distribution of each section. An example of the use of elastic stress analysis results for modeling an ST model is illustrated in Figure 2.6.

Nevertheless, orienting struts and ties using elastic stress analysis results may not be the best option due to the change of the profile and the distribution of the stresses as the applied load increases. But, limited plastic ductility of concrete can be taken into account to prevent excessive deviation from occurring. Furthermore, ties are allowed to be placed according to the practical application of reinforcements. Struts and ties should be placed within ±15 degrees from the direction of their respective principal stress trajectories.

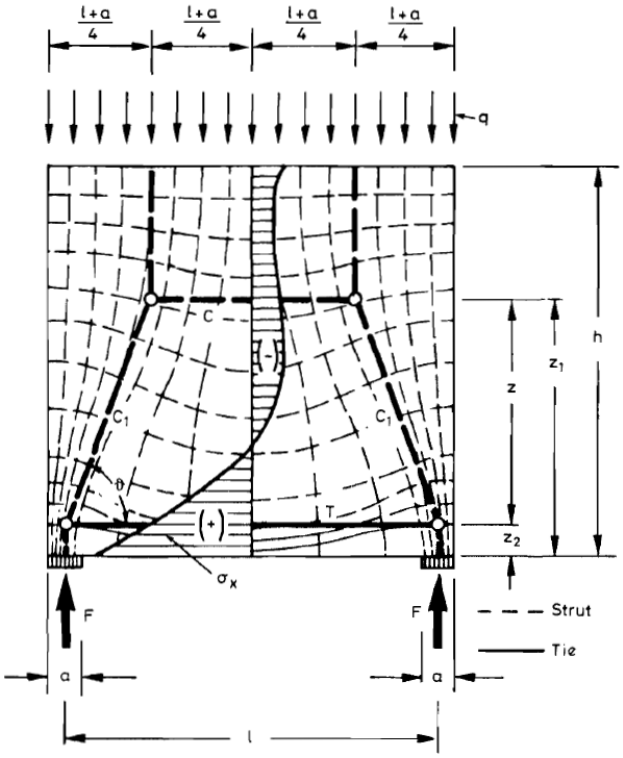

Figure 2.6: Elastic stress trajectories, distribution of elastic stresses, and corresponding ST model [25].

2.1.2.1.3 Model optimization

In the process of designing a D-region with STM, it is possible to obtain multiple statically-admissible ST models for a particular load configuration. In selecting one optimal solution from the others, it is helpful to realize the fact that a force always tries to find a path with the least resistance (strain energy) and deformation. Since reinforcement bars have much higher deformation capacity than concrete, a truss model with the least and shortest ties is the preferred choice, as illustrated in Figure 2.7. This simple criterion for optimizing a truss model may be formulated as follow:

$$\Sigma F_i l_i \epsilon_{mi} = minimum \tag{2.1}$$

where:

- F_i the force in strut or tie 'i'
- l_i the length of member 'i'

ϵ_{mi} mean strain of member 'i'

In doubt, equation 2.2 can be utilized as a simplified criterion for model optimization.

$$\Sigma T_i l_i = minimum \tag{2.2}$$

where:

T_i the tension force in tie 'i'

l_i the length of member 'i'

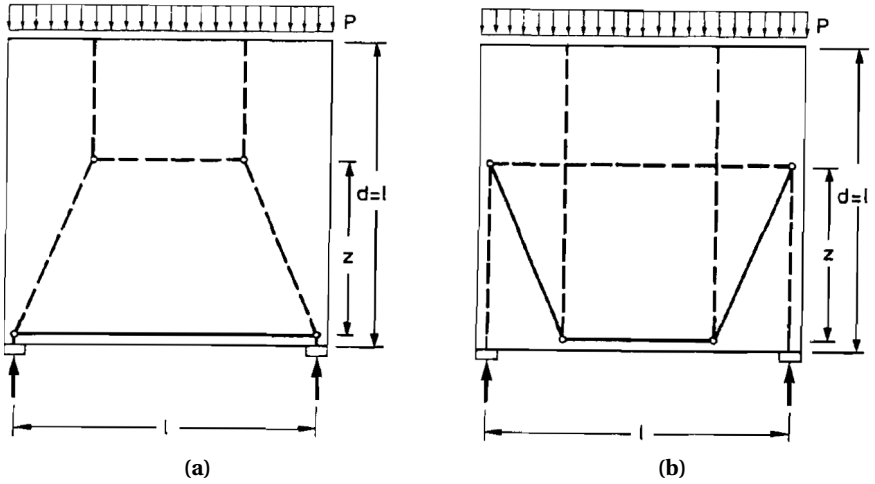

Figure 2.7: Preferred (a) vs. less preferred (b) truss model [24]

2.1.2.2. A way with topology optimization method

In recent attempts to automate the ST modeling process, many researchers proceed with an approach of implementing the topology optimization method to the computer-aided design of D-region. The method functions as an algorithmic tool to redefine the original topology of a structural concrete into a truss-like system that can carry the same load configuration in a rather more optimal topology and performance. The method iteratively optimizes a structure's topology by adding (or removing) material resources to (or from) any point in the structure's domain until a new structure which has obtained the maximum performance possible is defined [11]. The resulting topology is later used as a template to develop an ST model by placing struts and ties at the location of compression and tension members of the newly defined structure. An example of the iteration process of topology optimization for a deep beam with a large opening and its application as an ST model's template by Liang et al. [16] is presented in Figure 2.8.

The process of optimizing a structural concrete's topology has two main steps. At the first step, the process starts with discretization of the structural (or design) domain with meshing. In general, the type of finite elements used for meshing is either solid (continuum) or discrete (truss) elements, depending on the governing mechanics.

The second step is the iteration process of adding and/or removing the finite elements until an optimal element composition in accordance with the objective of the algorithm is achieved. With continuum elements, the topology of a structure is optimized by identifying every element as either

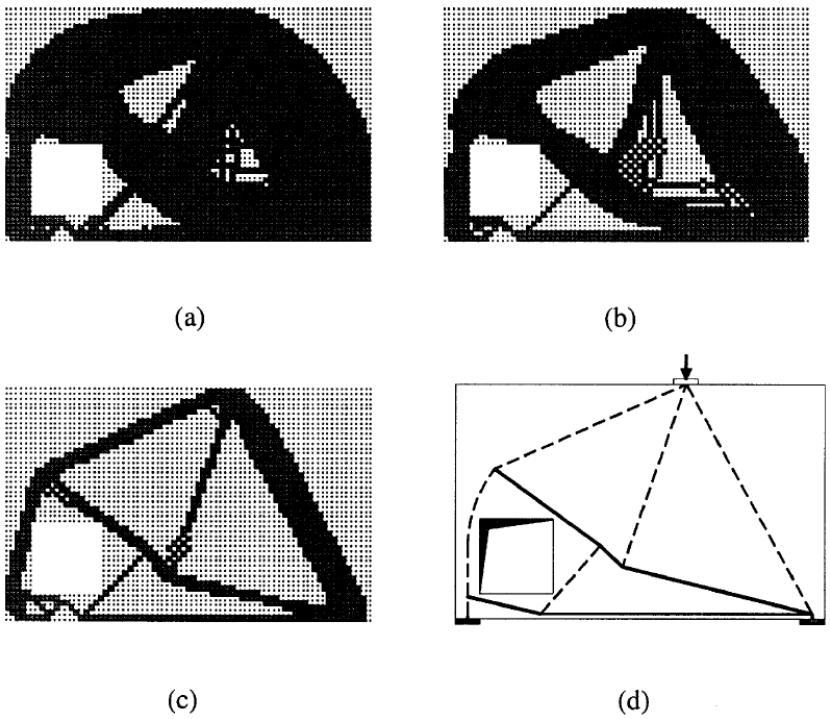

Figure 2.8: Optimization history of a ST model in deep beam with a large opening: (a) topology at iteration 20; (b) topology at iteration 40; (c) optimized topology; and (d) optimized ST model [16].

solid or void material using an indicator variable known as volume fraction (ρ^e). If an element is a solid then $\rho^e = 1$ and if an element is a void then $\rho^e = 0$. The connectivity of the solid elements then defines the topology of the structure. Conversely, with discrete elements, optimization is typically done by following a ground structure approach, where the design domain is discretized with a dense, redundant structural system. In this approach, elements that are deemed inefficient are then removed from the ground structure, while forming the optimal structure design. An illustration of the ground truss approach application is presented in Figure 2.9.

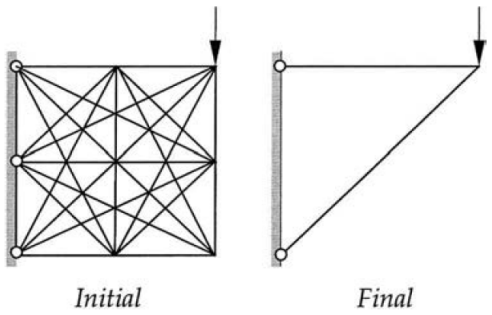

Figure 2.9: Topology optimization with ground truss approach [30].

While it is a useful and straightforward approach to automate STM, topology optimization is still fundamentally and numerically challenging to solve and often leads to a structural design that is impractical to construct, as shown in Figure 2.8(d), or excessively sensitive to uncertainties, e.g., imperfections or random loads. Current research on STM with the application of topology optimization has been focused on developing algorithms that can mitigate these drawbacks. Several

examples of the researched topology optimization algorithms are ground truss method [30], evolutionary structural optimization (ESO) method [16], full homogenization method [13], solid isotropic microstructure with penalty (SIMP) method [5], etc. Most of the available algorithms solve the most common topology optimization formulation, which is the minimum compliance. The goal of this formulation is to minimize the internal strain energy in a structure of fixed mass with a certain load case and boundary conditions while maximizing its stiffness.

2.1.3. Dimensioning the struts, ties, and nodes

In STM, dimensioning is a process of sizing and reinforcing the elements of an ST model in correspond to the concentrated stress fields and reinforcement layout they represent. This step follows after the truss analysis process in the current STM procedure. The purpose of dimensioning is to ensure that a proper load transfer will occur between each element by examining the nodal zones detail. The examination is essential because the detail given to a nodal zone can affect the force flow at that zone. The detailing process of a nodal zone can also change the initially chosen ST model, and thus modeling and dimensioning an ST model is an iterative process.

There are basically three types of struts and ties that need to be dimensioned:

- Concrete struts in compression (C_c)
- Concrete ties in tension without reinforcement (T_c)
- Ties in tension with reinforcement (T_s)

C_c and T_c are types of truss member that cover two- (or three-) dimensional principal stress fields that tend to spread in between two adjacent nodes. A dimensioned C_c can have three basic shapes: a prismatic, a bottle, or a fan shape, as shown in Figure 2.10, depending on the compressive principal stress field it represents. In the case of bottle-shaped strut or tie, a C_c or a T_c may be required to be strengthened by reinforcement bars due to the presence of transverse tensile or transverse compressive stress. The dimension of C_c and T_c depend on the failure criterion of their respective concrete strength, which is compressive concrete strength for C_c and tensile concrete strength for T_c.

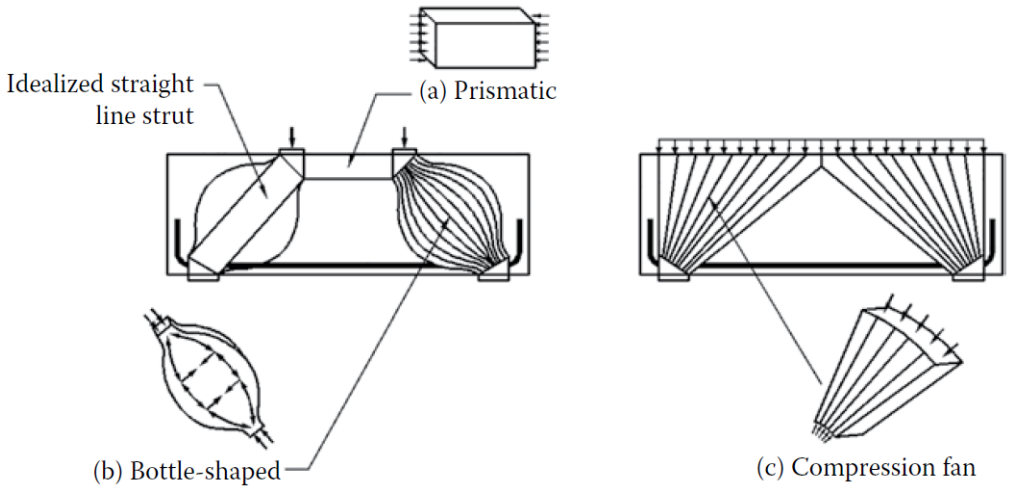

Figure 2.10: Three basic shapes of strut [8].

Conversely, T_s is a type of truss member that is substantially a linear or one-dimensional element between two nodes. Its failure criterion is the yield strength of reinforcement bars or prestressing tendons that carry the tension force from the ties.

The last dimensioned element to be described is the nodal zone. A nodal zone is a dimensioned version of a node. It represents a locally concentrated area at which the stress resultants from three or more joining truss members deviate from their initial trajectories.

There are two types of the nodal zone: singular (or concentrated) nodes and smeared (or continuous) nodes. In a singular node, the forces acting on its zone equilibrate more abruptly than in a smeared node, and thus the deviation of forces at singular nodes occur at a relatively smaller area. According to Schlaich et al.[25], since D-regions usually contain both smeared and singular nodes, the latter will be critical and a check of concrete stresses in smeared nodes becomes unnecessary, except for a case at which a smeared C-C-T node is assumed to remain uncracked. Singular nodes can be founds near a point load and support reactions, and also near concentrated forces introduced by the reinforcement through anchor plates, bond, or radial pressure inside bent reinforcement bars such as loops. An illustration of singular and smeared nodes in an ST model is presented in Figure 2.11.

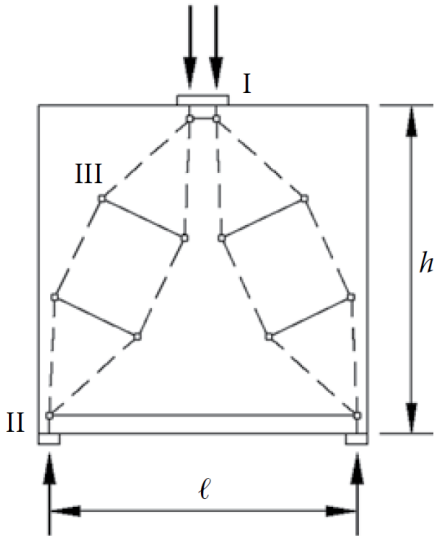

Figure 2.11: Types of nodal zones: singular nodes (I and II) and smeared nodes (III) [8].

Defining the geometry of singular nodes is required for calculating the stresses that can be applied at each nodal face. There are two established techniques for proportioning a node: by shaping it into a hydrostatic or nonhydrostatic node. Hydrostatic nodes are nodes which are proportioned in such a manner that the in-plane stresses acting on each node are equivalent and directed perpendicularly toward its nodal faces. In contrast, nonhydrostatic nodes are proportioned based on the origin of the applied stress, and therefore, the in-plane stress on each nodal face does not need to be equal. Proportioning a hydrostatic node is rather simpler than proportioning a nonhydrostatic node, but applying hydrostatic node can have a consequence of having unrealistically large struts at structures with relatively wide shear span (a/d), as illustrated in Figure 2.12. For nonhydrostatic node, Schlaich et al. [25] suggested that the ratio of the maximum stress on a face of a node to the minimum stress on another face of the same node should be less than 2. The stress state difference between hydrostatic and nonhydrostatic node is presented in Figure 2.13.

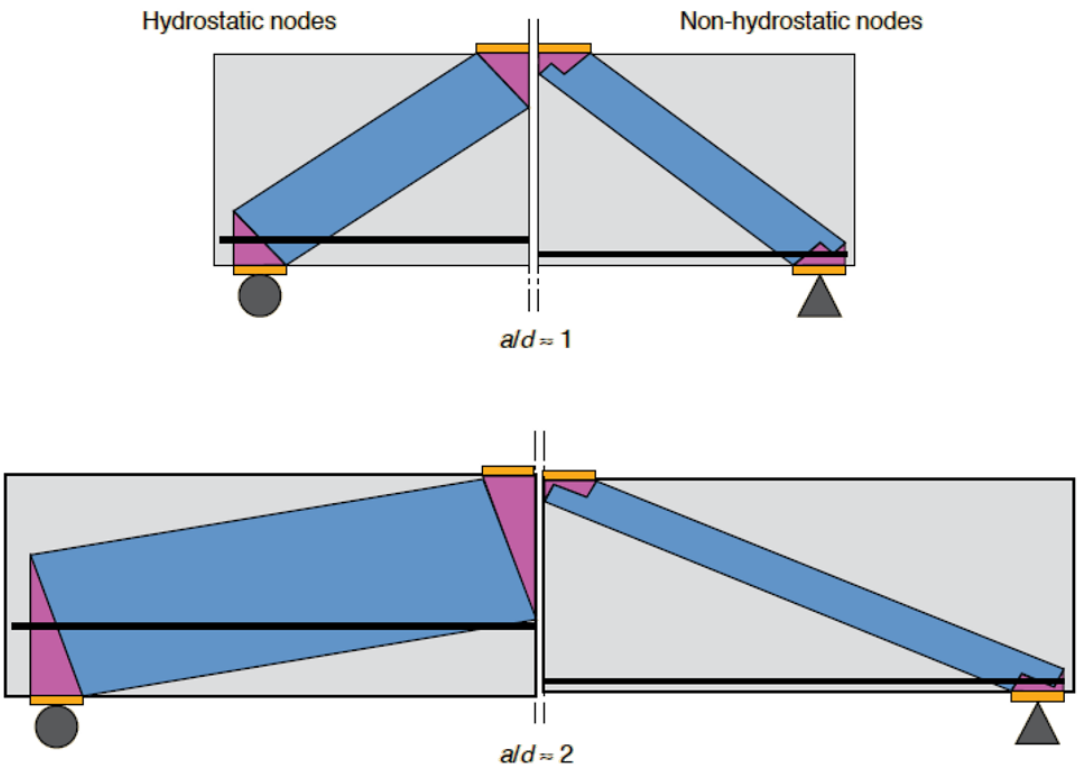

Figure 2.12: Influence of hydrostatic vs. nonhydrostatic node at strut width [27].

According to ACI 318-08 [2], C-C-C nodes and C-C-T nodes can be designed as nonhydrostatic nodes by following the arrangements given in Figure 2.14 and Figure 2.15, respectively. In these arrangements, h_a is defined as two times the distance from the nearest extreme fiber of the analyzed structure to the centroid of the node, while h_s can be determined using equation 2.3.

$$h_s = \beta_1 c = \frac{\left(A_s f_s - A'_s f_s\right)}{0.85 b_w f'_c} \tag{2.3}$$

where:

- β_1 factor for proportioning the depth of the equivalent stress block in the flexural compression region
- c distance from extreme compression fiber to neutral axis
- A_s area of tension reinforcement
- $A_s{}'$ area of compression reinforcement
- $f_c{}'$ specified compressive strength of concrete
- b_w web width
- $f_s{}'$ stress in compression reinforcement

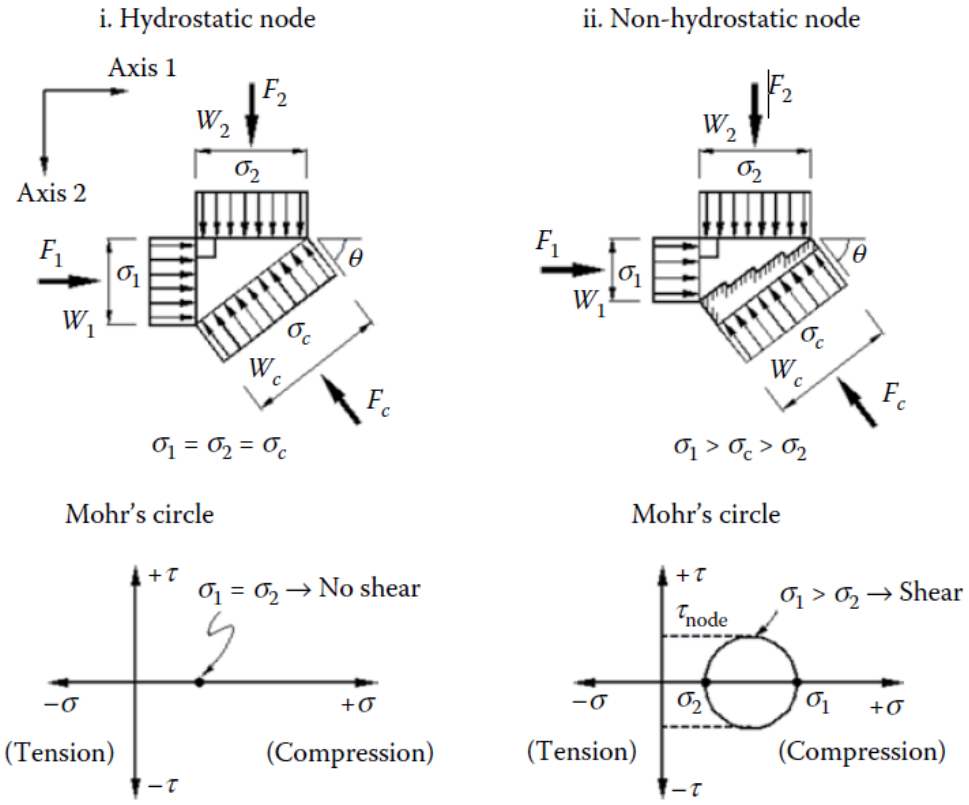

Figure 2.13: Stress states in hydrostatic and nonhydrostatic nodes [4].

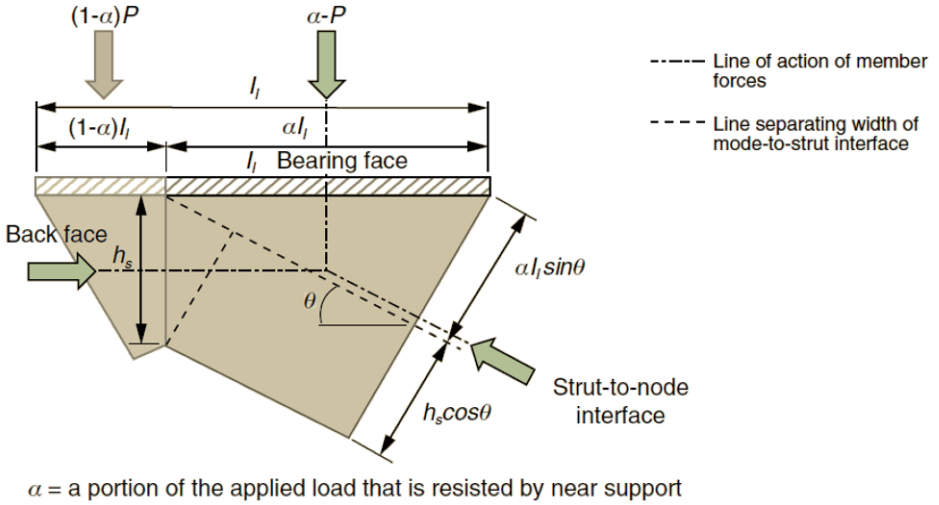

Figure 2.14: Arrangement for proportioning C-C-C node as a nonhydrostatic node [27].

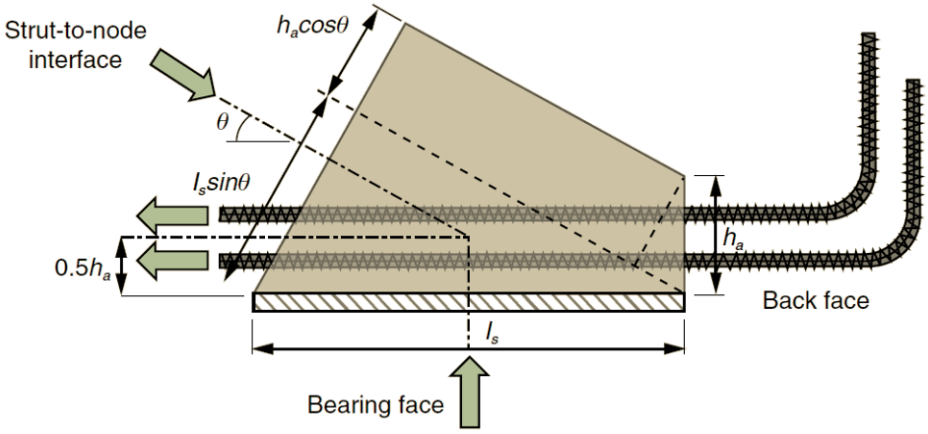

Figure 2.15: Arrangement for proportioning C-C-T node as a nonhydrostatic node [27].

2.1.4. Code provisions for dimensioning a strut-and-tie model

In the following paragraphs, code provisions for STM issued in EN 1992-1-1:2004 [28] is described. These provisions regulates the allowable stress that could occur in a strut and in a nodal zone on a set of cases. Two distinct compressive strength values were utilized in the given empirical equations to obtain the allowable stress values: design values of concrete compressive strength (f_{cd}) or concrete compressive strength at concrete elastic state (f_{Ecd}). However, since the purpose of ST model evaluations in this thesis is to check their performances based on the experimental results, the aforementioned strength values were replaced with mean values of concrete compressive strength (f_{cm}) during the evaluation. The value of f_{cm} is obtained from concrete cylindrical tests mentioned in the literature.

Struts

If there is transverse compressive stress or no transverse stress at all acting at the same region of a concrete strut (see Figure 2.16), the design strength of the strut may be calculated using equation 2.4.

$$\sigma_{max} = f_{cm} \tag{2.4}$$

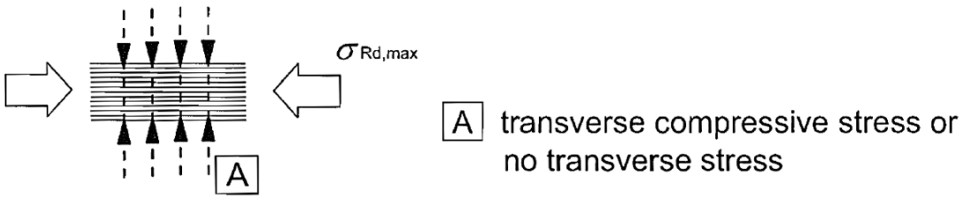

Figure 2.16: Design strength of concrete struts without transverse tension [28].

However, if there is transverse tensile stress acting at the same region of a concrete strut (see Figure 2.17), the design strength of the strut should be reduced in accordance to equation 2.5, unless a more rigorous approach is used. Recommended value of ν' is given by equation 2.6.

$$\sigma_{max} = 0.6\nu' f_{cm} \tag{2.5}$$

$$\nu' = 1 - \frac{f_{ck}}{250} \tag{2.6}$$

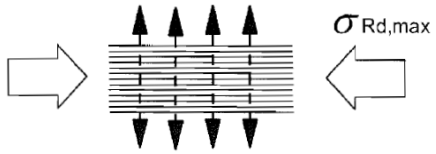

Figure 2.17: Design strength of concrete struts with transverse tension [28].

Nodes

In designing nodal zones, σ_{max} is the maximum compressive stress which can be applied at any nodal faces of a nodal zone.

For compression nodes without any ties anchored at the node (C-C-C nodes), as illustrated in Figure 2.18, equation 2.7 may be used to determine the design values of compressive stress within nodes. Recommended value of k_1 is 1.0.

$$\sigma_{max} = k_1 \, \nu' \, f_{Ecm} \tag{2.7}$$

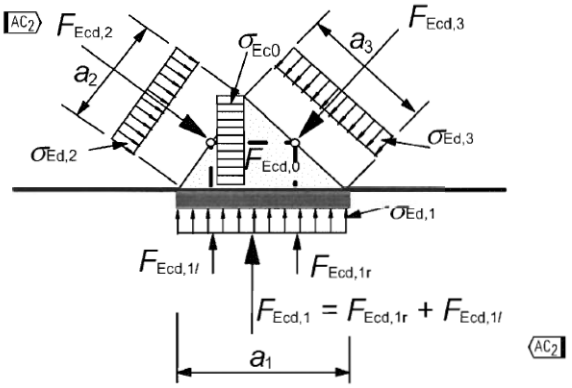

Figure 2.18: Compression node without ties [28].

For compression-tension nodes with anchored ties provided in one direction (C-C-T nodes), as ilustrated in Figure 2.19, equation 2.8 may be used to determine the design values of compressive stress within nodes. Recommended value of k_2 is 0.85.

$$\sigma_{max} = k_2 \, \nu' \, f_{Ecm} \tag{2.8}$$

For compression-tension nodes with anchored ties provided in more than one direction (C-T-T nodes), as ilustrated in Figure 2.20, equation 2.9 may be used to determine the design values of compressive stress within nodes. Recommended value of k_3 is 0.75.

$$\sigma_{max} = k_3 \, \nu' \, f_{Ecm} \tag{2.9}$$

2.1.5. Remaining challenges to be resolved in strut-and-tie modeling

In their research paper, Tjhin and Kuchma [26] stated that there are five remaining challenges that have to be solved before STM can turn into an efficient and transparent method. The current STM has difficulties in:

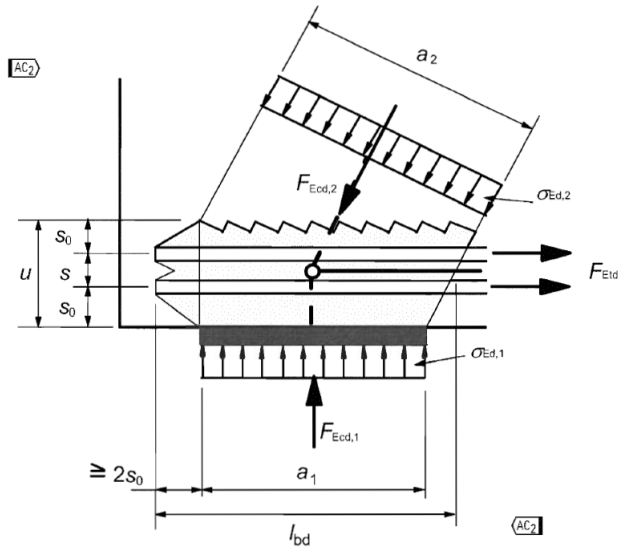

Figure 2.19: Compression-tension node with reinforcement provided in one direction [28].

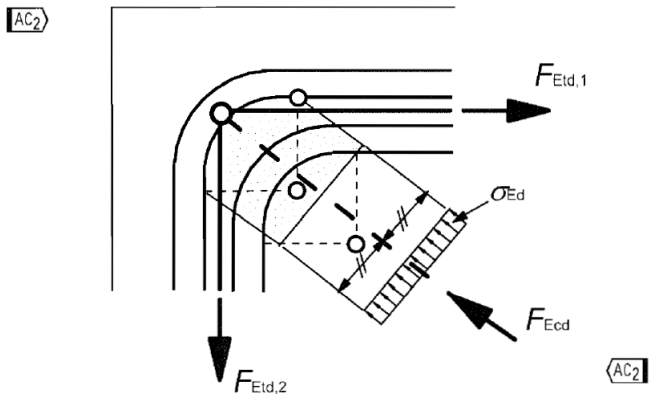

Figure 2.20: Compression-tension node with reinforcement provided in two direction [28].

Determining the capacity of struts

There is still much debate over the effective compressive strength of a strut. This situation is reflected in the inconsistency of compressive strength values specified in either building codes, guidelines, or research results. What is agreed is that the strength of a strut is a fraction of the uniaxial concrete compressive strength obtained from cylinder tests. There are five factors that can influence the ultimate compressive stress capacity of a strut: the shape of a strut, disturbance in a strut, the use of distributed reinforcement, confinement, and the angle of a strut.

Estimating load-displacement response of struts and ties

Finding an accurate estimation of load-displacement response is a feature that current STM still does not have. STM is not reliable for obtaining load-displacement response because the process for determining the stiffness characteristics of struts and ties has not been entirely figured out.

Determining anchorage and distribution of tie reinforcement

Selecting the correct detailing for the nodal zone is important to ensure a proper force transfer to occur. However, there exist some uncertainties in terms of anchorage requirements and the necessity to distribute the reinforcements for the tie throughout the nodal zone.

Defining the size, shape, and strength of complex nodal zones
It is considered to be a difficult task to define the geometry of nodal zones due to a large number of configuration variation could form depending on the number of stress resultants acting on a node. Currently, the code provisions for proportioning nodal zones in standard building codes only cover nodal zones with three acting forces, such as C-C-C node, C-C-T node, etc. In a case where more than three forces intersect at a node, engineers often have to resolve some of the forces to end up with just three resulting forces.

Designing for serviceability limit state
Up until now, the development of STM has been focused on analyzing the ultimate limit state of structural concrete, while serviceability limit state has only been considered implicitly through the selection of the appropriate ST model that fit the serviceability limit state requirements. To be able to analyze the deflection and crack widths at service load level, STM requires stiffness characteristic of the truss members and effective concrete area in tension around the ties, respectively.

2.2. Application of nonlinear finite element method on structural concrete

2.2.1. General

Nonlinear finite element method (NLFEM) is a numerical simulation tool for assessing the behavior of a structure outside its elastic phase which occurs due to nonlinearity phenomenon. In structural engineering, NLFEM is typically used to investigate the consequences of a structure's nonlinear behavior. The solution produced by NLFEM is obtained by solving the stress analysis (field) problems in the analyzed structure. The result of the stress analysis then provides an approximate response of the structure at its nonlinear phase which is handy for studying the damages that can occur at the structure's serviceability and ultimate limit state due to high localized strains that surpass the strain energy of the applied material.

In NLFEM, nonlinearity phenomenon can be differentiated into three common types [7]:

- *Material nonlinearity*, in which material properties become the functions of the state of stress or strain. Examples include nonlinear elasticity, plasticity, and creep.
- *Contact nonlinearity*, which happens when the following conditions occur: a gap between adjacent parts may open or close, the contact area between parts changes as the contact force changes, or there is sliding contact with frictional forces.
- *Geometric nonlinearity*, in which deformation of a structure is relatively large enough to cause equilibrium equation to be rewritten with respect to the deformed topology of a structure. Also, loads may change direction as the deformation increases, as when pressure inflates a membrane.

Furthermore, it is important to mention that the numerical solution given by NLFEM is just an approximation from the actual condition. The approximated solution is generated as the result of the requirement to create a finite element model through the abstraction of the physical structure with several assumptions, generalizations, and idealizations [20]. The abstraction process has two distinct steps: first is the abstraction from the actual structure to the mechanical model, and second is the abstraction from the mechanical model to the finite element model through discretization of the mechanical model into a mesh of finite elements connected with nodes. An example of the abstraction process of a tapered support post is presented in Figure 2.21.

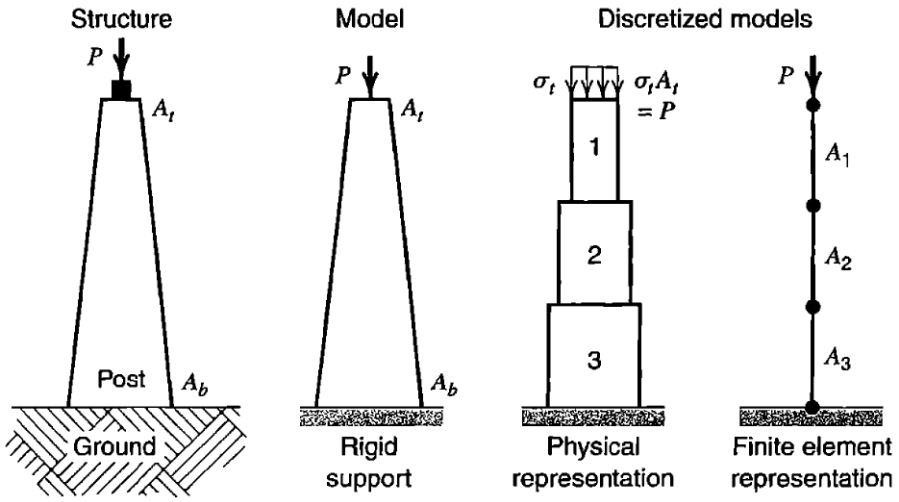

Figure 2.21: An illustration of the abstraction process for creating a finite element model from an actual structure [7].

As one of the engineering analyses, NLFEA results commonly suffer from uncertainties that can come from three different sources: physical uncertainty, statistical uncertainty, and modeling uncertainty [31]. Physical uncertainty is associated with the probability distribution estimated from observed data, whereas statistical uncertainty is associated with the statistical distribution parameters of random variables identified in physical uncertainty. In contrast, modeling uncertainty comes from both probabilistic and mechanical models and exists in model accuracy and model selection. In Section 2.2.2, further description about modeling uncertainty is presented.

Moreover, to obtain a solution from NLFEM, a solution strategy needs to be defined. According to Engen et al. [9], solution strategy is a term used to denote all of the choices made regarding force equilibrium, kinematic compatibility, and constitutive relations in order to shape a reliable approach for obtaining a solution from NLFEA. Any disparate choices related to this matter will influence the level of modeling uncertainty in an NLFEA result. Therefore, having a consistent and robust solution strategy with a low modeling uncertainty is essential to make NLFEM a dependable numerical simulation tool. Solution strategy used in this thesis is further explained in Section 2.2.3.

Additionally, there are two types of crack model available for modeling the fracture mechanics of structural concrete in NLFEM [1]:

- *Discrete crack model*, in which cracking is modeled to form at the interface elements located between two continuum elements. This approach is fit for cases with one distinct crack and requires remeshing and mesh refinement near the tip of the modeled crack during its propagation. Properties of the fractures are described by the interface's constitutive law.
- *Smeared crack model*, in which cracking is modeled by assuming the occurrence of orthotropic damage to the concrete within an area assigned to a continuum element or an integration point. The crack itself is modeled as a crack band, at which tensile strain localizes during crack propagation. The localization within the crack band happens due to the softening nature of the constitutive law of crack opening. The objectivity of the solution (low mesh sensitivity) is ensured by considering the crack band size as a regularization parameter of the strain localization.

The constitutive law of crack opening is described by three parameters: concrete tensile strength,

the shape of the softening function, and fracture energy, which are discussed further in Section 2.2.3.

2.2.2. Modeling uncertainties in nonlinear finite element analysis result for structural concrete

As explained by Zhang and Mahadevan [31], modeling or model uncertainties in engineering analysis are uncertainties that related to the selection and the accuracy of both probabilistic and mechanical model. In the probabilistic model, uncertainties accumulate from the distribution parameter estimation and the approximation in the computational procedure. The former is usually taken into account by statistical uncertainty. On the other hand, the uncertainties from the mechanical model manifest from the mathematical idealization of the physical problem of the model, as well as from the approximations in the numerical solution procedure.

According to Roache [22], modeling uncertainty can be quantified using verification and validation. Verification helps to assess the means used for solving the equations that are derived in accordance to the mechanical model, while validation is beneficial for evaluating the quality of the equations in capturing the actual physical behavior of the analyzed structure. In relation to NLFEM, verification thus relates to the iterative solution of the equilibrium equations and the discretization of the model into finite elements, whereas validation relates to the idealization of the geometry of the model and the material behavior. Additionally, following the multiplicative formulation in the Probabilistic Model Code [15], modeling uncertainty can be expressed as the following equation:

$$\Theta = \frac{R_{exp}}{R_{NLFEA}} \tag{2.10}$$

where:

$R_{exp,i}$ = experimental capacity of specimen 'i'

$R_{NLFEA,i}$ = predicted capacity of specimen 'i' according to NLFEA

In his attempt on quantifying the modeling uncertainty in NLFEA results of large concrete structures using 38 benchmark analyses, Engen demonstrated that the uncertainty could be represented as a log-normally distributed random variable of Θ [10], as shown in Figure 2.22, with a mean of 1.10 and standard deviation of 0.12. To obtain this result, he implemented the solution strategy recommended in the Dutch guideline [20] for simulating the nonlinear behavior of the structures and incorporated Θ in a probabilistic analysis by using Bayesian inference. Following that, he concluded that the global safety factor for modeling uncertainty of numerical models subjected to a high level of validation (suggested as 1.06 in Model Code 2010) is truly valid.

2.2.3. Solution strategy for nonlinear finite element analysis for structural concrete

For this thesis, a solution strategy composed as Dutch guidelines for NLFEA of concrete structures [20] was put to use for modeling the finite element models of the experimental specimens from the test cases [3, 19]. This strategy is only valid for time-independent cases. The following paragraphs are going to explain the detail of every option available chosen for creating the strategy.

2.2.3.1. Constitutive relation

Constitutive relation, or also known as material model, is a term in finite element context to specify the assumed constitute behavior (or stress-strain relationship) of the material used to build the analyzed structure. Constitutive relation is often just a simplified abstraction of the actual material behavior. For reinforced concrete structure, constitutive relations for concrete and reinforcement are required to be determined.

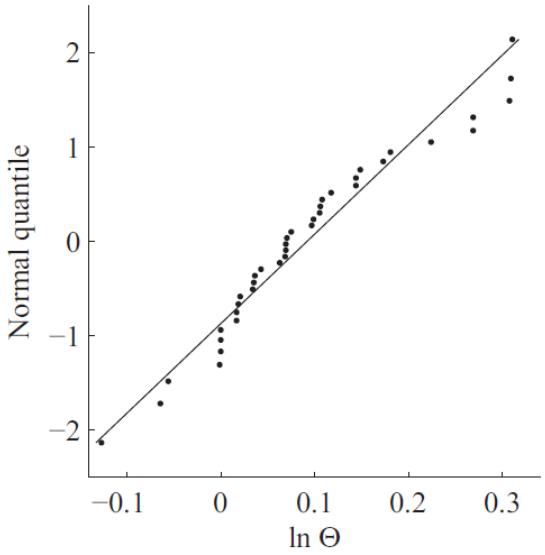

Figure 2.22: Probability plot for modeling uncertainty Θ assuming log-normal distribution [10].

Constitutive relation for concrete

Constitutive relation for concrete consists of concrete's cracking models, linear-elastic properties, tensile behavior, shear behavior, compressive behavior, compression-compression interaction, tension-compression interaction, and crack-band width (or equivalent length). In modeling cracking in concrete, a total strain-based rotating crack or fixed crack model is preferred. As a note, the rotating crack model usually produced a lower-limit ultimate load when compared to the fixed crack model because it does not suffer as much from spurious stress locking.

Then, in determining the linear-elastic properties of concrete, an isotropic, linear-elastic material model based on Young's modulus and Poisson's ratio should be used. For any concrete strength level, Poisson's ratio should be assumed to be equal to 0.15 in its application. Poisson's ratio value should be reduced after cracking process initiates. If the applied cracking model does not include the decrease of Poisson's effect during progressive cracking, additional analysis with a Poisson's ratio equal to 0.0 should be considered. Furthermore, Young's modulus should be inputted with a reduced value. A reduction factor of 0.85 should be used to account for initial cracking due to creep, shrinkage, and alike. The reduced Young's modulus can be calculated using equation 2.11.

$$E_c = 0.85E_{ci} = 0.85E_{c0}\left(\frac{f_{cm}}{f_{cm0}}\right)^{0.3} \tag{2.11}$$

where:

E_{ci} = initial Young's modulus

E_{c0} = 22,000 MPa

f_{cm0} = 10 MPa

As for the tensile behavior of concrete, an exponential type of softening diagram is preferred, e.g., exponential softening diagram and Hordijk softening diagrams, as presented in Figure 2.23a and Figure 2.23b, respectively. They are favored because this type of diagram produces more localized

cracks that help in avoiding large areas of diffuse cracking. The parameters of the diagram are tensile strength (f_t), fracture energy (G_F) and equivalent length (h_{eq}). Nevertheless, if the exponential type of softening diagrams is not available, a multi-linear approximation of the exponential uniaxial stress-strain diagram, as shown in Figure 2.23c, is allowed to be used. According to the fib Model Code 2010 [1], fracture energy may be calculated using the following equation:

$$G_F = 0.073 {f_{cm}}^{0.18} \tag{2.12}$$

To compensate for an underestimation of crack-band width for cracks with an inclination of 45 degrees, the value of G_F should be divided by a factor of $\sqrt{2}$, as in equation 2.13. This reduction factor has to be applied because the ratio of G_F/h_{eq} in smeared cracking determines the actual softening. Therefore, the value of G_F should be decreased in order to obtain a conservative result [20]. This compensation is also mentioned in the validation of Dutch guidelines for NLFEA of reinforced concrete structure [12].

$$G_{F,reduced} = \frac{G_F}{\sqrt{2}} \tag{2.13}$$

Additionally, Hordijk softening curve is expressed using a mathematical expression created by Hordijk [14] presented in equation 2.14.

$$\sigma = \begin{cases} f_t \left(1 + \left(c_1 \frac{\varepsilon^{cr}}{\varepsilon_u}\right)^3 \exp\left(-c_2 \frac{\varepsilon^{cr}}{\varepsilon_u}\right) - \frac{\varepsilon^{cr}}{\varepsilon_u}\left(1 + c_1^3\right) \exp\left(-c_2\right)\right) & 0 \le \varepsilon^{cr} \le \varepsilon_u \\ 0 & \varepsilon^{cr} > \varepsilon_u \end{cases} \tag{2.14}$$

where:

f_t = concrete tensile strength

ε_{cr} = concrete tensile strain

ε_u = concrete ultimate tensile strain

c_1 = 3.00

c_2 = 6.93

Ultimate strain parameter for Hordijk softening curve is calculated using equation 2.15.

$$\varepsilon_u = 5.136 \frac{G_F}{h_{eq} f_t} \tag{2.15}$$

Furthermore, shear behavior is essential to be defined when the fixed crack model is used. A variable shear retention model is strongly recommended to be applied in this situation. For beams and slabs without stirrups, the adequacy of the variable shear retention mode should be verified explicitly.

For modeling compressive behavior of concrete, the concrete compressive strength should be modeled in such way that it has its maximum limit. The use of parabolic stress-strain diagram with softening branch, as illustrated in Figure 2.24 is then recommended. The parabolic compression diagram was designed based on compressive fracture energy (G_C) normalized with a crushing-band width (h) which determination follow the same rules as for tension softening and cracking-band width. The diagram is designed based on G_C in order to reduce mesh size sensitivity during

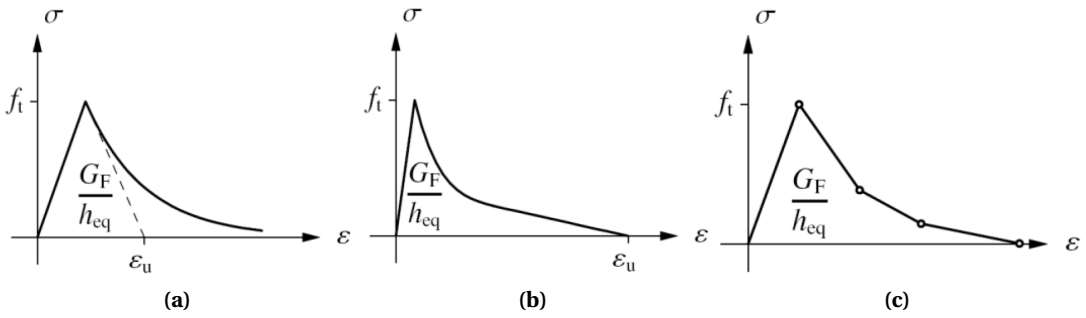

Figure 2.23: Exponential type of softening diagram: (a) exponential softening diagram, (b) Hordijk softening diagram, and (c) multi-linear softening diagram [20].

compressive strain localization. The parabolic compression diagram is defined using the following equation:

$$f = \begin{cases} -f_c \frac{1}{3} \frac{\alpha_j}{\alpha_{c/3}} & \text{if } \alpha_{c/3} < \alpha_j \leq 0 \\ -f_c \frac{1}{3} \left(1 + 4\left(\frac{\alpha_j - \alpha_{c/3}}{\alpha_c - \alpha_{c/3}}\right) - 2\left(\frac{\alpha_j - \alpha_{c/3}}{\alpha_c - \alpha_{c/3}}\right)^2\right) & \text{if } \alpha_c < \alpha_j \leq \alpha_{c/3} \\ -f_c \left(1 - \left(\frac{\alpha_j - \alpha_c}{\alpha_u - \alpha_c}\right)^2\right) & \text{if } \alpha_u < \alpha_j \leq \alpha_c \\ 0 & \text{if } \alpha_j \leq \alpha_u \end{cases} \tag{2.16}$$

where:

α_j = (negative) concrete compressive strain

$\alpha_{c/3} = -\frac{1}{3}\frac{f_c}{E}$

$\alpha_c = 5\alpha_{c/3}$

$\alpha_u = \alpha_c - \frac{3}{2}\frac{G_C}{h f_c}$

$G_C = 250 G_F$, as proposed by Nakamura and Higai [18]

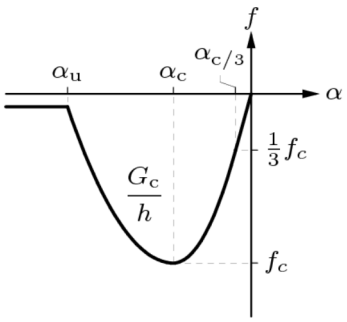

Figure 2.24: Parabolic compression diagram.

In a case of lateral cracking in plane stress models due to tension-compression interaction, concrete compressive strength should be reduced. Inclusion of tension-compression interaction is important in NFLEA of structural concrete since ignoring it is a nonconservative assumption. One reduction model introduced by Vecchio and Collins [29] is shown in Figure 2.25. The reduction coefficient β_σ is expressed as follow:

$$\beta_{\sigma_{cr}} = \frac{1}{1+K_c} \leq 1 \tag{2.17}$$

where:

K_c = $0.27\left(\frac{\alpha_{lat}}{\epsilon_0} - 0.37\right)$

α_{lat} = concrete tensile strain

ϵ_0 = concrete compressive peak strain

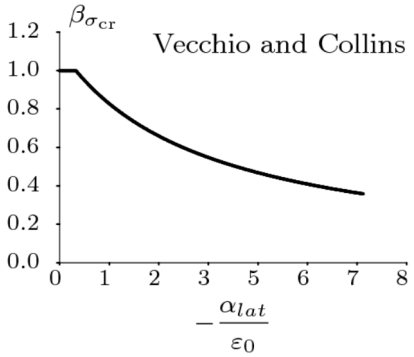

Figure 2.25: Reduction of concrete compressive strength due to tension-compression interaction by Vecchio and Collins.

Nevertheless, the reduction of the compressive strength should be limited to avoid excessive reduction that leads to a nonrealistic response of the structure. The lower limit of the reduction factor ($\beta_\sigma^{\min}$) is 0.4.

In contrast, compression-compression interaction is not necessary to be modeled, despite its importance for simulating the confinement effect. Neglecting the confinement effect is a conservative assumption, and thus it is allowed.

Moreover, equivalent length, which is also known as crack-band width, is one of the essential parameters in constitutive relation for describing the softening stress-strain relationship. It is related to the dimensions of the applied finite element, and its usage is crucial to reduce mesh size dependency. User-assigned values for this parameter is usually inaccurate and therefore using an automatic procedure for determining the equivalent length provided by the finite element software should be applied. The preferred method for determining the equivalent length is the one that based on the initial crack direction and finite element dimension. Optionally, a method based on the area or volume of the finite element can also be used [23], although it can cause some inaccuracy when applied to distorted elements or elements with a high aspect ratio.

Constitutive relation for reinforcement bars

An elastoplastic material model with hardening, as illustrated in Figure 2.26 is the preferred model for reinforcing steel. The hardening, should be modeled according to the specifications of the reinforcement bar. If no hardening specifications available, a nominal hardening modulus (E_{har}) is allowed to be used, and it can be calculated using the following equation:

$$E_{har} = 0.02E_s \tag{2.18}$$

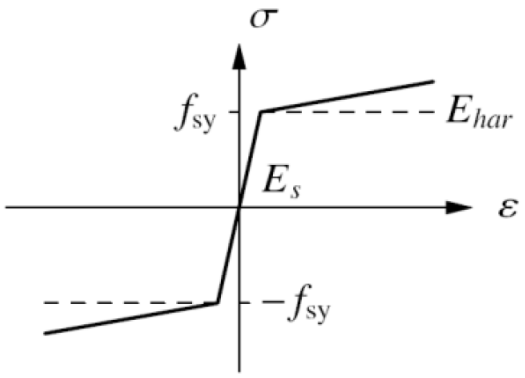

Figure 2.26: Elastoplastic material model for reinforcement bars.

2.2.3.2. Kinematic compatibility

Since the mechanical model of a structure is required to be discretized into numerous finite elements in finite element analysis, having elements that are kinematically compatible with each other and the boundary conditions are important for obtaining a sufficiently accurate finite element solution. To ensure that the compatibility is achieved, various aspects need to be considered, but the most important ones are the shape of the elements used, the degree of interpolation of the displacement field, and the numerical integration scheme for the internal state (or the stress-strain relationship in this case). For reinforced concrete structures, elements that represent the concrete and the reinforcement bars need to be selected separately.

Finite elements for concrete

As for the shape and degree of interpolation, continuum elements with a quadrilateral (2D) or hexahedral shape (3D) that allow quadratic interpolation of displacement field are preferred. Linear elements are not favorable because they show locking behavior in certain cases, while quadratic elements can express more deformation modes and better in simulating more complex failure modes, such as shear failure. If necessary, quadratic triangular and quadratic tetrahedral elements are allowed to be present in analyzing 2D and 3D cases, respectively. An illustration of the mentioned elements are presented in Figure 2.27.

In addition, full integration for quadratic elements should be applied instead of reduced-order integration. The reason is that the use of the latter can lead to spurious modes when the stiffness of the element becomes small due to extensive cracking. The continuum elements mentioned in the previous paragraph are favored to be integrated with the integration rules presented in Figure 2.28 for each respective element type.

Finite elements for reinforcement bars

Regarding modeling the reinforcement bars, application of embedded reinforcement elements are preferred over grid elements. Embedded element has the advantage over explicitly modeling reinforcement with truss elements overlayed on the elements for concrete. With it, the connectivity of the truss elements does not have to be altered to model the reinforcement layout. Conversely, the use of grid elements has the disadvantage of having shear stiffness, which is neglected in embedded elements. Also, to be kinematically compatible with the continuum elements, truss elements with the same order of interpolation should be used. Either full or reduced integration can be used on the elements since they will not exhibit spurious mode due to the inhibition by the embedding elements.

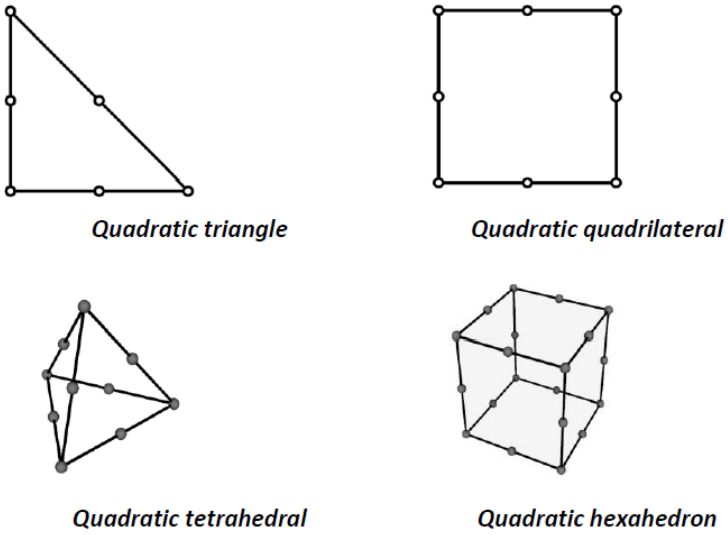

Figure 2.27: Preferred continuum elements to be used to represent concrete [20].

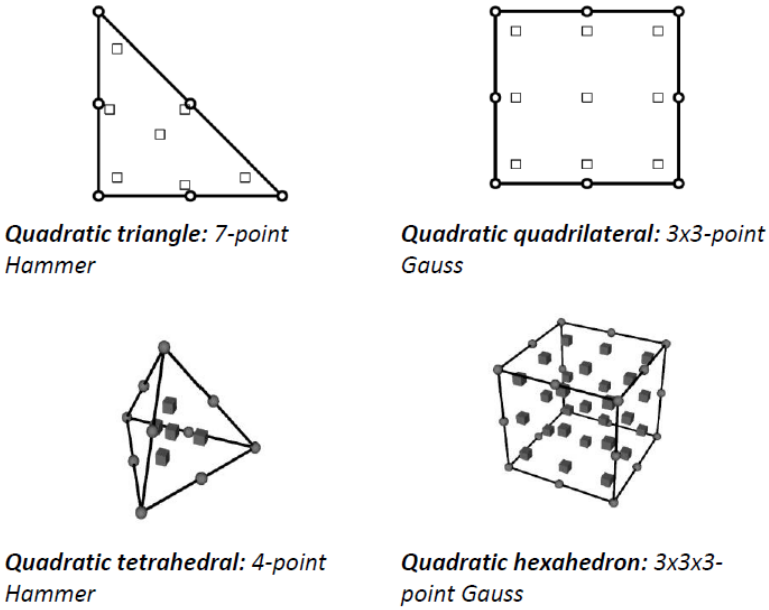

Figure 2.28: Integration points and integration rules for each preferred continuum elements [20].

2.2.3.3. Force equilibrium

Finding an appropriate approach for solving every unique equilibrium equation obtained at every geometrical nonlinearity condition is one of the aspects that have to be taken into account in developing a sound solution strategy. This aspect has a function for decrypting the relations between internal and external forces in establishing equilibrium, which results then form a complete response of the analyzed structure under a specific load configuration. To create the approach, suitable equilibrium iteration procedure and convergence criteria have to be first selected.

In selecting an equilibrium iteration procedure, the Newton-Raphson (NR) method with an arc-length procedure is preferred. NR method is the most commonly used procedure and provides sufficiently accurate and efficient results by using tangent stiffness. There are two types of NR pro-

cedures available: full and modified NR, as illustrated in Figure 2.29a and Figure 2.29b, respectively. The full NR proceeds to obtain a solution with an updated stiffness matrix in every iteration, while modified NR proceeds with a stiffness matrix which is only got updated at the initial iteration. Furthermore, the arc-length procedure is recommended to adjust the load increment during the iteration process. Its usage allows the nonlinear simulation to continue beyond a local or global maximum in the load-displacement response.

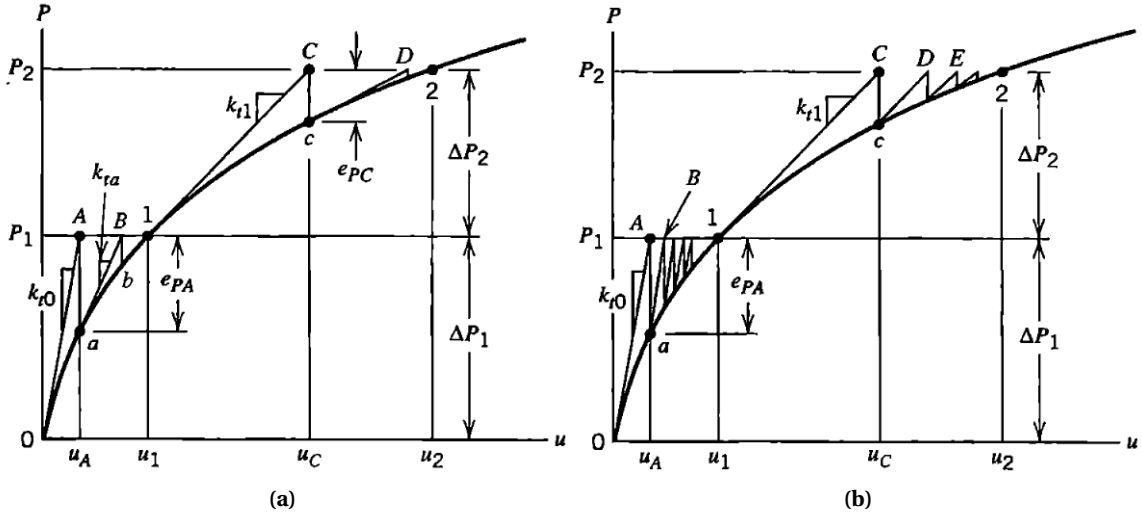

Figure 2.29: Illustration of (a) full Newton-Raphson iteration and (b) modified Newton-Raphson iteration application for achieving convergence at load level P1 and P2 [7].

Subsequently, selecting convergence criteria is the next step in developing an approach for obtaining force equilibrium. Convergence criteria itself is an acceptable error from an engineering point of view for getting an equilibrium solution. Convergence criteria need to be set up to prevent an excessive number of iteration for achieving absolute equilibrium. A convergence criterion is often enhanced with a predefined maximum number. The most frequently used criteria are a norm of the unbalance force vector, the incremental displacement vector, or a norm that based on energy. Although there is no consensus on which criterion that must be used, the Dutch guideline suggested the use of energy-norm together with force-norm convergence criterion with a tolerance of 0.01 and 0.001, respectively. A solution can be considered as converged if at least one of the two norms is satisfied. Load or displacement increments that do not fully comply with the convergence criteria might still be admissible if they are followed by converged load increments and a plausible explanation for the temporary nonconvergence state is given. The sole use of displacement-norm convergence criterion should be avoided.

2.3. Eurocode provision for anchorage length

According to EN 1992-1-1:2004 [28], the basic anchorage length for longitudinal reinforcements, or $l_{b,rqd}$ (see Figure 2.30a), to anchor a tension force in a straight bar while assuming constant bond stress (f_{bd}) can be calculated using the following equation:

$$l_{b,rqd} = (\phi/4)(\sigma_{sd}/f_{bd}) \tag{2.19}$$

where:

ϕ is the diameter of the bar in mm.

σ_{sd} is the design stress of the bar at the position from where the anchorage is measured from.

f_{bd}, which is used for denoting the design value of ultimate bond stress for ribbed bars, may be taken as:

$$f_{bd} = 2.25\eta_1\eta_2 f_{ctd} \tag{2.20}$$

where:

f_{ctd} is the design value of concrete tensile strength.

η_1 is a coefficient related to the quality of the bond condition and the position of the bar during concreting.
$\eta_1 = 1.0$, when 'good' conditions are obtained.
$\eta_1 = 0.7$, for all other cases and for bars in structural elements built with slip-forms, unless it can be shown that 'good' bond conditions exist.

η_2 is related to the bar diameter.
$\eta_2 = 1.0$, for $\phi \leq 32$mm
$\eta_2 = (132 - \phi)/100$, for $\phi > 32$mm

Then, the design anchorage length, or l_{bd}, can be calculated using the following relation:

$$l_{bd} = \alpha_1\alpha_2\alpha_3\alpha_4\alpha_5 l_{b,rqd} \leq l_{b,min} \tag{2.21}$$

where:

α_1 is for the effect of the form of the bars assuming adequate cover.

α_2 is for the effect of concrete minimum cover.

α_3 is for the effect of confinement by transverse reinforcement.

α_4 is for the influence of one or more welded transverse bars $(\phi_t > 0.6\phi)$ along the design anchorage length.

α_5 is for the effect of the pressure transverse to the plane of splitting along the design anchorage length.

$l_{b,min}$ is the minimum anchorage length if no other limitation is applied.
for anchorage in tension: $l_{b,min} \leq max\{0.3l_{b,rqd};\ 10\phi;\ 100\text{mm}\}$
for anchorage in compression: $l_{b,min} \leq max\{0.6l_{b,rqd};\ 10\phi;\ 100\text{mm}\}$

The product of $(\alpha_2\alpha_3\alpha_5)$ should be less or equal to 0.7. The values of α_1, α_2, α_3, α_4, and α_5 can be found in table 8.2 of EN 1992-1-1:2004. Moreover, it is important to mention that $l_{b,rqd}$ and l_{bd} of bent bars should be measured along the center line of the bar.

As a simplified alternative to l_{bd}, the tension anchorage length may be substituted with an equivalent anchorage length, or $l_{b,eq}$, which can be obtained for anchoring method shown in Figure 2.30b using the following equation:

$$l_{b,eq} = \alpha_1 l_{b,rqd} \tag{2.22}$$

According to table 8.2 [28], the value of α_1 is equal to 1.0 for straight type of anchorage.

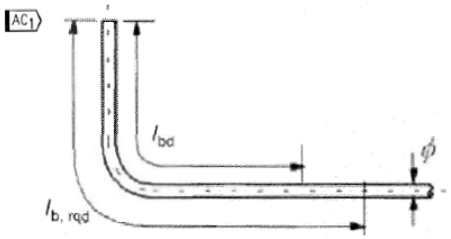

(a) Basic tension anchorage length, $l_{b,rqd}$, for any shape measured along the centerline

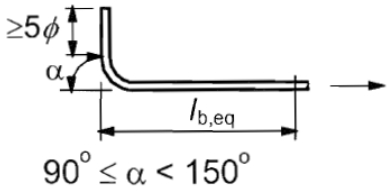

(b) Equivalent anchorage length $l_{b,eq}$ for standard bend

Part 1 - Validation of a numerical approach for verifying the nonlinear behavior of concrete elements

In this part of the thesis, the attempt to validate the use of nonlinear finite element analysis (NLFEA) that adopted a solution strategy recommended by the Dutch guidelines [20] in this research is discussed. The validation is done by verifying the experimental results of six concrete beam elements using their numerical results obtained from the NLFEA. The concrete elements utilized for the validation are experimental specimens that were tested by Oviedo and Maxwell & Breen (Chapter 3), which are later referred to as the test cases. The comparison between the experimental results and numerical results of the test cases to verify the numerical approach using NLFEA is presented in Chapter 4. For all nonlinear analyses executed in this report, a commercial software DIANA FEA 10.3 is used.

3

Description for the test cases

In this chapter, six concrete beam elements and their experimental results that were utilized for validating the use of NLFEA in this research are discussed. Three of those concrete elements are dapped beams with an opening that were selected from an experiment conducted by Oviedo [19]. The other three concrete elements are deep beam with an opening that was selected from an experiment conducted by Maxwell & Breen [3]. These concrete elements were chosen for their geometrical irregularities. In later sections, these concrete elements will be referred to as the test cases.

3.1. Dapped beams with an opening by Oviedo et al. (2016)

3.1.1. Introduction to the experiment

Nine RC beam specimens were experimented using three-point bending tests by Oviedo. Each one of these specimens is a dapped beam with an opening that has a geometry as presented in Figure 3.1. The dimension of the steel plates used to cover the loading and support areas are also specified in the same figure. Two geometric irregularities were presence in each of these specimens, namely a 127-mm dap at midspan and a 51-mm square opening located between the loading point and the left support. Oviedo held this experiment to investigate which of the two examined ST modeling techniques can produce an RC structure with better performance, steel efficiency, and crack growth control. The two techniques in comparison are the conventional ST modeling method (see Section 2.1.2.1) and the full homogenization method, which is a TO method researched by Herranz et al. [13].

In his research paper, Oviedo provided the material properties of the dapped beam in term of mean values. The mean values were obtained from independent tests on the concrete and steels used to construct the specimens. Based on those tests, the concrete appeared to have an average compressive strength (f_{cm}) of 65.8 MPa according to cylindrical samples tested on the same day as the experiment, while the rebars had average values of yield strength (f_{ym}) and ultimate strength (f_{um}) as presented in Table 3.1. Additionally, the rebars had an average measured modulus of elasticity of 202 GPa. The high strength value of concrete was not expected by Oviedo since initially he planned for the dapped beams to have a nominal concrete compressive strength of 30 MPa.

Furthermore, the dapped beams tested in this experiment can be categorized according to their ST model's design method. Five dapped beams had rebar layouts that were generated from ST models designed in accordance with the optimal topology of the dapped beam shown in Figure 3.2. The other four specimens had rebar layouts which were derived from ST models produced using conventional ST modeling method.

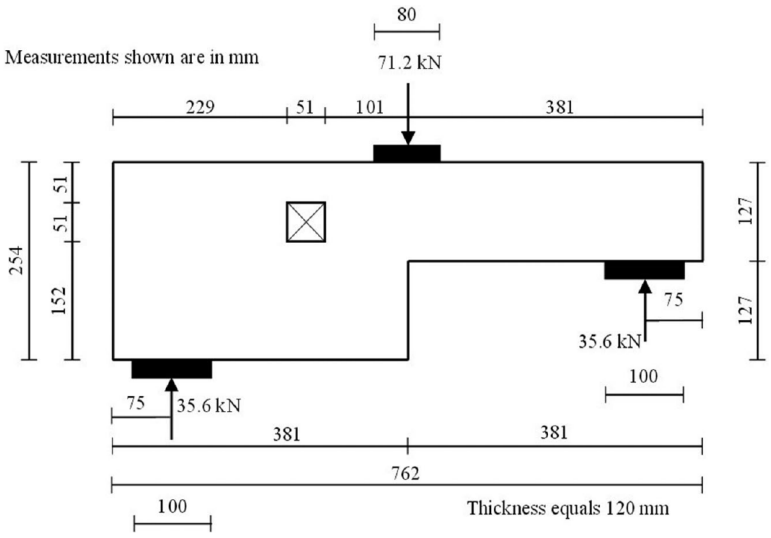

Figure 3.1: Geometry of the tested dapped beam [19].

Table 3.1: Measured strength and strain of the rebars [19]

Bar diameter (mm)	Area (mm^2)	Yield Strength (MPa)	Ultimate strength (MPa)	Ultimate strain (‰)
4	12.6	522	604	10.0
4.6	16.6	508	603	15.0
7	38.5	532	623	11.8
10	78.5	625	650	11.5

For the purpose of research in this thesis, three dapped beam specimens were selected. They are the dapped beams that are denoted as F-1, G-1, and H-1 and their rebar layouts are illustrated in Figure 3.3. Specimen F-1, G-1, and H-1 are the first series dapped beams which rebar layouts designed to coincide with the orientation of the ties of their respective ST models. An example of the actual assembly of the specimens' rebars is shown in Figure 3.4 for specimen F-1.

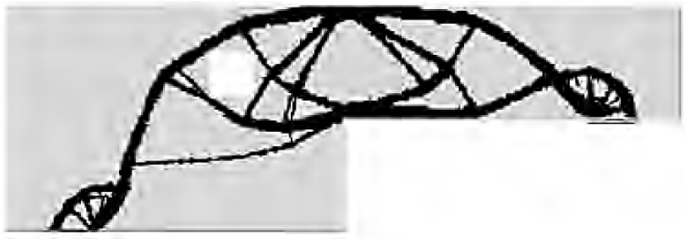

Figure 3.2: The optimal topology of a dapped beam with an opening according to full homogenization method [13].

During the test, the dapped beams were simply supported while being loaded with a hydraulic jack from the middle top of the beam, as shown in Figure 3.5. The concentrated load given to the dapped beams was increased monotonically until the load applied by the hydraulic jack began to decrease, specifying the degradation of specimen stiffness. The beams were expected to fail at a load level of 71.2 kN, at the very least. That load level is a factored load which was calculated under an assump-

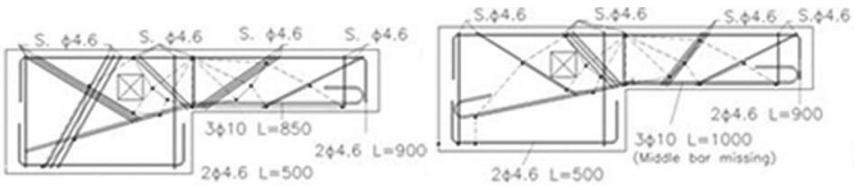

(a) F-1 **(b)** G-1

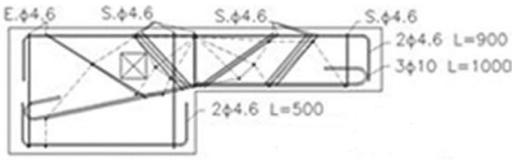

(c) H-1

Figure 3.3: Rebar layouts of specimen F-1, G-1, and H-1 [19].

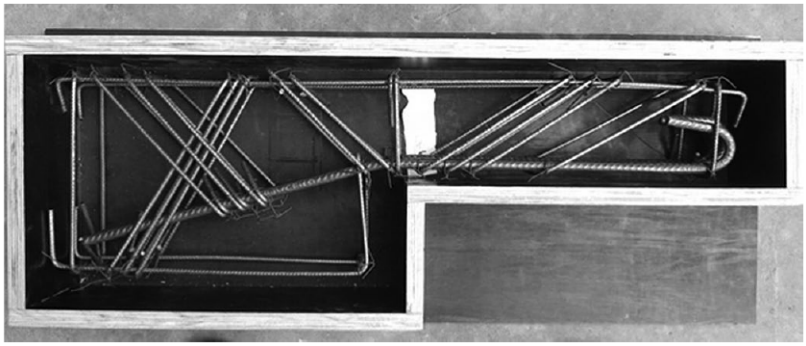

Figure 3.4: Reinforcement cage of specimen F-1 [19].

tion that the specimen should be able to bear a load combination of 1.4DL + 1.7LL (DL is dead load and LL is live load, and this combination was taken from ACI 318-99 for static loading) with a resistance factor, ϕ, of 1.0. Using that assumption, Oviedo calculated the factored load by multiplying the predetermined service load at the level of 45.9 kN with a factor of 1.55, which is the average of the factors from the assumed load combination. That same factored load is then also used as design load for the ST models.

To measure the deflection of the specimens under the applied load, three linear variable differential transducers or LVDT were placed. They are placed at the quarter points of the beam length and the midspan, as shown in Figure 3.6. Also, a digital image correlation or DIC procedure was implemented on the dapped beams to obtain the displacement field measurements which later used to calculate the occurring strains at various load levels.

3.1.2. Strut-and-tie models of the test cases of Oviedo

To develop the rebar layouts of specimen F-1, G-1, and H-1, three ST models which shapes were modeled after the optimal topology of the dapped beam were generated. These ST models are shown in Figure 3.7. The F-series ST model was the first truss model that is designed by Oviedo from the optimal topology. This ST model appeared to contain a flaw by having a set of strut and tie near the left support that forms an angle of 20 degrees, which is less than the minimum angle (25 degrees) recommended in ACI 318-08 [2].

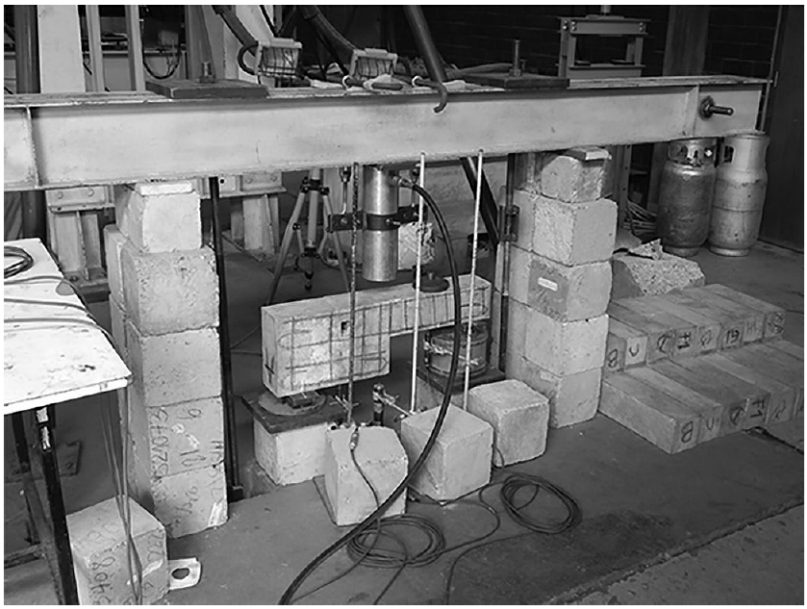

Figure 3.5: Load frame for experimental setup [19].

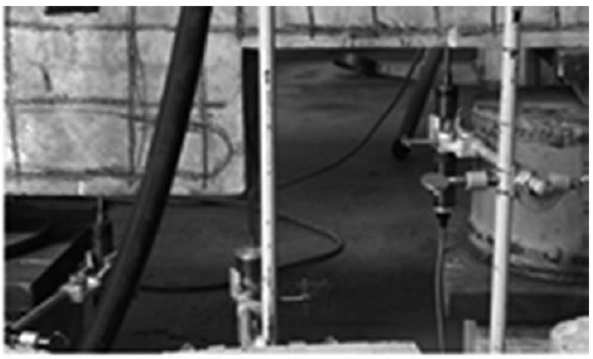

Figure 3.6: LVDT instruments [19].

Then, the second truss model was created as an improvement toward the former ST model, and it is labeled as the G-series ST model. The flaw in the F-series ST model was eliminated by lifting the node located over the left support and elongating the tie that extends from the location of the dap toward the newly positioned node.

Due to the concern over the G-series ST model's capability to control the diagonal tension crack growth at the right part of the dapped beam, the H-series ST model was developed. This third ST model was designed to be more capable of handling the development of diagonal tension crack by modifying the inclination and the length of the right-most diagonal tie of the G-series ST model. This diagonal ties had its angle of inclination changed to 45 degrees and its upper node raised to the same height level as its adjacent node. In Herranz's paper, the G-series and H-series ST models can also be found to be labeled as FH and FH modified ST models, respectively [13].

It is important to mention that, in Oviedo's paper, the information regarding the axial forces in the truss members is provided, but there is no information that can indicate if any strut-and-tie dimensioning process had been done.

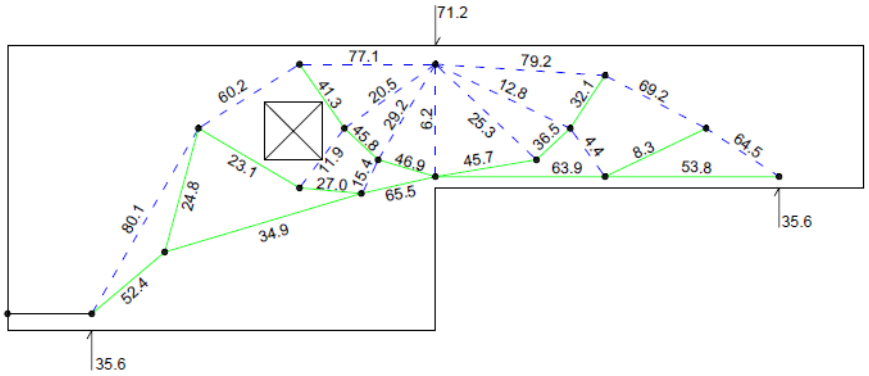

(a) F-series ST model

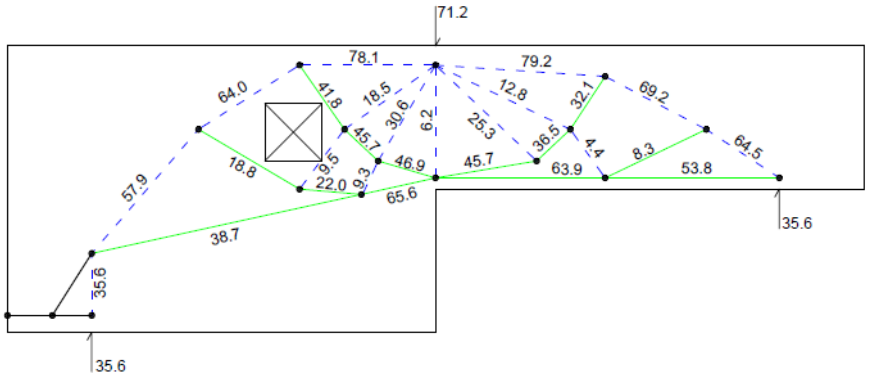

(b) G-series ST model

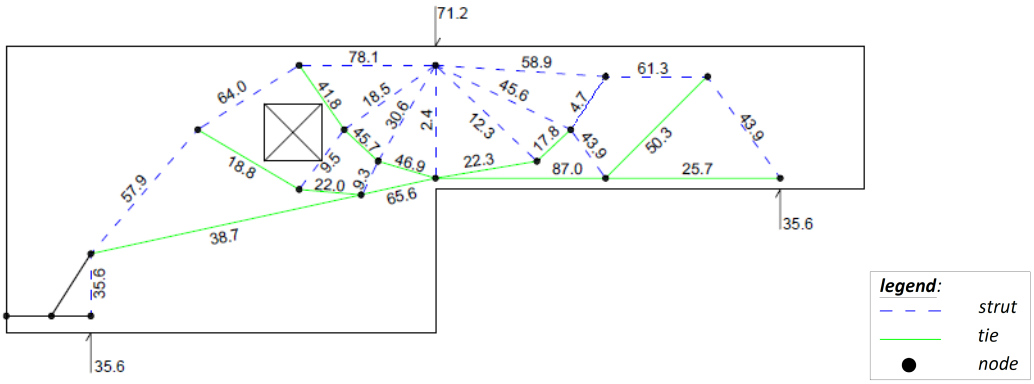

(c) H-series ST model

Figure 3.7: ST models of specimen F, G, and H series [19].

3.1.3. Experimental results of the test cases of Oviedo

Oviedo's explanations regarding the crack patterns, failure mechanisms, and ultimate capacities for each tested specimen are presented in this section. As a start, the recorded response of all specimens presented as load-displacement curves can be seen in Figure 3.8.

In his paper, Oviedo reported that the first series specimens appeared to experience a similar kind of flexural failure mechanism which occurred due to the uncontained growth of a flexural crack at the reentrant corner. The consequence of the flexural failure to specimen F-1, G-1, and H-1 are respectively shown in Figure 3.9a, 3.9b and 3.9c. The failure initialized from a crack that traveled from the reentrant corner towards the loading point and later widened progressively as the applied load

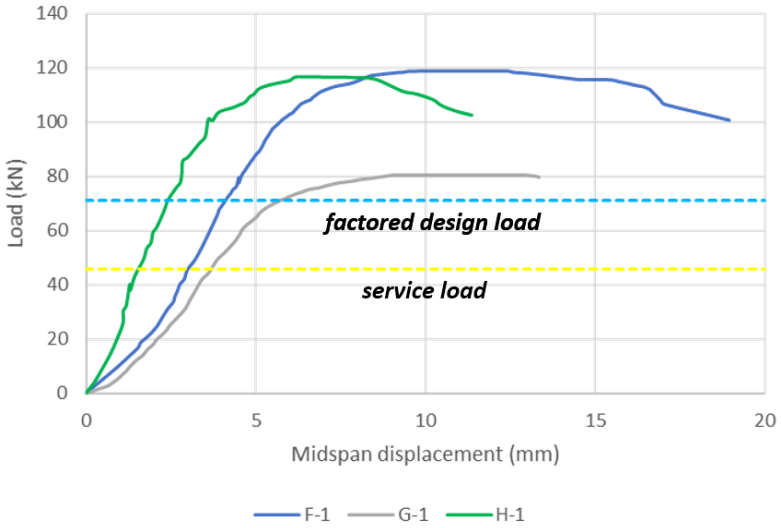

Figure 3.8: Load-displacement curves of specimen F-1, G-1, and H-1 [19].

increased until it ultimately caused the beams to collapsed with a flexural failure mode. Furthermore, Oviedo also described several observable narrow inclined cracks that emerged on the right side of these beams, as well as at the corners of the opening. He believed that these cracks did not advance into a failure mechanism because the installed diagonal rebars at those areas managed to contain the growth of those cracks.

Moreover, the measured response of first series specimens showed that specimen F-1 and H-1 respectively failed at the load level of 118.9 kN and 116.8 kN, whereas G-1 failed at the load level of 80.3 kN, as displayed in Table 3.3. The measured ultimate capacity of specimen G-1 was relatively much lower than its first series counterparts due to the fact that one of its main longitudinal rebars was unintentionally not installed (rebar 10 mm), as specified in Figure 3.3b.

Table 3.2: Failure modes and crack patterns at failure [19]

Specimen ID	Failure mode and location	Cracking at reentrant corner	Cracking at opening	Cracking on the right side
F-1	flexural/midspan	wide vertical	short, narrow	narrow, flexural cracks
G-1	flexural/midspan	wide vertical	no cracks	flexural cracks
H-1	flexural/midspan	wide vertical	short, narrow	narrow, flexural cracks

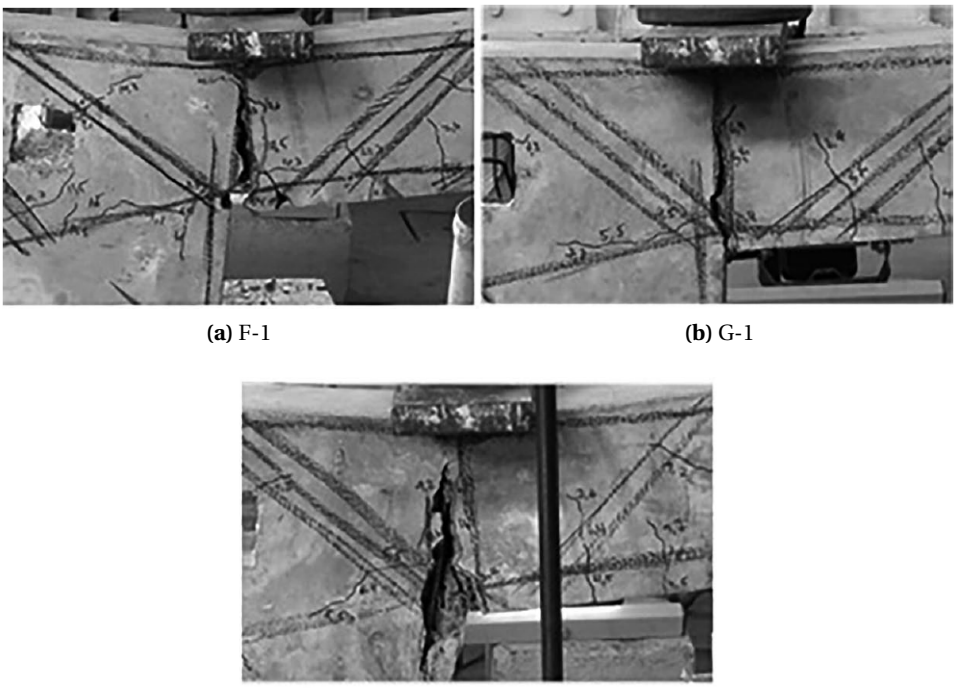

(a) F-1 **(b)** G-1

(c) H-1

Figure 3.9: Pictures of specimen series F, G, and H at failure [19].

Table 3.3: Cage weight and measured ultimate capacity [19]

Specimen ID	**Cage weight W_c (kg)**	**Measured capacity P_{ult} (kN)**
F-1	3.30	118.9
G-1	2.50*	80.3
H-1	3.25	116.8

**) this cage weight does not include the uninstalled longitudinal rebar*

3.2. Deep beams with a large opening by Maxwell and Breen (2000)

3.2.1. Introduction to the experiment

An investigation over the behaviour of a deep beam with a large opening designed with STM was held by Maxwell & Breen. For this investigation, four specimens of the deep beam were constructed and were tested with unsymmetrical three-point bending tests. The constructed specimens had a geometry as illustrated in Figure 3.10 and a beam thickness of 89 mm. The dimensions of the neoprene pads used to cover the loading and support areas were also shown in the same figure and they were approximated based on the original illustration of the beam. Additionally, the deep beams were designed with one geometric irregularity, which is a 273-mm square opening located near the left support. The objective of this study was to verify the basic concepts of ST modeling [24] as well as its applicability and versatility.

The specimens from this experiment were selected for the numerical studies in this thesis because

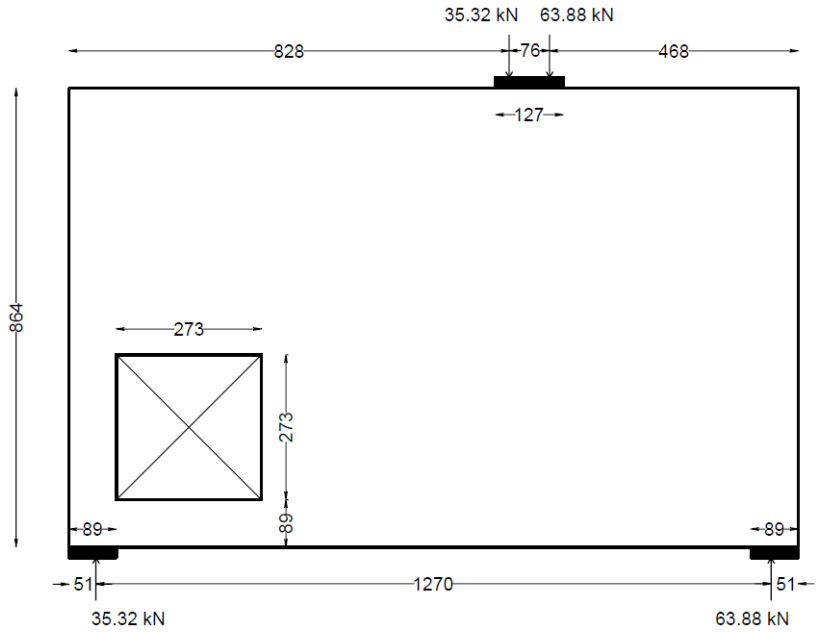

Figure 3.10: Geometry of the tested specimens (in mm) [3].

the design of the ST models used in this test had compatibility with a TO result which were produced for the same deep beam with a large opening by Herranz using full homogenization method [13] (see Figure 3.11). Due to this compatibility, the author of this thesis decided to take an assumption that the ST models from Maxwell & Breen's experiment were directly modeled after Herranz's TO result for the deep beam in order to align this experiment with the topic of the study. This assumption has to be taken since there is a lack of experimental researches in regards of studying the robustness of TO results and the author could only find the experimental study by Oviedo [19] that is available.

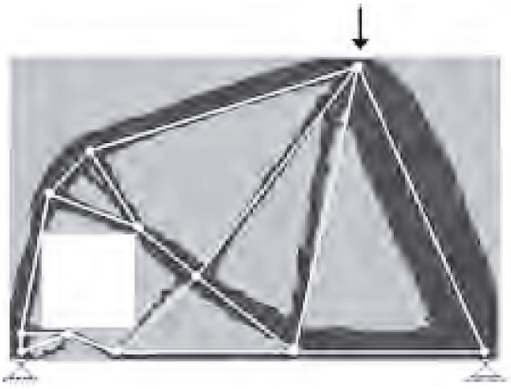

Figure 3.11: Optimal topology of deep beam with a large opening according to full homogenization method [13].

Before they began the construction, Maxwell & Breen tested the concrete and steel used to build the specimens to acquire the mean values of these materials' strength. The average concrete compressive strength (f_{cm}) of the deep beams were obtained from 28-day concrete strength tests and their values are presented in Table 3.4. In a separate test, the concrete was also showed to have an average compressive strength (f_{cm}) of 28.3 MPa. Meanwhile, the rebars were shown to have average yield

strengths (f_{ym}) of 586 MPa and 565 MPa for steel with a diameter of 3 mm and 6 mm, respectively.

Table 3.4: Average concrete compressive strength of the specimens [3]

Specimen ID	f_{cm} **(MPa)**
2	27.72
3	27.85
4	28.68

For investigating the influence of a certain ST model design toward the behavior of the deep beam, every tested specimen was constructed with a particular rebar layout. Four rebar layouts were designed for the experiment with respect to four different ST models developed for a deep beam with a large opening. The specimens with those rebar layouts were labeled as specimen 1, 2, 3, and 4, as shown in Figure 3.12. For the purpose of this thesis, only specimen 2, 3, and 4 are discussed in this section. An example of the actual assembly of the specimens' rebars is shown in Figure 3.13 for specimen 3. Further detailed information regarding the ST models are discussed in Section 3.2.2.

To do the unsymmetrical three-point bending tests, all four specimens were simply supported and were loaded with a concentrated load using a universal test machine. The simple supports were placed below neoprene pads that were supported with concrete blocks. To prevent out-of-plane movements, Maxwell & Breen installed a steel guide frame around the bottom of each specimen, but none of the specimens experienced any out-of-plane movements in the end. During the experiment, the displacement-based test machine administered the load incrementally through a neoprene pad placed at the loading area. The specimens were expected to fail at the load level of 99.2 kN, at the very least. That expected capacity came from a factored load that was calculated under an assumption that the specimen should be able to bear a load combination of 1.4DL + 1.7LL (DL is dead load and LL is live load and the combination was taken from ACI 318-99 for static loading) with a resistance factor, ϕ, of 1.0. Using that assumption, Maxwell & Breen calculated the factored load by multiplying the predetermined service load at the level of 64 kN with a factor of 1.55, which is the average of the factors from the assumed load combination. That same factored load is then also used as a design load for the ST models. Moreover, to monitor the deflection of the beam during the loading, it is only mentioned that Maxwell & Breen used a dial gauge, which was removed before any of the specimens experience any failures.

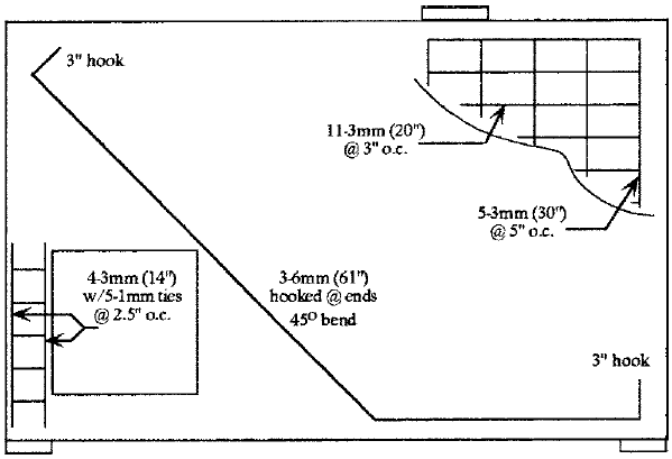

(a) Specimen 2

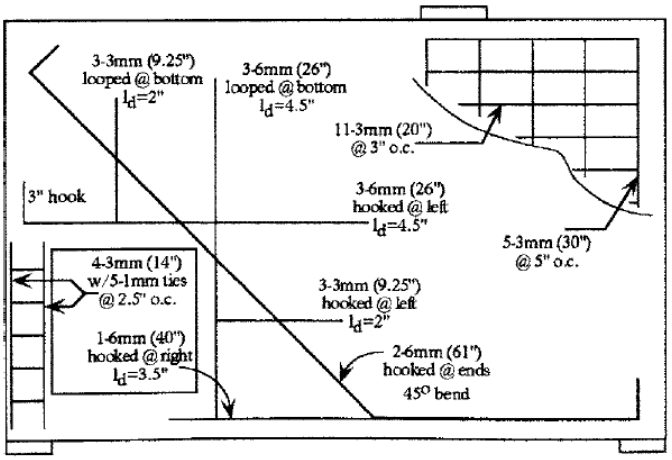

(b) Specimen 3

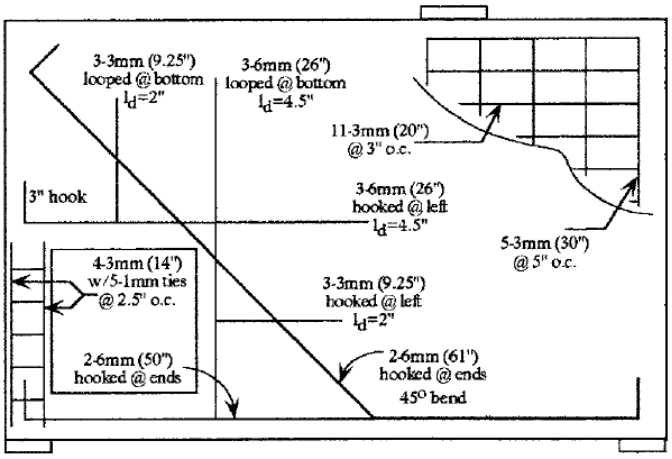

(c) Specimen 4

Figure 3.12: Rebar layouts of specimen 2, 3, and 4 [3].

3.2.2. Strut-and-tie models of the test cases of Maxwell & Breen

To design the reinforcements of the tested specimens, Maxwell & Breen utilized various ST models for a deep beam with a large opening that was developed using conventional ST modeling technique

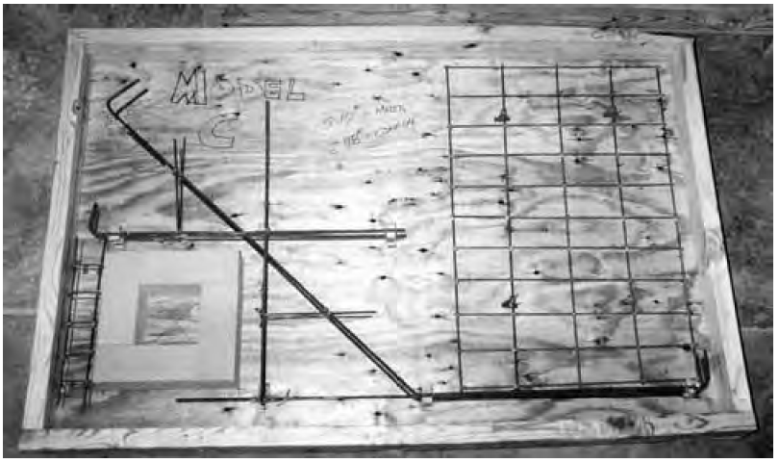

Figure 3.13: Actual rebar installation of specimen 3 [3].

(see chapter 2.1.2.1). These ST models are shown in Figure 3.14 for each specimen. The design of these truss models was inspired by an ST model proposed by Schlaich et al. [24] for a similar deep beam. In the original design, one substructure was created for the right part of the beam for dealing with a large bottle-shaped strut inclining toward the right support, while two superpositioned substructures that surround the opening were created for the left part of the beam. Then, these substructures were conjoined as one complete truss model for the deep beam. This original ST model was then used by Maxwell & Breen as the ST model for designing specimen 3, while specimen 2 utilized the same truss model, but only used the triangle-like substructure as a load path at the left part of the beam. Meanwhile, the ST model for specimen 4 is a modified version of specimen 3's ST model which was produced by having the left-top most node moved slightly to the right to let a tie to develop below the opening.

It is important to mention that, in Maxwell & Breen's paper, the information regarding the axial forces in the truss members is provided, but there is no information that can indicate if any strut-and-tie dimensioning process had been done.

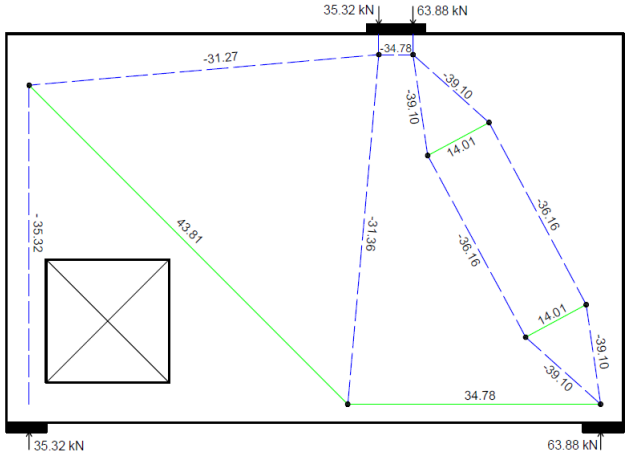

(a) Specimen 2

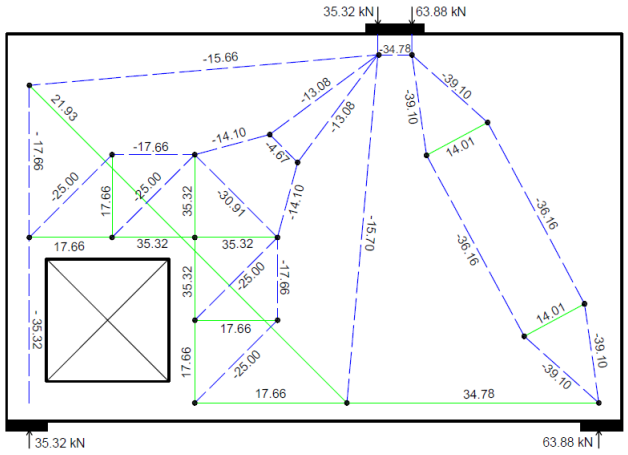

(b) Specimen 3

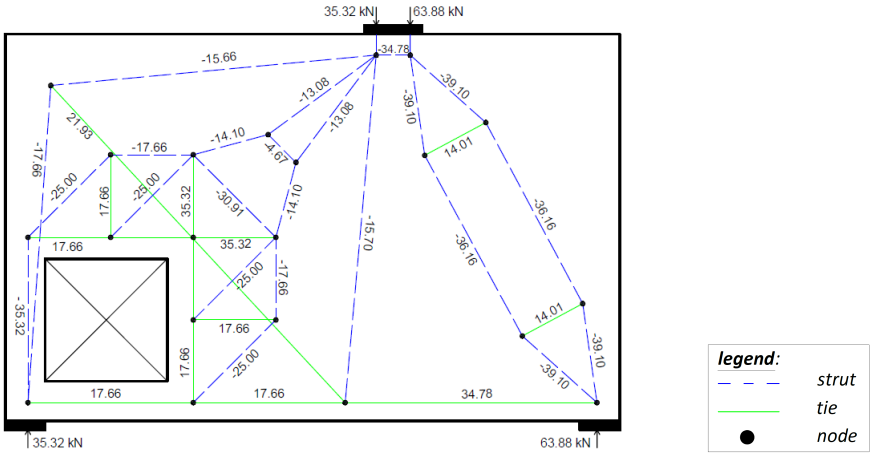

(c) Specimen 4

Figure 3.14: ST models of specimen 2, 3, and 4 [3].

3.2.2.1. Experimental results of the test cases of Maxwell & Breen

Maxwell & Breen's explanations regarding the crack patterns, failure mechanisms, and ultimate capacity that the specimens had as the result of the tests are presented in this section. The explanation starts with specimen 2 and continued with specimen 3 and 4. As a start, the original recorded re-

sponse of these specimens during their tests are presented as load-displacement curves shown in Figure 3.15 and the summary of the results of the tests are presented in Table 3.5.

It is important to mention that the information regarding the ultimate capacity and displacement of these deep beams are not included in the load-displacement curves. The data about these two parameters are not presented in the curves because the dial gauge used to measure the displacement of these models were removed right before every beam experienced failure. Therefore, Maxwell & Breen could not record the ultimate displacement of the beams, and they have to present the ultimate load data as a separate information. To complete the information provided in the load-displacement curves, the ultimate load data of each beam is incorporated in the form of horizontal dashed lines that match the color of their respective curves. Additionally, an arrow is added to the end of each curve to indicate that there is still a response continuation after that end.

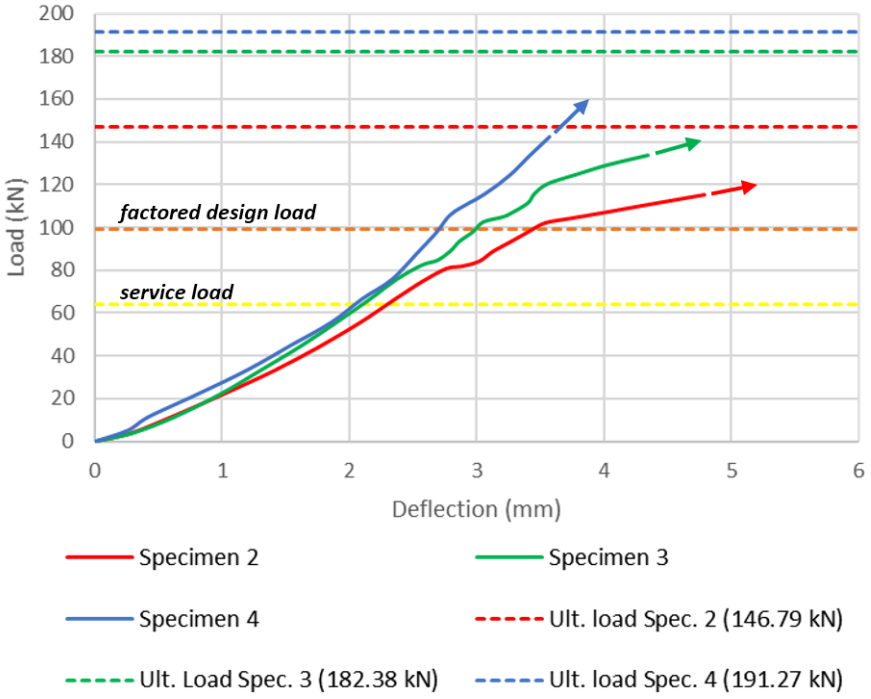

Figure 3.15: Load-displacement curve of specimen 2, 3, and 4 [3].

Table 3.5: Summary of Maxwell & Breen experimental results [3]

Specimen ID	Measured ultimate capacity (kN)	Deflection at factored design load (mm)	Total weight of steel (kg)
2	146.79	3.32	2.40
3	182.38	2.87	3.45
4	191.27	2.79	3.85

In the case of specimen 2, it was reported that the specimen failed due to flexural forces. According to Maxwell & Breen, the long inclined rebars located above the opening was significantly elongated during the test due to relatively high tension stresses near the top-right corner of the opening. The elongation caused the concretes below those strained rebars to crumble and fell. Nevertheless,

these steels managed to prevent shear failure by controlling the growth of a diagonal shear crack that traveled from the loading point toward the top-right corner of the opening, as illustrated in Figure 3.16a. Ultimately, the specimen was described to experience a split due to uncontained crack growth, which propagated perpendicularly from the middle of the inclined rebars. Compared to the other specimens, specimen 2 was the specimen with the largest deflection and the widest crack width.

In the case of specimen 3, the deep beam was reportedly collapsed due to a flexural failure mechanism. It was described that the specimen initially displayed a diagonal shear crack that took form at the left-top corner of the beam and a flexural crack that propagated from the loading point toward the middle of the long inclined rebars, as shown in Figure 3.16b. Despite that, the steels placed around the opening managed to control the development of both cracks. At higher load level, flexural cracks began to form around a node at the bottom-middle of the beam (node 't'), and later, one of them began to propagate through the unreinforced part at the middle the beam toward the loading point which eventually caused the flexural failure, as shown in Figure 3.17. In addition, it was also observed that the column-like part of the beam at the left side of the opening was crushed at a relatively high load level.

Conversely, despite having a similar rebar layout characteristically with specimen 3, specimen 4 was described to experience a shear failure mechanism. Maxwell & Breen explained that due to the presence of the extra longitudinal rebars below the opening, the deep beam became more prone to a shear failure that degraded the left-top part of the beam rather than becoming susceptible to a flexural failure mode as exhibited by specimen 3. The shear failure initialized as a shear crack above the orthogonally-arranged steels that later traveled around the left of that steel layout toward the left-top corner of the opening. When the load level got closer to the ultimate load level, the concrete at the bottom of the opening suffered severe damage by flexural cracks, and the column-like part of the beam at the left side of the opening was extensively crushed. The final crack pattern of specimen 4 is illustrated in Figure 3.16c. According to the recorded response of specimen 4, it turned out to be the stiffest beam to tested in the experiment, while also being the specimen with the highest ultimate capacity.

Additionally, Maxwell & Breen also gave a separate explanation regarding the performance of the concrete below the opening of specimen 2 and 3 while comparing it with the performance of the same concrete part at specimen 4. They expected for this concrete part to perform poorly at specimen 2 and 3 since there was no rebar installed at that location. Unlike specimen 4's, this concrete section immediately developed a vertical crack at its bottom left which continued with the propagation of another vertical crack below the bottom-right corner of the opening as the test proceeded. After both vertical cracks fully developed, this beam section then fell to the ground. Despite the occurrence of this predicted situation in specimen 2 and 3, the author stated that the load capacity of these specimens was not affected.

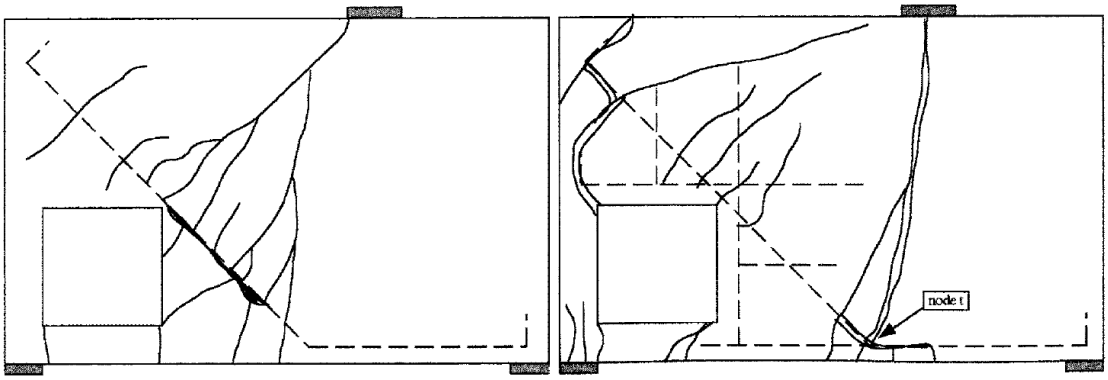

(a) Specimen 2 **(b)** Specimen 3

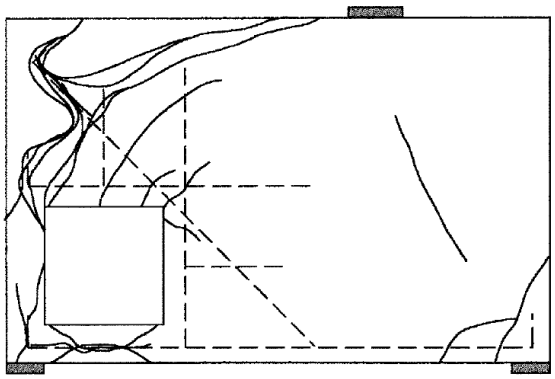

(c) Specimen 4

Figure 3.16: Illustration of specimen 2, 3, and 4 crack patterns [3].

Figure 3.17: Specimen 3 after failure [3].

4

Numerical validation on the experimental results

4.1. Description of the numerical models of the test cases

4.1.1. Geometry of the numerical models

The numerical models of the test cases were generated based on the geometry of the concrete specimens tested by Oviedo and Maxwell & Breen. They are reproduced in a two-dimensional environment. To reimagine the three-point bending tests of each concrete specimen using displacement control, points supports were applied on the support plates and the loading plate of each model. Typical numerical models of a dapped beam with an opening and a deep beam with a large opening are presented in Figure 4.1a and 4.1b, respectively. Additionally, typical meshed model of a dapped beam with an opening and a deep beam with a large opening are presented in Figure 4.2a and 4.2b, respectively.

4.1.2. Plate-to-concrete interface

For all numerical models, the support and loading plates were modeled as linear elastic steel that has Young's modulus of 210,000 MPa. The interface between the steel plates and the concrete specimens were then defined to prevent the steel plates acting as outer reinforcements to the concrete models. Since the concrete specimens are reimagined in 2D environment, the interfaces were also modeled as 2D interface elements (CL12I).

The plate-to-concrete interface has two properties that need to be determined: normal stiffness and shear stiffness. They are determined based on the properties of the concrete specimens. For example, normal stiffness is defined as equal to Young's modulus of concrete, while shear stiffness is defined as Young's modulus of concrete divided by 1000. The properties of the interface elements that are determined for the dapped beams and deep beams model are shown in Table 4.1.1. The thickness of these interface elements are assumed to be 1 mm.

4.1.3. Solution strategy adopted for the nonlinear simulation

To obtain reasonable results from the nonlinear analysis of the test cases, a solution strategy is adopted. This strategy was developed based on validated recommendations provided in the Dutch guidelines for NLFEA of concrete structures [20].

For meshing the numerical models, finite element size of the model of each concrete element type need to be determined. Finite elements with the size of 10 mm were selected for Oviedo's dapped

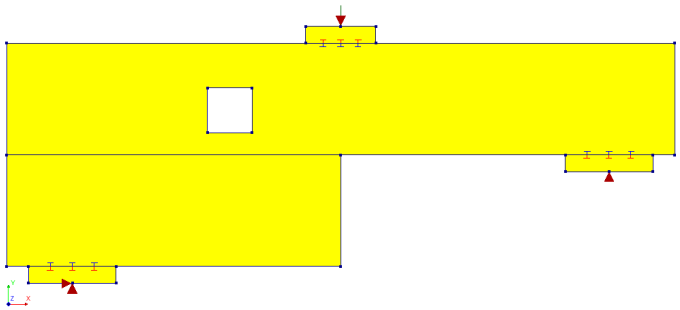

(a) Dapped beam model

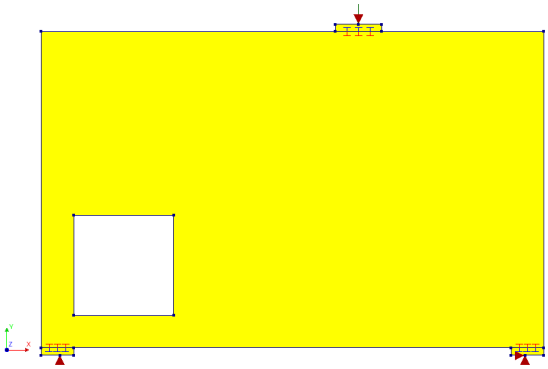

(b) Deep beam model

Figure 4.1: Typical numerical models for each type of experimented specimens

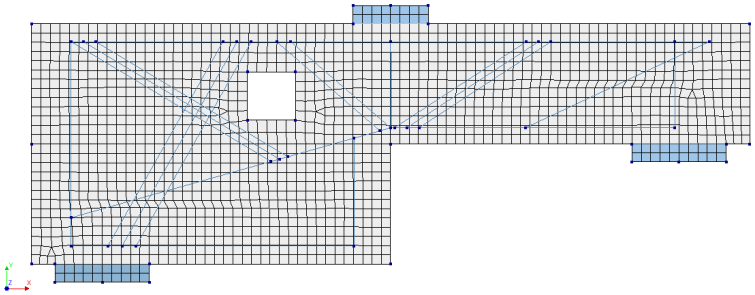

(a) Dapped beam model (meshed)

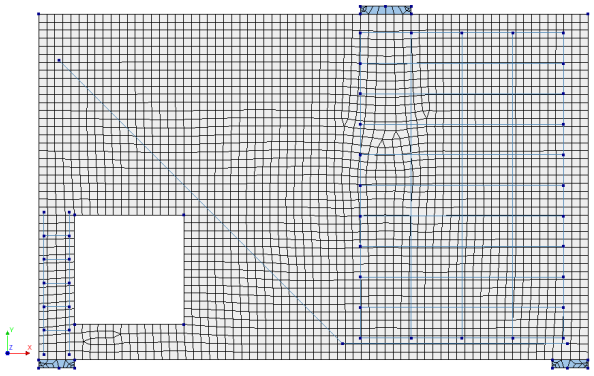

(b) Deep beam model (meshed)

Figure 4.2: Typical meshed numerical models for each type of experimented specimens

Table 4.1: Plate-to-concrete interface properties for the dapped beams and deep beams model

Experiment	Property	Value
Oviedo et al.	Normal stiffness	$32,908\ ^{N}/_{mm^3}$
	Shear stiffness	$32.91\ ^{N}/_{mm^3}$
Maxwell & Breen	Normal stiffness	$25,549\ ^{N}/_{mm^3}$
	Shear stiffness	$25.55\ ^{N}/_{mm^3}$

beam models, while Maxwell & Breen's deep beam models had 20-mm element size. Several linear finite element analyses (LEFEA) results were used to determine the suitability of those element sizes in terms of accuracy and computational cost, while the maximum element size limit was determined in regards to a suggestion given in the Dutch guideline [20]:

$$maximum\ element\ size = min\left(\frac{l}{50}, \frac{h}{6}\right) \tag{4.1}$$

where l is the span of the analyzed structure, and h is the depth of the analyzed structure. Additionally, the idealization of their mechanical models toward the physical problems of the test cases was also implemented on the finite element models. They were modeled as 2D models, hence the quadratic 2D element type (CQ16M), with point supports and point load. Quadratic element type was selected over linear element type in order to obtain more accurate NLFEA results.

Furthermore, the constitutive relations in the solution strategy were developed using the concrete and steel properties of the test cases. Each of those properties was defined using the mean values of the material strengths provided in the literature of the experiments [3, 19]. Since not all material parameters were presented in the literature, the undisclosed parameter values had to be assumed. Most of the assumed values were computed using recommended formulas given in the Dutch guidelines [20], which described the relation between each material parameter. Exceptionally, the ultimate strength of the rebars installed in the Maxwell & Breen's deep beams were assumed using a relation defined in ASTM A615, which stated that the required ultimate strength of grade 75 (520 MPa) rebars is about 1.33 times its yield strength. The ultimate strain of those rebars were then derived from the assumed ultimate strength values. All material parameters used to build the constitutive relations of the concrete and reinforcement bars are presented in Table 4.4 and Table 4.5, respectively.

On top of that, the concrete and reinforcement bar models and behaviors were also determined based on the recommendations [20]. Rotating crack model was chosen to represent the cracking behavior of concrete, with its crack-band width specification following Rots' recommendation [23]. Then, Hordijk softening curve [14] and parabolic compressive curve were applied to direct the concrete's tensile and compressive behavior of the test cases models, respectively. The application of both types of concrete behaviors on Oviedo's and Maxwell & Breen's numerical models are shown in Figure 4.3 and 4.4, respectively. Several strain values from this curves are utilized to define the nonlinear behavior of the beam models in the generated NLFEA results. For defining the tensile strain condition at the principal tensile strain (Ecw1) contour plots, the minimum tensile strain of that plot is set at the crack strain of the concrete, while the maximum tensile strain of that plot is set at the tensile strain when the concrete only have 10% left of its tensile strength during the softening. Meanwhile, for defining the compressive strain condition at the principal compressive strain (E2) contour plots, the maximum compressive strain of that plot is set at $\alpha_{c/3}$ value, while the minimum compressive strain of that plot is set at the α_c value. The minimum and maximum strain values

applied on the numerical models of Oviedo and Maxwell & Breen are summarized in Table 4.2

Additionally, the reduction of the compressive strength due to lateral cracking was also chosen to be modeled using Vecchio & Collins's (1993) model [29] and the reduction of the tensile strength due to Poisson's ratio is also modeled (damage based). Meanwhile, the reinforcement bars behavior were chosen to be governed with a bi-linear elastoplastic material model with hardening. This type of material behavior is presented in Figure 4.5 and 4.6, for Oviedo's and Maxwell & Breen's experiments respectively.

The solution strategy was then applied to the NLFEA of the test cases. The point load on each beam model was applied incrementally in a displacement-controlled fashion with 500 steps of 0.2% of the applied displacement. Full Newton-Raphson method was applied on all test cases to do the equilibrium iteration of their NLFEA, with force and energy norms as the parameters for finding the solution. Tolerance of those norms were 0.01 and 0.001, respectively, and the option to satisfy all specified norm was not used.

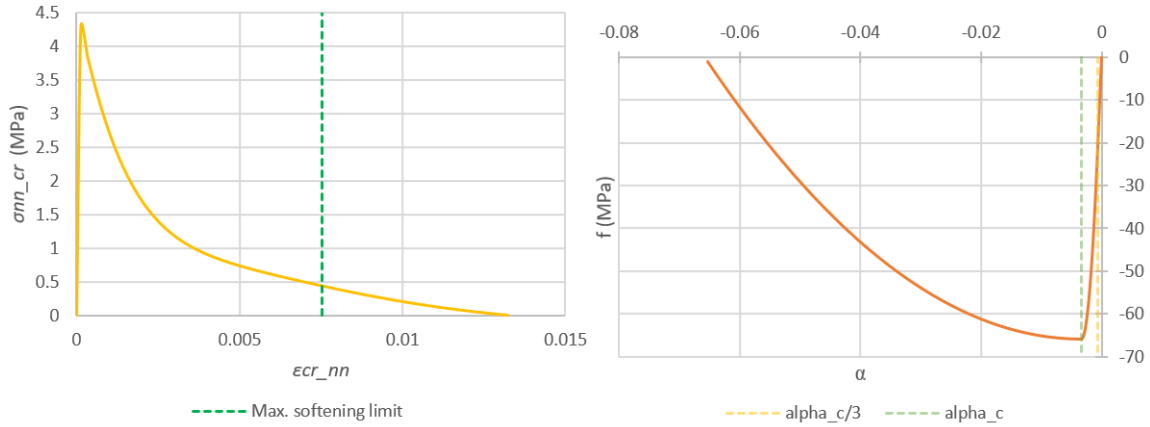

(a) Hordijk softening curve **(b)** Parabolic compressive behavior

Figure 4.3: Constitutive relations of Oviedo's dapped beam models' concrete properties

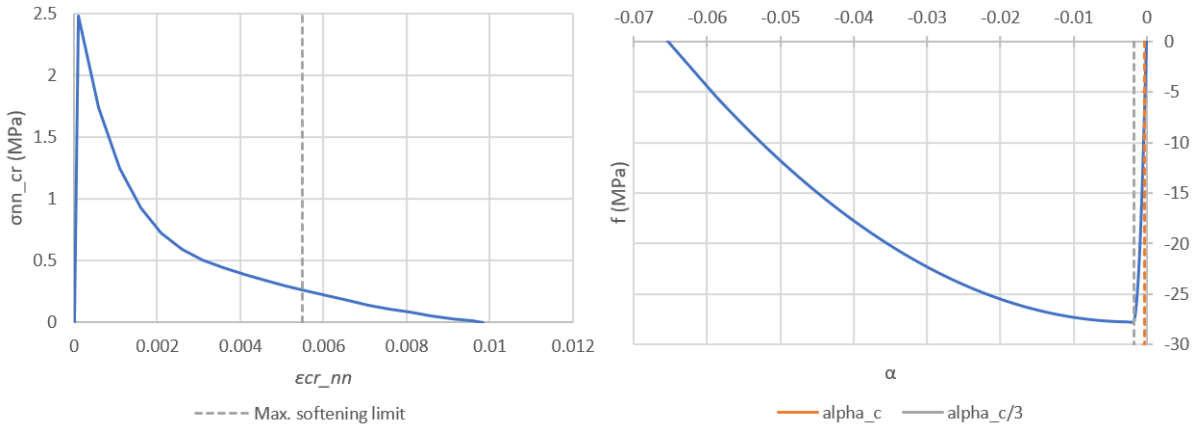

(a) Hordijk softening curve **(b)** Parabolic compressive behavior

Figure 4.4: Constitutive relations of Maxwell & Breen's dapped beam models' concrete properties

Table 4.2: A summary of the minimum and maximum strain values used to defined the principal strain contour plots for Oviedo's and Maxwell & Breen's numerical models.

Oviedo				Maxwell & Breen			
Min. tensile strain	Max. tensile strain	Min. compressive strain	Max. compressive strain	Min. tensile strain	Max. tensile strain	Min. compressive strain	Max. compressive strain
0.0001	0.0075	-0.0033	-0.00067	0.0001	0.0056	-0.0018	-0.00036

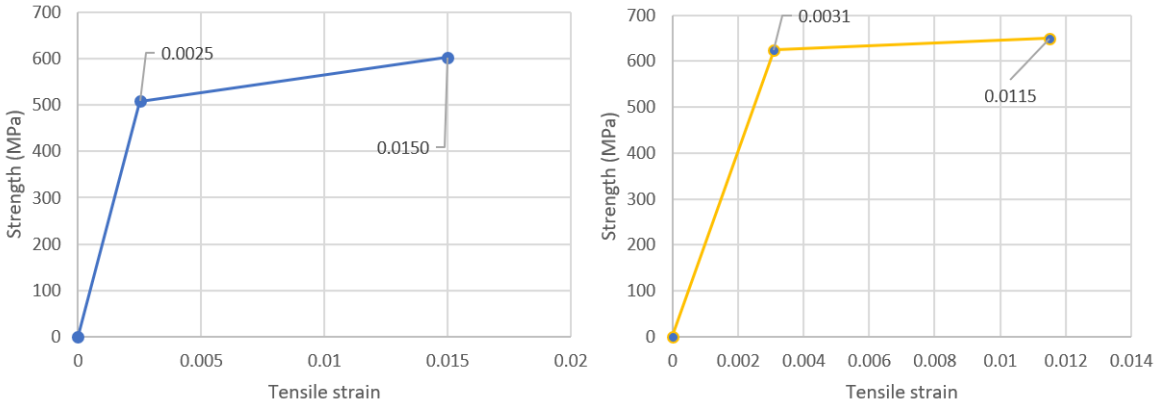

(a) 4.6-mm rebar **(b)** 10-mm rebar

Figure 4.5: Material behavior of the reinforcements in Oviedo's numerical models

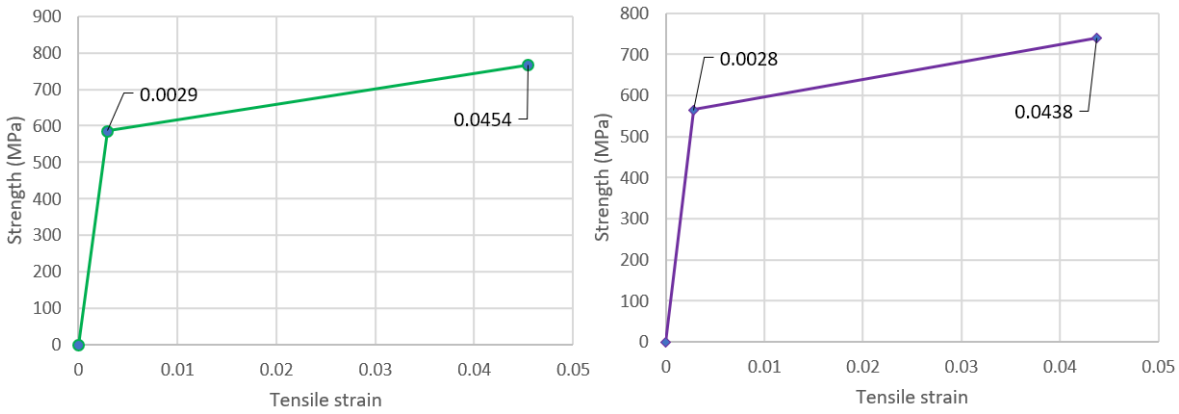

(a) 3-mm rebar **(b)** 6-mm rebar

Figure 4.6: Material behavior of the reinforcements in Maxwell & Breen's numerical models

Table 4.3: Adopted solution strategy

CONCRETE

	Oviedo et al.	**Maxwell and Breen**
Finite element		
Element type	Plane stress element CQ16M	
Element size	10	20
Interpolation scheme	Quadratic	
Integration scheme	Full integration (2x2) point Gauss	
Constitutive relation		
Crack model	Total strain based rotating crack model	
Crack-band width specification	Rots	
Tensile behavior	Hordijk softening	
Compressive behavior	Parabolic	
Compressive strength reduction model	Vecchio & Collins 1993	
Lower bound reduction curve	0.4	
Stress confinement model	Selby & Vecchio	
Poisson's ratio reduction model	Damage based	
Fracture energies		
Fracture energy, G_F	0.15	0.13
Reduced fracture energy, $G_{F,red}$	0.11	0.09
Compressive fracture energy, G_C	38.77	33.40
Reduced compressive fracture energy, $G_{C,red}$	27.42	23.62

REINFORCEMENT STEEL

Finite element	
Embedded reinforcement	Yes
Interpolation scheme	Quadratic
Integration scheme	Full integration
Constitutive relations	
Material model	Bi-linear elastoplastic material model with hardening

LOADING, ITERATION, AND CONVERGENCE CRITERIA

Loading type	Displacement controlled	
Load steps	0.002(500)	
Equilibrium iteration	Full Newton-Raphson	
Maximum number of iteration	50	100
Force norm tolerance	0.01	
Energy norm tolerance	0.001	
Satisfy all specified norm option	Not used	
No convergence	Continue	

Table 4.4: Concrete material parameters of Oviedo's and Maxwell & Breen's specimens

Material parameters	Formula	Origin literatures	
		Oviedo et al.	Maxwell & Breen
Mean compressive strength, f_{cm} (MPa)		65.8	28.3
Characteristic compressive strength, f_{ck} (MPa)	$f_{cm}-4$	61.8	24.3
Mean tensile strength, f_{ctm} (for ≤ C50) (MPa)	$0.3{f_{ck}}^{2/3}$	-	2.52
Mean tensile strength, f_{ctm} (for > C50) (MPa)	$2.12\ln\left(1+f_{ck}/10\right)$	4.29	-
Poisson's ratio, ν		0.15	0.15
Young's modulus, E_c (MPa)	2.11	32,908.60	25,549.21

Table 4.5: Reinforcement material parameters of Oviedo's and Maxwell & Breen's specimens

OVIEDO

Bar diameter (mm)	Area (mm^2)	Yield Strength (MPa)	Ultimate strength (MPa)	Ultimate strain (‰)
4	12.6	522	604	10.0
4.6	16.6	508	603	15.0
7	38.5	532	623	11.8
10	78.5	625	650	11.5

MAXWELL & BREEN

3	7.1	586	$768^{(*)}$	$45^{(*)}$
6	28.3	565	$740^{(*)}$	$44^{(*)}$

GENERAL

Material parameters	Formula	Origin literatures	
		Oviedo et al.	Maxwell & Breen
Young's modulus, E_s (MPa)		202,000	$200{,}000^{(*)}$
Hardening modulus, E_{har} (MPa)	$0.02E_s$	4,040	4,000

$^{(*)}$*: assumed*

4.2. Comparison of the numerical results and experimental results of the test cases

To validate the results acquired from the experimentation of the test cases, the recorded data of these concrete elements failure are compared with the numerical failure predictions obtained from the nonlinear analyses. To assess the validity of those recorded data, three type of data that will be compared: failure mode, load-displacement (LD) curve, and ultimate capacity.

4.2.1. Failure mode comparison

After all numerical analyses were complete, it was found that five out of six numerical models of the test cases generated failure modes that are consistent with the actual failure modes. Those five numerical models are the numerical model of specimen F-1, G-1, and H-1 (Oviedo), as well as specimen 2 and 3 (Maxwell & Breen). The failure of these numerical models is governed by the combination of concrete softenings and rebar rupture. They can be observed exclusively from the crack pattern (Ecw1) and the rebar strain (Exx) contour plots collected from the last converging load-step in each numerical analysis. The failure mode of dapped beam model F-1, G-1, and H-1 can be checked in Figure 4.7, 4.8, and 4.9, while the failure mode of deep beam model 2, 3, and 4 can be checked in Figure 4.10, 4.11, and 4.12. A summary of all numerical failure mode compared with its experimental failure mode is presented in Table 4.8.

In the case of specimen F-1, G-1, and H-1, their numerical models showed matching results by showing a type of failure mode that their actual specimens also experienced at the end of their tests. That failure mode is a flexural failure mechanism that occurred at the midspan due to the rupture of 10-mm longitudinal rebars near the re-entrance corner. In the numerical models, this failure mode can be perceived from the isolated red vertical crack at the midspan in the Ecw1 plots (the cracks softened at concrete strain of 7.5×10^{-3}), and the red section of rebars in the Exx plots (rebars rupture at rebar strain of 4.38×10^{-2}).

Likewise, the numerical models of specimen 2 and 3 also showed matching results by showing the same failure mode that their actual specimen also experienced. For specimen 2, that failure mode is a failure that does not involve any rebar ruptures, which will be categorized as a premature failure in this thesis. This failure is caused by multiple yielding points that manifested along the inclined rebars, especially at their middle sections, and generated many flexural cracks. The manifestation of these yielding points also generated a wide diagonal crack that split the concrete from the right-top corner of the opening to the loading point. In the numerical model of specimen 2, the multiple flexural cracks and the diagonal crack are displayed as red color cracks in its Ecw1 plot (Figure 4.10a), while the multiple yielding points at the inclined rebars displayed as cyan dots in its Exx plot (Figure 4.10b).

For specimen 3, the failure mode that its numerical model and actual specimen generated is a flexural failure mechanism that occurred due to the rupture of the rebars at node 't' which allowed the concrete to split open vertically from the that node towards the loading point (Figure 4.11c). In the numerical model of specimen 3, the definitive vertical flexural crack can be seen in red color in the midspan of model's Ecw1 plot (Figure 4.11a), the rebar rupture at node 't' are indicated as red rebar section in the model's Exx plot (Figure 4.11b).

One numerical model that is not agreeing with its experimental result is the numerical model of specimen 4. The numerical result of this model suggested that the real specimen should have had a flexural failure that is comparable to the flexural failure that occurred on specimen 3 (Figure 4.12a and 4.12b). In contrast, specimen 4 actually collapsed with a shear failure that occurred due to a

shear diagonal crack that propagated from the left-top corner of the opening toward the loading point (Figure 4.12c). The shear failure separated the left-top part of the beam from the main body. The contrasting failure modes cause other experimental results of specimen 4 cannot be fairly compared with its numerical results.

Nevertheless, the failure mode difference can be justified. The shear failure mechanism that occurred on the actual specimen was most probably initiated by the highly concentrated compressive strain that built up at the left-top corner of the opening, as shown in the compressive strain contour plot (E2) in Figure 4.13a. But, a shear failure due to this factor alone seems to be unlikely, since the tensile strain region at the right-top corner of the opening and the bottom of the right side of the beam, as shown in the LEFEA result (Figure 4.13b), seem to be more critical. Thus, the occurrence of the shear failure might be supported by an imperfection that went unnoticed during the experiment. The imperfection could be anything unideal in the experiment that triggered the occurrence of the shear crack at the top of the opening and lead the beam toward a shear failure.

Table 4.6: Failure mode of the test cases according to the numerical and experimental results.

Specimen ID	**Failure mode/location**	
	Numerical	**Experimental**
F-1	flexural/midspan	flexural/midspan
G-1	flexural/midspan	flexural/midspan
H-1	flexural/midspan	flexural/midspan
2	premature/along inclined rebar	premature/along inclined rebar
3	flexural/node 't' to loading point	flexural/node 't' to loading point
4	flexural/node 't' to loading point	shear/left-corner opening to loading point

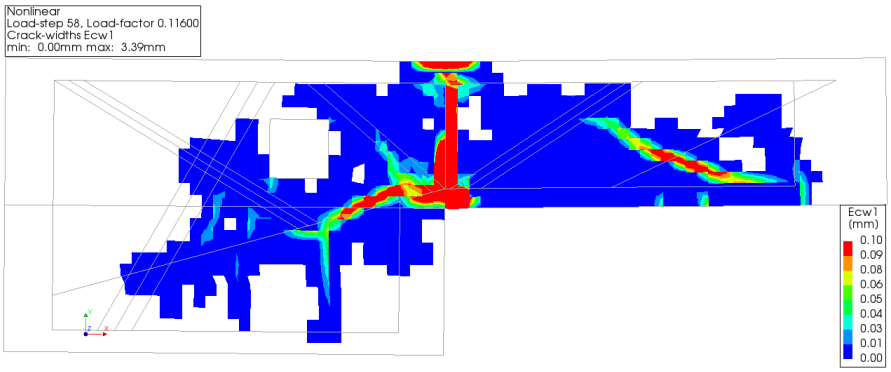

(a) Crack pattern (Ecw1)

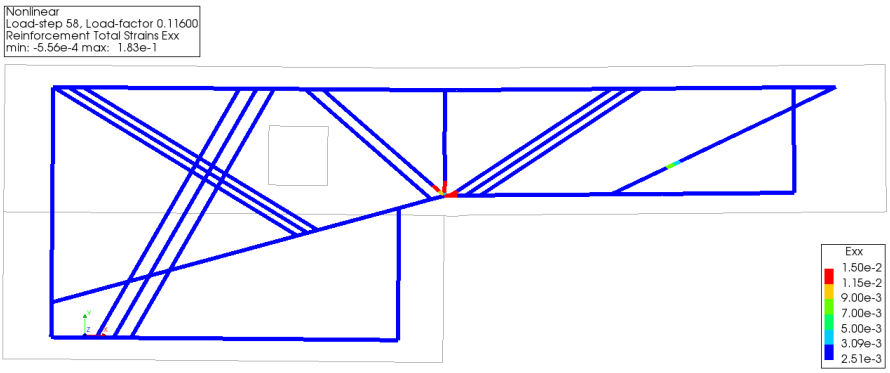

(b) Rebar strain at local X-direction (Exx)

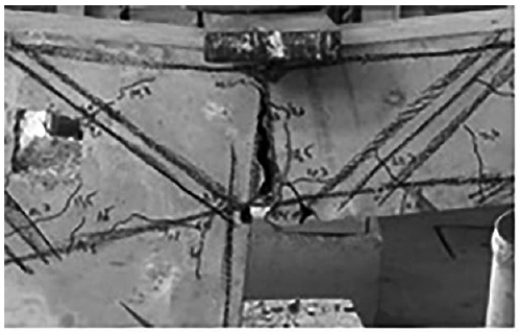

(c) Actual failure of specimen F-1 [19]

Figure 4.7: Failure mode of specimen F-1 according to: (a,b) numerical results (c) experimental results.

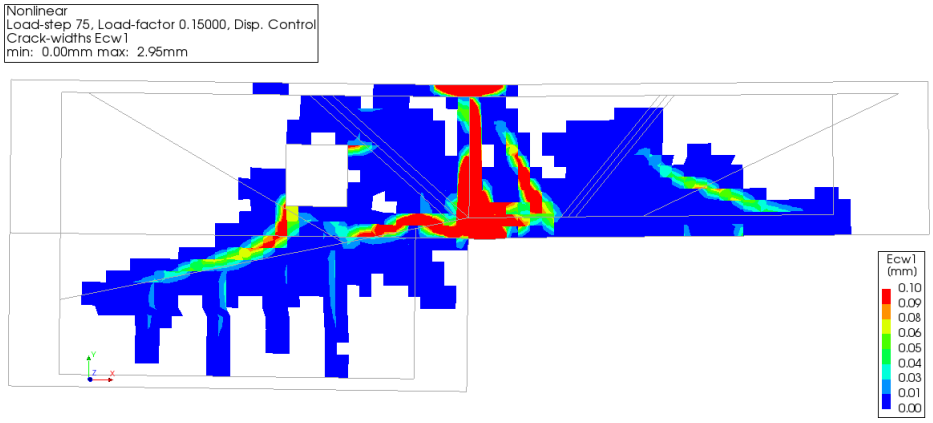

(a) Crack pattern (Ecw1)

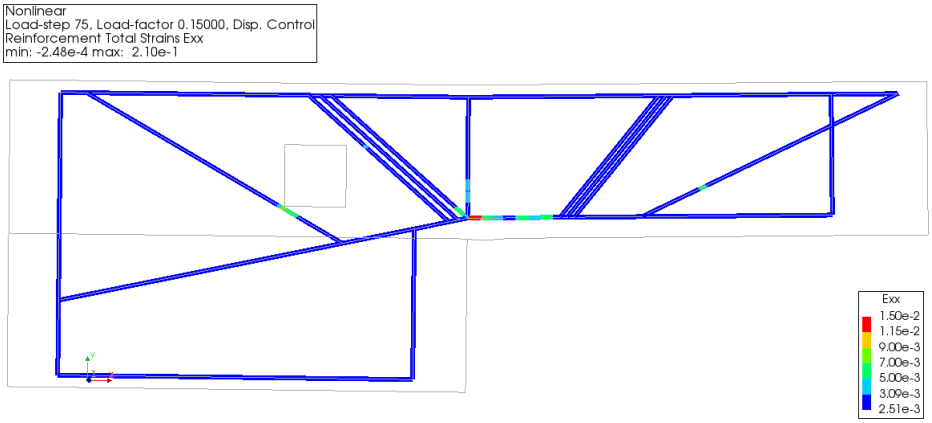

(b) Rebar strain at local X-direction (Exx)

(c) Actual failure of specimen G-1
[19]

Figure 4.8: Failure mode of specimen G-1 according to: (a,b) numerical results (c) experimental results.

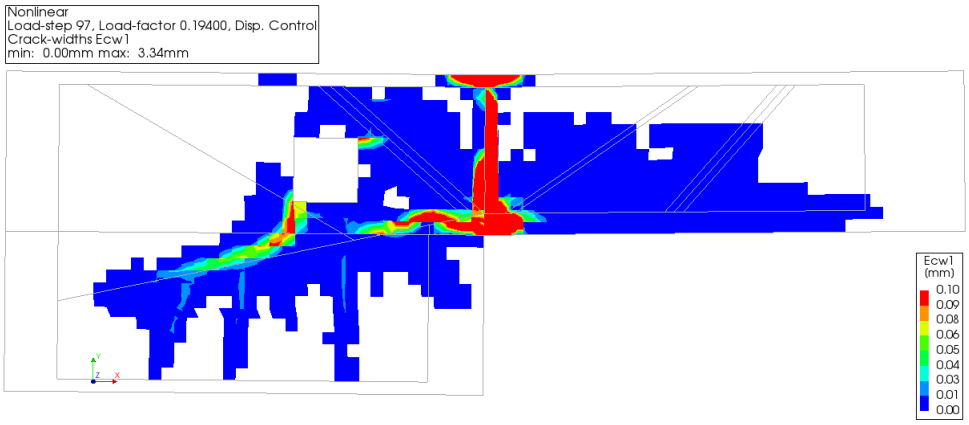

(a) Crack pattern (Ecw1)

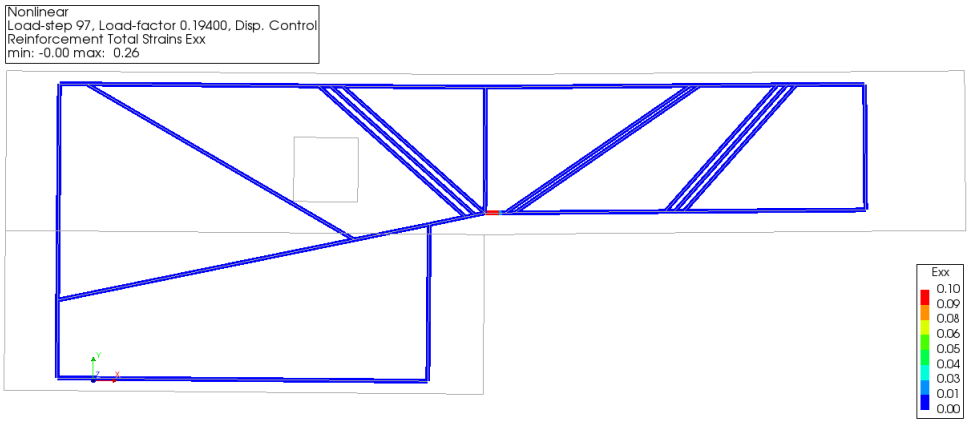

(b) Rebar strain at local X-direction (Exx)

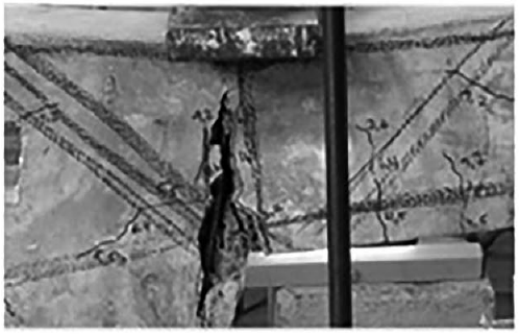

(c) Actual failure of specimen H-1
[19]

Figure 4.9: Failure mode of specimen H-1 according to: (a,b) numerical results (c) experimental results.

(a) Crack pattern (Ecw1)

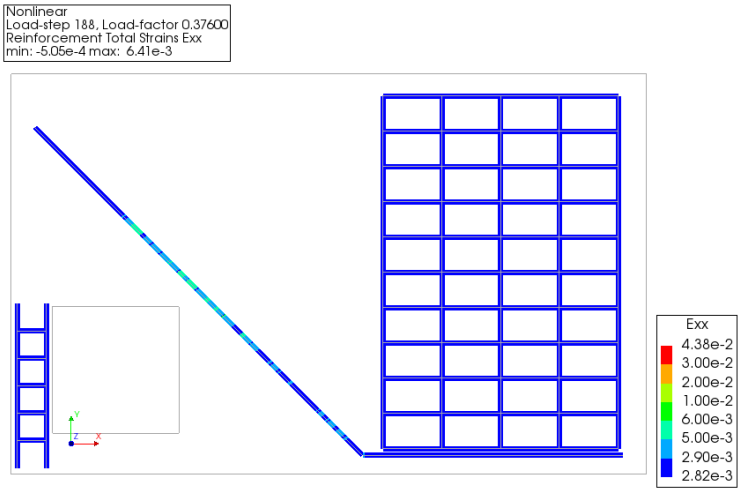

(b) Rebar strain at local X-direction (Exx)

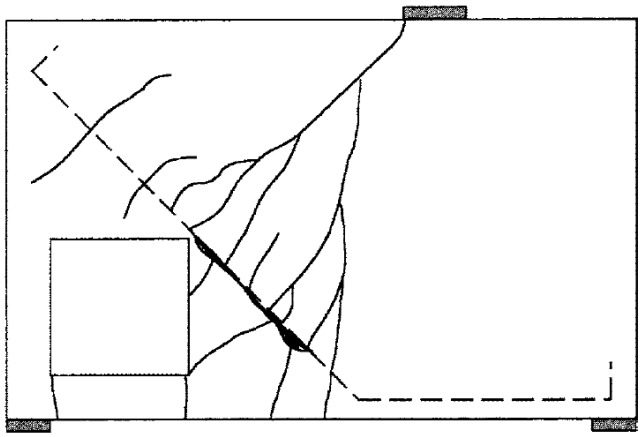

(c) Illustration of specimen 2 crack pattern at failure [3]

Figure 4.10: Failure mode of specimen 2 according to: (a,b) numerical results (c) experimental results.

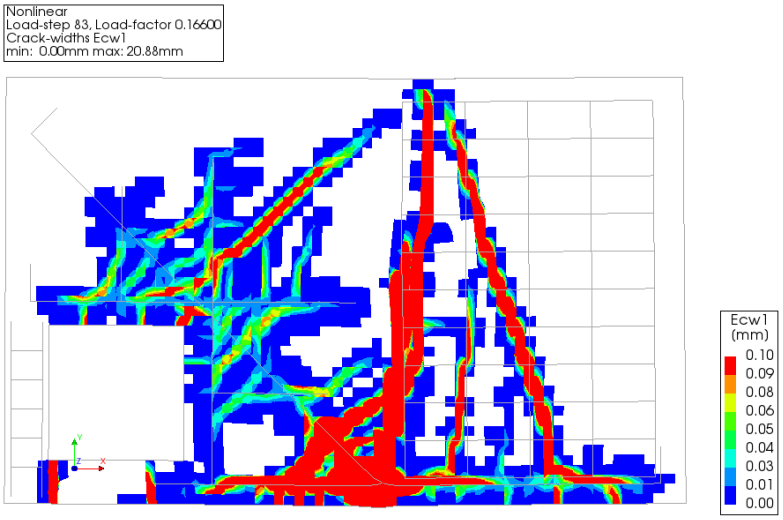

(a) Crack pattern (Ecw1)

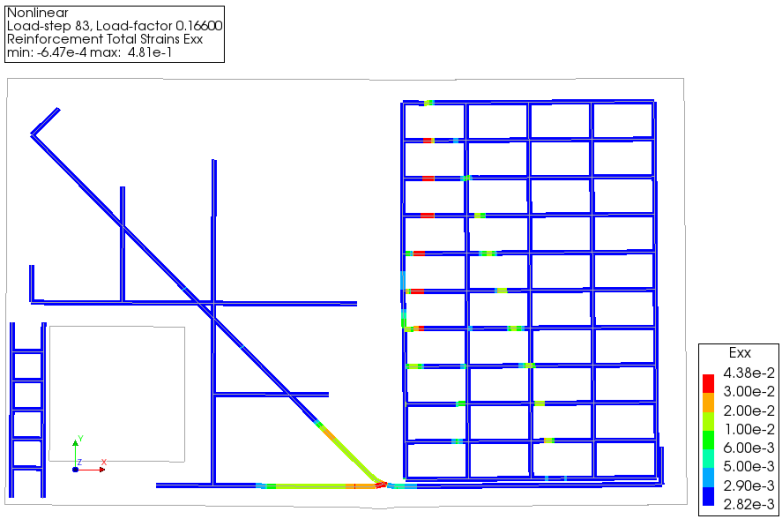

(b) Rebar strain at local X-direction (Exx)

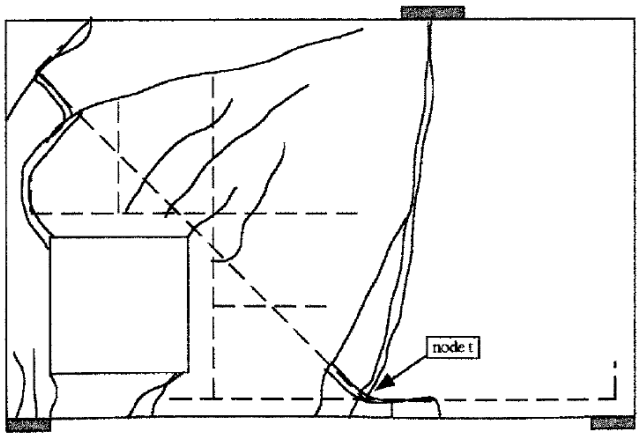

(c) Illustration of specimen 3 crack pattern at failure [3]

Figure 4.11: Failure mode of specimen 3 according to: (a,b) numerical results (c) experimental results.

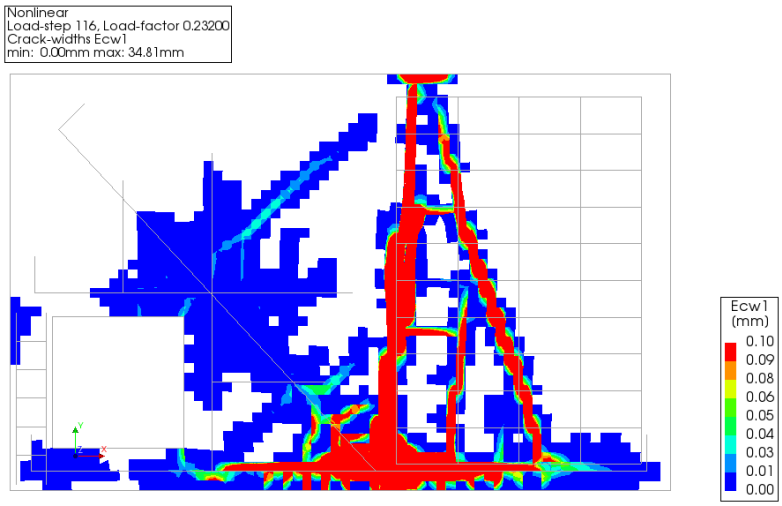

(a) Crack pattern (Ecw1)

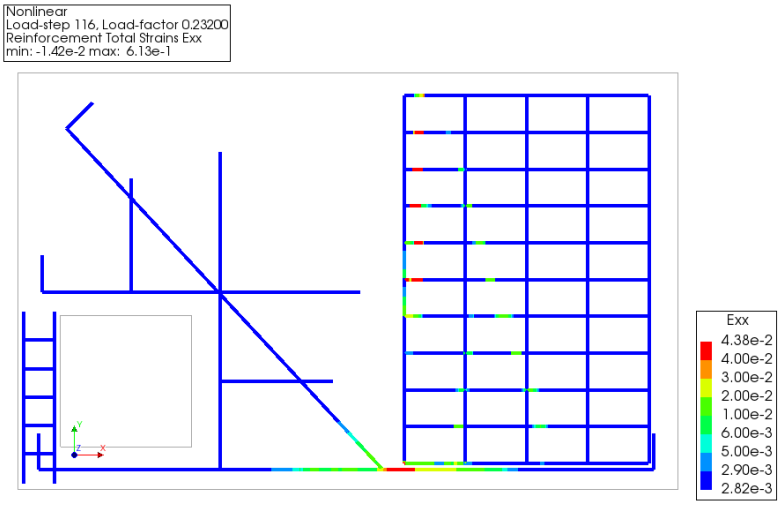

(b) Rebar strain at local X-direction (Exx)

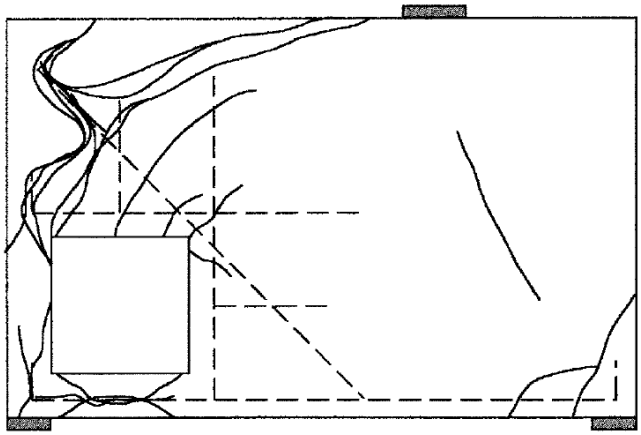

(c) Illustration of specimen 4 crack pattern at failure [3]

Figure 4.12: Failure mode of specimen 4 according to: (a,b) numerical results (c) experimental results.

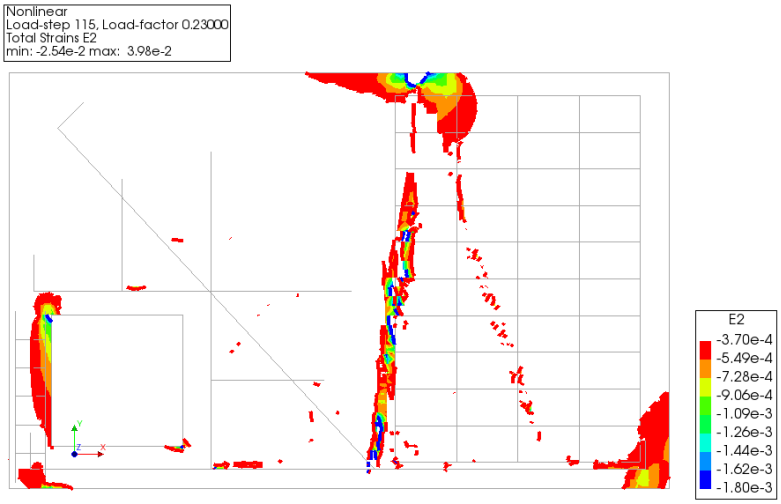

(a) Principal compressive strain of Specimen 4 at its last converging load-step (116)

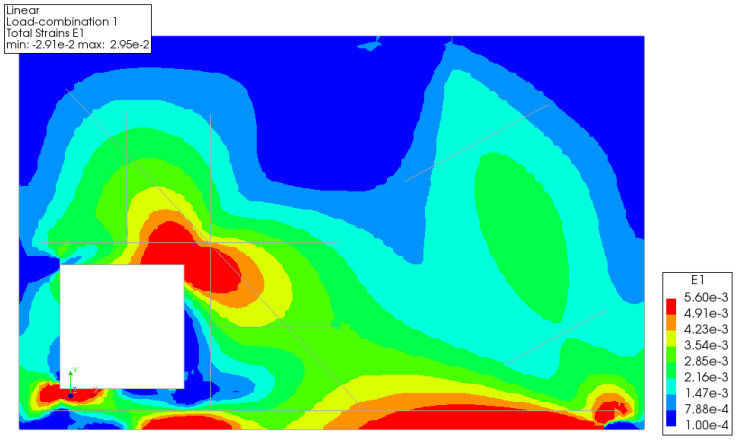

(b) Principal tensile strain of Specimen 4 from LEFEA

Figure 4.13: Principal compressive strain and principal tensile strain (LEFEA) plots that help justifying the failure mode different between the numerical and experimental results of Specimen 4.

4.2.2. Load-displacement curve comparison

Figure 4.14 presented six charts that display the comparison between the load-displacement (LD) curve of each numerical model with the LD curve of its respective concrete elements. The numerical and experimental LD curves of Oviedo (F-1, G-1, and H-1) are presented in Figure 4.14a, 4.14b, and 4.14c, while the numerical and experimental LD curves of Maxwell & Breen's (specimen 2, 3, and 4) are presented in Figure 4.14d, 4.14e, and 4.14f, respectively. However, it is important to mention that because the numerical model of specimen 4 did not collapse in a similar fashion as its actual concrete specimen (numerical = flexural, actual = shear), the comparison between the numerical and experimental LD curves of specimen 4 will be exempted.

From comparing the numerical and experimental LD curves of the other five specimens (F-1, G-1, H-1, 2, and 3), it appears that the characteristics of the numerical LD curves do not straightforwardly match the characteristic of the experimental LD curves. For Oviedo's, similarities between their numerical and experimental LD curves can be found at their nonlinear behavior and the load level at which the curves stop developing (indicating the failure of the specimen/model). For Maxwell & Breen's, there is only one similarity that can be evidently observed, and that is the ultimate load level of the models/specimens indicated by the LD curves.

Despite the similarities, two things appear clearly different between the numerical and experimental LD curves: initial (elastic) stiffness and total displacement. The LD curve of each numerical model of the test cases indicated that every numerical model always has significantly higher elastic stiffness (indicated by the initial inclination of the LD curves) and shorter total deformation. However, the following reasons can be used to justify these differences:

- **Low angle of inclination at the initial loading phase of the experimental LD curve might have been caused by an unideal experimenting environment**. It is suspected that, at the start of the test, the applied concentrated load was not immediately received by the tested beam, but by another test components with much less stiffness. Thus, the initial response of the beam from the experimental results might not be reliable.
- **Modeling the reinforcements as embedded rebars might have caused the numerical models to have less total deformation**. By using this assumption, a reinforcement action in concrete, i.e. bond-slip between concrete and reinforcement, was not accounted for in the numerical simulation of the as-drawn model. If the bond-slip action were simulated, the local deformation caused by each slip could have contributed to the total deformation of the numerical models.
- **The application of the bi-linear elastoplastic material model with hardening for the reinforcements might have reduced the ability of the numerical models to produce larger total deformation**. By having this simplified material model, there might be unaccounted hardening behavior that was not included in the nonlinear simulation. The hardening behavior might allow more sections of the embedded rebars to yield before one of them got ruptured. More yielding means that there are more plastic deformations and they would produce local deformations that could have contributed to the total deformation of the numerical models.

Since the validation was not intended to investigate the correctness of the experimentation done in the literature, the validation will be focused on the characteristics of the matching result, and not at their differences. Thus, through these justifications, the similarities in terms of the ultimate load between the two types of LD curves can be considered sufficient to validate the experimental results, and the displacement information can be considered unreliable.

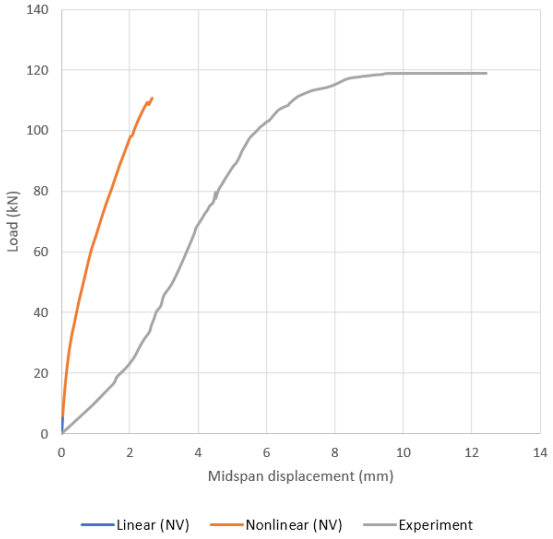

(a) F-1 NV vs. F-1 exp.

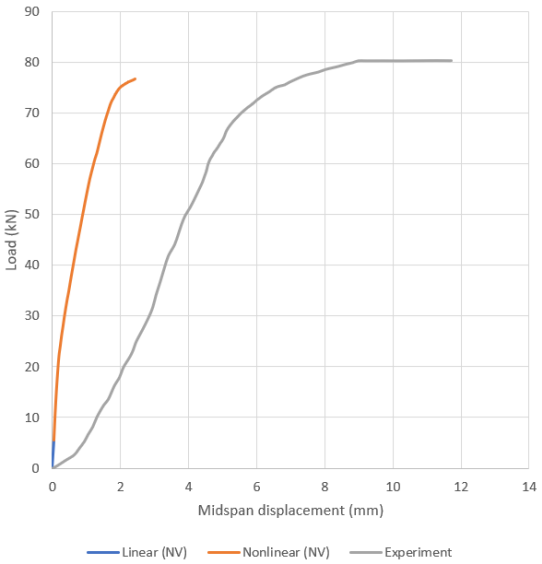

(b) G-1 NV vs. G-1 exp.

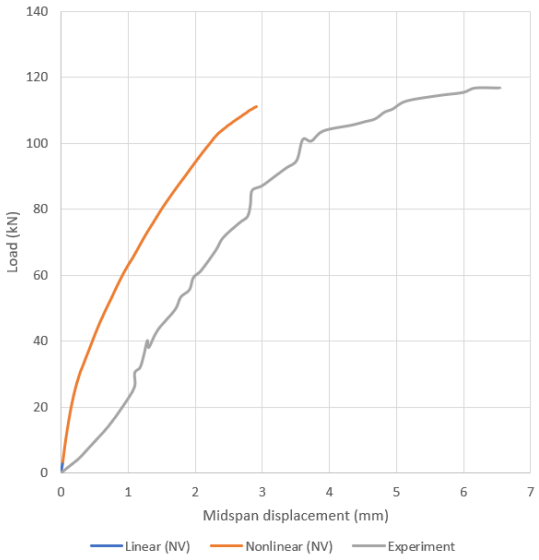

(c) H-1 NV vs. H-1 exp.

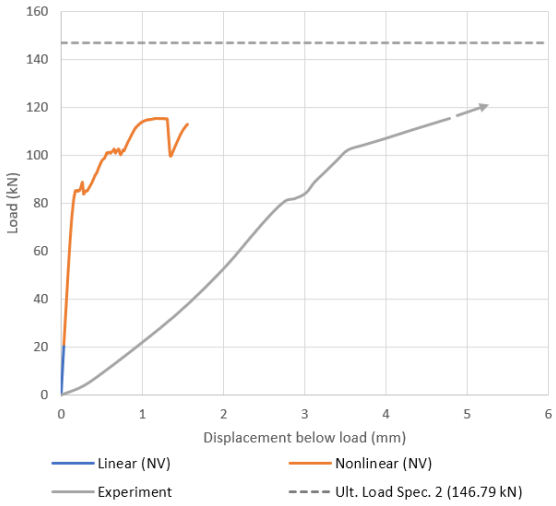

(d) 2's NV vs. 2's exp

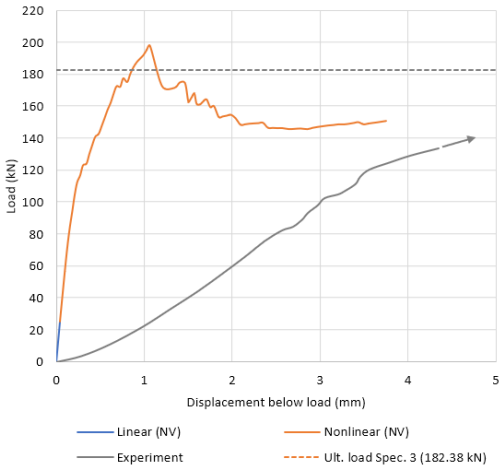

(e) 3's NV vs. 3's exp

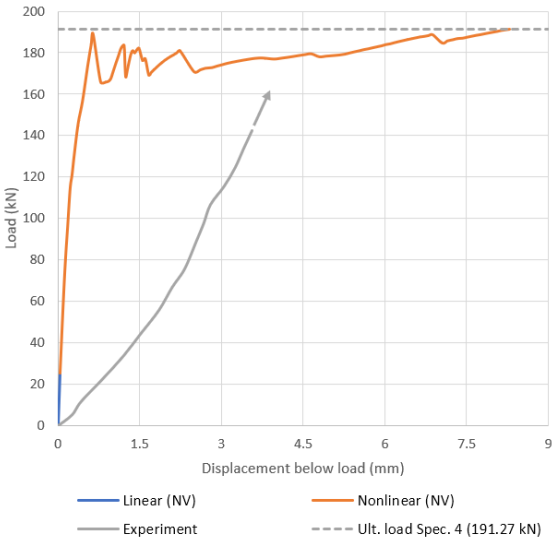

(f) 4's NV vs. 4's exp

Figure 4.14: Comparison between the LD curves of the numerical models and the experimented specimens.

4.2.3. Ultimate capacity comparison

In the end of all nonlinear analyses, it was found that the failure of each numerical model was generated at a load level that is similar to the ultimate capacity of its actual specimen. This similarity can be observed at Table 4.7, in which the ultimate capacity of the numerical models (R_{NV}) and the actual specimens (R_{exp}) are summarized and put side to side.

To show the equivalence level between the numerical and experimental ultimate capacities, a ratio of R_{NV} to R_{exp} is introduced. This ratio is denoted as Θ_1. However, it is important to mention that the R_{NV} and R_{exp} of specimen 4 cannot be compared since its numerical and actual failure mode is different. Thus, Θ_1 ratio for specimen 4 is not presented.

In Table 4.7, the Θ_1 ratio of all specimens show values that range between 1.05 to 1.30. With all Θ_1 showing a value that is above 1.00, it means that the numerical results tend to suggest conservative ultimate capacity values when compared to the experimental results. When all Θ_1 ratios is averaged (μ_{Θ_1}), a mean value of 1.14 was obtained. Additionally, the mean value was acquired with a coefficient of variation (CoV_{Θ_1}) of 8.9%. From those μ_{Θ_1} and CoV_{Θ_1} values, it can be deduced that the prediction of ultimate capacity by the numerical models can match the experimental result prediction with relatively low variability of Θ_1 ratios. In that sense, the experimental results of the test cases are also verified in terms of ultimate capacity.

Table 4.7: Comparison between the ultimate capacity of the numerical models and the actual specimens.

Experiment	Specimen	R_{exp}	R_{NV}	$\Theta_1 = R_{exp}/R_{NV}$
Oviedo	F-1	118.90 kN	110.69 kN	1.07
	G-1	80.30 kN	76.75 kN	1.05
	H-1	116.80 kN	111.15 kN	1.05
Maxwell & Breen	2	146.79 kN	112.82 kN	1.30
	3	182.38 kN	150.94 kN	1.21
	4	191.27 kN	191.37 kN	-

Table 4.8: Average and coefficient of variation of Θ_1.

Mean value of Θ_1 (μ_{Θ_1})	Coefficient of variation of Θ_1 (CoV_{Θ_1})
1.14	8.9%

5

Conclusion - Part 1

An attempt to validate the use of NLFEA that adopted a solution strategy recommended by the Dutch guidelines [20] in this research was presented. The validation is done by comparing the experimental results of six complex concrete beam elements using their numerical results. They were compared in terms of failure mode and ultimate capacity. From the comparison, it was found that five numerical models of the test cases were able to mimic the nonlinear behavior of their respective concrete specimens. Those five numerical models are the numerical model of specimen F-1, G-1, and H-1, as well as specimen 2 and 3. These five models were able to collapse in a similar fashion as their actual specimens. In addition, those failures were generated at comparable ultimate load level. The similarity in terms of ultimate capacity is signified through the ratio of experimental and numerical ultimate capacities of these five specimens ($\Theta_1 = {}^{R_{exp}}/_{R_{NV}}$). The Θ_1 ratio of all five specimens has a mean value $\left(\mu_{\Theta_1}\right)$ of 1.14 and a coefficient of variation $\left(\mathtt{CoV}_{\Theta_1}\right)$ of 8.9%. These two values indicated that the ultimate capacity of the numerical models can match the experimental ultimate capacity with relatively low variability.

The numerical model of specimen 4 was not included in that list because it generated a failure mode (flexural) that is dissimilar to the failure mode of its concrete element (shear). However, the failure mode differences can be justified. It is possible that the shear failure at the actual specimen 4 was triggered by an imperfection that went unnoticed during the experiment. The imperfection could be anything unideal in the experiment, such as a notch at the top-left corner of the opening that causes the shear failure to develop instead of a flexural failure.

Thus, from all similarities that the numerical models and actual specimens have in common, it can be considered that the numerical results verified the experimental results of the test cases. Simultaneously, those similarities also validated the applied numerical approach (adopted solution strategy built from recommendations of the Dutch guidelines) for producing accurate numerical results.

Part 2 - Proposed technique for evaluating strut-and-tie models using the validated numerical approach

In this part of the thesis, the proposed evaluation technique is introduced and tested. The introduction of the technique is given in Chapter 6 and the results of its implementation on the ST models of the test cases are presented in Chapter 7. Before those implementation results were checked against the numerical results of the test cases to validate them (Chapter 9), an attempt to validate the proposed technique results using the STM analyses results of the test cases are presented in Chapter 8.

6

The proposed evaluation technique

6.1. Introduction

In this chapter, an evaluation technique proposed as a solution for reducing STM reliance on engineering experience and intuition in generating a suitable ST model is presented. It is designated as a supplement to the current STM provisions in order to promote STM to become a more data-driven method. The technique is devised to allow engineers to find a fitting ST model for a particular physical problem using objective information instead of personal judgement. When included into the main STM evaluation procedure, the technique acts as an intermediary evaluation phase between the truss analysis and ST dimensioning, as presented in Figure 6.1.

To attain objective information, the proposed technique employs a well-known numerical tool, namely the NLFEM. NLFEM is used to examine a truss model as a concrete element model with embedded reinforcements and to produce additional information, such as failure mode and ultimate capacity, that can provide insights on the influence of an ST model design toward the nonlinear behavior of the actual structure. Evidently, in the process of the analysis, the struts and the ties of the truss would have to be converted into finite elements to allow them to be analyzed by the numerical tool. The finite element model created for this purpose is specified as a 'ties-as-extended-rebars' model or TER model. The design and evaluation steps of TER models within the proposed technique is elaborated in Section 6.2.

6.2. Outline of the design and evaluation steps within the proposed technique

The process for generating and evaluating a TER model can be divided into four steps:

Step 1: Assigning ties as rebars and struts as concrete

In order to allow NLFEM to evaluate an ST model, each member of the truss model has to be assigned as either concrete or steel depending on the type of force that is acting on them. Since the whole concrete continuum of an analyzed structure is intended to be modeled as finite elements, it is unnecessary to model the struts individually. Compression force acting in the struts will be handled by the concrete and therefore, each of them can be perceived as an integral part of the concrete continuum.

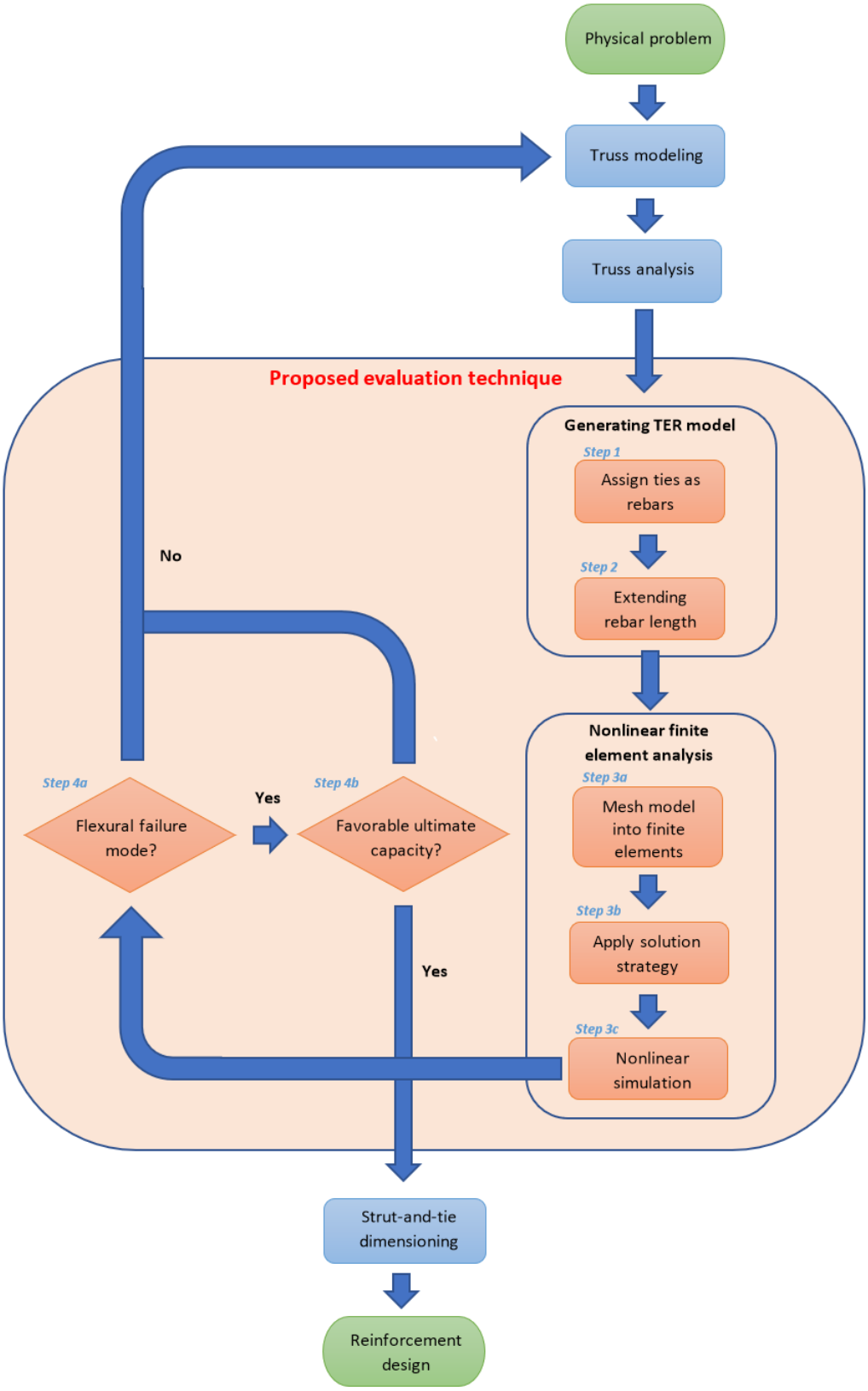

Figure 6.1: Inclusion of the proposed evaluation technique in the current STM evaluation procedure.

Unlike its opposite truss members, the ties have to be separately assigned as rebars. In identifying the rebars specification, it is recommended to apply steel properties, e.g. yield strengths and ultimate strengths, that is similar to the ones considered for designing the flexural rebars of the actual structure. As for determining the number of rebars that need to be assigned, a division of 'force in a tie' to 'a unit force capacity in a rebar' will provide the amount of steel to be applied. Applying identical steel properties helps to maintain the NLFEA results accuracy in predicting the effect of a certain truss model geometry toward the nonlinear behavior of a structure. In addition, a group of connected ties that approximately has a similar alignment can be collected as one 'leg'. A leg represents a set of rebars that can withstand the maximum tensile force occurring on one of the ties in the leg. An illustration on the process of grouping the ties as one leg is presented in Figure 6.2 using the ST model of specimen F-1 (a dapped beam with an opening) from Oviedo's experiment [19].

Step 2: Extending the rebars length with straight anchorage length

Rebar legs defined in the previous step now become the subjects of lengthening. In this step, each tip of a leg that is located in the proximity of high tensile stress regions in the concrete continuum has to be extended. The position of those highly tensioned areas can be detected using linear elastic finite element analysis, or LEFEA. It is recommended to calculate the additional length given to each tip using a code provision dedicated for determining straight anchorage length for longitudinal rebar in EN 1992-1-1:2004 [28], as described in Chapter 2.3. As an example, a dapped beam with an opening that has its rebar legs extended with straight anchorage length is shown in Figure 6.3. Models with extended rebar legs in this procedure are denoted as TER model.

Step 3: NLFEA

After completing the design process, the next step is to convert the TER model into a finite element model before it can be examined through an NLFEA procedure. A valid solution strategy for executing an NLFEA should be selected beforehand in order to obtain justifiable results. In this thesis, a solution strategy described in the Dutch guidelines for NLFEA of concrete structures[20] is utilized in all nonlinear simulations of the test cases mentioned in Chapter 3.

Step 4: Assessing the robustness of the ST model with the NLFEA results

At the end of a nonlinear simulation, all the notable results should be collected for the purpose of assessing the influence of an ST model to the ultimate limit state behavior of the analyzed structure. There are four notable results that should be collected for this purpose: principal tensile strains, crack pattern, load-displacement response, and rebar strain in local X-direction. These results can be interpreted as evaluative parameters (e.g. failure mode and ultimate capacity) which later are exploited as additional indicators for selecting a suitable ST model. If the NLFEA results indicate unfavorable failure condition, such as a shear failure mechanism or low ultimate capacity, then the analyzed ST model has to be improved.

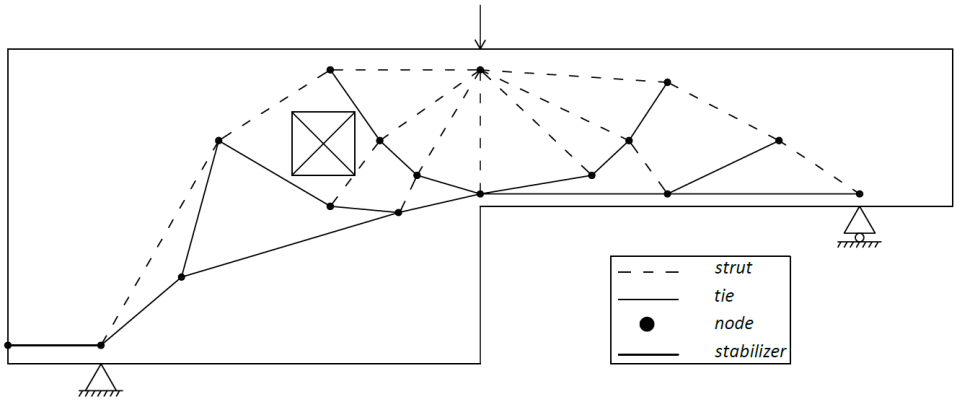

(a) ST model of a dapped beam with an opening (specimen F-1) [19]

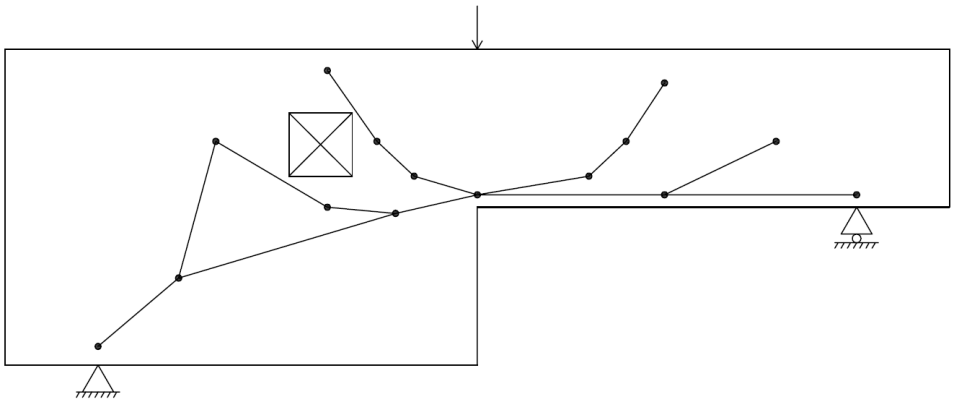

(b) Ties layout of the ST model

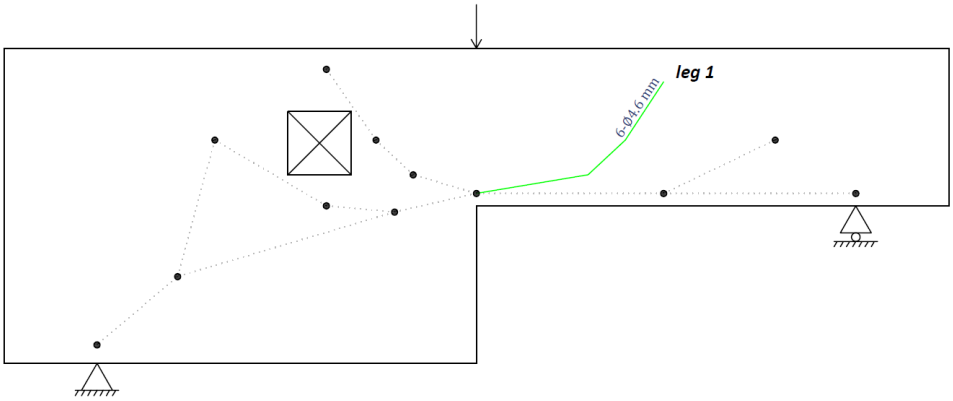

(c) Determining of one of the rebar legs

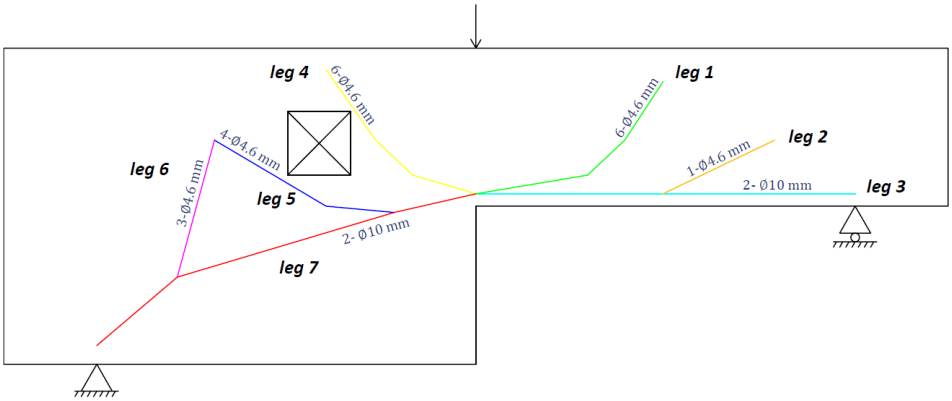

(d) All of the ties are completely grouped as rebar legs (TR model)

Figure 6.2: Process of determining the rebar 'legs'.

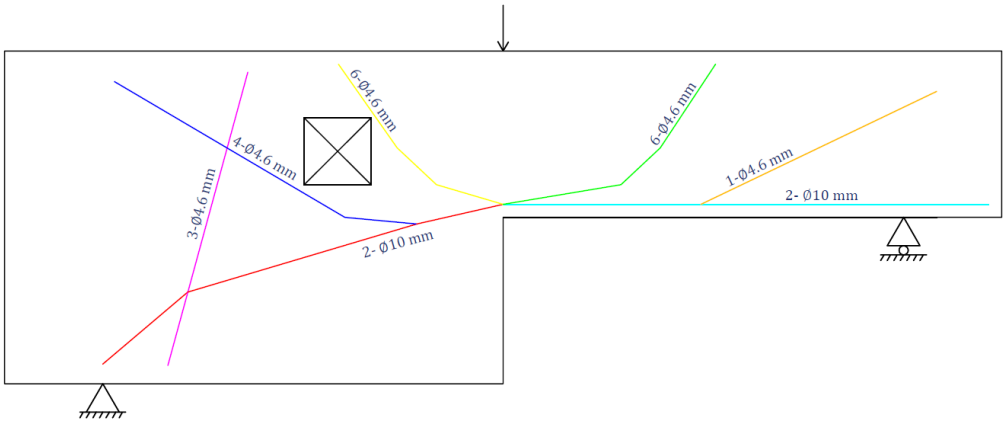

(a) Dapped beam with opening model with extended rebar legs (TER model)

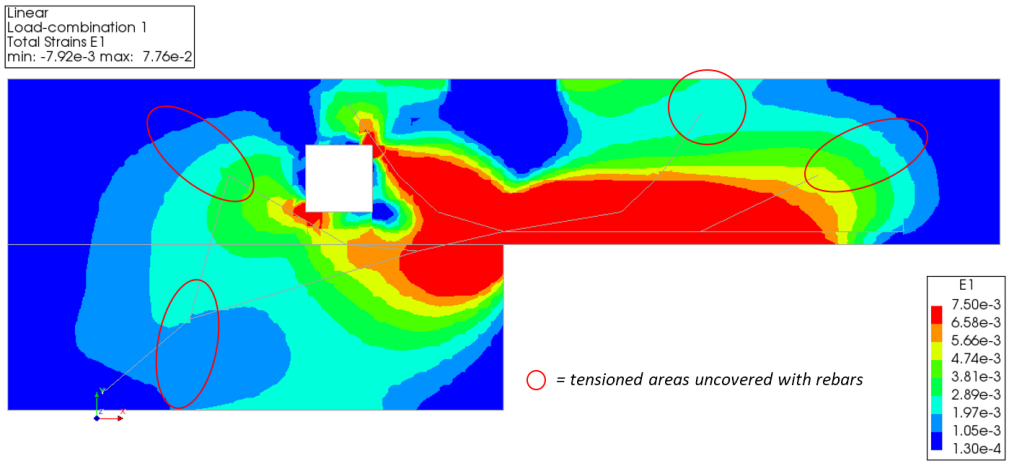

(b) Principal tensile strain (E1) contour of the dapped beam with an opening obtained from LEFEA and its uncovered tensioned areas

Figure 6.3: Rebar legs extended with anchorage length.

6.3. Reason for extending the embedded rebars

In one of the steps for designing a TER model, it is recommended to provide additional length to the rebar legs for nonlinear simulations. The purpose of the extension is to ensure that this type of model simulates a failure mechanism that closely resembles the actual failure of its structure. Having a resembling failure mechanism is an essential quality for TER models to possess since the proposed technique should allow engineers to look into the ultimate limit state of the analyzed structure without even going into the reinforcement design process.

During the research, dissimilar failure mechanisms emerged on models that keep the original ties layout as their rebar layout (later denoted as 'ties-as-rebars' model or TR model). TR models suffer from this issue due to the fact that ties layout has a relatively short reach to cover all tensioned areas in the concrete continuum, especially those which are located at the critical regions. Due to the absence of reinforcement, plain concrete cracks can quickly develop at those areas and escalate into a failure mechanism. With the lengthening, nearby rebar legs should be able to add steel capacity to the tensile regions and allow the tensile stresses to be redistributed during plastic deformation of the structure.

As evidence, NLFEA results of the TR models from the test cases (see Section 3) are presented. Crack pattern and rebar strain at failure load level are used to describe the obtained information. Results of the TR models made from Oviedo's ST models (i.e. F, G, and H series ST models) are shown in Figure 6.4, 6.5, and 6.6, while results of the TR models made from Maxwell & Breen's ST models (i.e. specimen 2, 3, and 4 ST models) are shown in Figure 6.7, 6.8, and 6.9. In those figures, the failure modes of their respective experimental specimens, which were constructed with ties-coinciding rebar layouts, are also included for comparison. NLFEA results of Oviedo's TR models are specifically compared with the first series specimens (i.e. F-1, G-1, and H-1), whereas NLFEA results of Maxwell & Breen's TR models are compared with tested specimen 2, 3, and 4.

According to the results, Oviedo's TR models appear to generate failure modes that are dissimilar to the ones occurred to the first series specimens. Those models collapsed with a shear failure mechanism, while in contrast, the tested specimens failed with flexural failure mechanism at their midspan. The shear failures occurred due to a diagonal shear crack that traveled either from the right support toward the loading point (in case of F and G-series TR models) or from the middle of the right part of the dapped beam toward the loading point (in case of H-series TR model). Shear failure mechanism occurred on these models because tensioned areas near leg 1 and leg 2 are left unreinforced (see Figure 6.3b). Consequently, the tensile stresses in these shear-prone regions could easily induce a wide and continuous diagonal shear failure on the concretes above the embedded rebars legs, despite having a lower tensile stress level than the stresses around the re-entrance corner.

Unlike the previous models, Maxwell & Breen's TR models seem to be able to simulate failure conditions that are similar to what their actual specimens experienced, except for TR model of specimen 4. TR models of specimen 2 and 3 managed to closely replicate the flexural failure condition of their respective specimens, but it was only TR model of specimen 2 that ended up failing in a similar fashion as its tested specimen. The TR model of specimen 3 did not collapse with a flexural failure mechanism due to the extensive damages on the concrete around its opening. These damages caused the load that was applied to the model to drop before it could rupture the bottom flexural rebar at node 't' (see Figure 6.8c), and lead the model to a failure that cannot be categorized as neither flexural nor shear. Nevertheless, these two TR models were still capable in producing a failure condition that corresponds to the actual condition due to the fact that the uncovered tensioned areas, shown in Figure 6.10, were not located at critical regions that can cause substantial damage to the concrete.

With these results, it is evident that extending rebar legs toward uncovered tensioned areas is an essential design step in the proposed evaluation procedure. It is required for ensuring the accuracy of the NLFEA of an ST model in predicting the collapse conditions of its actual structure constructed with reinforcement design made from that ST model. In the next chapter, TER models, as the revamped version of TR models, are nonlinearly simulated and their results are presented.

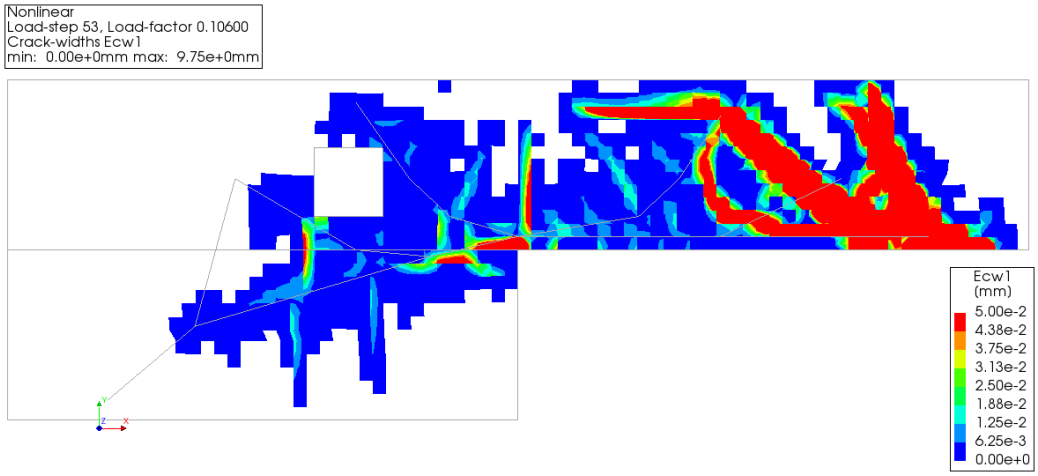

(a) Crack pattern (Ecw1) of F-series TR model

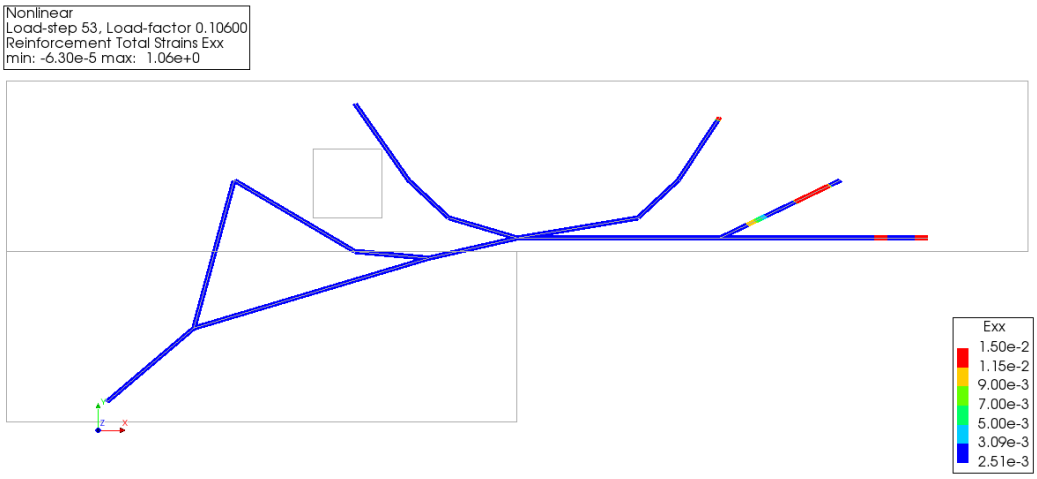

(b) Rebar strain (Exx) at F-series TR model

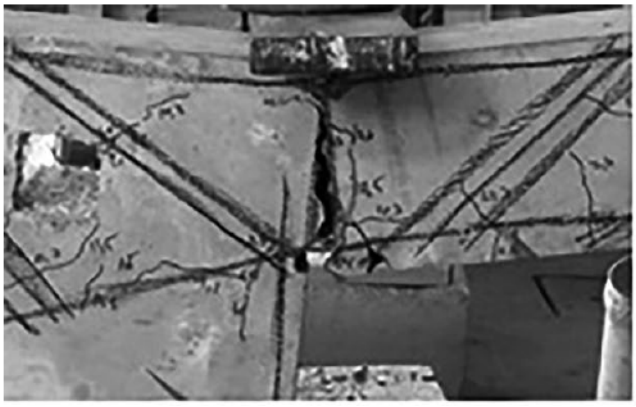

(c) Actual failure of specimen F-1 [19]

Figure 6.4: NLFEA results at failure load level vs. the actual failure of F-series TR models (Oviedo).

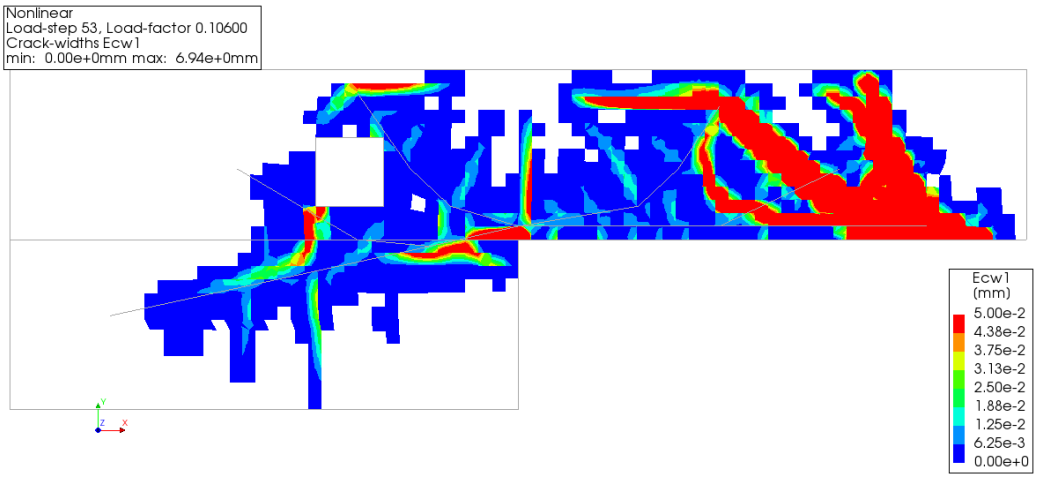

(a) Crack pattern (Ecw1) of G-series TR model

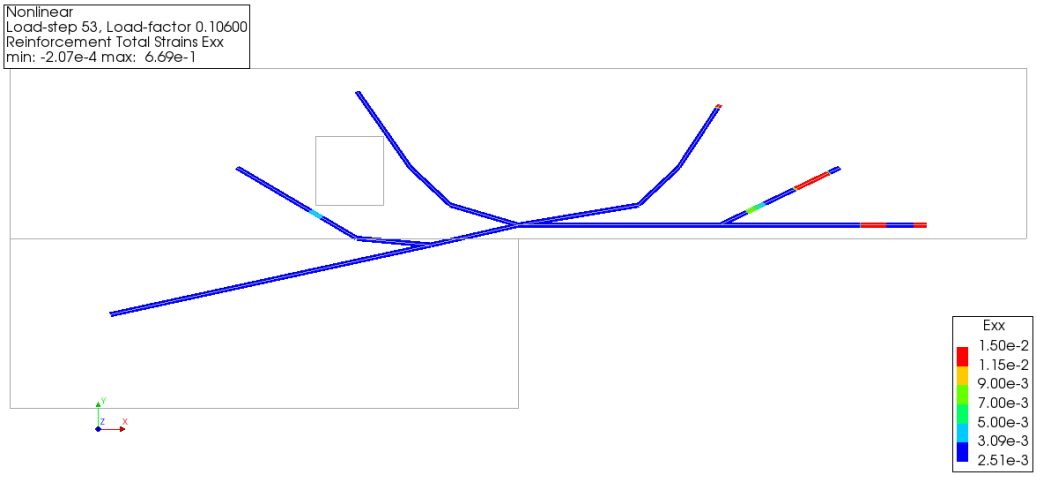

(b) Rebar strain (Exx) at G-series TR model

(c) Actual failure of specimen G-1 [19]

Figure 6.5: NLFEA results at failure load level vs. the actual failure of G-series TR models (Oviedo).

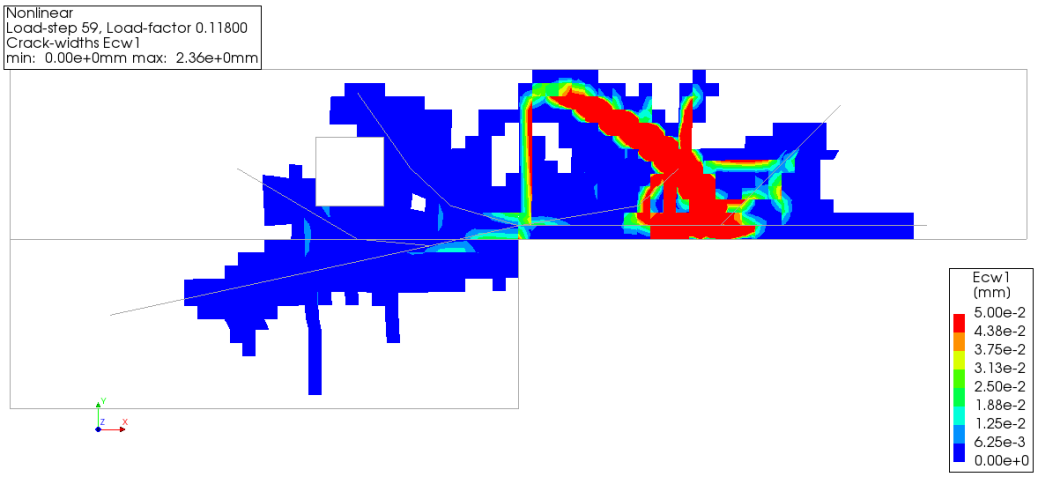

(a) Crack pattern (Ecw1) of H-series TR model

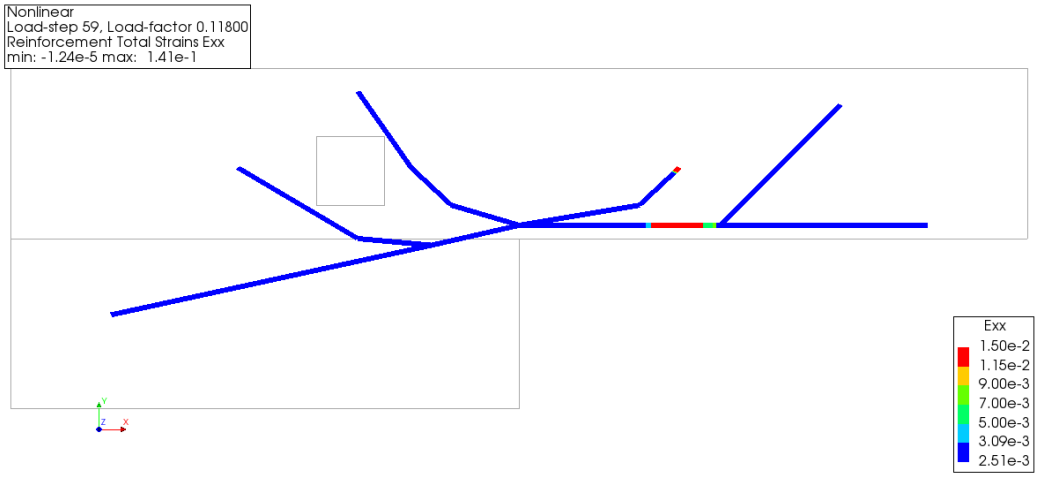

(b) Rebar strain (Exx) at H-series TR model

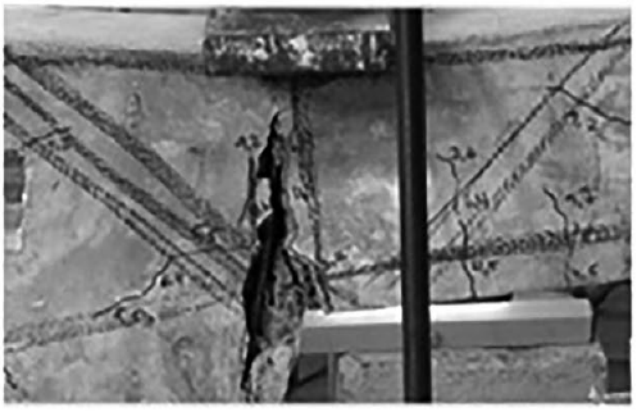

(c) Actual failure of specimen H-1 [19]

Figure 6.6: NLFEA results at failure load level vs. the actual failure of H-series TR models (Oviedo).

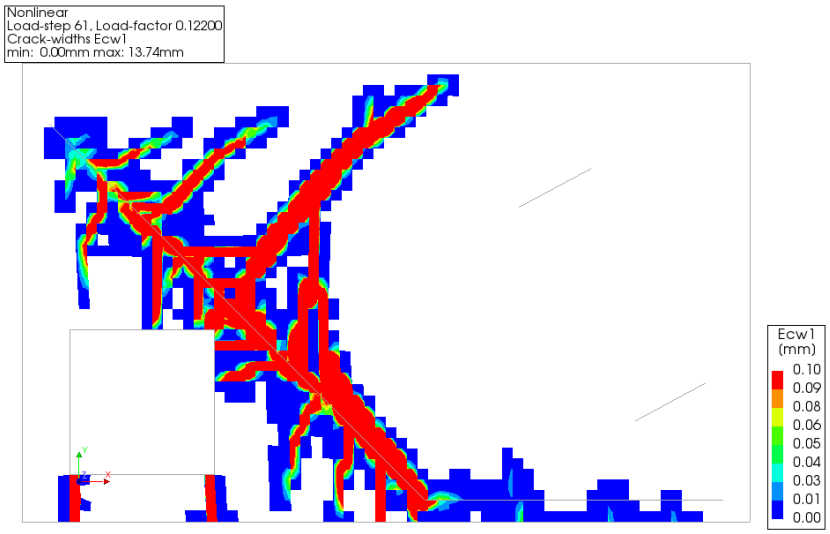

(a) Crack pattern (Ecw1) of specimen 2 TR model

(b) Rebar strain (Exx) at specimen 2 TR model

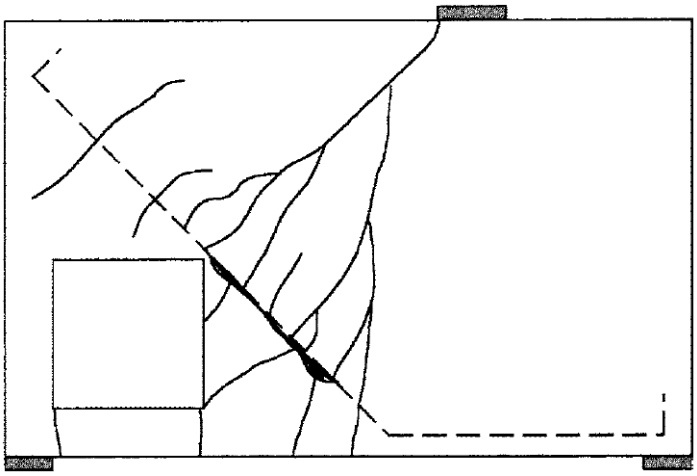

(c) Illustration of specimen 2 crack pattern at failure [3]

Figure 6.7: NLFEA results at failure load level vs. the actual failure of specimen 2 TR models (Maxwell & Breen).

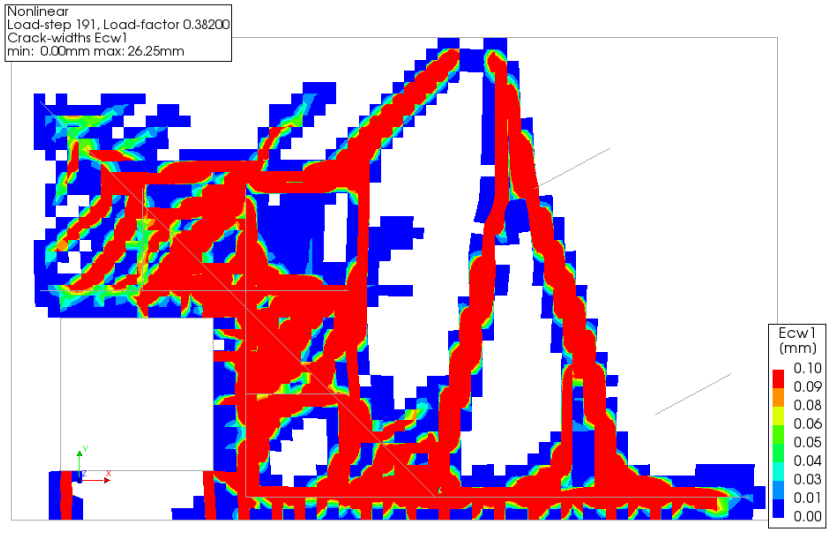

(a) Crack pattern (Ecw1) of specimen 3 TR model

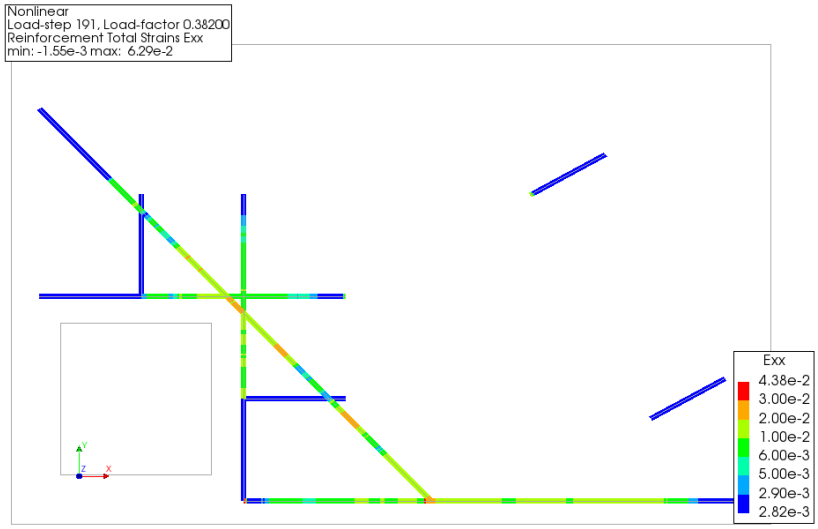

(b) Rebar strain (Exx) at specimen 3 TR model

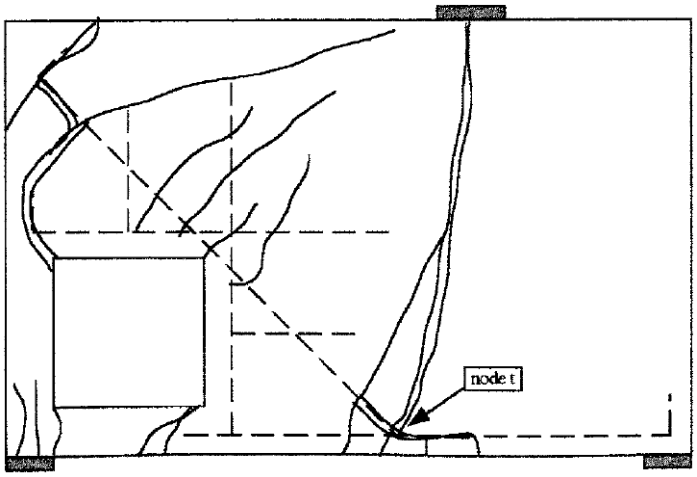

(c) Illustration of specimen 3 crack pattern at failure [3]

Figure 6.8: NLFEA results at failure load level vs. the actual failure of specimen 3 TR models (Maxwell & Breen).

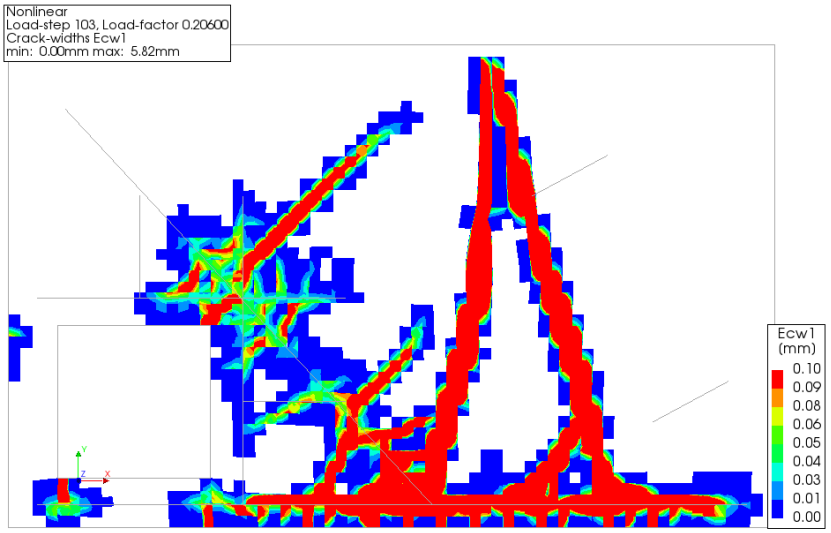

(a) Crack pattern (Ecw1) of specimen 4 TR model

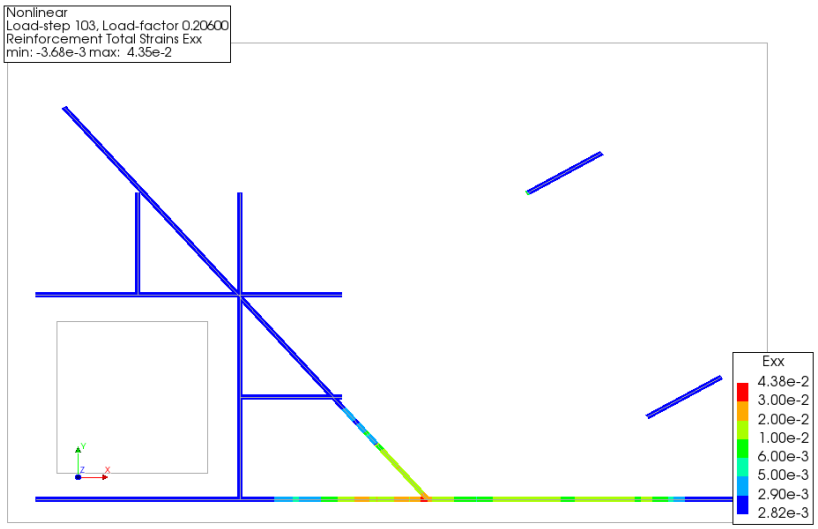

(b) Rebar strain (Exx) at specimen 4 TR model

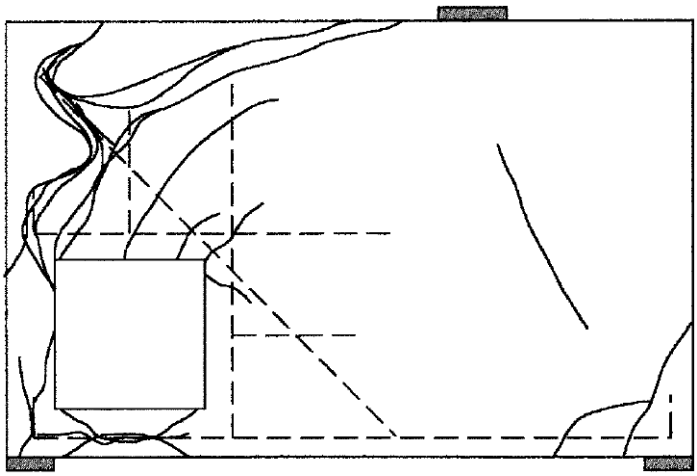

(c) Illustration of specimen 4 crack pattern at failure [3]

Figure 6.9: NLFEA results at failure load level vs. the actual failure of specimen 4 TR models (Maxwell & Breen).

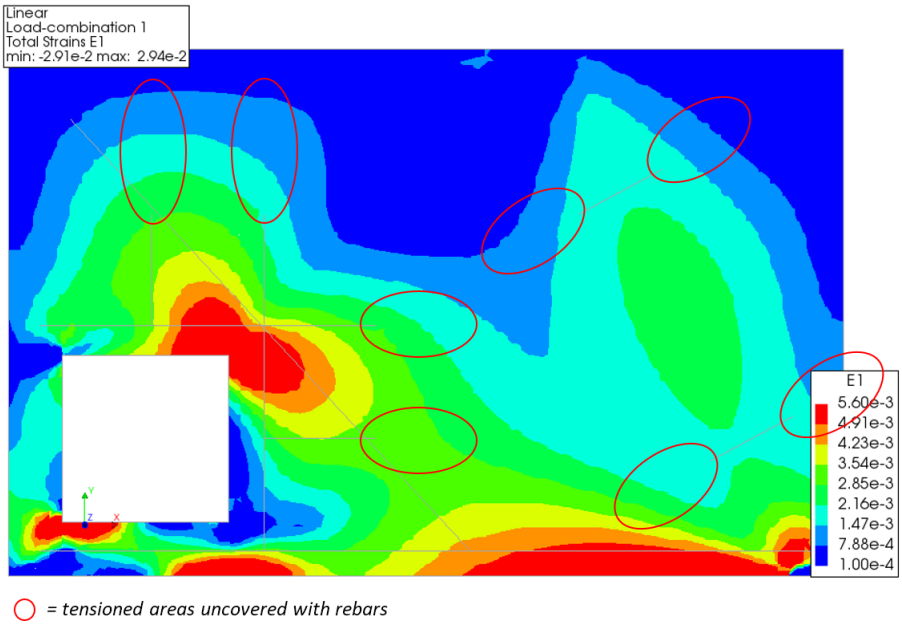

Figure 6.10: Principal tensile strain (E1) contour of the deep beam with a large opening obtained from LEFEA and its uncovered tensioned areas.

7

The numerical result of the ties-as-extended-rebars models

In this chapter, the numerical results obtained from implementing the proposed technique on the ST models of the test cases, or TER models' results, are presented. Those results will be discussed in terms of failure mode, load-displacement curve, and ultimate capacity. Additionally, an extensive description on complete proposed technique implementation will be given for ST model of specimen F-1 as an example.

7.1. F-series ties-as-extended-rebars model results

Having the TER model allows the F-series truss model (Figure 7.1) to be nonlinearly analyzed as a dapped beam with an opening and embedded rebars. To create the embedded rebars for the TER model, the ST model's ties layout (Figure 7.2) was projected as the initial rebars layout. Then, each group of connected ties that approximately has a similar alignment in that rebar layout was collected as one 'leg' to simplify the material assignment process (as explained in Section 6.2). The rebar legs defined for the F-series TER model is shown in Figure 7.3.

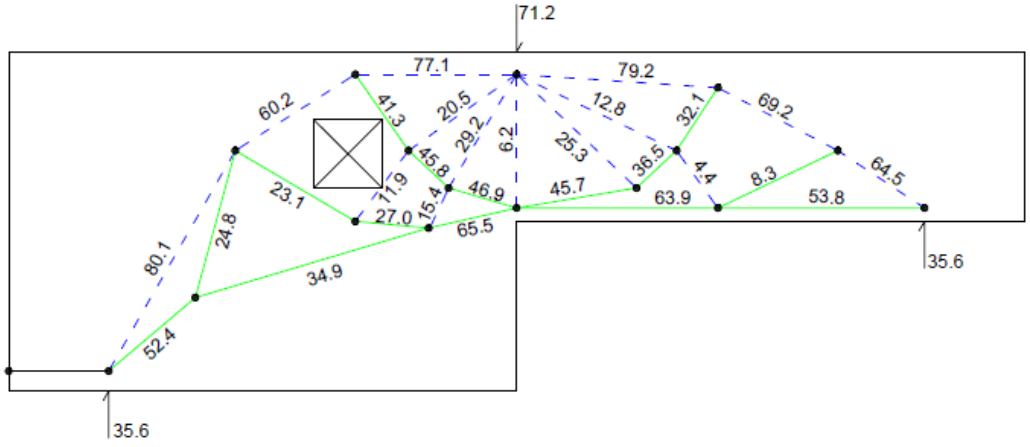

Figure 7.1: F-series ST model [19].

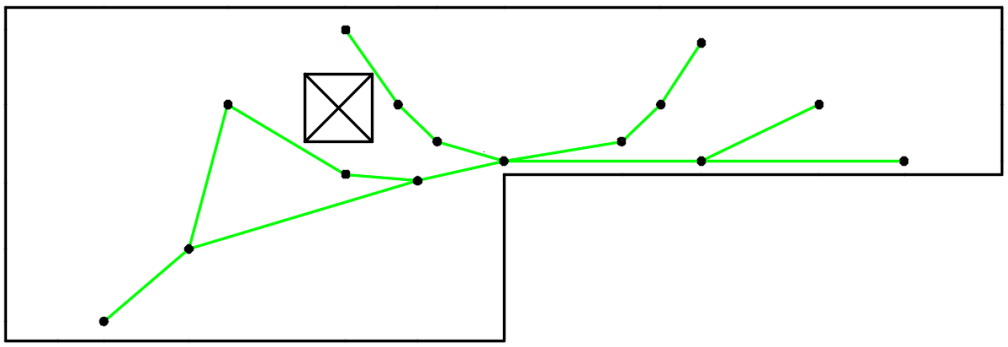

Figure 7.2: F-series ties layout.

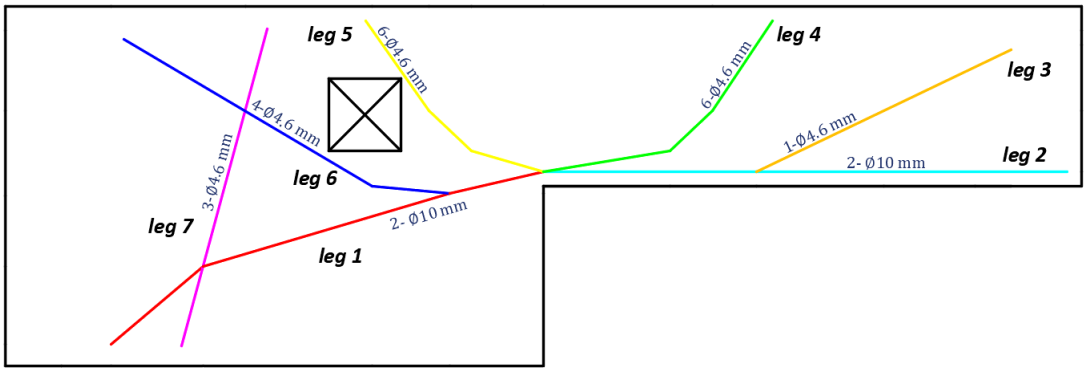

Figure 7.3: Rebar legs definitions for the F-series TER model.

The tip of these rebar legs were then extended with anchorage length toward nearby tensile stress region, as explained in Section 6.2. The type of anchorage length given to the embedded rebars is straight anchorage length. The additional length was calculated in accordance to equation 2.22 for obtaining equivalent anchorage length, or $l_{b,eq}$, with $\alpha_1 = 1.0$ for straight type of anchorage. If the length provided by $l_{b,eq}$ is shorter than the minimum anchorage length $(l_{b,min})$, the minimum length is then used (see Section 2.3).

The steel specification of the rebar legs was then determined. Specification of rebar with diameter 4.6 mm and 10 mm from Oviedo's experiment (i.e. diameter, yield strength, etc.) was assigned to the rebar legs of the F-series TER model. The main flexural rebar legs (leg 1 and 2) were assigned as 10-mm rebars, whereas the other rebar legs were assigned as 4.6-mm rebars. The amount of rebars that each rebar leg need were estimated through a stress check between the tensile force on the ties with the capacity of a rebar set. The stress check results on the amount of rebars applied on each rebar leg are summarized in Table 7.1.

The load-displacement curve of the F-series TER model is displayed in Figure 7.4. The loads which are presented in this curve are the reaction forces from the prescribed deformation that was placed at the loading point. Meanwhile, the information regarding the displacements were obtained from a node located precisely at the re-entrance corner.

The curve immediately starts with the nonlinear behavior of the dapped beam model. It appears that the linear response of the model is almost nonexistence since a minuscule crack appeared at the re-entrance corner when the beam withstand a low-level load at load-step 1 (load level = 5.79 kN). When progressing to further load steps, the dapped beam model seems to lose its stiffness

Table 7.1: Amount of rebars applied to the rebar legs of the F-series TER model and their stress check results.

Rebar leg ID	Tie force (kN)	Representing rebar	Total area (mm^2)	Tension stress per rebar (MPa)	Mean yield strength of rebar (MPa)	Stress Ratio
1	52.40	2 - 10 mm	157.08	333.59	625.00	0.53
	34.90	2 - 10 mm	157.08	222.18	625.00	0.36
	65.50	2 - 10 mm	157.08	416.99	625.00	0.67
2	63.90	2 - 10 mm	157.08	406.80	625.00	0.65
	53.80	2 - 10 mm	157.08	342.50	625.00	0.55
3	8.30	1 - 4.6 mm	16.62	499.43	508.00	0.98
4	32.10	6 - 4.6 mm	99.71	321.92	508.00	0.63
	36.50	6 - 4.6 mm	99.71	366.05	508.00	0.72
	45.70	6 - 4.6 mm	99.71	458.31	508.00	0.90
5	46.90	6 - 4.6 mm	99.71	470.34	508.00	0.93
	45.80	6 - 4.6 mm	99.71	459.31	508.00	0.90
	41.30	6 - 4.6 mm	99.71	414.18	508.00	0.82
6	27.00	4 - 4.6 mm	66.48	406.16	508.00	0.80
	23.10	4 - 4.6 mm	66.48	347.49	508.00	0.68
7	24.80	3 - 4.6 mm	49.86	497.42	508.00	0.98

gradually while resisting the applied load. However, the model was able to maintain its ability to resist heavier load at every load step until the numerical model ultimately reached failure.

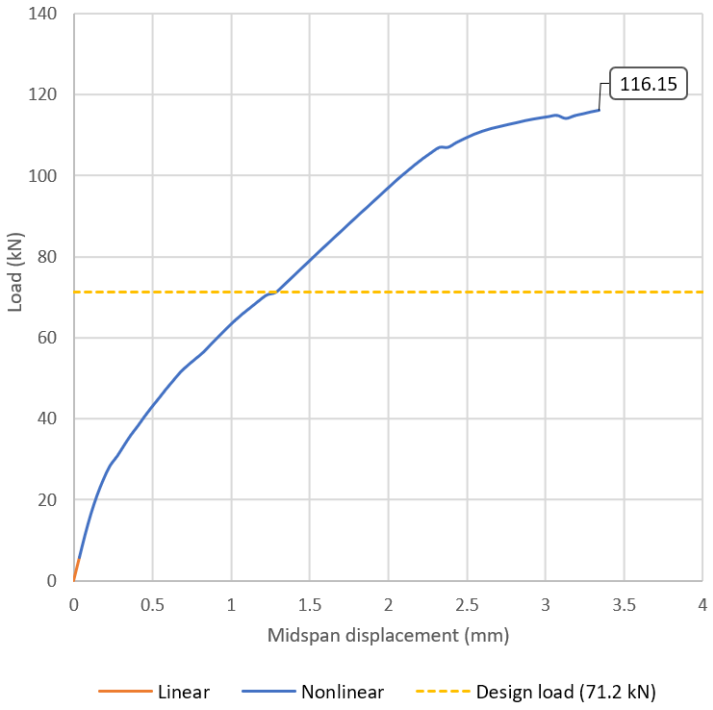

Figure 7.4: Load-displacement curve of the F-series TER model.

After the NLFEA progressed to load-step 69, the dapped beam model stopped presenting a converging solution. Its complete failure can be observed at this load step. The crack pattern plot, displayed in Figure 7.5a, showed that most of the wide cracks had their gap narrowing, except for the vertical flexural crack at the midspan. This flexural crack ultimately caused the beam to split right at its midspan due to the rupture of the 10-mm rebar leg at a local strain of 0.015 from preventing the

flexural crack to open (Figure 7.5b). With this split, the TER model gave away its capability in resisting the concentrated load and failed with a flexural failure mechanism. The ultimate capacity of this model is 116.15 kN.

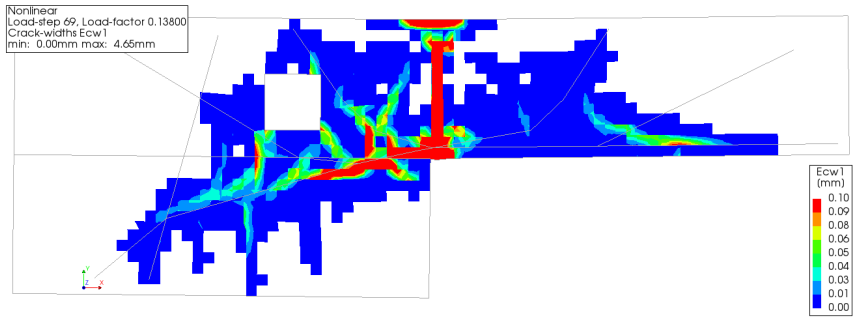

(a) Ecw1

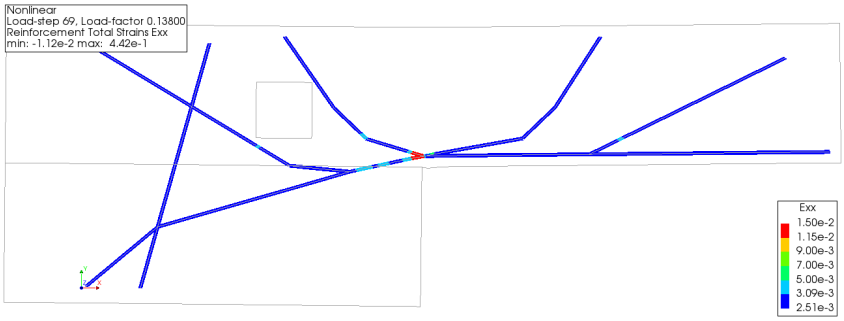

(b) Exx

Figure 7.5: (a) Crack pattern (Ecw1) and (b) rebar strain at local X-direction (Exx) of the F-series TER model after last converging load step.

7.2. G-series ties-as-extended-rebars model results

Having the TER model allows the G-series truss model (Figure 7.6) to be nonlinearly analyzed as a dapped beam with an opening and embedded rebars. The rebar legs defined for the G-series TER model is shown in Figure 7.7.

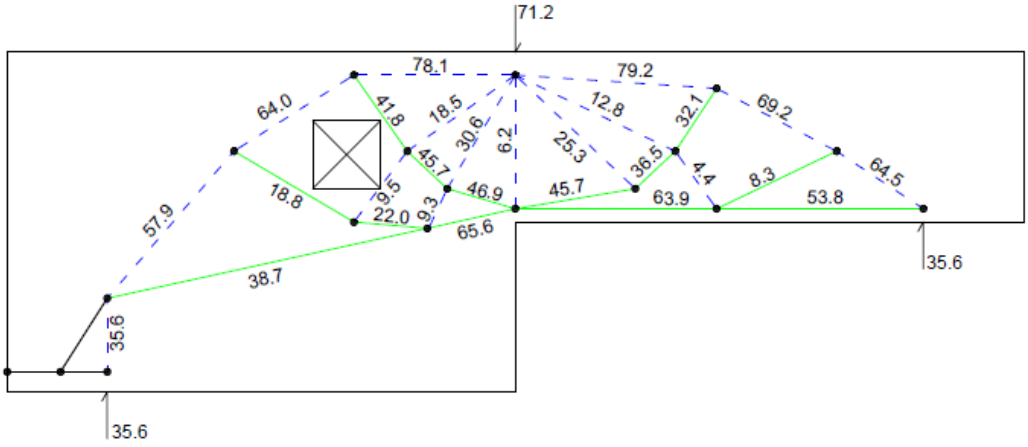

Figure 7.6: G-series ST model [19].

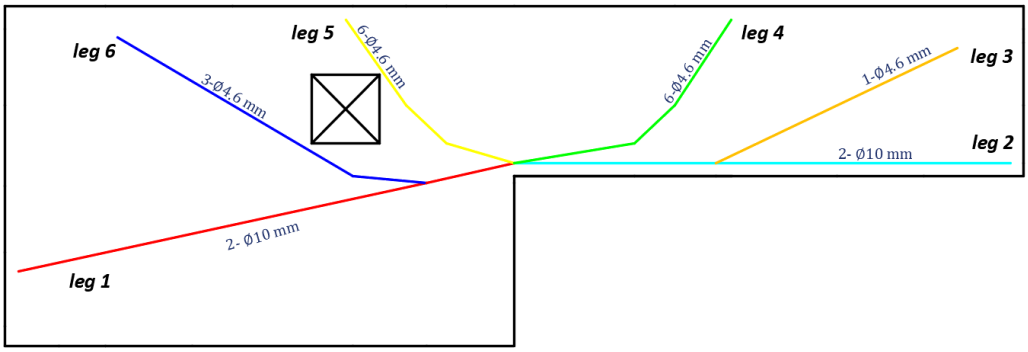

Figure 7.7: Rebar legs definitions for the G-series TER model.

The load-displacement curve of the G-series TER model is displayed in Figure 7.8. The loads which are presented in this curve are the reaction forces from the prescribed deformation that was placed at the loading point. Meanwhile, the information regarding the displacements were obtained from a node located precisely at the re-entrance corner.

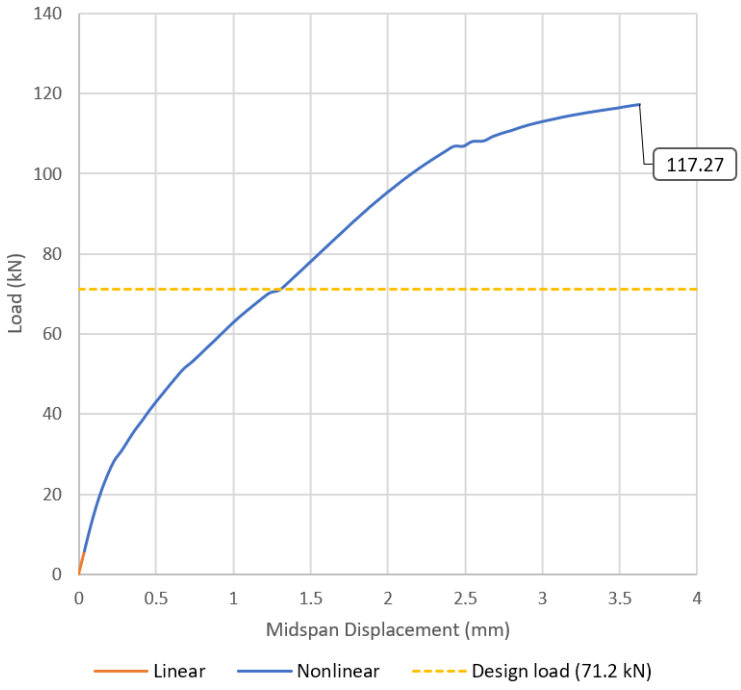

Figure 7.8: Load-displacement curve of the G-series TER model.

The curve immediately starts with the nonlinear behavior of the dapped beam model. It appears that the linear response of the model is almost nonexistence since a minuscule crack appeared at the re-entrance corner when the beam withstand a low-level load at load-step 1 (load level = 5.78 kN). When progressing to further load steps, the dapped beam model seems to lose its stiffness gradually while resisting the applied load. However, the model was able to maintain its ability to resist heavier load at every load step until the numerical model ultimately reached failure.

After the NLFEA progressed to load-step 73, the dapped beam model stopped presenting a converging solution. Its complete failure can be observed in this load step. The crack pattern plot, displayed in Figure 7.9a, showed that most of the wide cracks had their gap narrowing, except for the vertical

flexural crack at the midspan. This flexural crack ultimately caused the beam to split right at its midspan due to the rupture of the 10-mm rebar leg at a local strain of 0.015 from preventing the flexural crack to open (Figure 7.9b). With this split, the TER model gave away its capability in resisting the concentrated load and failed with a flexural failure mechanism. The ultimate capacity of this model is 117.27 kN.

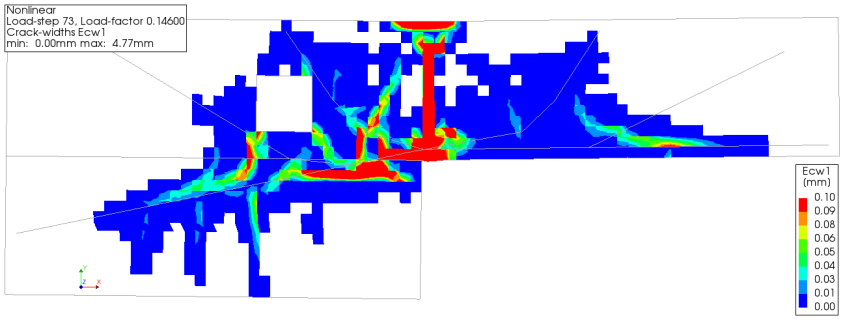

(a) Ecw1

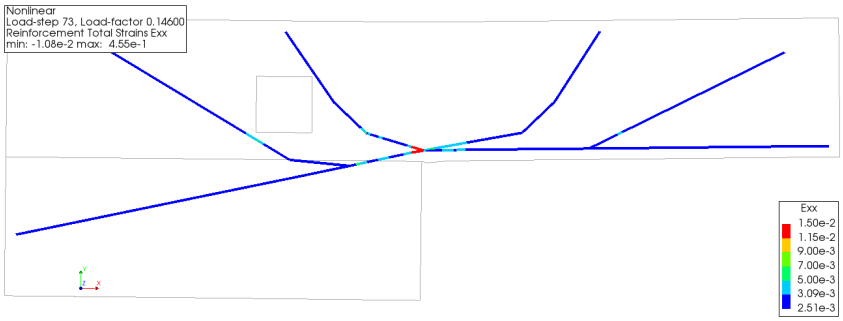

(b) Exx

Figure 7.9: (a) Crack pattern (Ecw1) and (b) rebar strain at local X-direction (Exx) of the G-series TER model after last converging load step.

7.3. H-series ties-as-extended-rebars model results

Having the TER model allows the H-series truss model (Figure 7.10) to be nonlinearly analyzed as a dapped beam with an opening and embedded rebars. The rebar legs defined for the H-series TER model is shown in Figure 7.11.

The load-displacement curve of the H-series TER model is displayed in Figure 7.12. The loads which are presented in this curve are the reaction forces from the prescribed deformation that was placed at the loading point. Meanwhile, the information regarding the displacements were obtained from a node located precisely at the re-entrance corner.

The curve immediately starts with the nonlinear behavior of the dapped beam model. It appears that the linear response of the model is almost nonexistence since a minuscule crack appeared at the re-entrance corner when the beam withstand a low-level load at load-step 1 (load level = 5.74 kN). When progressing to further load steps, the dapped beam model seems to lose its stiffness gradually while resisting the applied load. However, the model was able to maintain its ability to resist heavier load at every load step until the numerical model ultimately reached failure.

After the NLFEA progressed to load-step 65, the dapped beam model stopped presenting a converg-

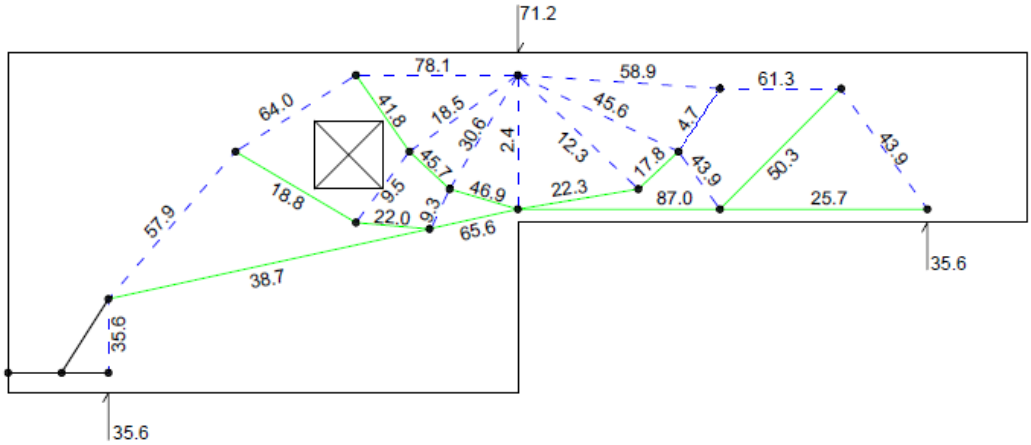

Figure 7.10: H-series ST model [19].

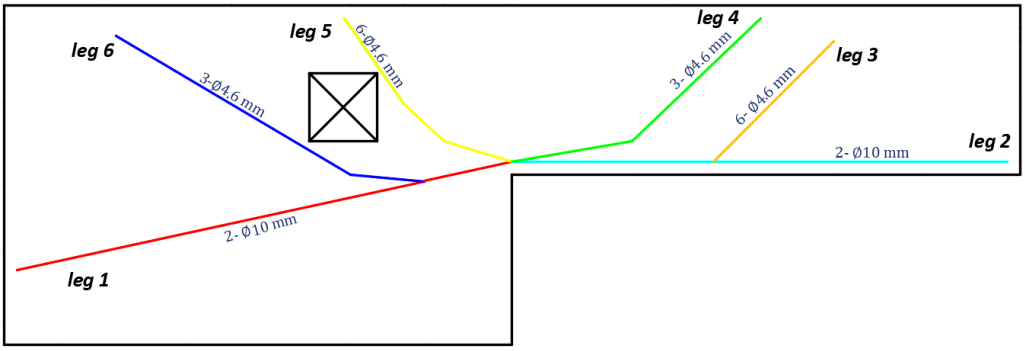

Figure 7.11: Rebar legs definitions for the H-series TER model.

ing solution. Its complete failure can be observed in this load step. The crack pattern plot, displayed in Figure 7.13a, showed that most of the wide cracks had their gap narrowing, except for the vertical and the inclining flexural cracks at the midspan. The former flexural crack ultimately caused the beam to split right at its midspan due to the rupture of the 10-mm rebar leg at a local strain of 0.015 from preventing the flexural crack to open (Figure 7.13b). With this split, the TER model gave away its capability in resisting the concentrated load and failed with a flexural failure mechanism. The ultimate capacity of this model is 101.64 kN.

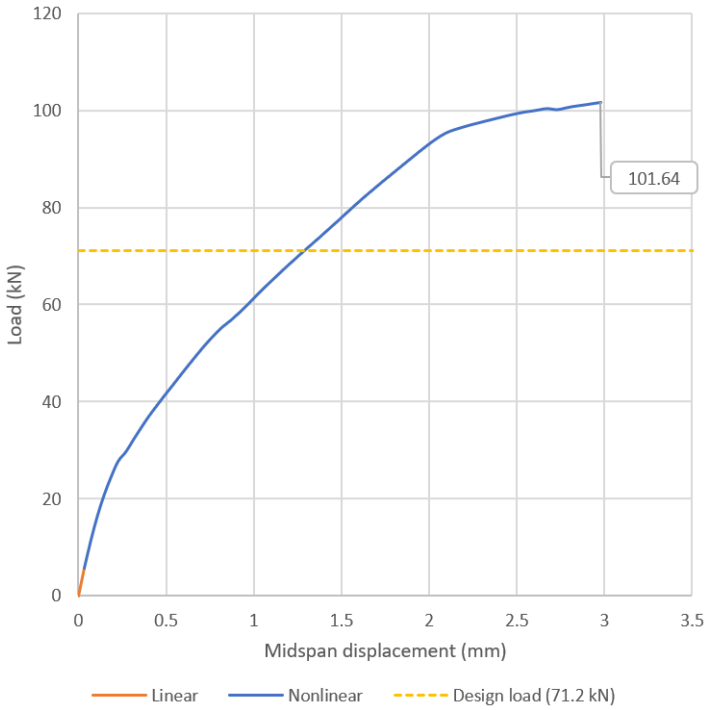

Figure 7.12: Load-displacement curve of the H-series TER model.

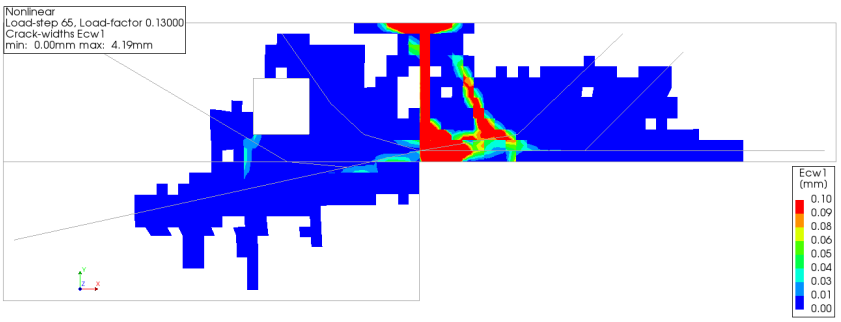

(a) Ecw1

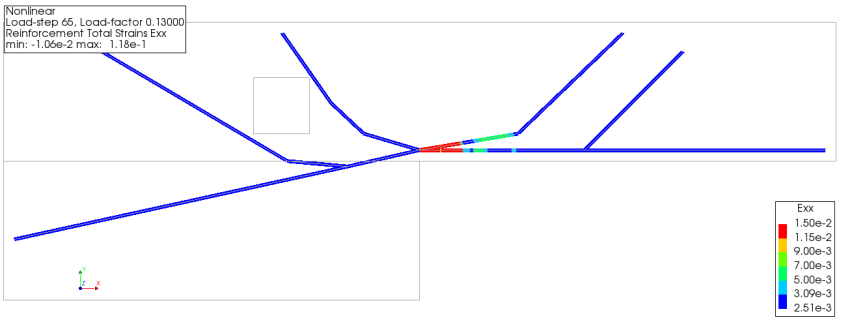

(b) Exx

Figure 7.13: (a) Crack pattern (Ecw1) and (b) rebar strain at local X-direction (Exx) of the H-series TER model after last converging load step.

7.4. Specimen 2 ties-as-extended-rebars model results

Having the TER model allows Specimen 2 truss model (Figure 7.14) to be nonlinearly analyzed as a dapped beam with an opening and embedded rebars. The rebar legs defined for Specimen 2 TER

model is shown in Figure 7.15.

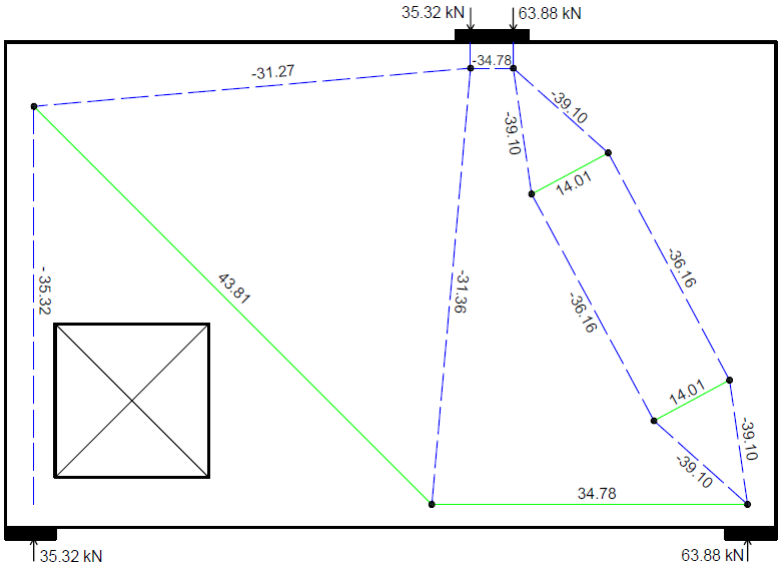

Figure 7.14: Specimen 2 ST model [19].

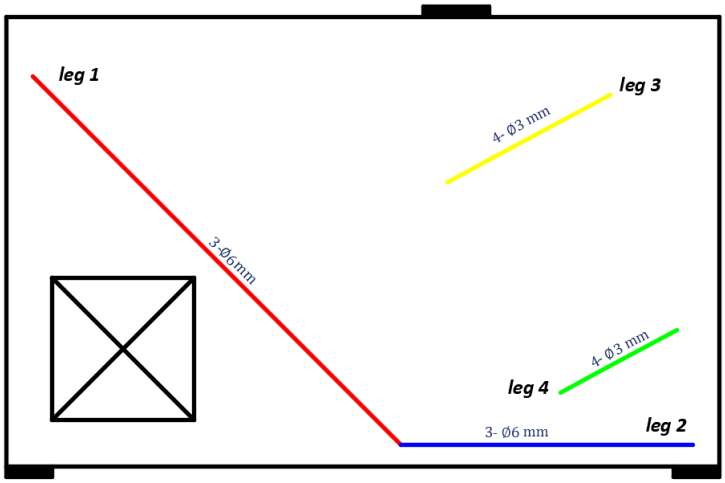

Figure 7.15: Rebar legs definitions for Specimen 2 TER model.

The load-displacement curve of Specimen 2's TER model is displayed in Figure 7.16. The load presented in this curve are the reaction forces from the prescribed deformation placed at the loading point, while the displacements were obtained from one of the most-bottom row nodes which is located precisely below the loading point. In this curve, the linear and the nonlinear responses of the TER model can be clearly distinguished and observed. According to this curve, the TER model was able to hold about 20 kN of the total applied load before it reached the end of its linear phase. Once it entered the nonlinear phase, the numerical model managed to maintain its stiffness for a brief deformation before it immediately lost most of its structural stiffness. Then, the increase of the load level caused the as-drawn model to have more deformation during the rest of the numerical simulation while gradually losing its remaining stiffness. Right before the NLFEA ended, the deep beam model experienced a sudden loss of stiffness, but then it managed to regain its load resistance and handled more loads before it reached its failure.

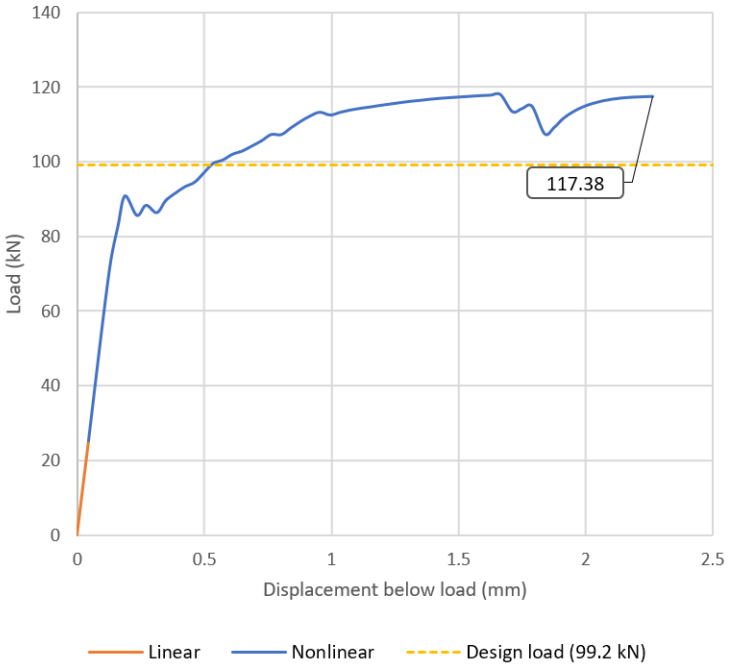

Figure 7.16: Load-displacement curve of the Specimen 2's TER model.

After the NLFEA progressed to load-step 62, the deep beam model stopped presenting a converging solution. The crack pattern plot presented in Figure 7.17a showed that the increase of the load only caused the TER model to develop more damage at the right-lower section of rebar leg 1. The model was not able to carry more load because most of its plain concrete parts around the opening had extensive concrete damages due to the continual elongation of rebar leg 1. Since the failure characteristic of this beam model matches neither shear nor flexural failure characteristics, it is difficult to classify this failure. Therefore, for further reference in this thesis, this type of failure will be mentioned as the 'premature' failure, since the failure of the model does not cause any rebars to rupture, as shown in Figure 7.17b. The ultimate capacity of this model is 117.38 kN.

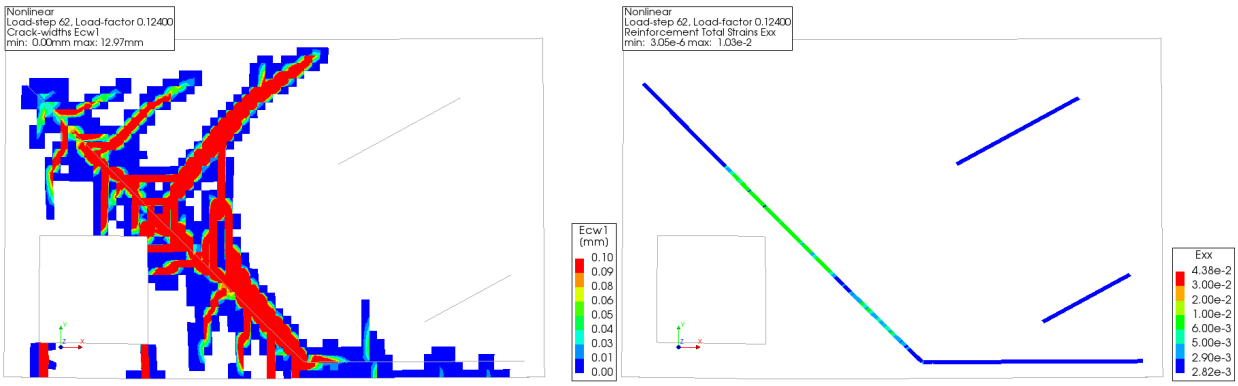

(a) Ecw1 **(b)** Exx

Figure 7.17: (a) Crack pattern (Ecw1) and (b) rebar strain at local X-direction (Exx) of the Specimen 2 TER model after last converging load step.

7.5. Specimen 3 ties-as-extended-rebars model results

Having the TER model allows Specimen 3 truss model (Figure 7.18) to be nonlinearly analyzed as a dapped beam with an opening and embedded rebars. The rebar legs defined for Specimen 3 TER model is shown in Figure 7.19.

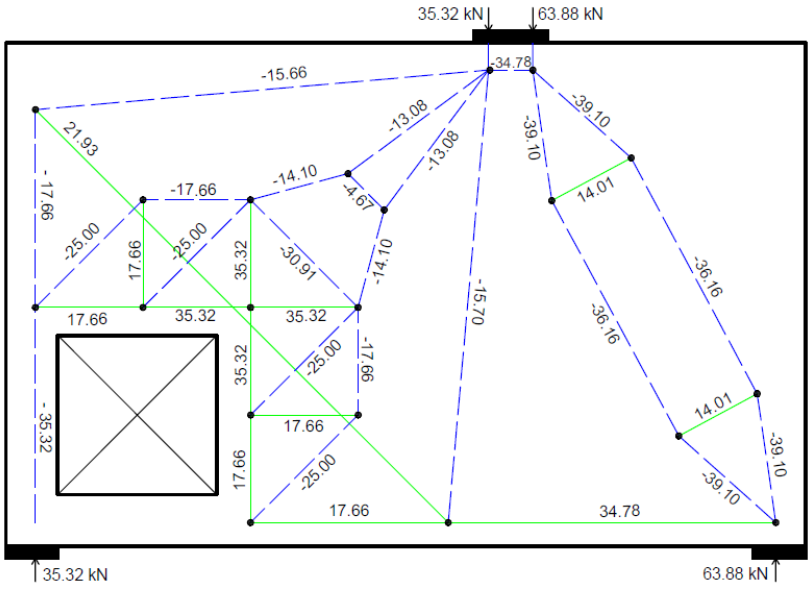

Figure 7.18: Specimen 3 ST model [19].

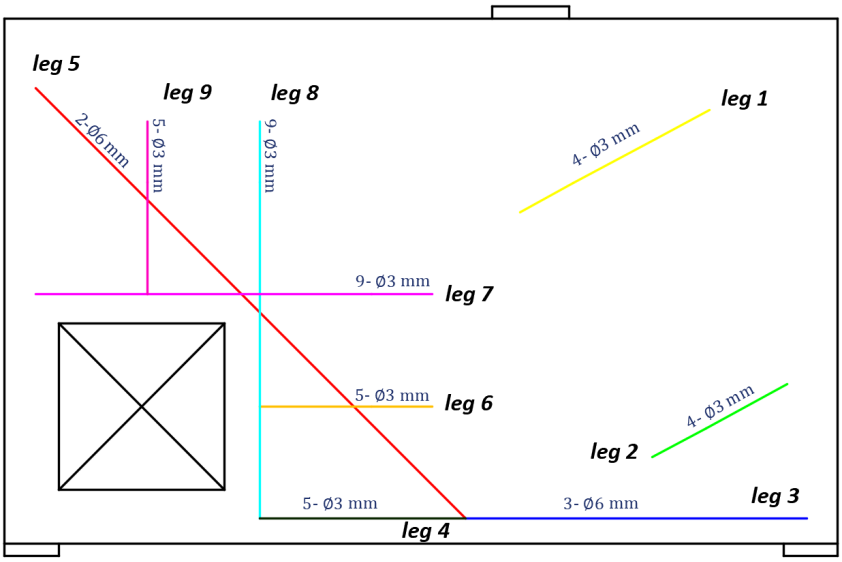

Figure 7.19: Rebar legs definitions for Specimen 3 TER model.

The load-displacement curve of Specimen 3's TER model is displayed in Figure 7.20. The load presented in this curve are the reaction forces from the prescribed deformation placed at the loading point, while the displacements were obtained from one of the most-bottom row nodes which is located precisely below the loading point. In this curve, the linear and the nonlinear responses of the TER model can be clearly distinguished and observed. According to this curve, the TER model was able to hold about 20 kN of the total applied load before it reached the end of its linear phase.

Once it entered the nonlinear phase, the numerical model managed to maintain its stiffness for a brief deformation before it immediately lost all of its structural stiffness, shown by a sudden drop of load resistance between 0 to 1-mm displacement after reaching a load level around 150 kN. Soon after, the deep beam model regained its load resistance and started to hold more load. At this part of nonlinear phase, the TER model has lost most of its stiffness and had a lot of deformation, which can be seen from the almost platonic part of the load-displacement curve. After reaching the peak load, the stiffness of the numerical model gradually degrade before the NLFEA ended.

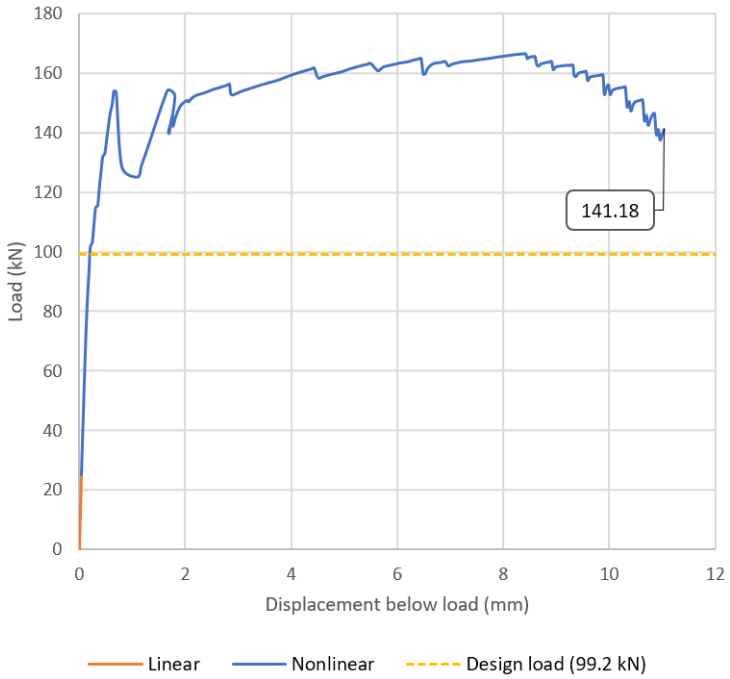

Figure 7.20: Load-displacement curve of the Specimen 3's TER model.

After the NLFEA progressed to load-step 239, the deep beam model stopped presenting a converging solution. The crack pattern plot presented in Figure 7.21a showed that the increase of the load only caused the TER model to develop more damage around the cracks that have developed and also closed parts of some open cracks. The model was not able to carry more load because most the concrete around rebar leg 3 and 4 has softened. The softening of the concrete at that area caused the redistribution of tensile stress to those rebar legs to be halted, and prevented the rupture of node 't'. Since the failure characteristic of this beam model matches neither shear nor flexural failure characteristics, it is difficult to classify this failure. Therefore, for further reference in this thesis, this type of failure will be mentioned as the 'premature' failure, since the failure of the model does not cause any rebars to rupture, as shown in Figure 7.21b. The ultimate capacity of this model is 141.18 kN.

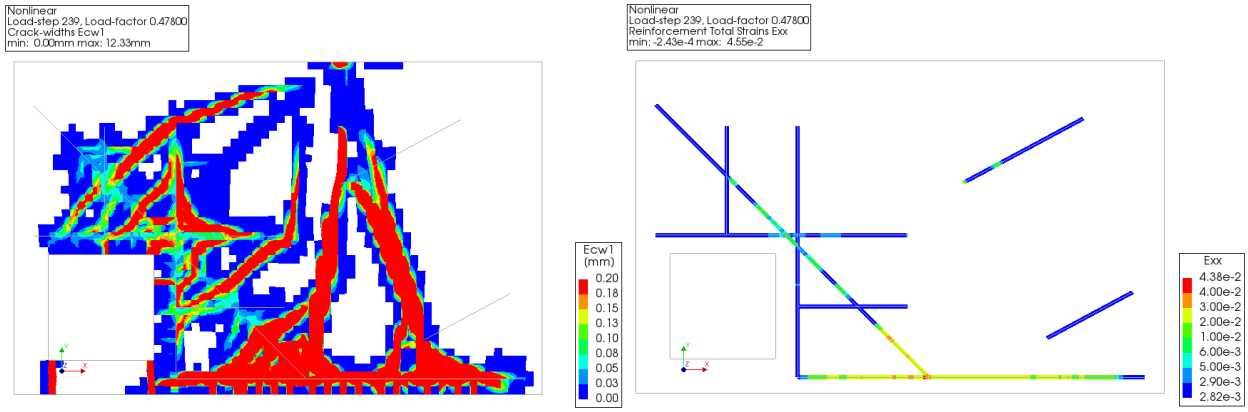

(a) Ecw1 **(b)** Exx

Figure 7.21: (a) Crack pattern (Ecw1) and (b) rebar strain at local X-direction (Exx) of the Specimen 3 TER model after last converging load step.

7.6. Specimen 4 ties-as-extended-rebars model results

Having the TER model allows Specimen 4 truss model (Figure 7.22) to be nonlinearly analyzed as a dapped beam with an opening and embedded rebars. The rebar legs defined for Specimen 4 TER model is shown in Figure 7.23.

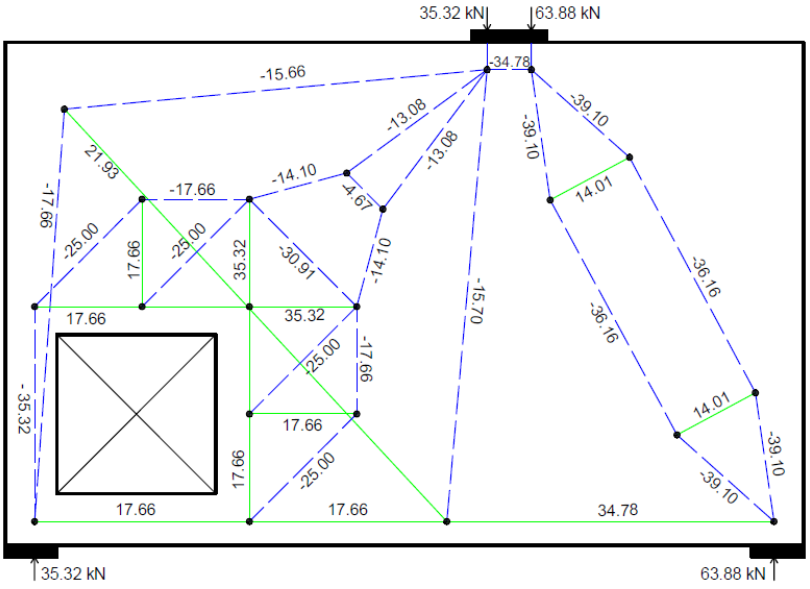

Figure 7.22: Specimen 4 ST model [19].

The load-displacement curve of Specimen 4's TER model is displayed in Figure 7.24. The load presented in this curve are the reaction forces from the prescribed deformation placed at the loading point, while the displacements were obtained from one of the most-bottom row nodes which is located precisely below the loading point. In this curve, the linear and the nonlinear responses of the TER model can be clearly distinguished and observed. According to this curve, the TER model was able to hold about 20 kN of the total applied load before it reached the end of its linear phase. Once it entered the nonlinear phase, the numerical model managed to maintain its stiffness for a brief deformation before it immediately lost all of its structural stiffness. The stiffness loss is shown

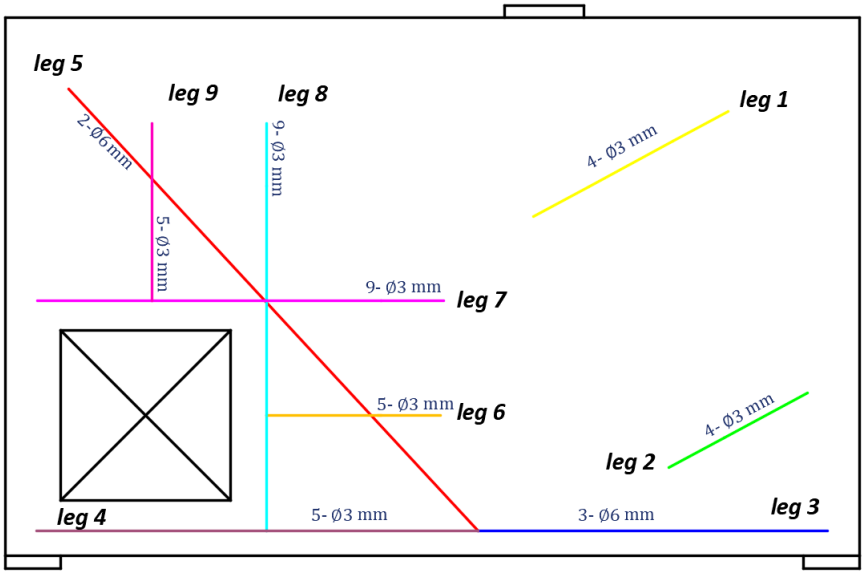

Figure 7.23: Rebar legs definitions for Specimen 4 TER model.

by a sudden drop of load resistance between 0.5 to 1-mm displacement after reaching a load level around 180 kN. Soon after, the deep beam model regained its load resistance and started to hold more load. At this part of nonlinear phase, the TER model has lost most of its stiffness and had a constant deformation, which can be seen from the almost platonic part of the load-displacement curve. Before the TER model reached its failure, the deep beam model lost its stiffness once more and had its load resistance dropped from about 170 kN to 150 kN. The constant deformation after the drop lead the beam model to its failure.

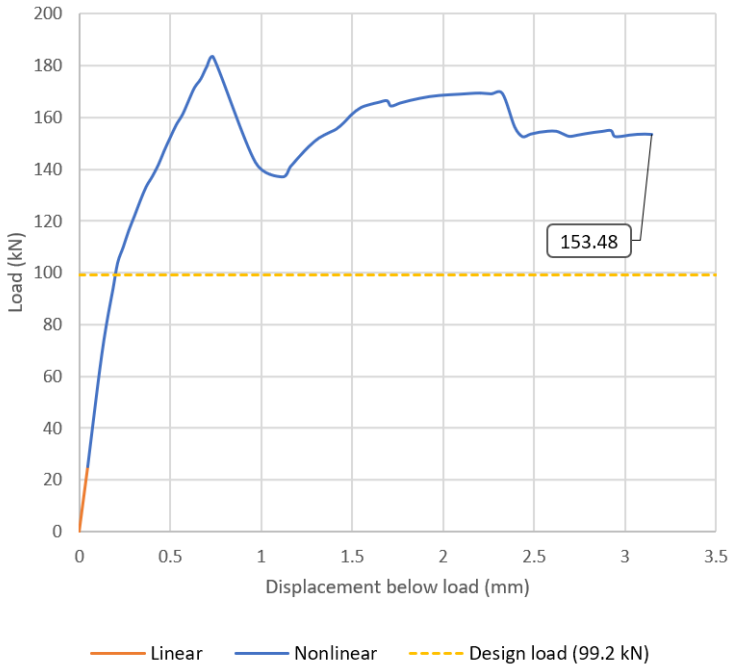

Figure 7.24: Load-displacement curve of the Specimen 4's TER model.

After the NLFEA progressed to load-step 71, the deep beam model stopped presenting a converging

solution. Its complete failure can be observed in this load step. The crack pattern plot, as displayed in Figure 7.25a, showed that most of the wide cracks become narrower, except for the vertical flexural crack in the middle of the beam and three other vertical flexural cracks at its right. However, only the flexural crack from node 't' that ultimately caused the beam to split right at its midspan due to the rupture of the rebar legs at that node (Figure 7.25b). With this split, the TER model of Specimen 4 gave away its capability in resisting the concentrated load and failed with a flexural failure mechanism. The ultimate capacity of this model is 153.48 kN.

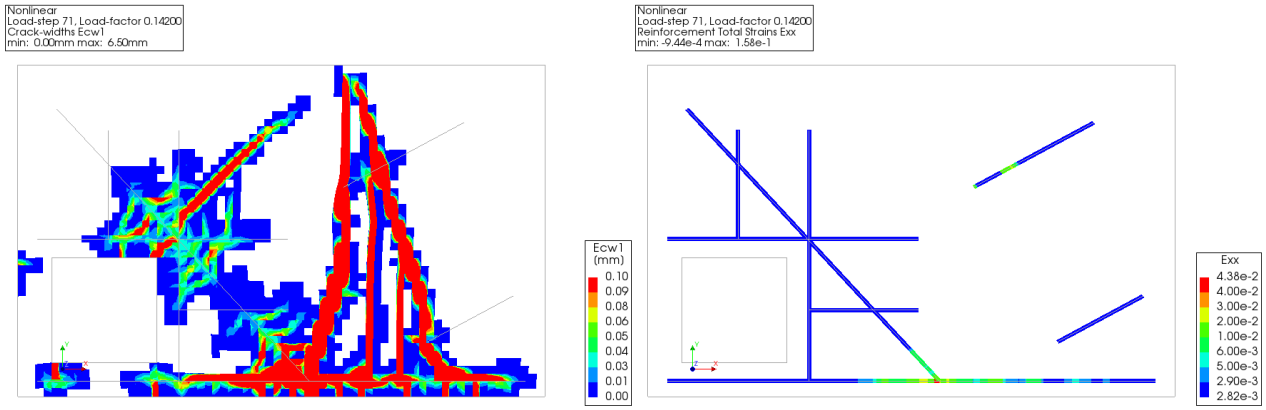

(a) Ecw1 **(b)** Exx

Figure 7.25: (a) Crack pattern (Ecw1) and (b) rebar strain at local X-direction (Exx) of the Specimen 4 TER model after last converging load step.

8

Validating the ties-as-extended rebars models results with the strut-and-tie method results

This chapter will discuss an attempt to validate the numerical results of the TER models of the test cases using STM results. The validation is done by confirming that the ultimate capacity predicted by the TER models has higher values than the factored design load of their respective ST models, which denotes the lower-bound expectation of the ultimate capacity. Before the comparison is given, it is important to check if the ST models provide a safe design to the test cases. Thus, the following sections will first discuss the stress check on the concrete elements using ST dimensioning process, which then followed by the discussion about the validation. As an example, an extensive description of complete ST dimensioning will be given for the ST model of specimen F-1, while ST dimensioning check of the other ST models can be found on Appendix A.

8.1. Strut-and-tie dimensioning check results

8.1.1. F-series strut-and-tie model

The results for dimensioning the F-series ST model is presented in this section. The struts, ties, and nodes of this ST model were dimensioned in accordance with the type and magnitude of the force acting on each truss member. After having their geometry defined, the truss members were analyzed for their stresses. Those resulting stresses were then measured against their respective failure criterion, which is the allowable stress. The allowable stress values were calculated using formulas provided in code provisions for designing an ST model in EN 1992-1-1:2004 [28] (see Section 2.1.4 for more detail).

Nodal zones

The first dimensioned truss members to be discussed are the nodes. After being shaped and sized, each node of the F-series ST model changed into a nodal zone. Based on the way forces equilibrate in its area, nodal zones can be distinguished into two different types: singular nodes and smeared nodes. Since it is unnecessary to check the concrete stresses at the smeared nodes [25], singular nodes were the only nodal zones of the F-series ST model that were checked. There are three nodes from the truss model that can be categorized as singular nodes: one near the loading point, one near the left support, and one near the right support, as indicated in Figure 8.1.

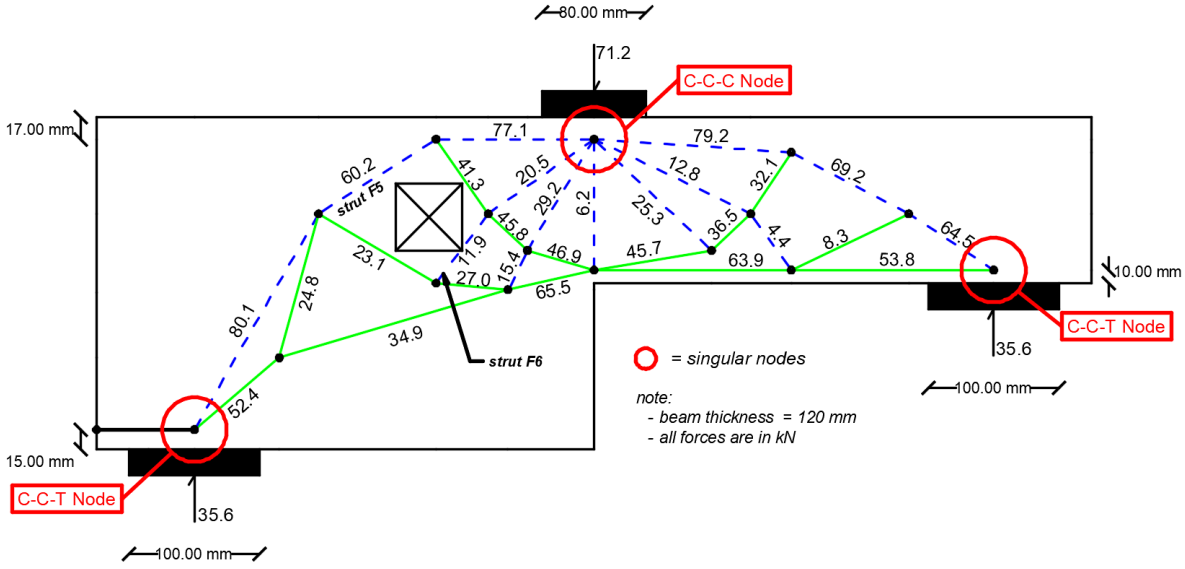

Figure 8.1: Singular nodes indicated at F-series ST model.

The singular node near the loading point is a C-C-C node. It was designed as a hydrostatic node, which means that all in-plane stresses acting on it are equivalent and directed perpendicularly toward its nodal faces. The geometry assigned to this C-C-C node is presented in Figure 8.2. According to the truss analysis result, the node initially had eight compression forces directed toward it. However, due to the limitation of the current regulations for designing nodal zones that only provide provisions for designing a nodal zone with maximum three nodal faces, the design of this C-C-C node had to be simplified and those compression forces had to be resolved into just three resulting forces. To obtain the resulting forces, the point load (71.2 kN) and the force from the left of the node (77.1 kN) were kept, and the rest of the forces were resolved into one new force with a magnitude of 104.9 kN. Furthermore, in determining the geometry of the C-C-C node, it was assumed that the width of the loading plate had less influence toward the width of the bearing face. Normally, the width of the bearing face follows the width of the loading plate, while the width of the other two nodal faces are to be adjusted until all three in-plane stresses are equivalent. But, since the width of the concrete for containing the force from the left of the node was governing the size of the C-C-C node (distance from the center of the force to the top extreme fiber = 17 mm), then the bearing face width has to be taken less than the loading plate width. After having this information, the hydrostatic state of the node was iteratively searched and it was found that the C-C-C node could achieve a hydrostatic state with in-plane stresses of 19 MPa.

In contrast, the singular nodes near the supports were identified as C-C-T nodes. These nodes were designed as nonhydrostatic nodes, which means that all in-plane stresses acting on it do not have to be equivalent, but they still have to be perpendicular toward its nodal faces. The geometries assigned to these C-C-T nodes are presented in Figure 8.3. To design the geometries of these nodal zones, the width of the back face and the bearing face of the nodes first had to be determined. Since the back face width (h_a) is defined as two times the distance from the nearest extreme fiber to the centroid of the node, h_a of the left C-C-T node is then equal to 30 mm, whereas h_a of the right C-C-T node is equal to 20 mm. Moreover, the bearing face width of a C-C-T node is typically defined as the width of its support plate. However, because the width of each support plate is relatively too wide to be used for designing the nodal zones, it was assumed that that the width of the loading plate had less influence toward the width of the bearing face. Therefore, the bearing face width of the C-C-T nodes was also taken less than the support plate width. Furthermore, to give the C-C-T

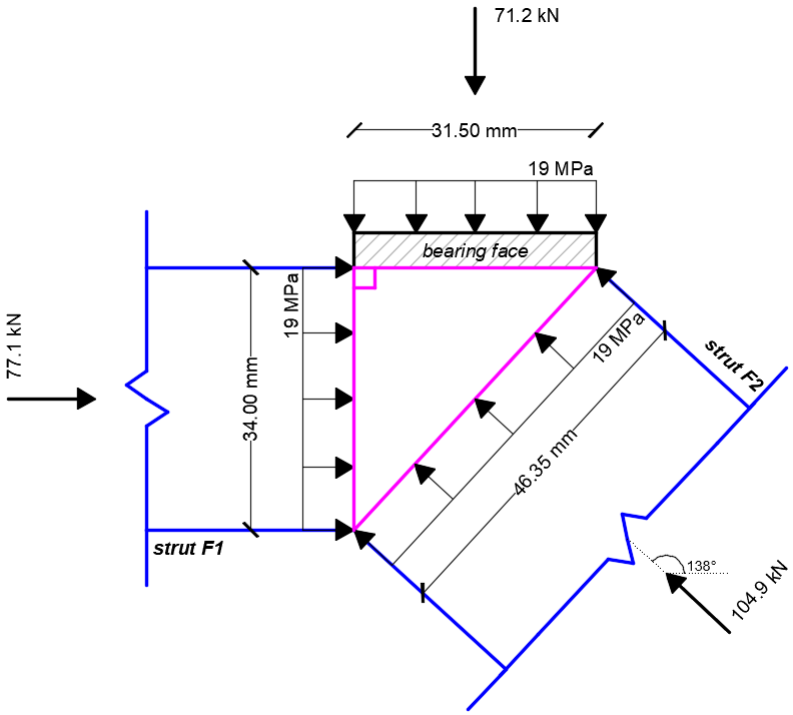

Figure 8.2: Geometry of the hydrostatic C-C-C node at F-series ST model.

nodes sensible nodal face widths, the governing nodal face width of the C-C-C node (the one with 34-mm width) was assumed to be the widths of the C-C-T nodes' nodal faces. With all the information mentioned above, the resulting stresses in the C-C-T nodes were calculated. The C-C-T node near the left support had resulting stress of 13.5 MPa at its bearing face and resulting stress of 19.6 MPa at its upper-side nodal face. Meanwhile, the C-C-T node near the right support had resulting stress of 9.3 MPa at its bearing face and resulting stress of 15.8 MPa at its upper-side nodal face.

After the resulting stresses occurring in the C-C-C and C-C-T nodes were computed, those stress values were checked against their respective allowable stresses (σ_{max}). Since the purpose of ST dimensioning in this thesis is to examine the ST models performances based on the experimental results, the strength parameters used in those formulas were replaced with mean values of concrete compressive strength obtained from the literature. Mean values of concrete compressive strength $\left(f_{cm}\right)$ of Oviedo's specimens is equal to 65.8 MPa. To calculate the allowable stresses, the value of ν' should be determined beforehand. The recommended value of ν' was determined in accordance to equation 2.6:

$$\nu' = 1 - \left(f_{cm}/250\right) = 1 - (65.8/250) = 0.74$$

After the value ν' was obtained, the allowable stress for C-C-C node was computed in accordance with equation 2.7:

$$\sigma_{max} = k_1\, \nu'\, f_{cm} = 1 * 0.74 * 65.8 = 45.58 \text{ MPa}$$

while the allowable stress for C-C-T node were computed in accordance with equation 2.8:

$$\sigma_{max} = k_2\, \nu'\, f_{cm} = 0.85 * 0.74 * 65.8 = 41.21 \text{ MPa}$$

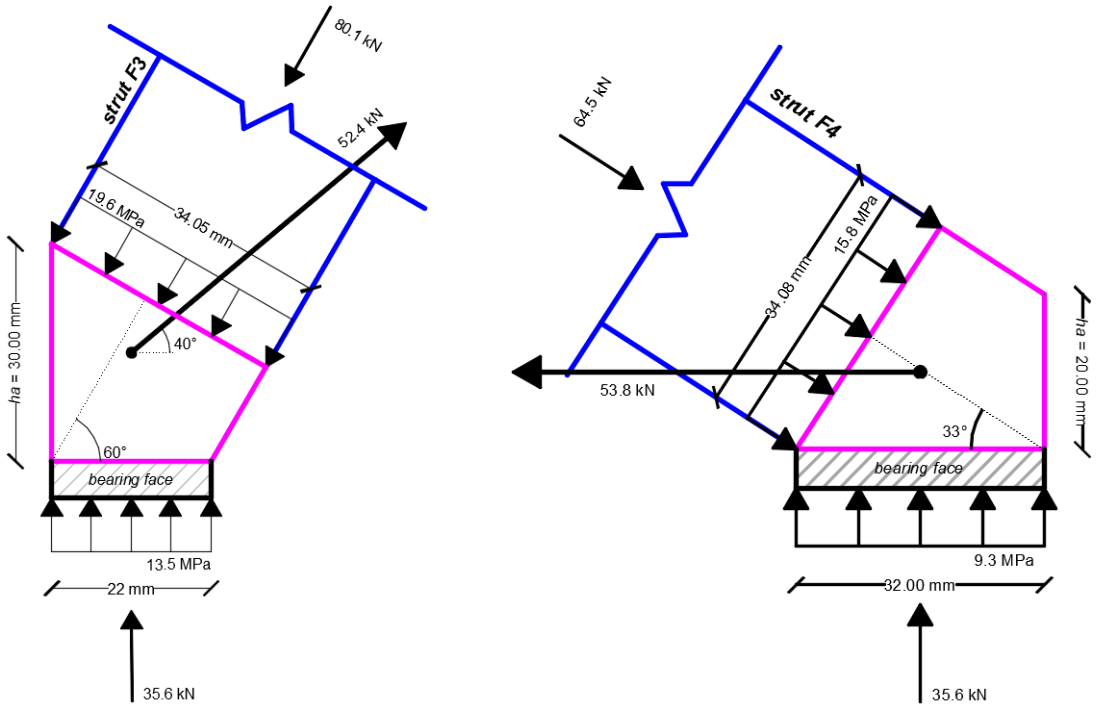

(a) Geometry of the C-C-T node near the left support

(b) Geometry of the C-C-T node near the right support

Figure 8.3: Geometries of the nonhydrostatic C-C-T nodes at F-series ST model.

The result of the stress check on C-C-C node is shown in Table 8.1, while the result of the stress check on C-C-T nodes is shown in Table 8.2. The end results were displayed as a ratio between resulting stress over allowable stress. According to the results, the stresses that works on the aforementioned nodal zones are relatively far from reaching their capacity limit. All comparisons with the allowable stresses produce ratios that have values below 0.5. These low ratios of stress were obtained even with every nodal zone having a bearing face width that is less than the loading/support plate width. Therefore, it is safe to assume that the stresses at the C-C-C and C-C-T nodal zones will not cause any compressive failure to the concrete of F-series specimens at the load level of 71.2 kN.

Table 8.1: Widths, resulting stresses, and the stress check results of F-series ST model C-C-C nodes.

C-C-C NODE			
Compression force (kN)	Nodal face width (mm)	Resulting Stress (MPa)	Stress Ratio
71.20	31.50	18.8	0.39
77.10	34.00	18.9	0.39
104.95	46.35	18.9	0.39

Struts

The second dimensioned truss members to be discussed are the struts. In the process of determining their dimension, each strut was assumed to have a prismatic shape. This assumption was taken because the LEFEA result of specimen F-1 showed that there are no principal tensile strains along those struts that neither resemble a bottle nor a fan (see Figure 8.4).

After the shape of the struts has been determined, these compressive truss members were analyzed

Table 8.2: Widths, resulting stresses, and the stress check results of F-series ST model C-C-T nodes.

C-C-T NODES							
Left support				Right support			
Compression force (kN)	Nodal face width (mm)	Resulting Stress (MPa)	Stress Ratio	Compression force (kN)	Nodal face width (mm)	Resulting Stress (MPa)	Stress Ratio
80.10	34.05	19.6	✓ 0.48	64.50	34.08	15.8	✓ 0.38
35.60	22.00	13.5	✓ 0.33	35.60	32.00	9.3	✓ 0.22

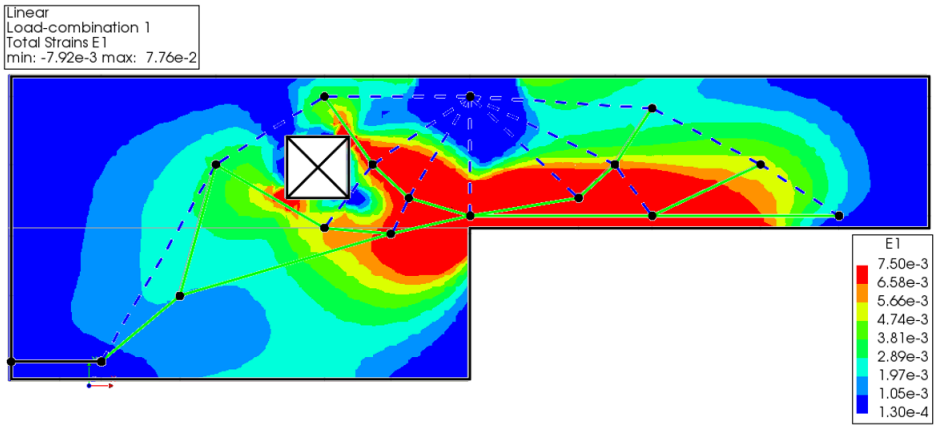

Figure 8.4: Alignment of the F-series ST model with the dapped beam's principal tensile strains (E1) from LEFEA.

for their stress. The stress analysis was carried out on the struts of the singular nodes of the F-series ST model (strut F1, F2, F3, and F4) since they are the critical ones. Due to their prismatic shape, the resulting stress and the width of each strut are equivalent to the stress and width properties of the nodal faces that they attached on. Additionally, the struts near the left-top corner (strut F-5) and the right-bottom corner (strut F-6) of the opening also had their stresses checked since they have limited width of concrete to form a prismatic strut. To check their stresses, strut F5 and F6 are dimensioned to the maximum width that they can have. Strut F5 can have a strut width of 24.26 mm at most, while strut F6 can have none since the center of the strut coincided with the right-bottom corner of the opening. Information regarding these two variables is summarized in Table 8.3. Following the stress analysis on the struts, the resulting stresses were then compared with the allowable stress of the compressive truss members. The allowable stress for the struts was computed in accordance with equation 2.5:

$$\sigma_{max} = 0.6\nu' f_{cm} = 0.6 * 0.74 * 65.8 = 29.1 \text{ MPa}$$

Similar to the nodal zones, the end results of the struts' stress check are also presented as a ratio between the resulting stress and the allowable stress. According to the comparison results shown in Table 8.3, all struts appear to have a medium level of stress, except for strut F6. Stress ratios of strut F1, F2, F3, F4, and F5 shows values between 0.5 and 0.75. These results mean that the concrete at these dimensioned struts can be considered safe from any compressive failure at the load level of 71.2 kN. In contrast, compressive failure might occur on the concrete around strut F6 since there is an insufficient amount of concrete available to contain the compressive force that acts on that strut. However, the damage to the concrete caused by this strut should be insignificant since strut F6 contains a relatively small compressive force compared to the other struts.

Table 8.3: Widths, resulting stresses, and the stress check results of F-series ST model dimensioned struts.

Strut ID	Compression force (kN)	Strut width (mm)	Resulting stress (MPa)	Stress Ratio
F1	77.10	34.00	18.9	✓ 0.65
F2	104.95	46.35	18.9	✓ 0.65
F3	80.10	34.05	19.6	✓ 0.67
F4	64.50	34.08	15.8	✓ 0.54
F5	60.20	24.26	20.7	✓ 0.71
F6	11.90	0.01	9916.7	✗ 340.91

Ties

The last dimensioned truss members to be discussed are the ties. Unlike struts and nodes, ties are dimensioned with reinforcement bars. Since the reinforcement designs for F-series specimens have been provided by Oviedo, the capacity of those rebars just had to be rechecked in accordance with the tensile forces acting on the ties. For the purpose of this stress check, the ties of the F-series ST model were ID-ed, as shown in Figure 8.5. The tensile forces in those ties were then compared with the steel design of specimen F-1, shown in Figure 8.6.

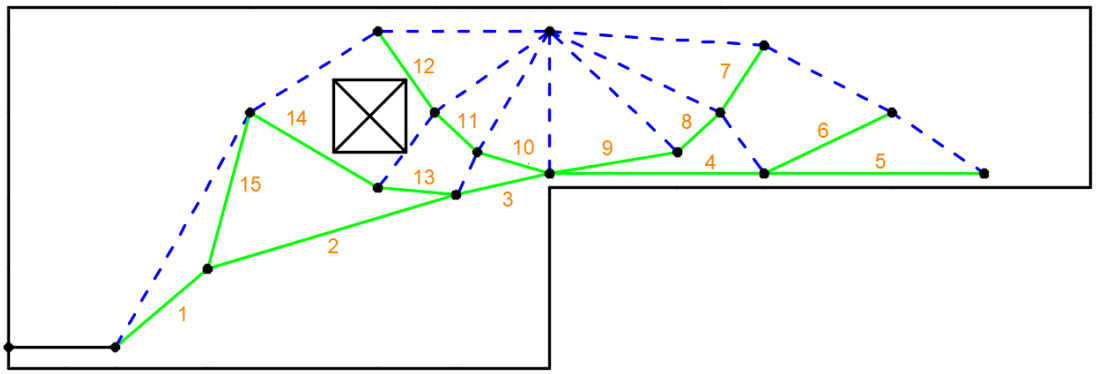

Figure 8.5: ID-ed ties of F-series ST model.

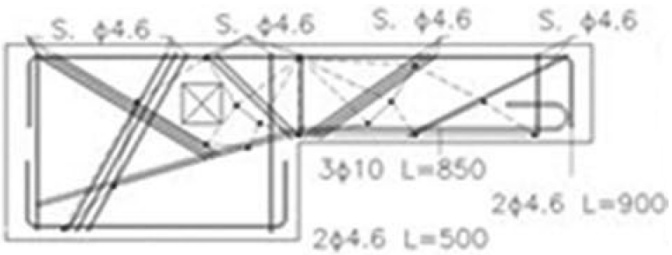

Figure 8.6: Reinforcements of specimen F-1 [19].

The results of the stress check on the rebars of specimen F-1 is presented in Table 8.5. The end results of the stress check are given as a ratio between the tensile stress per rebar over the mean yield strength (f_{ym}) of the rebar, shown in Table 8.4. In particular, each tensile stress per rebar (denoted as 'projected force') was calculated by projecting the tensile force in a tie to the alignment of its respective rebar in its specimen' rebar layout. Based on the stress check results, each rebar set appeared to have excessive strength in withstanding the tensile force from its respective tie without yielding, except for the rebar set on tie 10, 11, and 12. The rebar set provided for these three ties was

two stirrups with 4.6-mm rebar diameter (4 - ⌀4.6 mm) which were installed in alignment with the ties. The tensile forces surpassed the 4.6-mm rebars yield capacity margin by at least 19%. However, the other rebars were safe from any plastic deformation at the load level of 71.2 kN, especially the main flexural rebars (aligned with ties 2, 3, 4 and 5 and designed as 3 - ⌀10 mm) that have stress ratios below 0.5. Thus, the F-series ST model can be considered providing a safe design in terms of reinforcements.

Table 8.4: Rebar diameters used on specimen F-1 and their mean yield strengths.

Rebar diameter (mm)	Mean yield strength (MPa)
4.6	508
10	625

Table 8.5: Stress check results of F-series ST model dimensioned ties using specimen F-1 reinforcement design.

Tie ID	Tie force (kN)	Representing rebars	Angle toward the rebar (^{0})	Projected force (kN)	Total rebar area (mm^2)	Tensile Stress per rebar (MPa)	Stress Ratio
1	52.40	3 - Ø10 mm	25.0	47.49	235.62	201.56	0.40
2	34.90	3 - Ø10 mm	0.0	34.90	235.62	148.12	0.24
3	65.60	3 - Ø10 mm	0.0	65.60	235.62	278.42	0.45
4	63.90	3 - Ø10 mm	0.0	63.90	235.62	271.20	0.43
5	53.80	3 - Ø10 mm	0.0	53.80	235.62	228.33	0.37
6	8.30	2 - Ø4.6 mm	0.0	8.30	33.24	249.71	0.49
7	32.10	6 - Ø4.6 mm	24.0	29.32	99.71	294.09	0.58
8	36.50	6 - Ø4.6 mm	10.0	35.95	99.71	360.49	0.71
9	45.70	6 - Ø4.6 mm	24.0	41.75	99.71	418.69	0.82
10	46.90	4 - Ø4.6 mm	24.0	42.85	66.48	644.52	1.27
11	45.80	4 - Ø4.6 mm	2.0	45.77	66.48	688.55	1.36
12	41.30	4 - Ø4.6 mm	14.0	40.07	66.48	602.82	1.19
13	27.00	3 - Ø10 mm	21.0	25.21	235.62	106.98	0.17
14	23.10	6 - Ø4.6 mm	0.0	23.10	99.71	231.66	0.46
15	24.80	6 - Ø4.6 mm	14.0	24.06	99.71	241.32	0.48

8.2. Validation of the ties-as-rebars models numerical result

After the ST dimensioning process proved that all ST models designs can provide a safe design to the test cases, validation to the numerical results of the TER models will take place. It is done by comparing the ultimate capacity values of the TER models (R_{TER}) with the factored design loads of the ST models (R_{STM}). Table 8.6 provides the list of the R_{STM} and the R_{TER} values of each specimen.

The validation process can confirm the validity of the numerical results of the TER models if the R_{TER} values are higher than their respective R_{STM} values, which act as the lower-bound limit. For the TER models of Oviedo (F, G, and H-series TER models), their ultimate capacities have to surpass an R_{STM} of 71.2 kN and, for Maxwell & Breen's (Specimen 2, 3, and 4 TER models), ultimate capacities have to surpass an R_{STM} of 99.2 kN. To display their equivalence level, a ratio of R_{STM} to R_{TER}, which is denoted as Ψ_1, is introduced. It is expected for a Ψ_1 ratio to have a value below 1.00 to provide validation to the numerical results of a TER model.

In Table 8.6, the Ψ_1 ratio of all specimens show values that range between 0.61 to 0.85. With an average (μ_{Ψ_1}) of 0.69 and a coefficient variation (CoV_{Ψ_1}) of 11.7% (Table 8.7), it means that all R_{TER} produced by the TER models surpass their lower-bound limits. Thus, the numerical results of the TER models are validated with the STM results.

Table 8.6: Comparison between TER models ultimate capacities and the factored design load of the ST models.

Experiment	Specimen	R_{STM}	R_{TER}	$\psi_1 = {R_{STM}}/{R_{TER}}$
Oviedo	F-series	71.20 kN	116.15 kN	0.61
	G-series	71.20 kN	117.27 kN	0.61
	H-series	71.20 kN	101.64 kN	0.70
Maxwell & Breen	2	99.20 kN	117.38 kN	0.85
	3	99.20 kN	141.18 kN	0.70
	4	99.20 kN	153.48 kN	0.65

Table 8.7: Average and coefficient of variation of Ψ_1.

Mean value of Ψ_1 (μ_{Ψ_1})	Coefficient of variation of Ψ_1 (CoV_{Ψ_1})
0.69	11.7%

9

Verifying the ties-as-extended-rebars models results by the test cases numerical results

This chapter will discuss the comparison between the numerical results of TER models with the numerical validation (NV) results of the test cases. The aim of the comparison is to verify the reliability of the proposed technique in providing correct information regarding the nonlinear behavior of a structure to guide engineers in selecting a suitable ST model. For the verification, three types of numerical information will be compared: failure mode, load-displacement (LD) curve, and ultimate capacity. It is expected for the failure modes and ultimate capacities from the TER models and the NV models of the test cases to be analogous for the verification.

9.1. Failure mode comparison

Similar to the numerical validation (NV) results, the combination of concrete softenings and rebar rupture also governed the failure mode of the TER models. They can be observed exclusively from the crack pattern (Ecw1) and the rebar strain (Exx) contour plots collected from the last converging load-step in each numerical analysis. Figure 9.1, 9.2, and 9.3 present these contour plots for displaying the failure mode of F, G, and H-series TER models, while Figure 9.4, 9.5, and 9.6 present these contour plots for displaying the failure mode of Specimen 2, 3, and 4's TER models. These figures also present the same contour plots from NV results to exhibit the failure mode of the NV models. As a summary, Table 9.1 lists the failure mode definitions from each result.

According to those contour plots, five out of six TER models generated failure modes that are comparable with the failure modes exhibited by their counterparts. Those TER models are F, G, and H-series TER models (Oviedo), as well as Specimen 2 and 4 TER models (Maxwell & Breen). The failure mode of the Oviedo's TER models is a flexural failure mechanism that occurred at the midspan due to the rupture of the longitudinal rebars near the re-entrance corner. On the other hand, the failure mode of Specimen 2 TER model is a premature failure mode due to extensive elongation of the inclined rebars, and the failure mode of Specimen 4 TER model is a flexural failure mechanism due to the rupture of the rebars at node 't' (look at Figure 3.16c for this node reference) which allowed the concrete to split open vertically from that node towards the loading point. The obvious reason for why these TER models can mimic the failure of their respective NV models is because both types of numerical models have rebar layout that coincides with the ties layout of their respective ST model. Thus, each TER model will have the same weak points its counterpart has.

One TER model that is not agreeing with its NV model failure mode is the TER model of specimen 3. The TER model had an incomplete flexural failure (premature failure) due to extensive elongation of the bottom-most longitudinal rebars. In contrast, the NV model had a flexural failure that is similar to the failure mechanism of the TER and NV models of specimen 4. The numerical analysis of the TER model of specimen 3 diverged before it could give a definitive flexural failure to the numerical model, despite displaying a crack pattern that resembles the crack pattern of its respective NV model at its last converging load-step. The possible reason for why the TER model cannot produce the same failure mode as its NV model is because of the different style on how the bottle-shaped strut at the right side of the deep beam model is reinforced. In the TER model, the strut was only reinforced with two extended rebars, while the NV model had it reinforced with a steel mesh. The absence of steel mesh in the TER model prevents node 't' to show up as the weakest point in the deep beam model, which allows the flexural forces at the bottom of the TER model to redistribute along the longitudinal rebars.

In conclusion, despite the failure mode dissimilarity of specimen 4's TER model, the other TER models did show their capability in producing failure mode that is comparable to the failure mode of their respective NV models. They verify the reliability of the proposed technique in providing additional information regarding the failure mode of the specimen.

Table 9.1: Failure mode of the test cases according to their numerical validation results and TER models' results.

Specimen ID	**Failure mode/location**	
	NV result	**TER result**
F-1	flexural/midspan	flexural/midspan
G-1	flexural/midspan	flexural/midspan
H-1	flexural/midspan	flexural/midspan
2	premature/along inclined rebars	premature/along inclined rebar
3	flexural/node 't' to loading point	premature/along the bottom-most longitudinal rebars
4	flexural/node 't' to loading point	flexural/node 't' to loading point

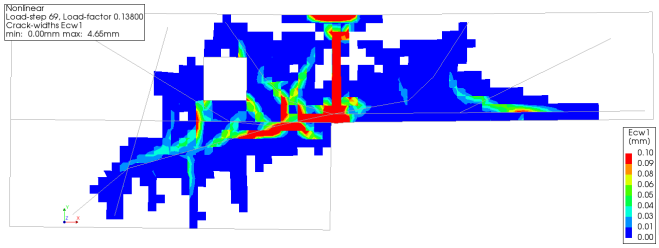

(a) TER's Crack pattern (Ecw1)

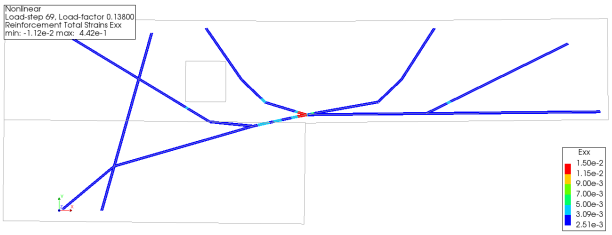

(b) TER's Rebar strain at local X-direction (Exx)

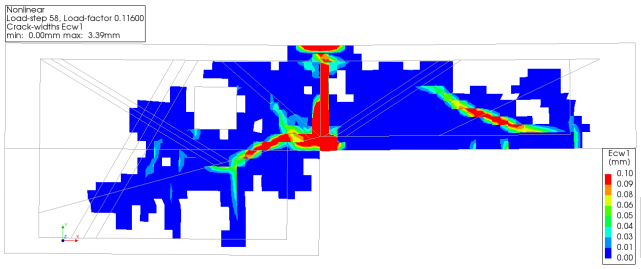

(c) NV's Crack pattern (Ecw1)

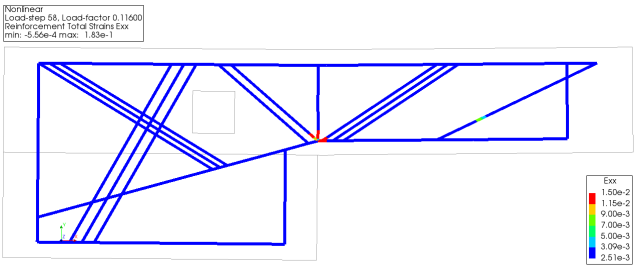

(d) NV's Rebar strain at local X-direction (Exx)

Figure 9.1: Failure mode of specimen F-1 according to: (a,b) TER models' results (c,d) NV results.

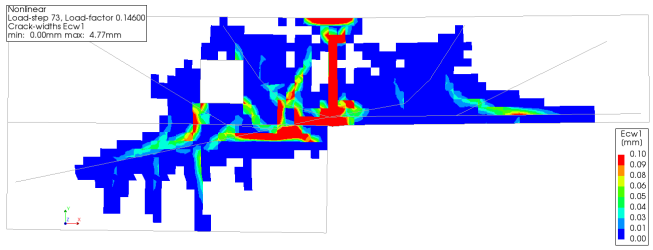

(a) TER's Crack pattern (Ecw1)

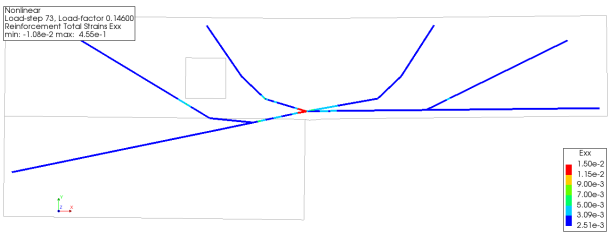

(b) TER's Rebar strain at local X-direction (Exx)

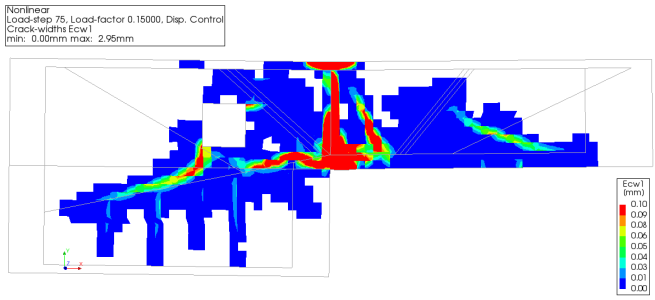

(c) NV's Crack pattern (Ecw1)

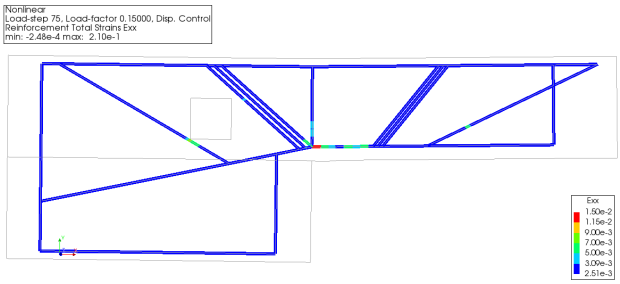

(d) NV's Rebar strain at local X-direction (Exx)

Figure 9.2: Failure mode of specimen G-1 according to: (a,b) TER models' results (c,d) NV results.

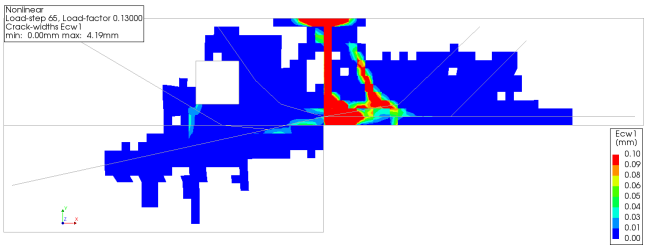

(a) TER's Crack pattern (Ecw1)

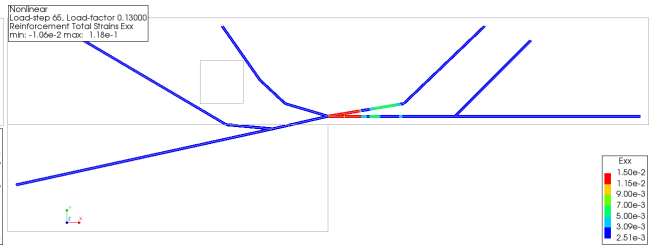

(b) TER's Rebar strain at local X-direction (Exx)

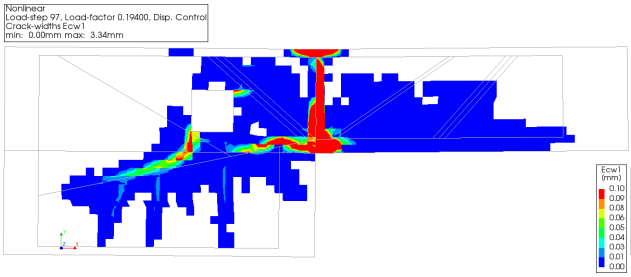

(c) NV's Crack pattern (Ecw1)

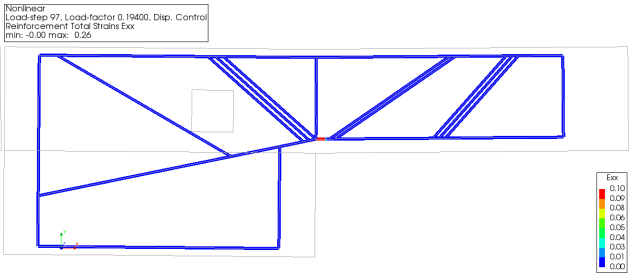

(d) NV's Rebar strain at local X-direction (Exx)

Figure 9.3: Failure mode of specimen H-1 according to: (a,b) TER models' results (c,d) NV results.

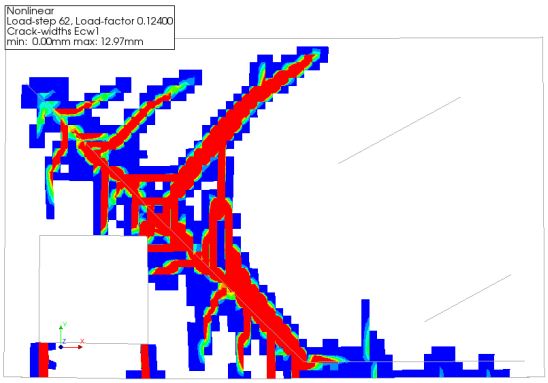

(a) TER's Crack pattern (Ecw1)

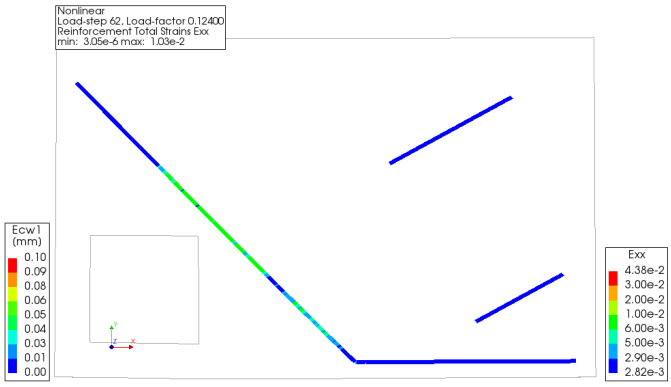

(b) TER's Rebar strain at local X-direction (Exx)

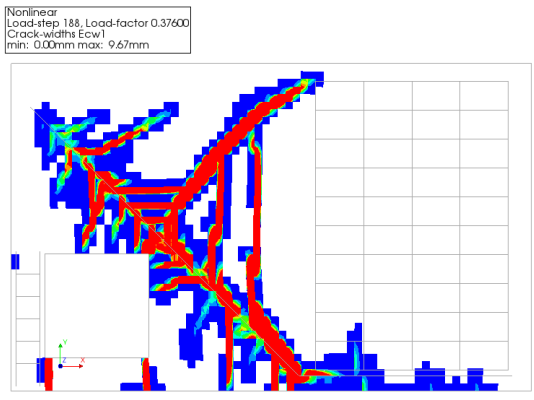

(c) NV's Crack pattern (Ecw1)

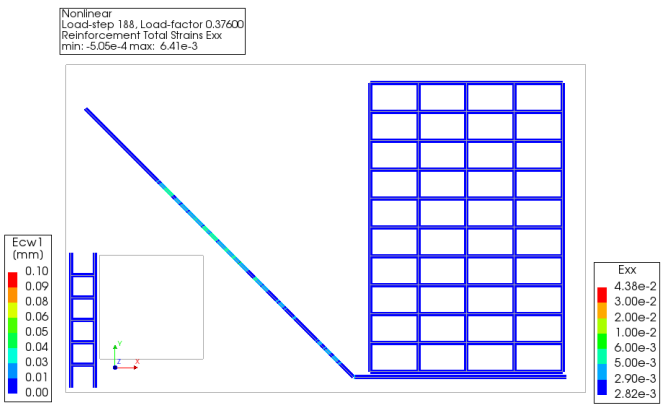

(d) NV's Rebar strain at local X-direction (Exx)

Figure 9.4: Failure mode of specimen 2 according to: (a,b) TER models' results (c,d) NV results.

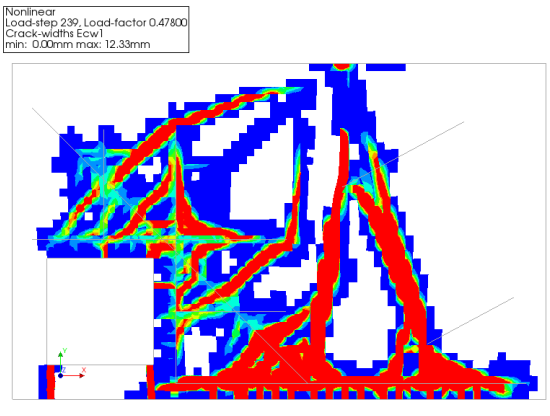

(a) TER's Crack pattern (Ecw1)

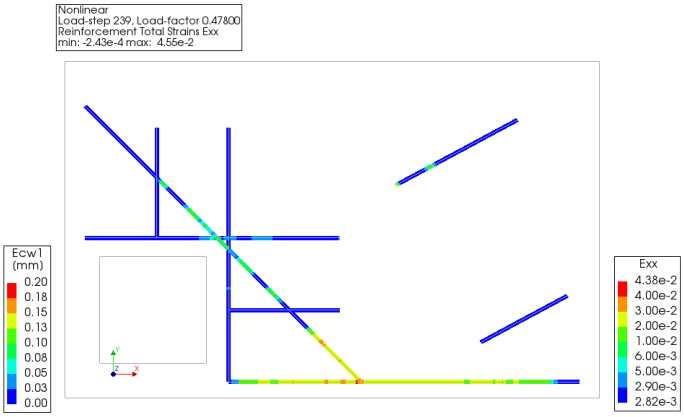

(b) TER's Rebar strain at local X-direction (Exx)

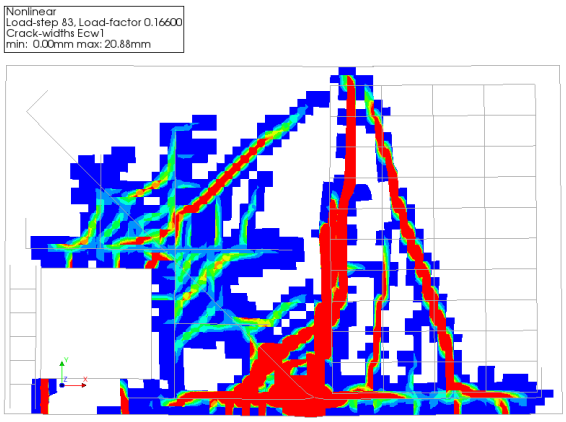

(c) NV's Crack pattern (Ecw1)

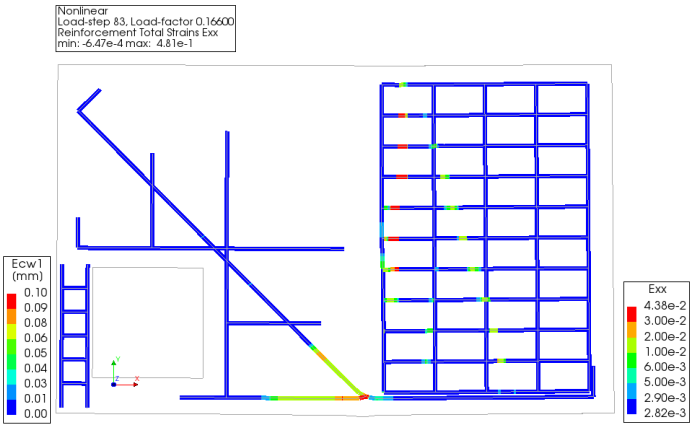

(d) NV's Rebar strain at local X-direction (Exx)

Figure 9.5: Failure mode of specimen 3 according to: (a,b) TER models' results (c,d) NV results.

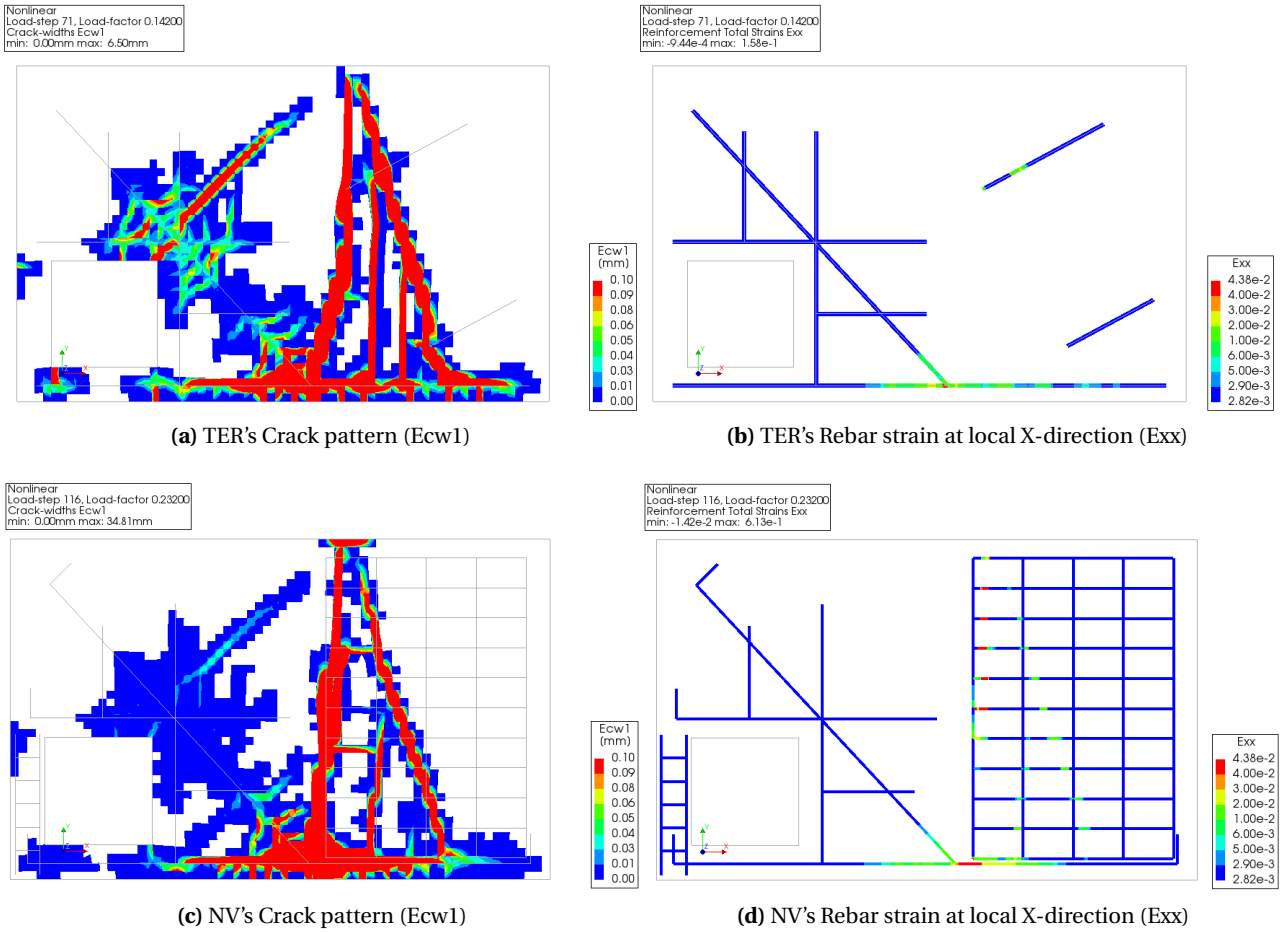

(a) TER's Crack pattern (Ecw1)

(b) TER's Rebar strain at local X-direction (Exx)

(c) NV's Crack pattern (Ecw1)

(d) NV's Rebar strain at local X-direction (Exx)

Figure 9.6: Failure mode of specimen 4 according to: (a,b) TER models' results (c,d) NV results.

9.2. Load-capacity curves comparison

Figure 9.7 presented six charts that display the comparison between the LD curve of each TER model with the LD curve of its respective NV model. The LD curves of Oviedo's (F, G, and H-series) TER and NV models are presented in Figure 9.7a, 9.7b, and 9.7c, while the LD curves of Maxwell & Breen's (specimen 2, 3, and 4) TER and NV models are presented in Figure 9.7d, 9.7e, and 9.7f, respectively. It is expected that the TER models with failure modes that are similar to their NV models' failure modes in the previous comparison should also have comparable LD curves with their NV models. Thus, LD curves of specimen 3 TER and NV models are not comparable since these two models had dissimilar failure modes.

Through the comparison, it was found that three out of six charts exhibit LD curves of TER models that resemble the LD curves of their respective NV models closely. Those charts are the charts for the LD curve of F-series, H-series, and specimen 2 TER models. The LD curves of these three TER models appear almost overlapping with their respective NV model' LD curves, which indicate that both types of models have similar linear and nonlinear responses in each case.

Unlike the aforementioned three pairs of LD curves, the LD curves of G-series and specimen 4 TER models do not fulfill the expectation despite the similarity that they have with the NV models in terms of failure mode. The LD curve of G-series TER model appears showing a response that has the higher ultimate capacity and more deformation than its counterpart (Figure 9.7b), while the LD curve of specimen 4 TER model appears showing a response that has significantly less total deformation than its counterpart although it has a similar early response to the loading. Nevertheless, there are some reasons that can explain these differences.

For the G-series TER model, the as-built condition of its actual specimen can justify the anomaly of its LD curve. In his paper, Oviedo mentioned that specimen G-1 was built with a defect, and that defect is a missing longitudinal rebar (as-built state). During its construction, one of the main (10 mm) flexural rebars was unintentionally not installed, which caused the specimen to have less ultimate capacity and deformation than expected at the end of its test. Since the NV model of this specimen was built based on this fact, the model carries the defect with it. However, when the reinforcement design of NV model of specimen G-1 is adjusted in accordance to its planned design (as-drawn state, with 3 - $\varnothing$10 mm, instead of 2 - $\varnothing$10 mm, Figure 3.3b), it turns out that the numerical model still collapse with the same flexural failure mechanism it had previously (Figure 9.8a and 9.8b) with a failure load level and deformation that match its TER model counterpart (Figure 9.8c).

For the specimen 4 TER model, the absence of steel mesh in this model can explain the shorter total deformation that it had. Despite its ability to simulate failure at a load that is similar to the ultimate load of its NV model, the TER model of specimen 4 has noticeably shorter total deformation than its counterpart according to its LD curve. The shorter deformation that it has is due to the fact that the model only has two extended rebars for covering a bottle-shaped strut located at the right part of the beam model, whereas the NV model has a steel mesh. Because of that, the presence of the steel mesh allows the NV model to have more plastic deformation before it collapsed. This condition exhibit the weakness of the proposed technique regarding its inability to allow the development a proper reinforcement for covering a bottle-shaped strut.

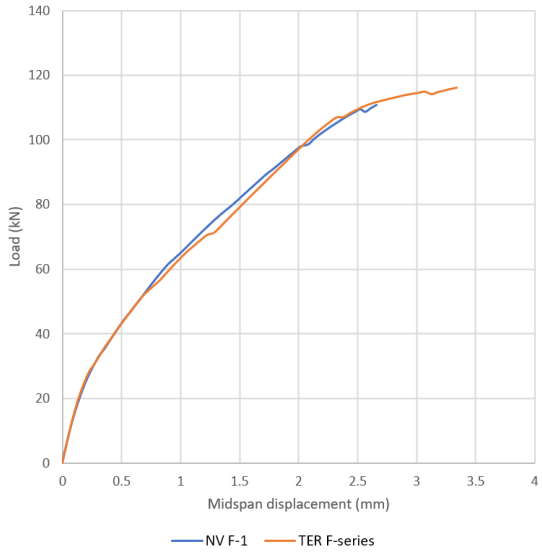

(a) F-1 NV vs. F-series TER

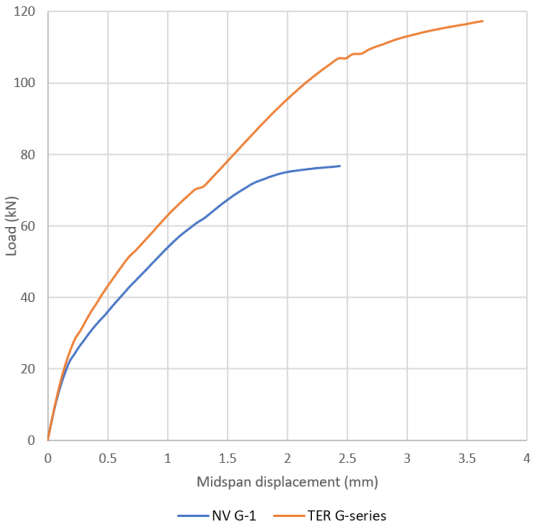

(b) G-1 NV vs. G-series TER

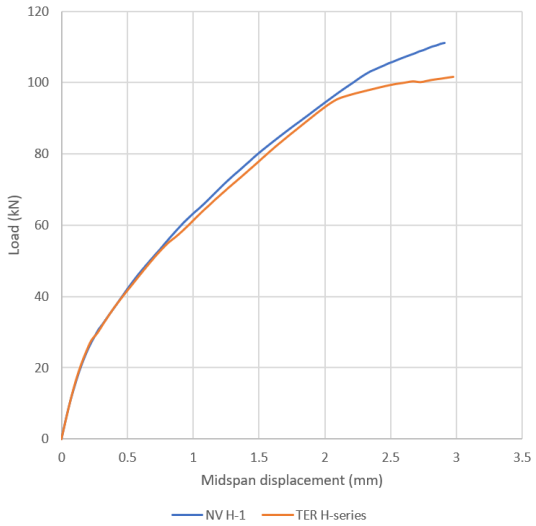

(c) H-1 NV vs. H-series TER

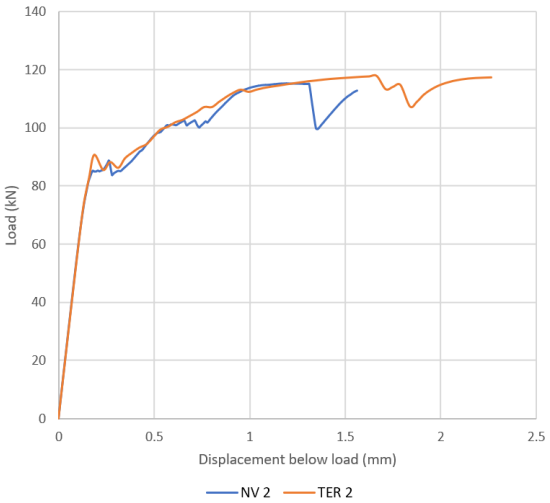

(d) 2's NV vs. 2's TER

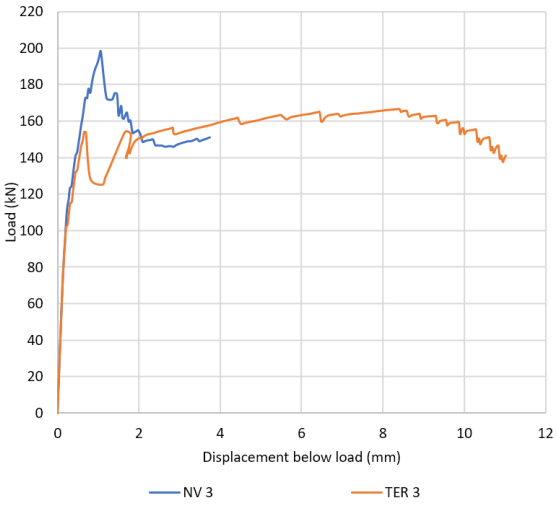

(e) 3's NV vs. 3's TER

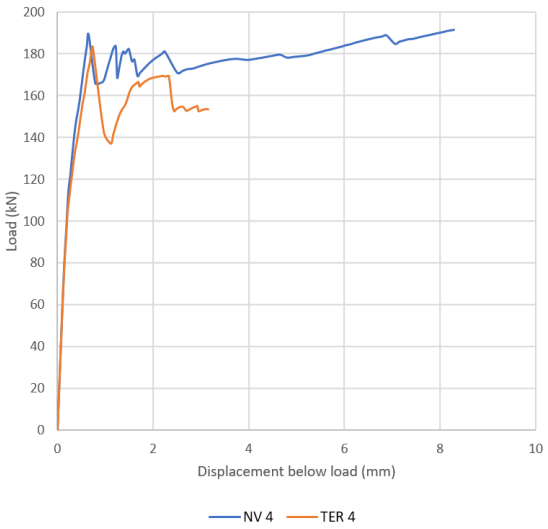

(f) 4's NV vs. 4's TER

Figure 9.7: Comparison between the LD curves of the TER models and the NV models.

However, the deformation data from the TER models' LD curves are not sufficiently accurate when compared to their experimental results. The reason is that some assumptions in the solution strategy used to execute their NLFEA, i.e. embedded rebars and elastoplastic material model for the reinforcement, prevent the numerical models to simulate the nonlinear behavior accurately. Thus, deformation data from these numerical models cannot be considered as reliable for selecting a suitable ST model.

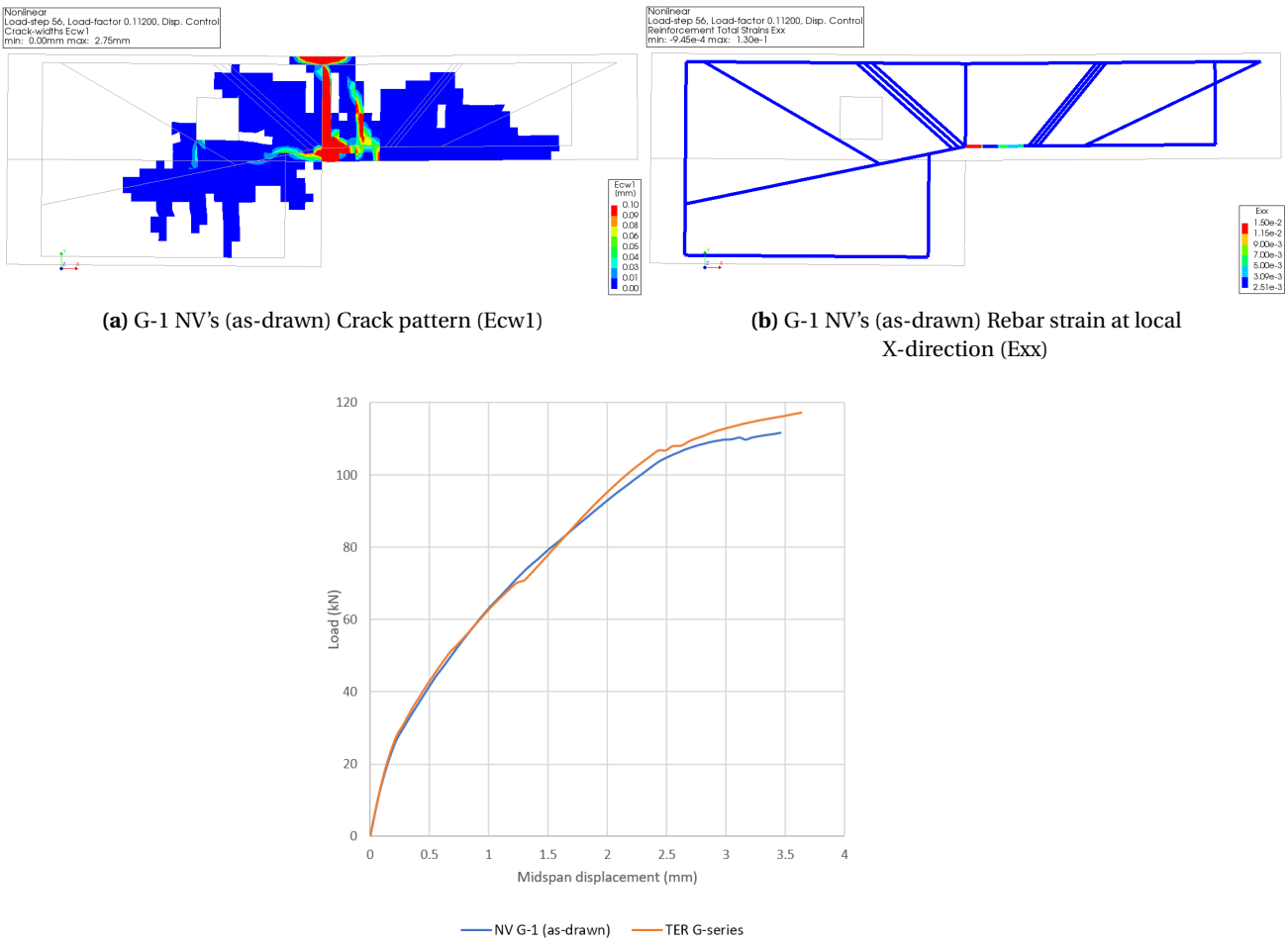

(a) G-1 NV's (as-drawn) Crack pattern (Ecw1)

(b) G-1 NV's (as-drawn) Rebar strain at local X-direction (Exx)

(c) G-1 NV vs. G-series TER LD curves

Figure 9.8: Failure mode of specimen G-1 according to (a,b) as-drawn NV results and (c) its LD curve compared with its respective TER model's

9.3. Ultimate capacity comparison

Table 9.2 presents the comparison between the ultimate capacities of the test cases that are suggested by both the TER models and the NV models. To show the equivalence level between the TER and NV models ultimate capacities, a ratio of R_{NV} to R_{TER}, which is denoted as Ψ_2, is introduced. It is important to mention that the R_{NV} and R_{TER} of specimen 3 will not be compared since the failure mode of its NV and TER models are unalike. Thus, Ψ_2 ratio for specimen 3 is not presented in Table 9.2.

According to that table, the Ψ_2 ratio of all specimens show values that range between 0.65 to 1.25.

These values have a mean (μ_{Ψ_2}) of 0.98 with a coefficient of variation $(\mathtt{CoV}_{\Psi_2})$ of 19.9% (Table 9.3). The relatively high value that the $\mathtt{CoV}_{\Psi_2}$ has is due to the fact that there is a μ_{Ψ_2} ratio with a value as low as 0.65, and that value comes from G-series models. However, there is a solution for this issue.

Table 9.2: Comparison between the ultimate capacity of the TER models and the NV model.

Experiment	Specimen	R_{NV}	R_{TER}	$\psi_2 = {R_{NV}}/{R_{TER}}$
Oviedo	F-1	110.69 kN	116.15 kN	0.95
	G-1	76.75 kN	117.27 kN	0.65
	H-1	111.15 kN	101.64 kN	1.09
Maxwell & Breen	2	112.82 kN	117.38 kN	0.96
	3	150.94 kN	141.18 kN	-
	4	191.37 kN	153.48 kN	1.25

Table 9.3: Average and coefficient of variation of Ψ_2.

Mean value of Ψ_2 (μ_{Ψ_2})	Coefficient of variation of Ψ_2 $(\mathtt{CoV}_{\Psi_2})$
0.98	19.9%

As previously mentioned, the NV model of specimen G-1 was developed based on the fact that specimen G-1 was constructed with one of the main (10 mm) flexural rebars that were unintentionally not installed during its construction. Under that premise, the ultimate capacity and deformation of the specimen ended up to be lower than it supposed to be. The NLFEA of NV model of specimen G-1 with its planned design specification (as-drawn state) predicted that it is possible for the specimen to have a higher ultimate capacity that reaches a value of 111.73 kN when it collapses with a comparable flexural failure mechanism (check Section 9.1 for the failure description). Knowing that, the ultimate capacity of the as-drawn state NV model of specimen G-1 can replace its former ultimate capacity for the comparison, as presented in Table 9.4. With this change, the Ψ_2 ratio of the G-series models become 0.95, and thus, the μ_{Ψ_2} and $\mathtt{CoV}_{\Psi_2}$ are revised to 1.04 and 11.1%, respectively (Table 9.5).

In conclusion, TER models did show their capability in predicting ultimate capacity that is comparable to the ultimate capacity of their respective NV models. They verify the reliability of the proposed technique in providing additional information regarding the ultimate capacity of the specimen.

Table 9.4: Comparison between the ultimate capacity of the TER models and the NV model with NV model of specimen G-1 following its planned design.

Experiment	Specimen	R_{NV}	R_{TER}	$\psi_2 = {R_{NV}}/{R_{TER}}$
Oviedo	F-1	110.69 kN	116.15 kN	0.95
	G-1	111.73 kN *	117.27 kN	0.95
	H-1	111.15 kN	101.64 kN	1.09
Maxwell & Breen	2	112.82 kN	117.38 kN	0.96
	3	150.94 kN	141.18 kN	-
	4	191.37 kN	153.48 kN	1.25

**) = ultimate capacity from its NV model at as-drawn state*

Table 9.5: Average and coefficient of variation of Ψ_2 with NV model of specimen G-1 following its planned design.

Mean value of Ψ_2 (μ_{Ψ_2})	Coefficient of variation of Ψ_2 (CoV_{Ψ_2})
1.04	11.1%

9.4. Verifying the proposed technique ability for selecting a suitable strut-and-tie model

In this section, the last comparison between the TER models and the NV models will take place. The aim of the comparison is to verify the ability of the proposed technique in suggesting a suitable ST model. The suggestion should be in agreement with the suggestion by the NV models since the data regarding failure mode and ultimate capacity from the TER models were verified using the NV models' results. As a note, a suitable ST model should allow its specimen to fail with a ductile failure mode (flexural failure) and has the highest ultimate capacity possible.

Table 9.6 presents a list of failure modes and ultimate capacities of the test cases suggested by the TER and NV models. For marking the selection, the blue color represents the ST model selection by the NV models, while the green color represents the ST model selection by the TER models. Based on the data presented in Table 9.6, both approaches managed to select the same best performing ST model (Oviedo = G-series, Maxwell & Breen = Specimen 4). Thus, they verify the reliability of the proposed technique in guiding engineers in selecting a suitable ST model.

Table 9.6: Comparison of the best performing ST model selection according to the TER models and the NV models results.

Experiment	Specimen	R_{NV}	Failure mode (NV)	R_{TER}	Failure mode (TER)
Oviedo	F-1	110.69 kN	flexural	116.15 kN	flexural
	G-1	111.73 kN	flexural	117.27 kN	flexural
	H-1	111.15 kN	flexural	101.64 kN	flexural
Maxwell & Breen	2	112.82 kN	premature	117.38 kN	premature
	3	150.94 kN	flexural	141.18 kN	premature
	4	191.37 kN	flexural	153.48 kN	flexural

Best specimen according to NV *Best specimen according to TER model results*

10

Conclusion - Part 2

The answer to each research question is briefly described below:

1. *What evaluation technique can be supplemented into the current STM-based evaluation framework to turn it into a more data-driven ST modeling process?*

   An evaluation technique that employs NLFEA was determined as a fit solution to promote the current STM-based evaluation framework to become a more data-driven design process. It is advantageous to incorporate NLFEA as one of the intermediate steps because it can provide nonlinear behavior of a structure as objective insights for making a more informed decision in determining a suitable ST model. Nonlinear behavior information, such as failure mode and ultimate capacity, can be extremely useful in developing an ST model, especially for a concrete structure with complex geometries which nonlinear behavior is hard to predict.

2. *How can the proposed technique be incorporated into the current ST modeling process?*

   To incorporate NLFEA to STM, the concept of 'ties-as-extended-rebars' or TER model is introduced. A TER model is a numerical model used to assess the influence of a certain ST model design toward the nonlinear behavior of a structure. Through TER model, an ST model is nonlinearly evaluated as a concrete structure with embedded reinforcements. Then, the information generated by the model, i.e. failure mode and ultimate capacity, can be utilized as additional information for determining a suitable ST model. Additionally, to allow the TER model to generate a representative failure, the rebars in the TER model are extended with straight anchorage length.

3. *How well does the proposed technique perform in suggesting a suitable strut-and-tie model?*

   Six ST models for complex concrete beam elements and their experimental results were utilized to assess the ability of the proposed technique. At the same time, the experimental results were validated using NLFEA, which generated six numerical validation (NV) results. From the implementation, it was found that five out of six TER models were able to simulate failure modes that are comparable with the failure mode of the numerical model of their respective specimens (NV models). Those five TER models were also able to achieve ultimate capacity values (R_{TER}) that have values that surpassed their ST models factored design load (R_{STM}), which are signified by R_{STM} to R_{TER} ratio (Ψ_1) that has an average of 0.69 and a coefficient of variation of 11.17%. Additionally, it was also found that these five TER models were

able to match their respective NV models in terms of ultimate capacities (R_{NV}), which are signified by R_{NV} to R_{TER} ratio (Ψ_2) that has an average of 1.04 and a coefficient of variation of 11.1%. From the results that they predicted, the TER models suggested ST models of specimen G-1 and specimen 4 as the most suitable ST model for each experimental case, which matches the suggestion obtained from the numerical validation.

4. *What improvements can be brought to the current ST modeling process by incorporating the proposed technique?*

   Incorporating the proposed technique into the current STM-based evaluation framework will allow engineers to look into the nonlinear behavior of a structure. It is something that is not possible with the current STM because it is developed based on the lower-bound theorem. NLFEA will provide information regarding beam response under loading since it will simulate an analyzed structure nonlinear behavior.

11

Recommendations

In the following paragraph, recommendations for future research and development related to this thesis are presented.

1. *Implementing the proposed technique on ST models built for different types of structural element and various geometrical irregularities.*

   In this thesis, the proposed technique was only trialed using ST models that were designed for a dapped beam with an opening and a deep beam with a large opening. These means that the proposed technique capability has only been verified on beam elements with at least one geometry irregularity. To confirm the extend of the proposed technique capability, implementing the technique on different types of structural element and various geometrical irregularities are necessary to find the possible flaws and weaknesses of this technique.

2. *Using nonlinear results from a TER model to complement the ST dimensioning process.*

   The application of ST dimensioning for analyzing the stress state of the analyzed structure has several limitations. Limitations of ST dimensioning process that are currently recognized are: limitations in determining the capacity of struts, in determining anchorage and distribution of tie reinforcements, and in defining the size, shape, as well as strength of complex nodal zones [26]. These limitations are especially felt in structures with geometry irregularities since they are covered with D-regions. Since the TER models were able to produce accurate information regarding the nonlinear condition of an analyzed structure under a particular ST model influence, it might be possible to complement those limitations of the ST dimensioning process with the nonlinear information from a TER model.

A

Appendix A

In this appendix, the ST dimensioning check on G-series, H-series, Specimen 2, Specimen 3, and Specimen 4 ST models are presented.

A.1. G-series strut-and-tie model

Nodal zones

The first dimensioned truss members to be discussed are the nodes. After being shaped and sized, each node of the G-series ST model changed into a nodal zone. Based on the way forces equilibrate in its area, nodal zones can be distinguished into two different types: singular nodes and smeared nodes. Since it is unnecessary to check the concrete stresses at the smeared nodes [25], singular nodes were the only nodal zones of the G-series ST model that were checked. There are two nodes from the truss model that can be categorized as singular nodes: one near the loading point and one near the right support, as indicated in Figure A.1. The singular node near the loading point is a hydrostatic C-C-C node, while the singular node near the right support is a nonhydrostatic C-C-T node. The hydrostatic stresses at the C-C-C node are 19 MPa (Figure A.3). On the other hand, the nonhydrostatic stresses at each nodal face of the C-C-T node are 9.3 MPa and 15.8 MPa (Figure A.3).

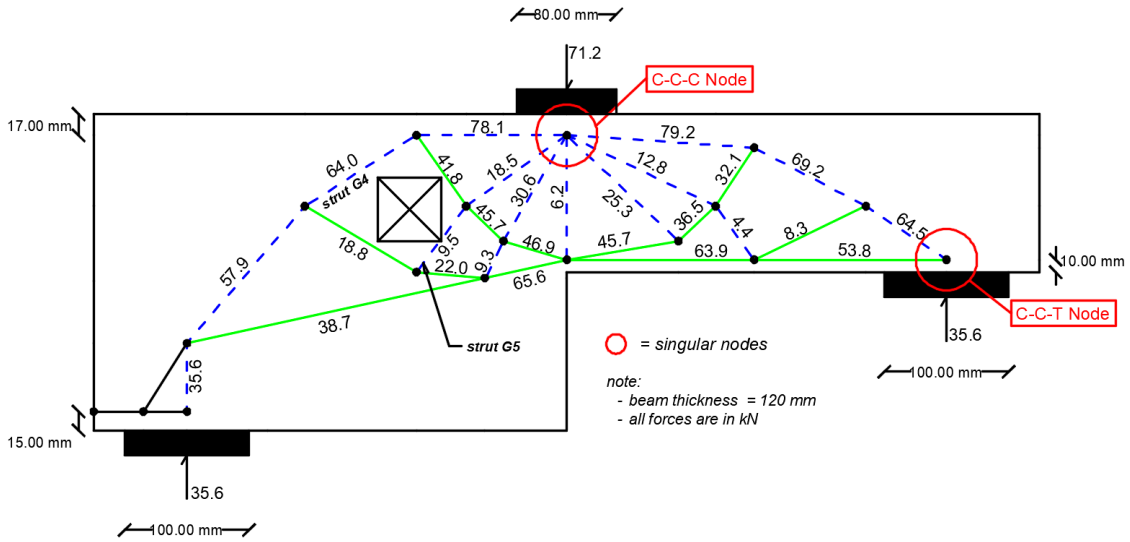

Figure A.1: Singular nodes indicated at G-series ST model.

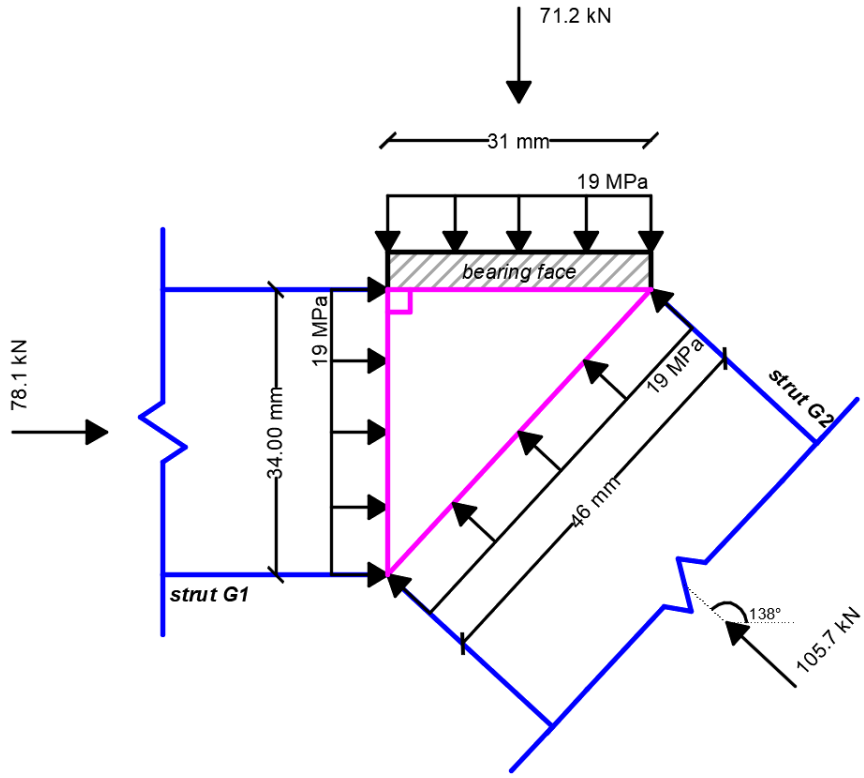

Figure A.2: Geometry of the hydrostatic C-C-C node at G-series ST model.

The result of the stress check on C-C-C node is shown in Table A.1, while the result of the stress check on C-C-T nodes is shown in Table A.2. The end results were displayed as a ratio between resulting stress over allowable stress. According to the results, the stresses that works on the aforementioned nodal zones are relatively far from reaching their capacity limit. All comparisons with the allowable stresses produce ratios that have values below 0.4. These low ratios of stress were obtained even with every nodal zone having a bearing face width that is less than the loading/support plate width. Therefore, it is safe to assume that the stresses at the C-C-C and C-C-T nodal zones will not cause any compressive failure to the concrete of G-series specimens at the load level of 71.2 kN.

Table A.1: Widths, resulting stresses, and the stress check results of G-series ST model C-C-C nodes.

C-C-C NODE			
Compression force (kN)	Nodal face width (mm)	Resulting Stress (MPa)	Stress Ratio
71.20	31.00	19.1	✓ 0.39
78.10	34.00	19.1	✓ 0.39
105.68	46.01	19.1	✓ 0.39

Table A.2: Widths, resulting stresses, and the stress check results of G-series ST model C-C-T nodes.

C-C-T NODE			
Compression force (kN)	Nodal face width (mm)	Resulting Stress (MPa)	Stress Ratio
64.50	34.08	15.8	✓ 0.38
35.60	32.00	9.3	✓ 0.22

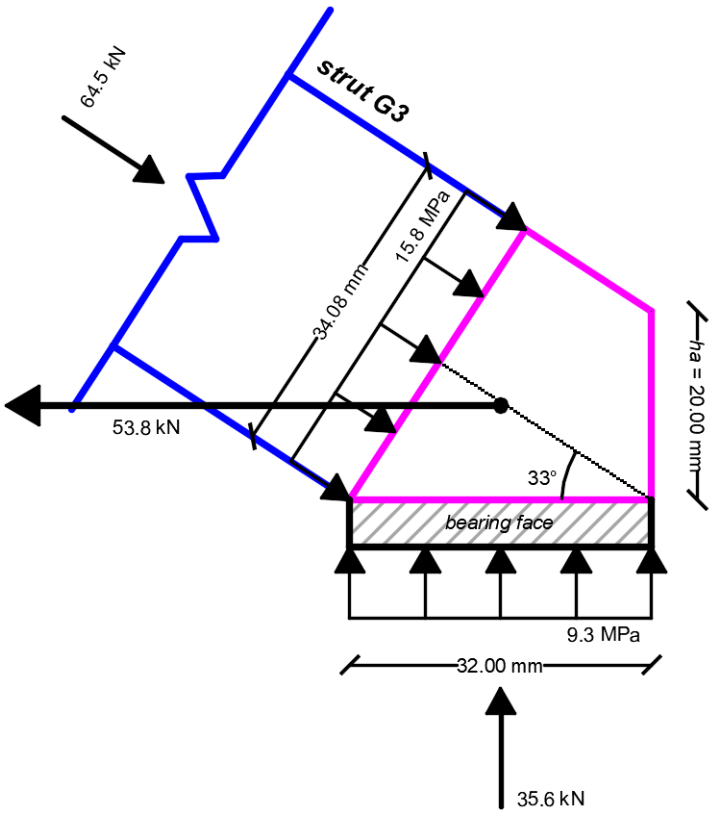

Figure A.3: Geometry of the nonhydrostatic C-C-T node near the right support at G-series ST model.

Struts

The second dimensioned truss members to be discussed are the struts. In the process of determining their dimension, each strut was assumed to have a prismatic shape. This assumption was taken because the LEFEA result of specimen G-1 showed that there are no principal tensile strains along those struts that neither resemble a bottle nor a fan (see Figure A.4).

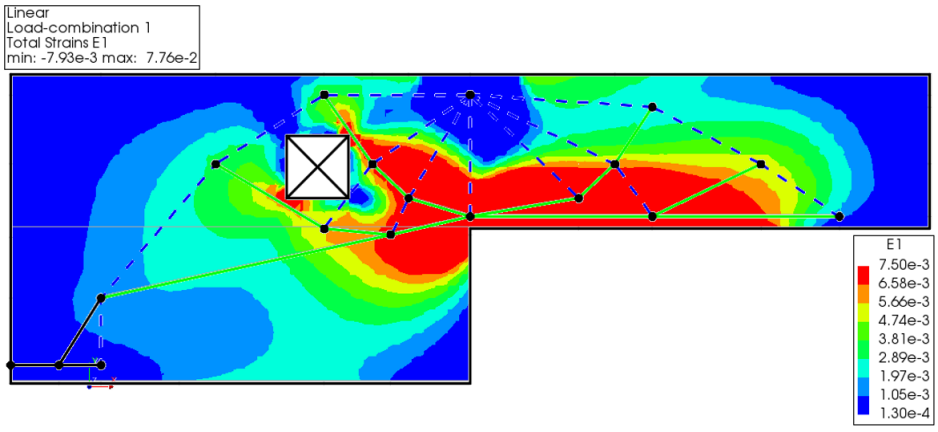

Figure A.4: Alignment of the G-series ST model with the dapped beam's principal tensile strains (E1) from LEFEA.

After the shape of the struts has been determined, these compressive truss members were analyzed

for their stress. The stress analysis was carried out on the struts of the singular nodes of the G-series ST model (strut G1, G2, and G3) since they are the critical ones. Due to their prismatic shape, the resulting stress and the width of each strut are equivalent to the stress and width properties of the nodal faces that they attached on. Additionally, the struts near the left-top corner (strut G-4) and the right-bottom corner (strut G-5) of the opening also had their stresses checked since they have limited width of concrete to form a prismatic strut. To check their stresses, strut G4 and G5 are dimensioned to the maximum width that they can have. Strut G4 can have a strut width of 24.26 mm at most, while strut G5 can have none since the center of the strut coincided with the right-bottom corner of the opening. Information regarding these two variables is summarized in Table A.3.

Similar to the nodal zones, the end results of the struts' stress check are also presented as a ratio between the resulting stress and the allowable stress. According to the comparison results shown in Table A.3, all struts appear to have a medium level of stress, except for strut G5. Stress ratios of strut G1, G2, G3, and G4 shows values between 0.5 and 0.8. These results mean that the concrete at these dimensioned struts can be considered safe from any compressive failure at the load level of 71.2 kN. In contrast, compressive failure might occur on the concrete around strut G5 since there is an insufficient amount of concrete available to contain the compressive force that acts on that strut. However, the damage to the concrete caused by this strut should be insignificant since strut G5 contains a relatively small compressive force compared to the other struts.

Table A.3: Widths, resulting stresses, and the stress check results of G-series ST model dimensioned struts.

Strut ID	Compression force (kN)	Strut width (mm)	Resulting stress (MPa)	Stress Ratio
G1	78.10	34.00	19.1	✓ 0.66
G2	105.68	46.01	19.1	✓ 0.66
G3	64.50	34.08	15.8	✓ 0.54
G4	64.00	24.26	22.0	✓ 0.76
G5	9.50	0.01	7916.7	✗ 272.15

Ties

The last dimensioned truss members to be discussed are the ties. Unlike struts and nodes, ties are dimensioned with reinforcement bars. Since the reinforcement designs for G-series specimens have been provided by Oviedo, the capacity of those rebars just had to be rechecked in accordance with the tensile forces acting on the ties. For the purpose of this stress check, the ties of the G-series ST model were ID-ed, as shown in Figure A.5. The tensile forces in those ties were then compared with the steel design of specimen G-1, shown in Figure A.6.

The results of the stress check on the rebars of specimen G-1 is presented in Table A.4. The end results of the stress check are given as a ratio between the tensile stress per rebar over the mean yield strength (f_{ym}) of the rebar, shown in Table 8.4. Based on those results, each rebar set appeared to have excessive strength in withstanding the tensile force from its respective tie without yielding, except for the rebar set on tie 12 and 13. The rebar sets provided for these two ties was two stirrups with 4.6-mm rebar diameter (4 - ⌀4.6 mm) which were installed in alignment with the ties. The tensile forces surpassed the 4.6-mm rebars yield capacity margin by at least 11%. However, the other rebars were safe from any plastic deformation at the load level of 71.2 kN, especially the main flexural rebars (aligned with ties 1, 2, 3, and 4 and designed as 3 - ⌀10 mm) that have stress ratios below 0.5. Thus, the G-series ST model can be considered providing a safe design in terms of reinforcements.

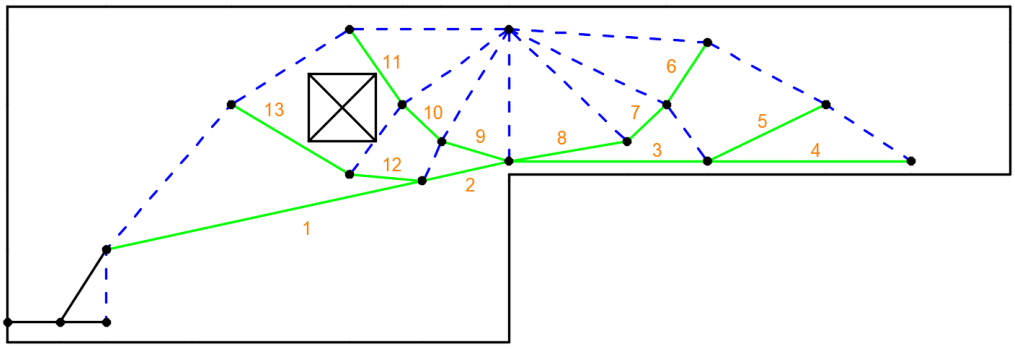

Figure A.5: ID-ed ties of G-series ST model.

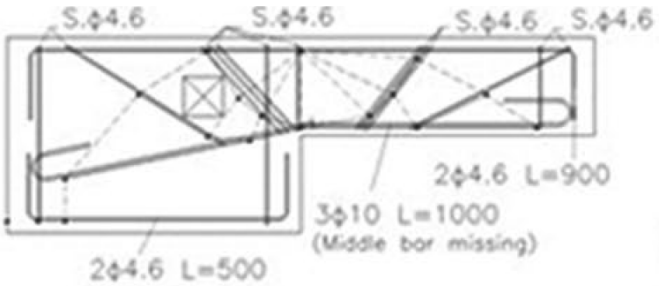

Figure A.6: Reinforcements of specimen G-1 [19].

Table A.4: Stress check results of G-series ST model dimensioned ties using specimen G-1 reinforcement design.

Tie ID	Tie force (kN)	Representing rebars	Angle toward the rebar (^{0})	Projected force (kN)	Total rebar area (mm^2)	Tensile Stress per rebar (MPa)	Stress Ratio
1	38.70	3 - Ø10 mm	0.0	38.70	235.62	164.25	0.26
2	65.60	3 - Ø10 mm	0.0	65.60	235.62	278.42	0.45
3	63.90	3 - Ø10 mm	0.0	63.90	235.62	271.20	0.43
4	53.80	3 - Ø10 mm	0.0	53.80	235.62	228.33	0.37
5	8.30	2 - Ø4.6 mm	0.0	8.30	33.24	249.71	0.49
6	32.10	6 - Ø4.6 mm	6.0	31.92	99.71	320.16	0.63
7	36.50	6 - Ø4.6 mm	7.0	36.23	99.71	363.32	0.72
8	45.70	6 - Ø4.6 mm	41.0	34.49	99.71	345.89	0.68
9	46.90	6 - Ø4.6 mm	25.0	42.51	99.71	426.28	0.84
10	45.70	6 - Ø4.6 mm	2.0	45.67	99.71	458.03	0.90
11	41.80	6 - Ø4.6 mm	14.0	40.56	99.71	406.75	0.80
12	22.00	2 - Ø4.6 mm	25.0	19.94	33.24	599.88	1.18
13	18.80	2 - Ø4.6 mm	0.0	18.80	33.24	565.62	1.11

A.2. H-series strut-and-tie model

Nodal zones

The first dimensioned truss members to be discussed are the nodes. After being shaped and sized, each node of the H-series ST model changed into a nodal zone. Based on the way forces equilibrate in its area, nodal zones can be distinguished into two different types: singular nodes and smeared nodes. Since it is unnecessary to check the concrete stresses at the smeared nodes [25], singular nodes were the only nodal zones of the H-series ST model that were checked. There are two nodes from the truss model that can be categorized as singular nodes: one near the loading point and one near the right support, as indicated in Figure A.7. The singular node near the loading point is

a hydrostatic C-C-C node, while the singular node near the right support is a nonhydrostatic C-C-T node. The hydrostatic stresses at the C-C-C node are 19 MPa (Figure A.9). On the other hand, the nonhydrostatic stresses at each nodal face of the C-C-T node are 10.8 MPa (Figure A.9).

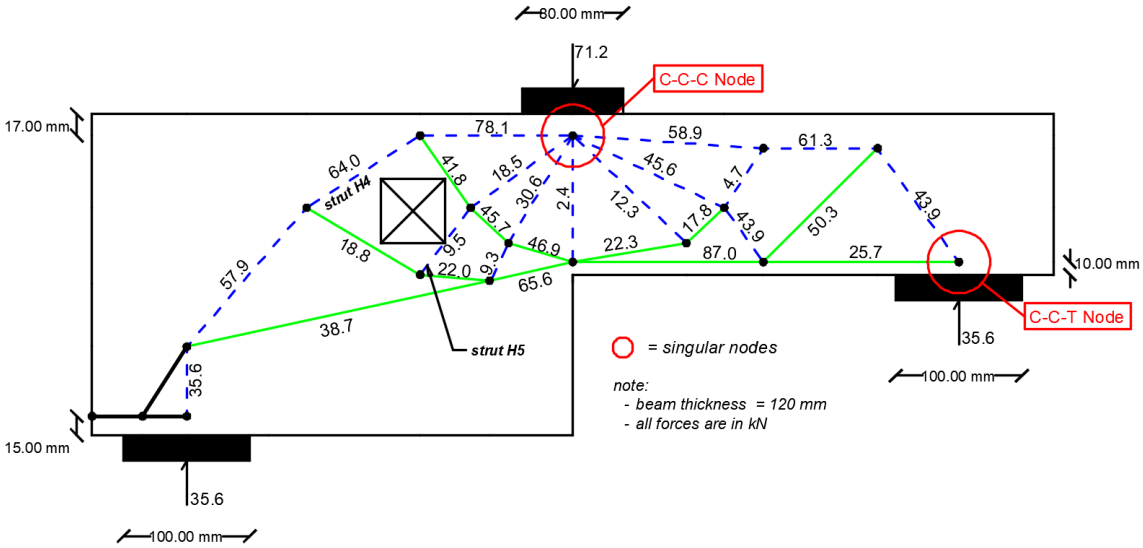

Figure A.7: Singular nodes indicated at H-series ST model.

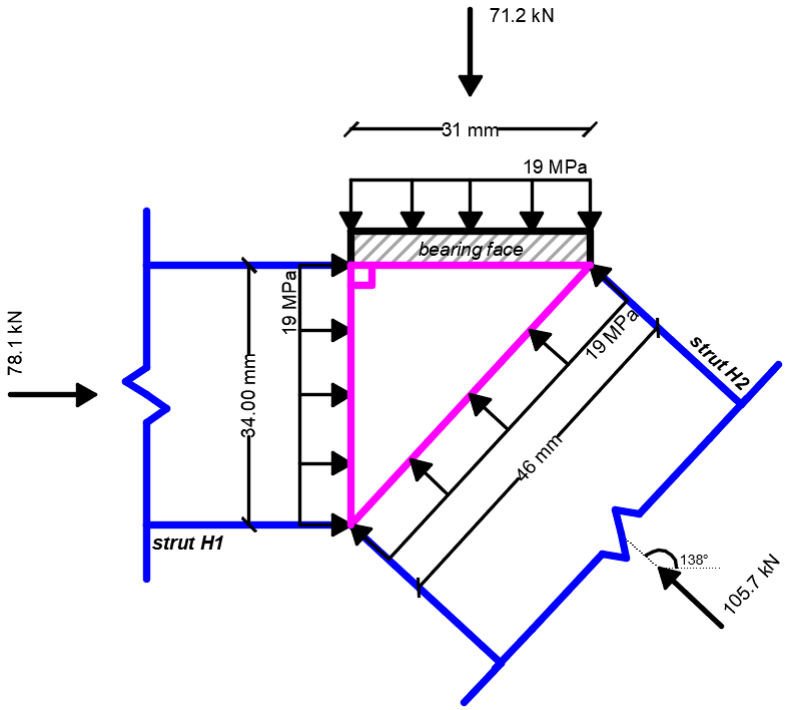

Figure A.8: Geometry of the hydrostatic C-C-C node at H-series ST model.

The result of the stress check on C-C-C node is shown in Table A.5, while the result of the stress check on C-C-T nodes is shown in Table A.6. The end results were displayed as a ratio between resulting stress over allowable stress. According to the results, the stresses that works on the aforementioned nodal zones are relatively far from reaching their capacity limit. All comparisons with the allowable

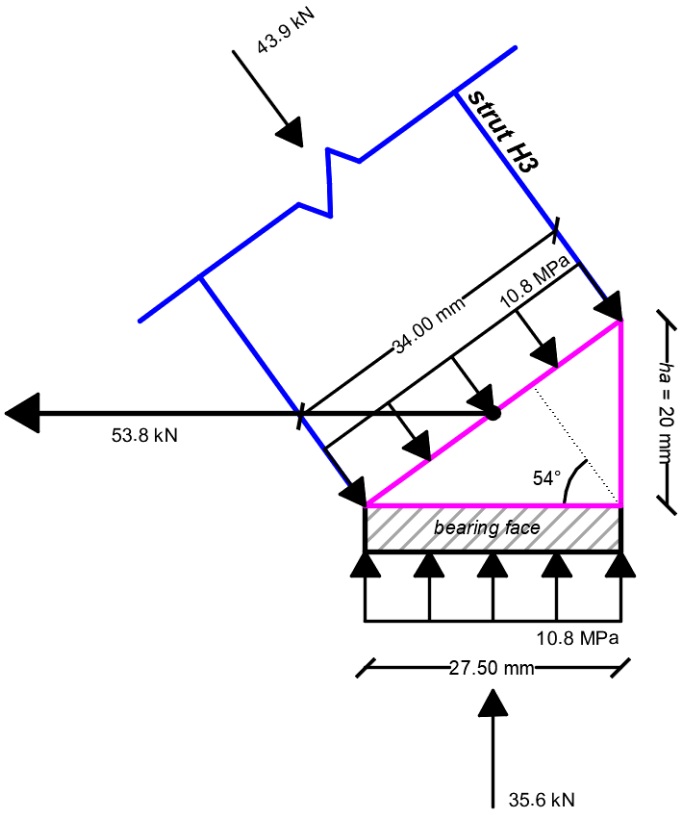

Figure A.9: Geometry of the nonhydrostatic C-C-T node near the right support at H-series ST model.

stresses produce ratios that have values below 0.4. These low ratios of stress were obtained even with every nodal zone having a bearing face width that is less than the loading/support plate width. Therefore, it is safe to assume that the stresses at the C-C-C and C-C-T nodal zones will not cause any compressive failure to the concrete of H-series specimens at the load level of 71.2 kN.

Table A.5: Widths, resulting stresses, and the stress check results of H-series ST model C-C-C nodes.

C-C-C NODE			
Compression force (kN)	Nodal face width (mm)	Resulting Stress (MPa)	Stress Ratio
71.20	31.00	19.1	0.39
78.10	34.00	19.1	0.39
105.68	46.01	19.1	0.39

Table A.6: Widths, resulting stresses, and the stress check results of H-series ST model C-C-T nodes.

C-C-T NODE			
Compression force (kN)	Nodal face width (mm)	Resulting Stress (MPa)	Stress Ratio
43.90	34.03	10.8	0.26
35.60	27.50	10.8	0.26

Struts

The second dimensioned truss members to be discussed are the struts. In the process of determining their dimension, each strut was assumed to have a prismatic shape. This assumption was taken because the LEFEA result of specimen H-1 showed that there are no principal tensile strains along those struts that neither resemble a bottle nor a fan (see Figure A.10).

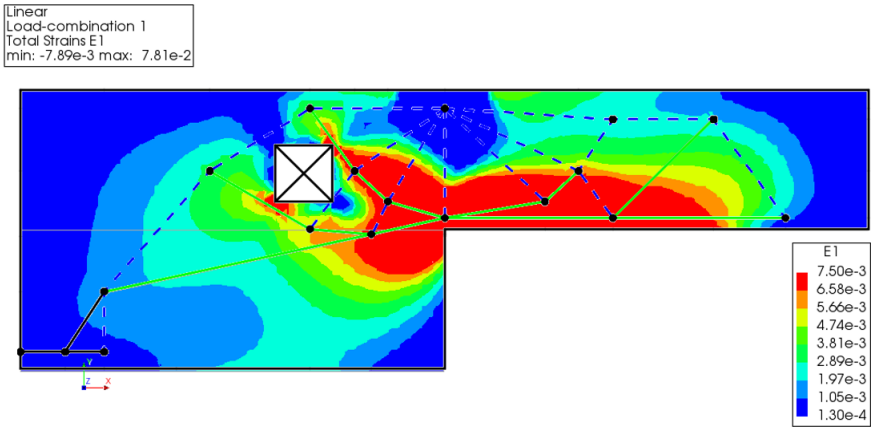

Figure A.10: Alignment of the H-series ST model with the dapped beam's principal tensile strains (E1) from LEFEA.

After the shape of the struts has been determined, these compressive truss members were analyzed for their stress. The stress analysis was carried out on the struts of the singular nodes of the H-series ST model (strut H1, H2, and H3) since they are the critical ones. Due to their prismatic shape, the resulting stress and the width of each strut are equivalent to the stress and width properties of the nodal faces that they attached on. Additionally, the struts near the left-top corner (strut H-4) and the right-bottom corner (strut H-5) of the opening also had their stresses checked since they have limited width of concrete to form a prismatic strut. To check their stresses, strut H4 and H5 are dimensioned to the maximum width that they can have. Strut H4 can have a strut width of 24.26 mm at most, while strut H5 can have none since the center of the strut coincided with the right-bottom corner of the opening. Information regarding these two variables is summarized in Table A.7.

Similar to the nodal zones, the end results of the struts' stress check are also presented as a ratio between the resulting stress and the allowable stress. According to the comparison results shown in Table A.7, all struts appear to have a medium level of stress, except for strut H5. Stress ratios of strut H1, H2, H3, and H4 shows values between 0.5 and 0.8. These results mean that the concrete at these dimensioned struts can be considered safe from any compressive failure at the load level of 71.2 kN. In contrast, compressive failure might occur on the concrete around strut H5 since there is an insufficient amount of concrete available to contain the compressive force that acts on that strut. However, the damage to the concrete caused by this strut should be insignificant since strut H5 contains a relatively small compressive force compared to the other struts.

Ties

The last dimensioned truss members to be discussed are the ties. Unlike struts and nodes, ties are dimensioned with reinforcement bars. Since the reinforcement designs for H-series specimens have been provided by Oviedo, the capacity of those rebars just had to be rechecked in accordance with the tensile forces acting on the ties. For the purpose of this stress check, the ties of the H-series ST model were ID-ed, as shown in Figure A.11. The tensile forces in those ties were then compared with the steel design of specimen H-1, shown in Figure A.12.

Table A.7: Widths, resulting stresses, and the stress check results of H-series ST model dimensioned struts.

Strut ID	Compression force (kN)	Strut width (mm)	Resulting stress (MPa)	Stress Ratio
H1	78.10	34.00	19.1	✓ 0.66
H2	105.68	46.01	19.1	✓ 0.66
H3	43.90	34.03	10.8	✓ 0.37
H4	64.00	24.26	22.0	✓ 0.76
H5	9.50	0.01	7916.7	✗ 272.15

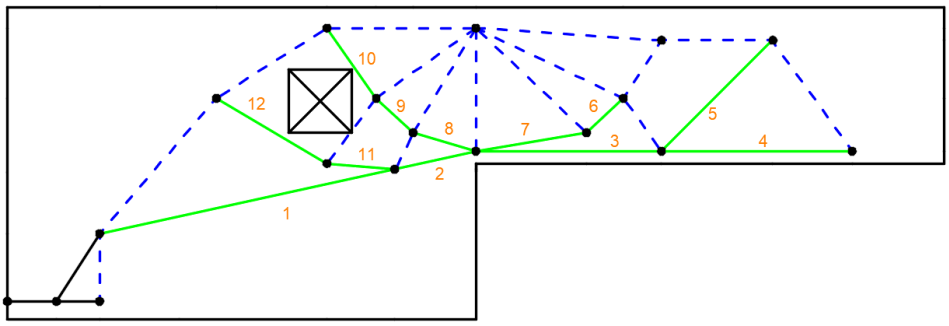

Figure A.11: ID-ed ties of H-series ST model.

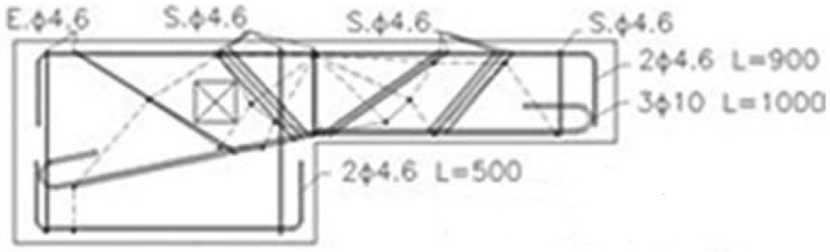

Figure A.12: Reinforcements of specimen H-1 [19].

The results of the stress check on the rebars of specimen H-1 is presented in Table A.8. The end results of the stress check are given as a ratio between the tensile stress per rebar over the mean yield strength (f_{ym}) of the rebar, shown in Table 8.4. Based on those results, each rebar set appeared to have excessive strength in withstanding the tensile force from its respective tie without yielding, except for the rebar set on tie 11 and 12. The rebar sets provided for these two ties was two stirrups with 4.6-mm rebar diameter (4 - ⌀4.6 mm) which were installed in alignment with the ties. The tensile forces surpassed the 4.6-mm rebars yield capacity margin by at least 11%. However, other rebars were safe from any plastic deformation at the load level of 71.2 kN, especially the main flexural rebars (aligned with ties 1, 2, 3, and 4 and designed as 3 - ⌀10 mm) that have stress ratios below 0.6. Thus, the H-series ST model can be considered providing a safe design in terms of reinforcements.

Table A.8: Stress check results of H-series ST model dimensioned ties using specimen H-1 reinforcement design.

Tie ID	Tie force (kN)	Representing rebars	Angle toward the rebar (^{0})	Projected force (kN)	Total rebar area (mm^2)	Tensile Stress per rebar (MPa)	Stress Ratio
1	38.70	3 - Ø10 mm	0.0	38.70	235.62	164.25	0.26
2	65.60	3 - Ø10 mm	0.0	65.60	235.62	278.42	0.45
3	87.00	3 - Ø10 mm	0.0	87.00	235.62	369.24	0.59
4	25.70	3 - Ø10 mm	0.0	25.70	235.62	109.07	0.17
5	50.30	6 - Ø4.6 mm	0.0	50.30	99.71	504.44	0.99
6	17.80	4 - Ø4.6 mm	7.0	17.67	66.48	265.77	0.52
7	22.30	4 - Ø4.6 mm	25.0	20.21	66.48	304.03	0.60
8	46.90	6 - Ø4.6 mm	25.0	42.51	99.71	426.28	0.84
9	45.70	6 - Ø4.6 mm	2.0	45.67	99.71	458.03	0.90
10	41.80	6 - Ø4.6 mm	14.0	40.56	99.71	406.75	0.80
11	22.00	2 - Ø4.6 mm	25.0	19.94	33.24	599.88	1.18
12	18.80	2 - Ø4.6 mm	0.0	18.80	33.24	565.62	1.11

A.3. Specimen 2 strut-and-tie model

Nodal zones

The first dimensioned truss members to be discussed are the nodes. After being shaped and sized, each node of the Specimen 2's ST model changed into a nodal zone. Based on the way forces equilibrate in its area, nodal zones can be distinguished into two different types: singular nodes and smeared nodes. Since it is unnecessary to check the concrete stresses at the smeared nodes [25], singular nodes were the only nodal zones of the Specimen 2 ST model that were checked. There are three nodes from the truss model that can be categorized as singular nodes: two near the loading point and one near the left support, as indicated in Figure A.13. The singular nodes near the loading point are hydrostatic C-C-C nodes, while the singular node near the left support is a nonhydrostatic C-C-T node. The hydrostatic stresses at the C-C-C nodes are 8.8 MPa (Figure A.14). On the other hand, the nonhydrostatic stresses at each nodal face of the C-C-T node are 8.8 MPa and 11.8 MPa (Figure A.15).

The result of the stress check on C-C-C node is shown in Table A.9, while the result of the stress check on C-C-T nodes is shown in Table A.10. The end results were displayed as a ratio between resulting stress over allowable stress. According to the results, the stresses that works on the aforementioned nodal zones are relatively far from reaching their capacity limit. All comparisons with the allowable stresses produce ratios that have values below 0.6. Therefore, it is safe to assume that the stresses at the C-C-C and C-C-T nodal zones will not cause any compressive failure to the concrete of Specimen 2 at the load level of 99.2 kN.

Table A.9: Widths, resulting stresses, and the stress check results of Specimen 2's ST model C-C-C nodes.

C-C-C NODES							
1				2			
Compression force (kN)	Nodal face width (mm)	Resulting Stress (MPa)	Stress Ratio	Compression force (kN)	Nodal face width (mm)	Resulting Stress (MPa)	Stress Ratio
35.32	45.21	8.8	0.35	63.88	81.79	8.8	0.35
34.78	44.50	8.8	0.35	34.78	44.50	8.8	0.35
49.57	63.44	8.8	0.35	72.73	93.11	8.8	0.35

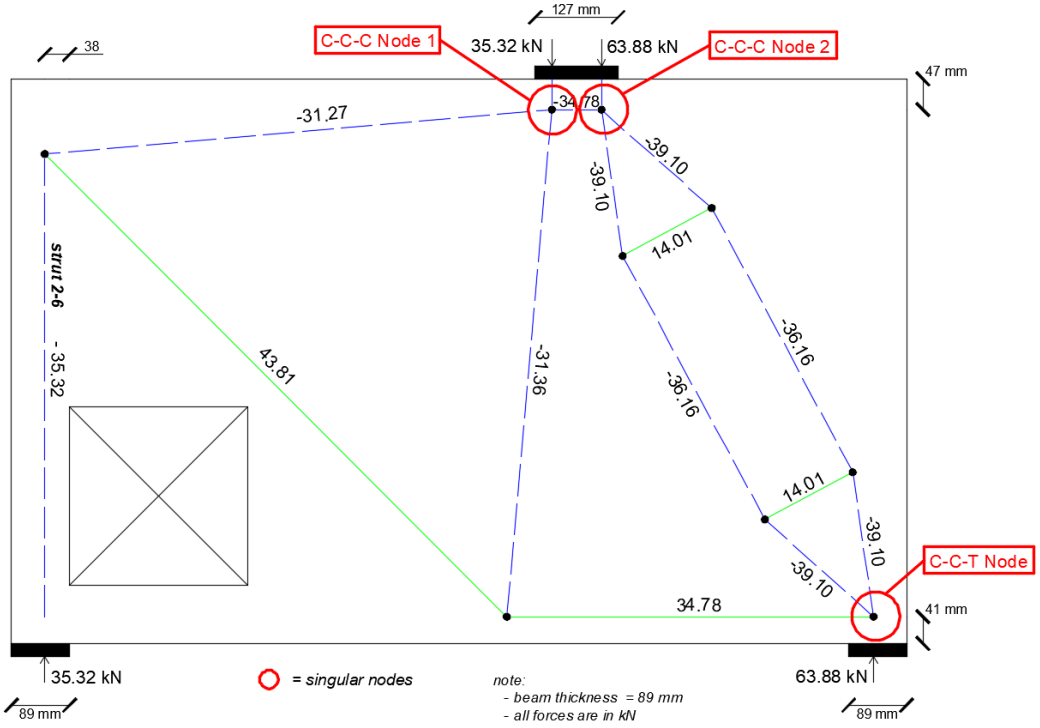

Figure A.13: Singular nodes indicated at Specimen 2's ST model.

Table A.10: Widths, resulting stresses, and the stress check results of Specimen 2 ST model C-C-T node.

C-C-T NODE			
Compression force (kN)	Nodal face width (mm)	Resulting Stress (MPa)	Stress Ratio
72.73	93.11	8.8	✓ 0.41
63.88	61.08	11.8	✓ 0.55

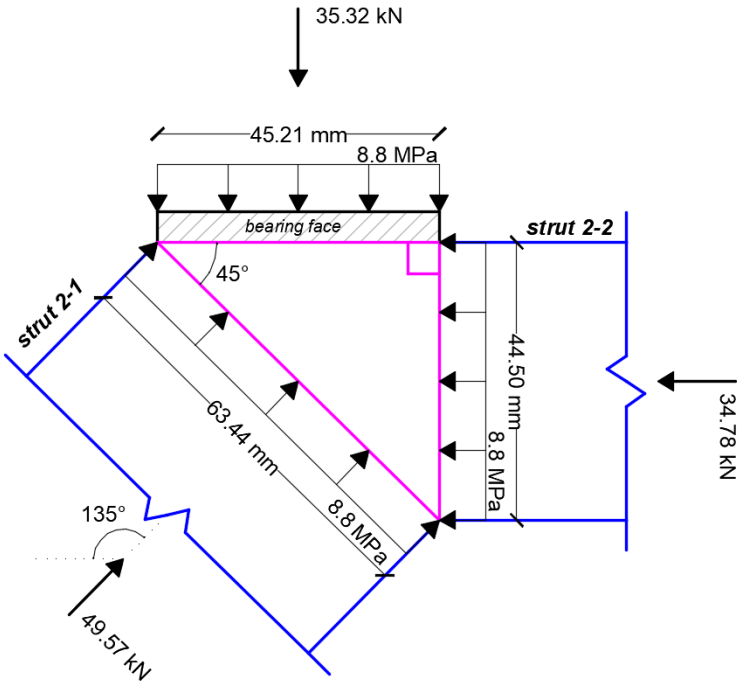

(a) Geometry of the C-C-C node 1

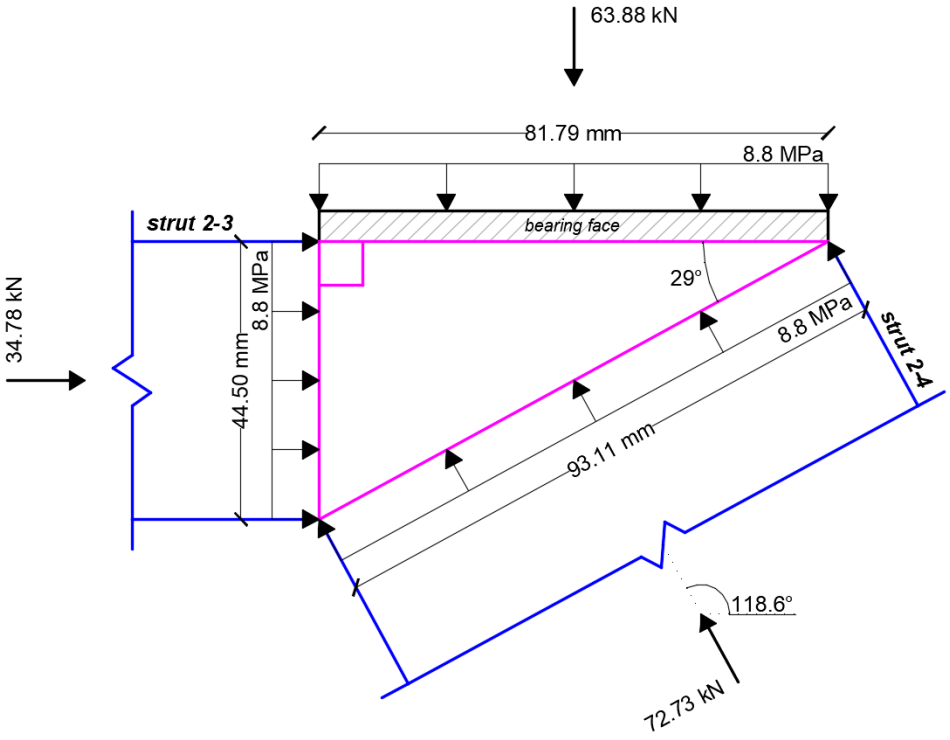

(b) Geometry of the C-C-C node 2

Figure A.14: Geometry of the hydrostatic C-C-C nodes near the loading point of Specimen 2.

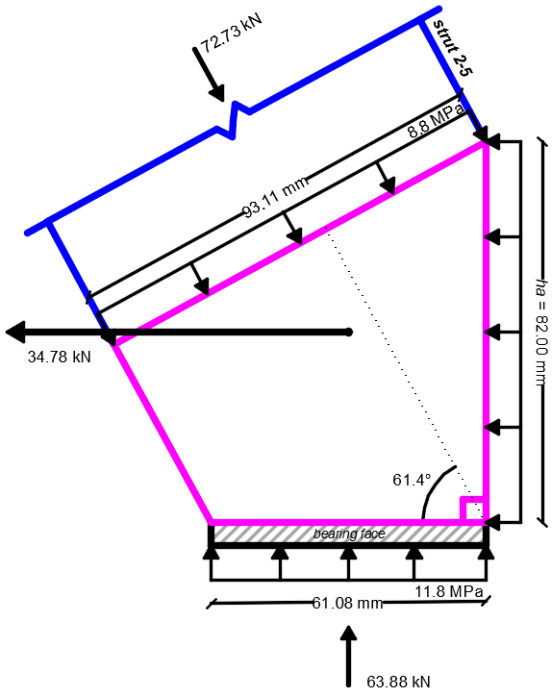

Figure A.15: Geometry of the nonhydrostatic C-C-T node at Specimen 2 ST model.

Struts

The second dimensioned truss members to be discussed are the struts. In the process of determining their dimension, each strut was assumed to have a prismatic shape. This assumption was taken because the LEFEA result of Maxwell & Breen's deep beam with a large opening showed that there are no principal tensile strains along those struts that neither resemble a bottle nor a fan (see Figure A.16).

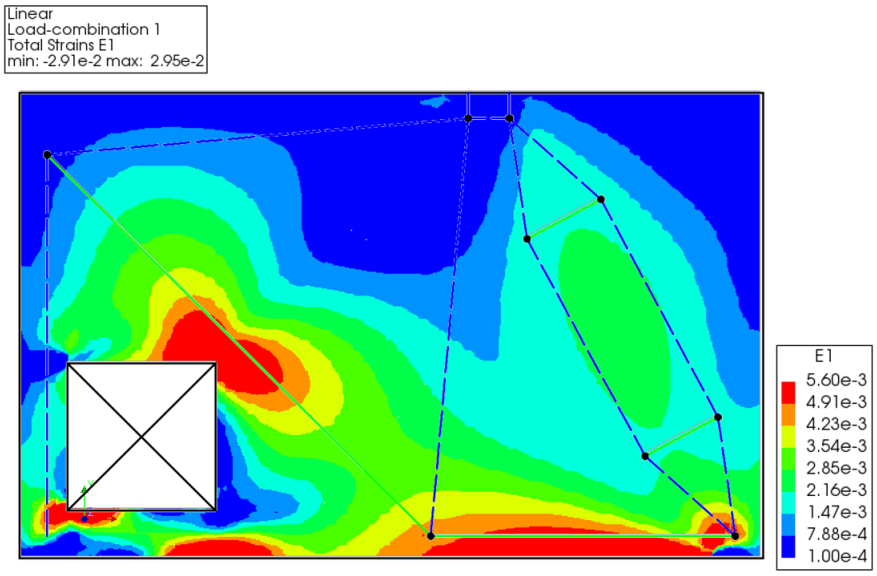

Figure A.16: Alignment of Specimen 2's ST model with the deep beam's principal tensile strains (E1) from LEFEA.

After the shape of the struts has been determined, these compressive truss members were analyzed for their stress. The stress analysis was carried out on the struts of the singular nodes (strut 2-1, 2-2, 2-3, 2-4 and 2-5) since they are the critical ones. Due to their prismatic shape, the resulting stress and the width of each strut are equivalent to the resulting stress and the width of the nodal faces that they attached on. Additionally, the left-most strut of Specimen 2's ST model (strut 2-6) also had its stress checked since it has a limited width of concrete at the left of the opening to transfer compressive stress to the left support. To check its stress, strut 2-6 is assumed to have the maximum width that it can have, which is 74 mm (twice the distance from the left side of the opening to the center of the strut. Information regarding these two variables are summarized in Table A.11.

Similar to the nodal zones, the end results of the struts' stress check were also presented as a ratio between the resulting stress and the allowable stress. According to the comparison results shown in Table A.11, all struts appeared to have a medium level of stress. Stress ratios of strut 2-1 to strut 2-6 showed values between 0.3 and 0.6. These results mean that the concrete at these dimensioned struts can also be considered safe from any compressive failure at the load level of 99.2 kN.

Ties

The last dimensioned truss members to be discussed are the ties. Unlike struts and nodes, ties are dimensioned with reinforcement bars. Since the reinforcement designs for Specimen 2 have been provided by Maxwell & Breen, the capacity of those rebars just had to be rechecked in accordance with the tensile forces acting on the ties. For the purpose of this stress check, the ties of Specimen 2's ST model were ID-ed, as shown in Figure A.17. The tensile forces in those ties were then compared

Table A.11: Widths, resulting stresses, and the stress check results of Specimen 2's ST model dimensioned struts.

Strut ID	Compression force (kN)	Strut width (mm)	Resulting stress (MPa)	Stress Ratio
2-1	49.57	63.44	8.8	0.58
2-2	34.78	44.50	8.8	0.58
2-3	34.78	44.50	8.8	0.58
2-4/5	72.73	93.11	8.8	0.58
2-6	35.32	74.00	5.4	0.36

with the steel design of Specimen 2, shown in Figure A.18.

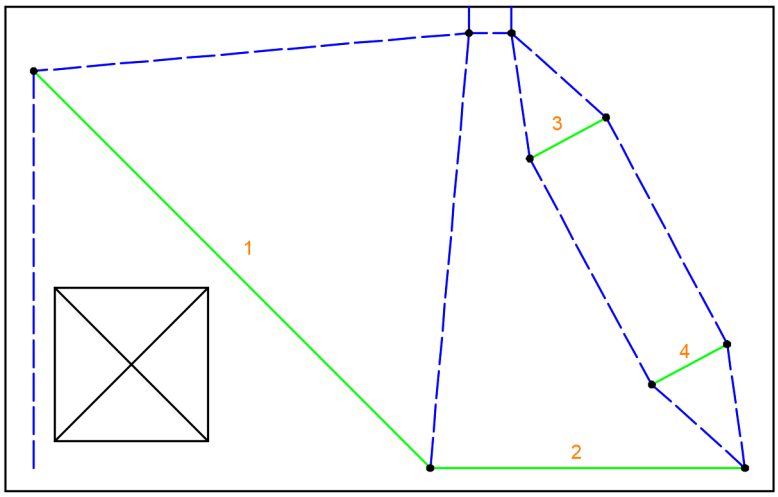

Figure A.17: ID-ed ties of Specimen 2's ST model.

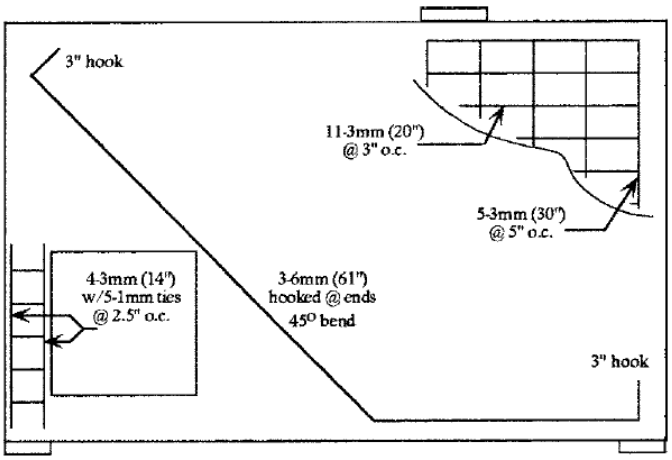

Figure A.18: Reinforcements of Specimen 2 [3].

The results of the stress check on the rebars of Specimen 2 is presented in Table A.13. The end results of the stress check are given as a ratio between the tensile stress per rebar over the mean yield strength (f_{ym}) of the rebar, shown in Table A.12. Based on those results, the 6-mm rebar set on tie 1 and 2 appear to have adequate strength in resisting the tensile forces from these two ties without yielding. The rebars at tie 1 were stressed up to a ratio of 0.91, while the rebars at tie 2 had a lower

stress ratio of 0.73. This means that the 6-mm rebar set should be secured from any plastic deformation at the load level of 99.2 kN.

Meanwhile, the 3-mm rebars that cover the tensile forces from tie 3 and 4 were stressed up to a ratio of 2.98. This high stress ratio means that these rebars should have yielded even before the load level reached 99.2 kN. However, the 3-mm rebars were parts of a steel mesh which was installed at the right-hand side of the deep beam. Therefore, the tensile stress redistribution from the concrete to the 3-mm rebars would also be handled by other steel bars on the mesh and the ST model of Specimen 2 can be considered providing a safe design in terms of reinforcements.

Table A.12: Rebar diameters used on Specimen 2 and their mean yield strengths.

Rebar diameter (mm)	Mean yield strength (MPa)
3	586.00
6	565.00

Table A.13: Stress check results of Specimen 2's ST model dimensioned ties using Specimen 2 reinforcement design.

Tie ID	Tie force (kN)	Representing rebars	Angle toward the rebar (^{0})	Projected force (kN)	Total rebar area (mm^2)	Tensile Stress per rebar (MPa)	Stress Ratio
1	43.81	3 - Ø6 mm	0.0	43.81	84.82	516.49 ✓	0.91
2	34.78	3 - Ø6 mm	0.0	34.78	84.82	410.03 ✓	0.73
3	14.01	1 - Ø3 mm	28.2	12.35	7.07	1746.75 ✗	2.98
4	14.01	1 - Ø3 mm	28.2	12.35	7.07	1746.75 ✗	2.98

A.4. Specimen 3 strut-and-tie model

Nodal zones

The first dimensioned truss members to be discussed are the nodes. After being shaped and sized, each node of the Specimen 3's ST model changed into a nodal zone. Based on the way forces equilibrate in its area, nodal zones can be distinguished into two different types: singular nodes and smeared nodes. Since it is unnecessary to check the concrete stresses at the smeared nodes [25], singular nodes were the only nodal zones of the Specimen 3 ST model that were checked. There are three nodes from the truss model that can be categorized as singular nodes: two near the loading point and one near the left support, as indicated in Figure A.19. The singular nodes near the loading point are hydrostatic C-C-C nodes, while the singular node near the left support is a nonhydrostatic C-C-T node. The hydrostatic stresses at the C-C-C nodes are 8.8 MPa (Figure A.20). On the other hand, the nonhydrostatic stresses at each nodal face of the C-C-T node are 8.8 MPa and 11.8 MPa (Figure A.21).

The result of the stress check on C-C-C node is shown in Table A.14, while the result of the stress check on C-C-T nodes is shown in Table A.15. The end results were displayed as a ratio between resulting stress over allowable stress. According to the results, the stresses that works on the aforementioned nodal zones are relatively far from reaching their capacity limit. All comparisons with the allowable stresses produce ratios that have values below 0.6. Therefore, it is safe to assume that the stresses at the C-C-C and C-C-T nodal zones will not cause any compressive failure to the concrete of Specimen 3 at the load level of 99.2 kN.

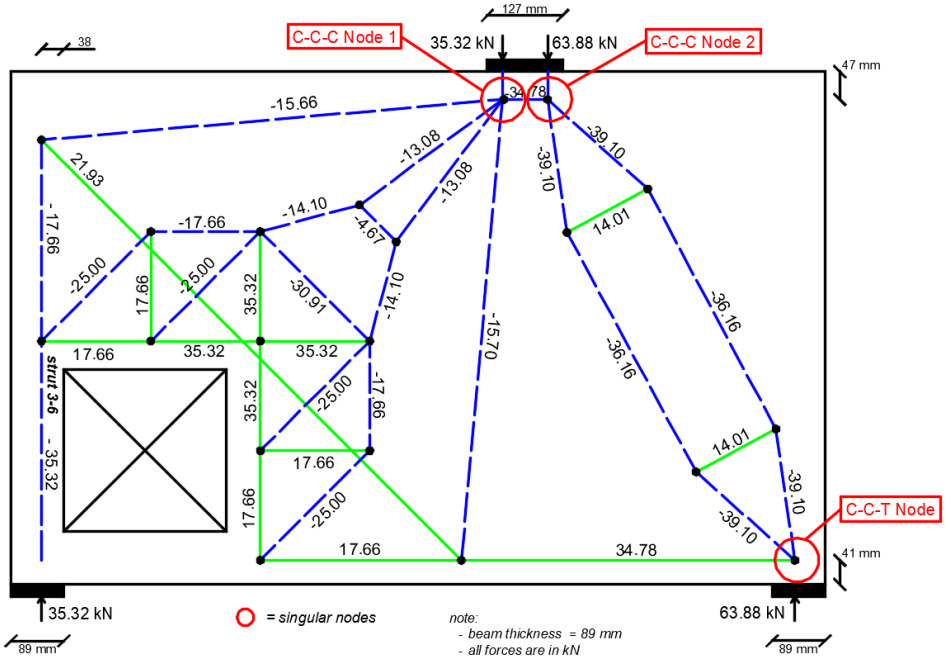

Figure A.19: Singular nodes indicated at Specimen 3's ST model.

Table A.14: Widths, resulting stresses, and the stress check results of Specimen 3's ST model C-C-C nodes.

C-C-C NODES							
1				2			
Compression force (kN)	Nodal face width (mm)	Resulting Stress (MPa)	Stress Ratio	Compression force (kN)	Nodal face width (mm)	Resulting Stress (MPa)	Stress Ratio
35.32	45.21	8.8	✓ 0.35	63.88	81.79	8.8	✓ 0.35
34.78	44.50	8.8	✓ 0.35	34.78	44.50	8.8	✓ 0.35
49.57	63.44	8.8	✓ 0.35	72.73	93.11	8.8	✓ 0.35

Table A.15: Widths, resulting stresses, and the stress check results of Specimen 3 ST model C-C-T node.

C-C-T NODE			
Compression force (kN)	Nodal face width (mm)	Resulting Stress (MPa)	Stress Ratio
72.73	93.11	8.8	✓ 0.41
63.88	61.08	11.8	✓ 0.55

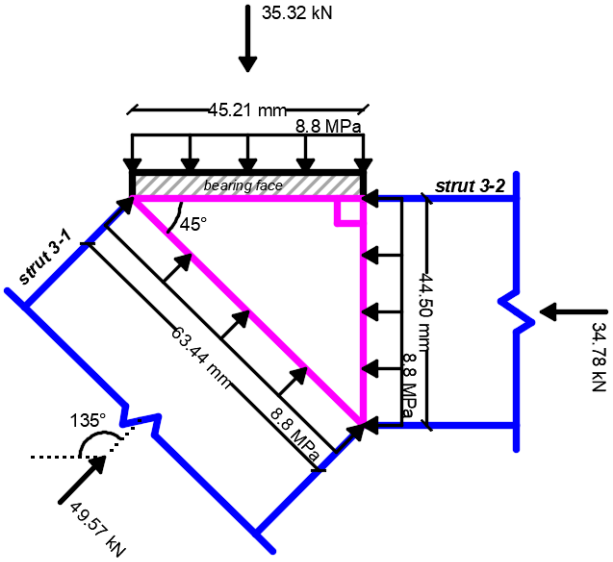

(a) Geometry of the C-C-C node 1

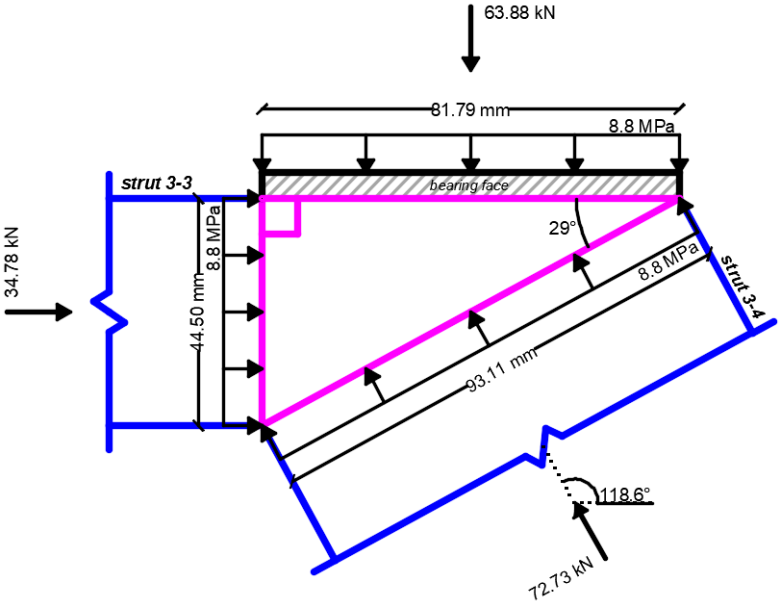

(b) Geometry of the C-C-C node 2

Figure A.20: Geometry of the hydrostatic C-C-C nodes near the loading point of Specimen 3.

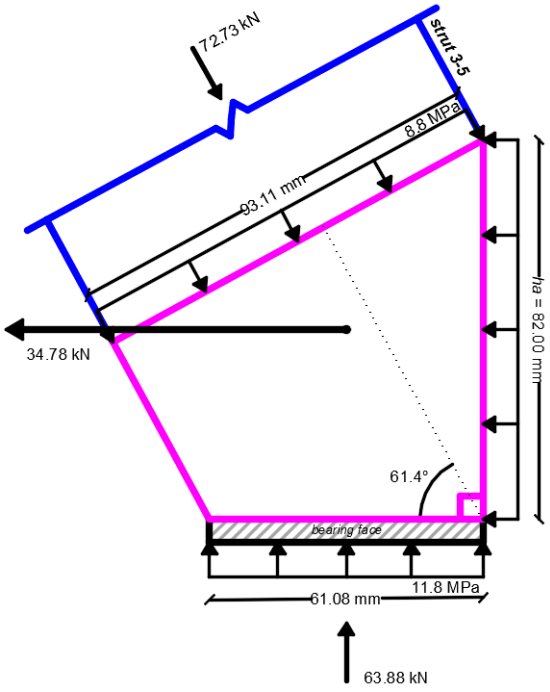

Figure A.21: Geometry of the nonhydrostatic C-C-T node at Specimen 3 ST model.

Struts

The second dimensioned truss members to be discussed are the struts. In the process of determining their dimension, each strut was assumed to have a prismatic shape. This assumption was taken because the LEFEA result of Maxwell & Breen's deep beam with a large opening showed that there are no principal tensile strains along those struts that neither resemble a bottle nor a fan (see Figure A.22).

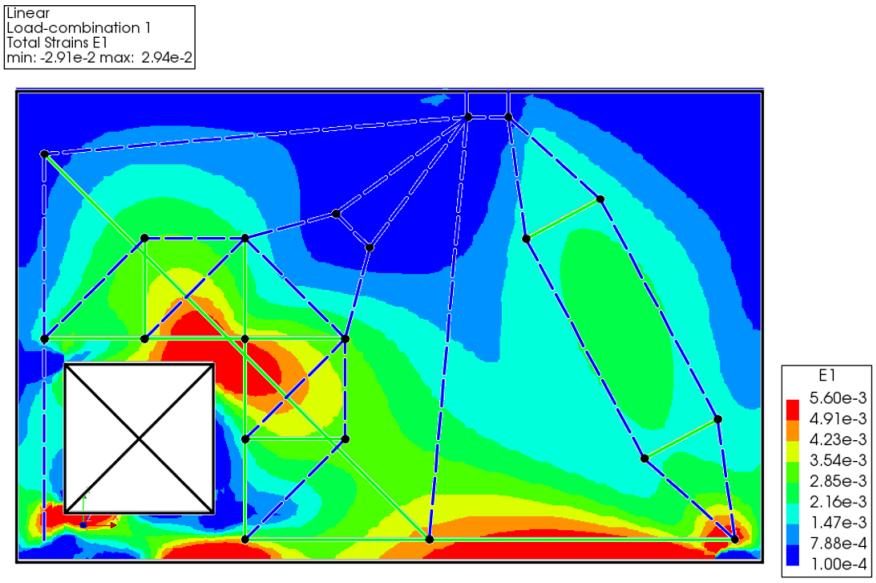

Figure A.22: Alignment of Specimen 3's ST model with the deep beam's principal tensile strains (E1) from LEFEA.

After the shape of the struts has been determined, these compressive truss members were analyzed for their stress. The stress analysis was carried out on the struts of the singular nodes (strut 3-1, 3-2, 3-3, 3-4 and 3-5) since they are the critical ones. Due to their prismatic shape, the resulting stress and the width of each strut are equivalent to the resulting stress and the width of the nodal faces that they attached on. Additionally, the left-most strut of Specimen 3's ST model (strut 3-6) also had its stress checked since it has a limited width of concrete at the left of the opening to transfer compressive stress to the left support. To check its stress, strut 3-6 is assumed to have the maximum width that it can have, which is 74 mm (twice the distance from the left side of the opening to the center of the strut. Information regarding these two variables are summarized in Table A.16.

Similar to the nodal zones, the end results of the struts' stress check were also presented as a ratio between the resulting stress and the allowable stress. According to the comparison results shown in Table A.16, all struts appeared to have a medium level of stress. Stress ratios of strut 3-1 to strut 3-6 showed values between 0.3 and 0.6. These results mean that the concrete at these dimensioned struts can also be considered safe from any compressive failure at the load level of 99.2 kN.

Ties

The last dimensioned truss members to be discussed are the ties. Unlike struts and nodes, ties are dimensioned with reinforcement bars. Since the reinforcement designs for Specimen 3 have been provided by Maxwell & Breen, the capacity of those rebars just had to be rechecked in accordance with the tensile forces acting on the ties. For the purpose of this stress check, the ties of Specimen 3's

Table A.16: Widths, resulting stresses, and the stress check results of Specimen 3's ST model dimensioned struts.

Strut ID	Compression force (kN)	Strut width (mm)	Resulting stress (MPa)	Stress Ratio
3-1	49.57	63.44	8.8	0.58
3-2	34.78	44.50	8.8	0.58
3-3	34.78	44.50	8.8	0.58
3-4/5	72.73	93.11	8.8	0.58
3-6	35.32	74.00	5.4	0.36

ST model were ID-ed, as shown in Figure A.23. The tensile forces in those ties were then compared with the steel design of Specimen 3, shown in Figure A.24.

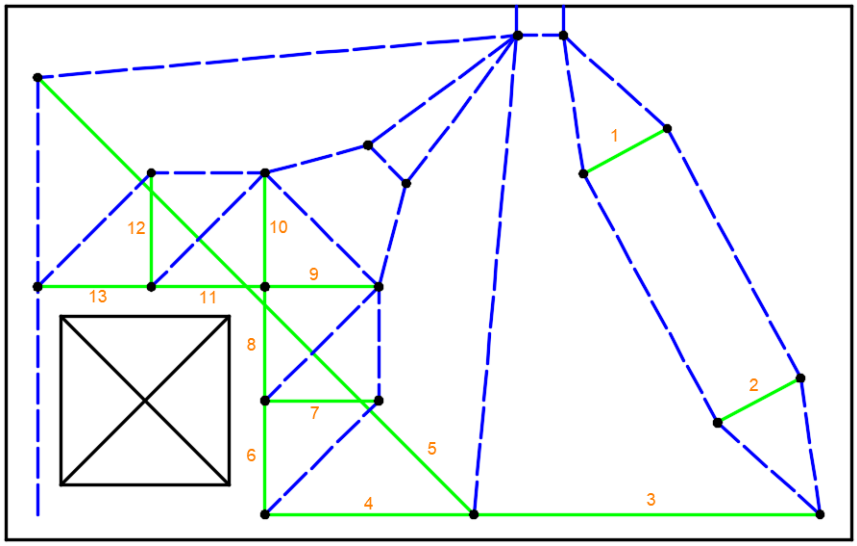

Figure A.23: ID-ed ties of Specimen 3's ST model.

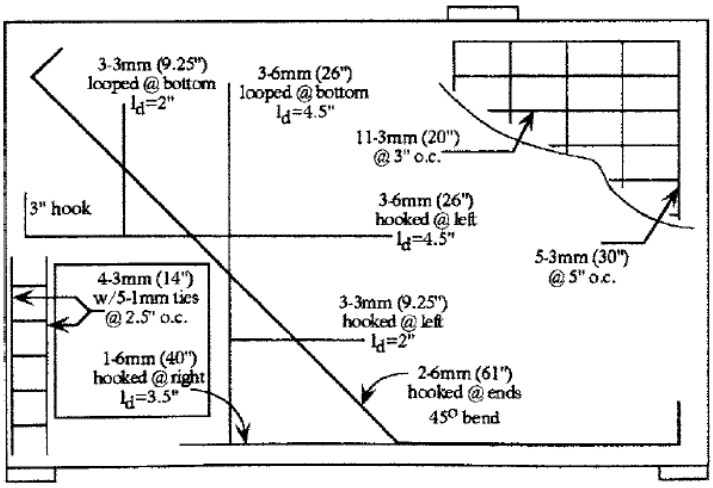

Figure A.24: Reinforcements of Specimen 3 [3].

The results of the stress check on the rebars of Specimen 3 is presented in Table A.17. The end re-

sults of the stress check are given as a ratio between the tensile stress per rebar over the mean yield strength (f_{ym}) of the rebar, shown in Table A.12. Based on those results, all rebars appear to have adequate strength in resisting the tensile forces from these two ties without yielding, except rebars at tie 1, 2, 4, 7, and 12.

The rebars that were installed to cover the tensile forces from tie 1 and 2 are 3-mm rebars, and they were stressed up to a ratio of 2.98. This high stress ratio means that these rebars should have yielded even before the load level reached 99.2 kN. However, the 3-mm rebars were parts of a steel mesh which was installed at the right-hand side of the deep beam. Therefore, the tensile stress redistribution from the concrete to the 3-mm rebars would also be handled by other steel bars on the mesh.

Meanwhile, the rebar set that were installed set to cover the tensile forces from tie 7 and 12 is 3 - ⌀3 mm rebar set, whereas tie 4 has 1 - ⌀6 mm rebar set. Although these ties are reinforced differently, they contain tensile forces that have the same magnitude, which is 17.66 kN. These tensile forces caused the rebar sets to be stressed for at least 11% above their yield strengths. This condition means that these rebars would yield when a load of 99.2 kN is applied to Specimen 3.

Beside rebars at tie 1, 2, 4, 7, and 12, the other rebars are safe from yielding at the load level of 99.2 kN. The rebars that handled the highest tensile forces in Specimen 3's ST model (rebars at tie 3, 8, 9, 10, and 11) were stressed up to a ratio of 0.74, while the rebars that handled smaller tensile forces were only stressed up to a ratio of 0.69 at most. Thus, the ST model of Specimen 3 can be considered providing a safe design in terms of reinforcements.

Table A.17: Stress check results of Specimen 3's ST model dimensioned ties using Specimen 3 reinforcement design.

Tie ID	Tie force (kN)	Representing rebars	Angle toward the rebar (^{0})	Projected force (kN)	Total rebar area (mm^2)	Tensile Stress per rebar (MPa)	Stress Ratio
1	14.01	1 - Ø3 mm	28.2	12.35	7.07	1746.75	2.98
2	14.01	1 - Ø3 mm	28.2	12.35	7.07	1746.75	2.98
3	34.78	3 - Ø6 mm	0.0	34.78	84.82	410.03	0.73
4	17.66	1 - Ø6 mm	0.0	17.66	28.27	624.59	1.11
5	21.93	2 - Ø6 mm	0.0	21.93	56.55	387.81	0.69
6	17.66	3 - Ø6 mm	0.0	17.66	84.82	208.20	0.37
7	17.66	3 - Ø3 mm	0.0	17.66	21.21	832.79	1.42
8	35.32	3 - Ø6 mm	0.0	35.32	84.82	416.40	0.74
9	35.32	3 - Ø6 mm	0.0	35.32	84.82	416.40	0.74
10	35.32	3 - Ø6 mm	0.0	35.32	84.82	416.40	0.74
11	35.32	3 - Ø6 mm	0.0	35.32	84.82	416.40	0.74
12	17.66	3 - Ø3 mm	0.0	17.66	21.21	832.79	1.42
13	17.66	3 - Ø6 mm	0.0	17.66	84.82	208.20	0.37

A.5. Specimen 4 strut-and-tie model

Nodal zones

The first dimensioned truss members to be discussed are the nodes. After being shaped and sized, each node of the Specimen 4's ST model changed into a nodal zone. Based on the way forces equilibrate in its area, nodal zones can be distinguished into two different types: singular nodes and smeared nodes. Since it is unnecessary to check the concrete stresses at the smeared nodes [25], singular nodes were the only nodal zones of the Specimen 4 ST model that were checked. There are three nodes from the truss model that can be categorized as singular nodes: two near the loading point and one near the left support, as indicated in Figure A.25. The singular nodes near the loading

point are hydrostatic C-C-C nodes, while the singular node near the left support is a nonhydrostatic C-C-T node. The hydrostatic stresses at the C-C-C nodes are 8.8 MPa (Figure A.26). On the other hand, the nonhydrostatic stresses at each nodal face of the C-C-T node are 8.8 MPa and 11.8 MPa (Figure A.27).

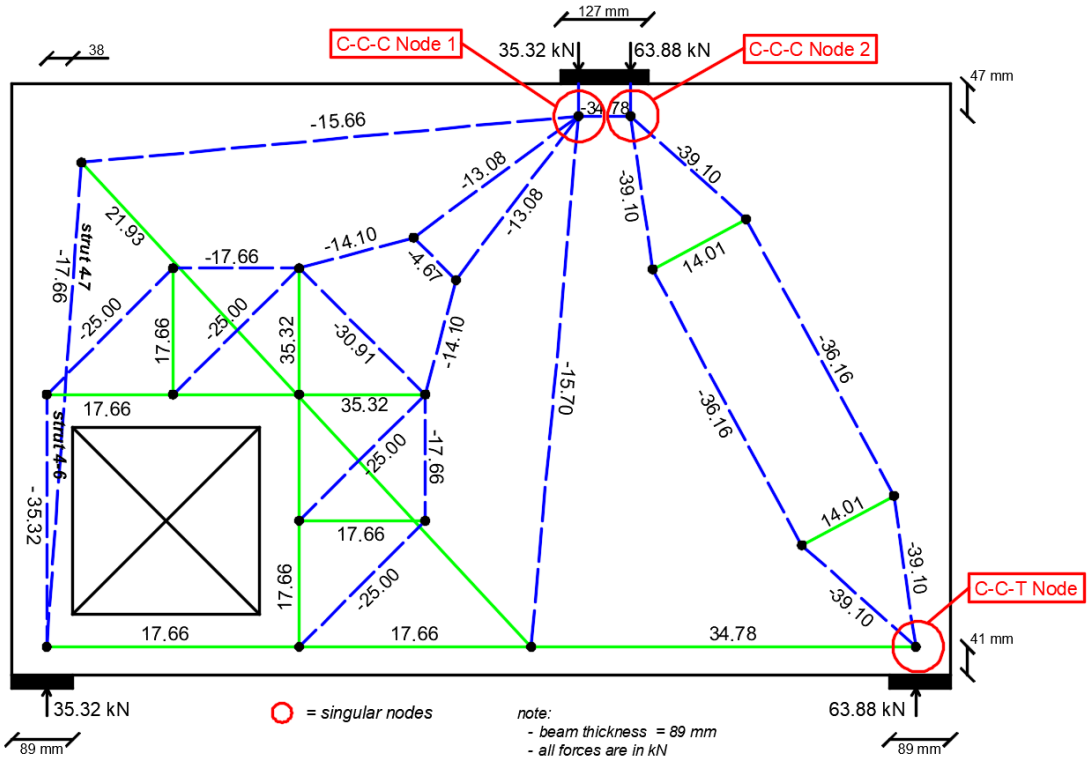

Figure A.25: Singular nodes indicated at Specimen 4's ST model.

The result of the stress check on C-C-C node is shown in Table A.18, while the result of the stress check on C-C-T nodes is shown in Table A.19. The end results were displayed as a ratio between resulting stress over allowable stress. According to the results, the stresses that works on the aforementioned nodal zones are relatively far from reaching their capacity limit. All comparisons with the allowable stresses produce ratios that have values below 0.6. Therefore, it is safe to assume that the stresses at the C-C-C and C-C-T nodal zones will not cause any compressive failure to the concrete of Specimen 4 at the load level of 99.2 kN.

Table A.18: Widths, resulting stresses, and the stress check results of Specimen 4's ST model C-C-C nodes.

C-C-C NODES							
1				2			
Compression force (kN)	Nodal face width (mm)	Resulting Stress (MPa)	Stress Ratio	Compression force (kN)	Nodal face width (mm)	Resulting Stress (MPa)	Stress Ratio
35.32	45.21	8.8	0.35	63.88	81.79	8.8	0.35
34.78	44.50	8.8	0.35	34.78	44.50	8.8	0.35
49.57	63.44	8.8	0.35	72.73	93.11	8.8	0.35

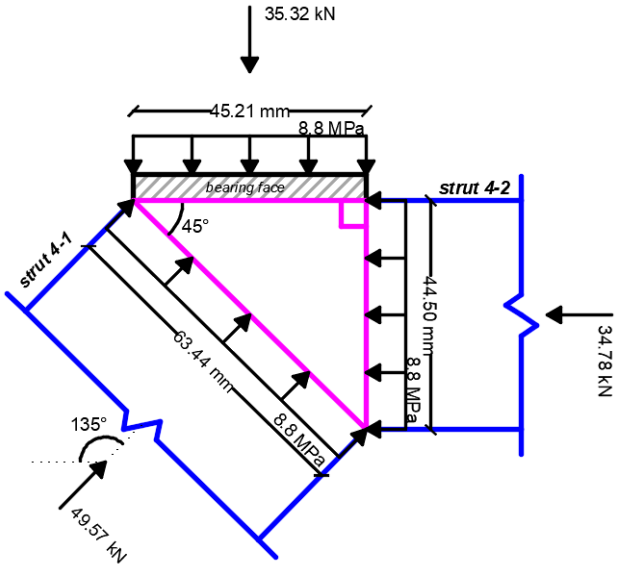

(a) Geometry of the C-C-C node 1

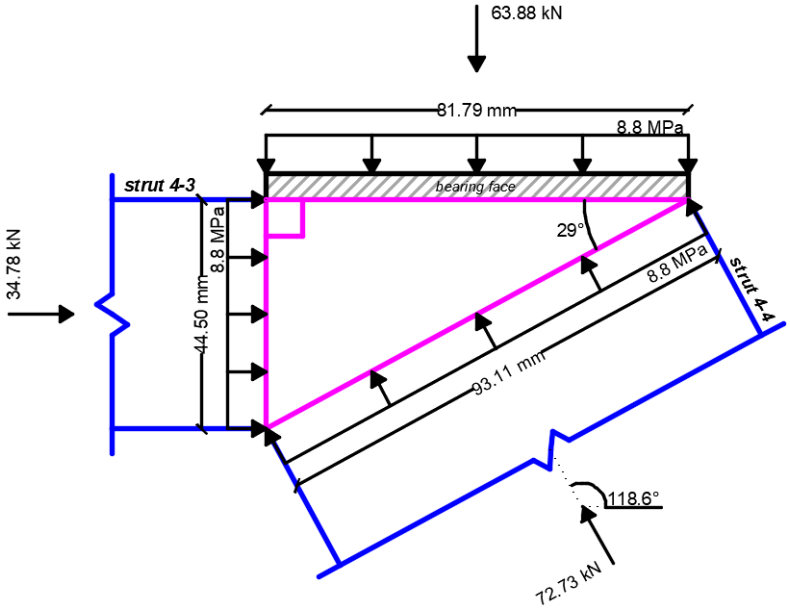

(b) Geometry of the C-C-C node 2

Figure A.26: Geometry of the hydrostatic C-C-C nodes near the loading point of Specimen 4.

Table A.19: Widths, resulting stresses, and the stress check results of Specimen 4 ST model C-C-T node.

C-C-T NODE			
Compression force (kN)	Nodal face width (mm)	Resulting Stress (MPa)	Stress Ratio
72.73	93.11	8.8	✓ 0.41
63.88	61.08	11.8	✓ 0.55

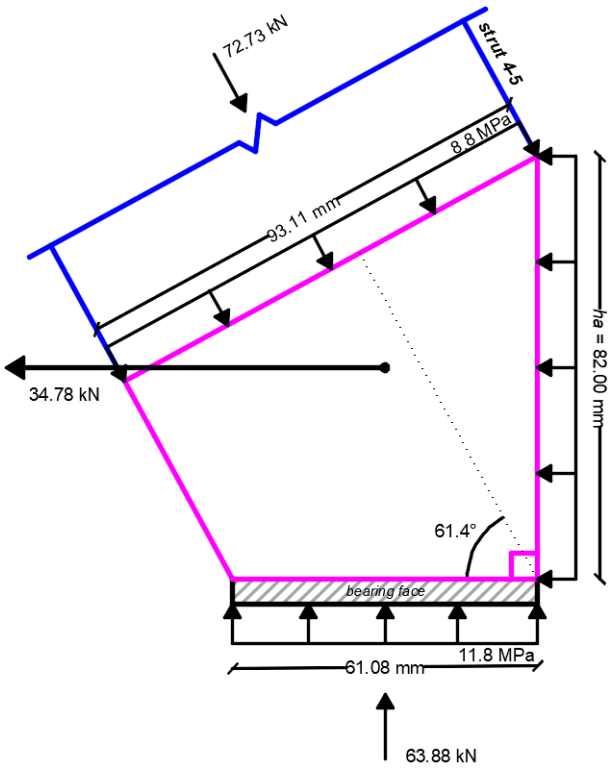

Figure A.27: Geometry of the nonhydrostatic C-C-T node at Specimen 4 ST model.

Struts

The second dimensioned truss members to be discussed are the struts. In the process of determining their dimension, each strut was assumed to have a prismatic shape. This assumption was taken because the LEFEA result of Maxwell & Breen's deep beam with a large opening showed that there are no principal tensile strains along those struts that neither resemble a bottle nor a fan (see Figure A.28).

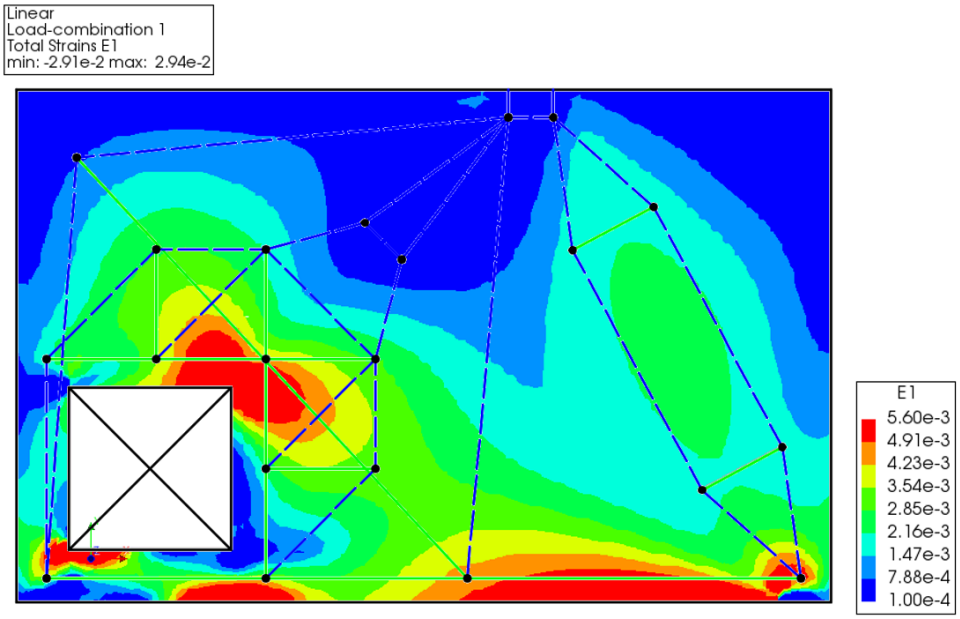

Figure A.28: Alignment of Specimen 4's ST model with the deep beam's principal tensile strains (E1) from LEFEA.

After the shape of the struts has been determined, these compressive truss members were analyzed for their stress. The stress analysis was carried out on the struts of the singular nodes (strut 4-1, 4-2, 4-3, 4-4 and 4-5) since they are the critical ones. Due to their prismatic shape, the resulting stress and the width of each strut are equivalent to the resulting stress and the width of the nodal faces that they attached on. Additionally, two of the left-most struts of Specimen 4's ST model (strut 4-6 and 4-7) also had their stress checked since it has a limited width of concrete at the left of the opening to transfer compressive stress to the left support. To check its stress, strut 4-6 and 4-7 are assumed to have the maximum width that it can have, which is 74 mm (twice the distance from the left side of the opening to the center of the strut and 30 mm, respectively. Information regarding these two variables are summarized in Table A.20.

Similar to the nodal zones, the end results of the struts' stress check were also presented as a ratio between the resulting stress and the allowable stress. According to the comparison results shown in Table A.20, all struts appeared to have a medium level of stress. Stress ratios of strut 4-1 to strut 4-7 showed values between 0.3 and 0.6. These results mean that the concrete at these dimensioned struts can also be considered safe from any compressive failure at the load level of 99.2 kN.

Ties

The last dimensioned truss members to be discussed are the ties. Unlike struts and nodes, ties are dimensioned with reinforcement bars. Since the reinforcement designs for Specimen 4 have been

Table A.20: Widths, resulting stresses, and the stress check results of Specimen 4's ST model dimensioned struts.

Strut ID	Compression force (kN)	Strut width (mm)	Resulting stress (MPa)	Stress Ratio
4-1	49.57	63.44	8.8	0.58
4-2	34.78	44.50	8.8	0.58
4-3	34.78	44.50	8.8	0.58
4-4/5	72.73	93.11	8.8	0.58
4-6	35.32	74.00	5.4	0.36
4-7	17.66	30.00	6.6	0.44

provided by Maxwell & Breen, the capacity of those rebars just had to be rechecked in accordance with the tensile forces acting on the ties. For the purpose of this stress check, the ties of Specimen 4's ST model were ID-ed, as shown in Figure A.29. The tensile forces in those ties were then compared with the steel design of Specimen 4, shown in Figure A.30.

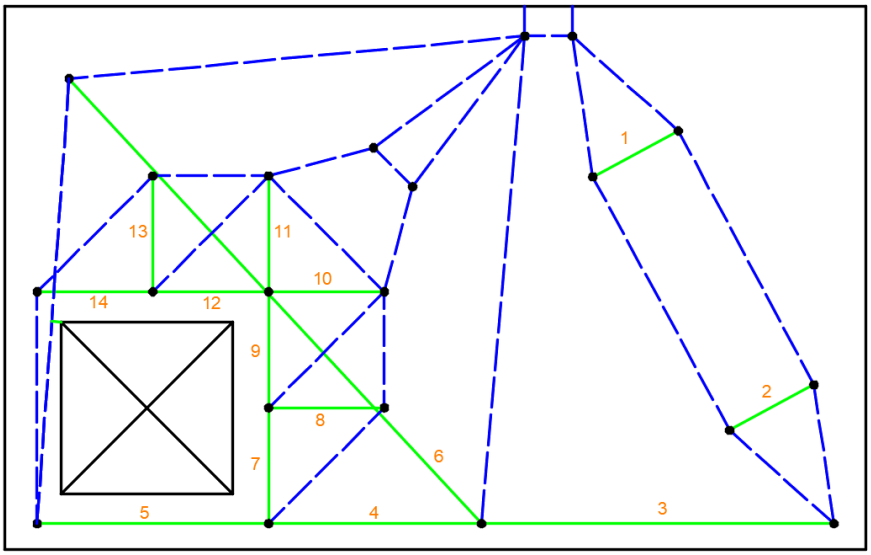

Figure A.29: ID-ed ties of Specimen 4's ST model.

The results of the stress check on the rebars of Specimen 4 is presented in Table A.21. The end results of the stress check are given as a ratio between the tensile stress per rebar over the mean yield strength (f_{ym}) of the rebar, shown in Table A.12. Based on those results, all rebars appear to have adequate strength in resisting the tensile forces from these two ties without yielding, except rebars at tie 1, 2, 8, and 13.

The rebars that were installed to cover the tensile forces from tie 1 and 2 are 3-mm rebars, and they were stressed up to a ratio of 2.98. This high stress ratio means that these rebars should have yielded even before the load level reached 99.2 kN. However, the 3-mm rebars were parts of a steel mesh which was installed at the right-hand side of the deep beam. Therefore, the tensile stress redistribution from the concrete to the 3-mm rebars would also be handled by other steel bars on the mesh.

Meanwhile, the rebar set that were installed set to cover the tensile forces from tie 8 and 13 is 3 - ⌀3 mm rebar set. These rebar sets contain tensile forces that have the same magnitude, which is

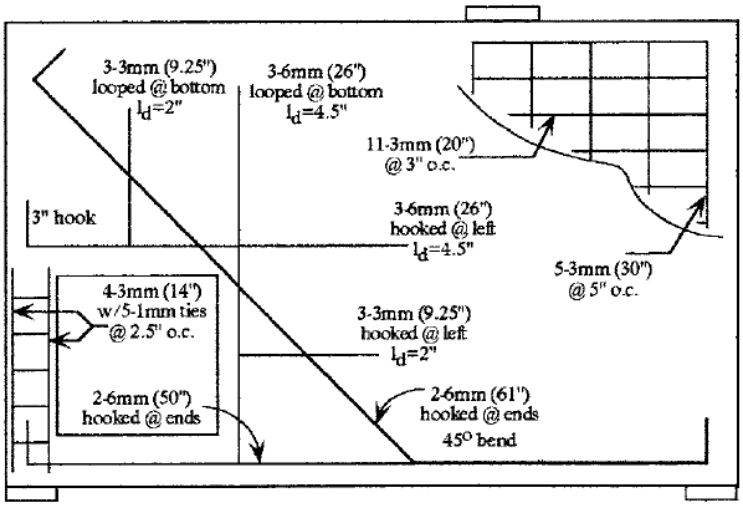

Figure A.30: Reinforcements of Specimen 4 [3].

17.66 kN. These tensile forces caused the rebar sets to be stressed for at least 42% above their yield strengths. This condition means that these rebars would yield when the 99.2-kN load is applied to Specimen 4.

Beside rebars at tie 1, 2, 8, and 13, the other rebars are safe from yielding at the load level of 99.2 kN. The rebars that handled the highest tensile forces in Specimen 4's ST model (rebars at tie 3, 9, 10, 11, and 12) were stressed up to a ratio of 0.74, while the rebars that handled smaller tensile forces were only stressed up to a ratio of 0.69 at most. Thus, the ST model of Specimen 4 can be considered providing a safe design in terms of reinforcements.

Table A.21: Stress check results of Specimen 4's ST model dimensioned ties using Specimen 4 reinforcement design.

Tie ID	Tie force (kN)	Representing rebars	Angle toward the rebar (^{0})	Projected force (kN)	Total rebar area (mm^2)	Tensile Stress per rebar (MPa)	Stress Ratio
1	14.01	1 - Ø3 mm	28.2	12.35	7.07	1746.75	2.98
2	14.01	1 - Ø3 mm	28.2	12.35	7.07	1746.75	2.98
3	34.78	3 - Ø6 mm	0.0	34.78	84.82	410.03	0.73
4	17.66	2 - Ø6 mm	0.0	17.66	56.55	312.30	0.55
5	17.66	2 - Ø6 mm	0.0	17.66	56.55	312.30	0.55
6	21.93	2 - Ø6 mm	0.0	21.93	56.55	387.81	0.69
7	17.66	3 - Ø6 mm	0.0	17.66	84.82	208.20	0.37
8	17.66	3 - Ø3 mm	0.0	17.66	21.21	832.79	1.42
9	35.32	3 - Ø6 mm	0.0	35.32	84.82	416.40	0.74
10	35.32	3 - Ø6 mm	0.0	35.32	84.82	416.40	0.74
11	35.32	3 - Ø6 mm	0.0	35.32	84.82	416.40	0.74
12	35.32	3 - Ø6 mm	0.0	35.32	84.82	416.40	0.74
13	17.66	3 - Ø3 mm	0.0	17.66	21.21	832.79	1.42
14	17.66	3 - Ø6 mm	0.0	17.66	84.82	208.20	0.37

Bibliography

[1] 2013. *fib Model Code for Concrete Structures 2010*. Ernst & Sohn.

[2] American Concrete Institute (ACI) Committee 318. 2008. *Building Code Requirements for Reinforced Concrete (ACI 318-08) and Commentary (ACI 318R-08)*. Farmington Hills, MI: ACI.

[3] Blaauwendraad, Johan, Brian S. Maxwell and John E. Breen. 2000. Experimental evaluation of strut-and-tie model applied to deep beam with opening. Paper by Brian S. Maxwell and John E. Breen. *ACI Structural Journal* **97**(6), pp. 913–914.

[4] Brown, Michael D., Cameron L. Sankovich, Oguzhan Bayrak and James O. Jirsa. 2006. Behavior and efficiency of bottle-shaped struts. *ACI Structural Journal* **103**(3), pp. 348–355.

[5] Bruggi, Matteo. 2009. Generating strut-and-tie patterns for reinforced concrete structures using topology optimization. *Computers and Structures* **87**(23-24), pp. 1483–1495. URL http://dx.doi.org/10.1016/j.compstruc.2009.06.003.

[6] Collins, Michael P. and Denis Mitchell. 1980. Shear and Torsion Design of Prestressed and Non-Prestressed Concrete Beams. *PCI Journal* **25**(5), pp. 32–100.

[7] Cook, Robert D., Davis S. Malkus, Michael E. Plesha and Robert J. Witt. 2002. *Concepts and Application of Finite Element Analysis*. John Wiley & Sons. Inc., 4th edn.

[8] El-Metwally, Salah and Wai-Fah Chen. 2017. *Structural Concrete: Strut-and-Tie Models for Unified Design*. CRC Press.

[9] Engen, Morten, Max A N Hendriks and Erik Åldstedt. 2015. Solution strategy for non-linear finite element (3), pp. 389–397.

[10] Engen, Morten, Max A N Hendriks, Jochen Köhler, Jan Arve and Erik Åldstedt. 2017. A quantification of the modelling uncertainty of non-linear finite element analyses of large concrete structures. *Structural Safety* **64**, pp. 1–8. URL http://dx.doi.org/10.1016/j.strusafe.2016.08.003.

[11] Guest, James K and Andrew T Gaynor. 2012. Structural Topology Optimization : Moving Beyond Linear Elastic Design Objectives , pp. 245–256.

[12] Hendriks, Max A N, Ane de Boer and Beatrice Belletti. 2017. Validation of the Guidelines for Nonlinear Finite Element Analysis of Concrete Structures - Part: Overview of results (June).

[13] Herranz, Juan Pablo, Hernán Santa Maria, Sergio Gutiérrez and Rafael Riddell. 2012. Optimal Strut-and-tie models using full homogenization optimization method. *ACI Structural Journal* **109**(5), pp. 605–613.

[14] Hordijk, Dirk Arend. 1991. *Local approach to fatigue of concrete*. Ph.D. thesis, Delft University of Technology.

[15] JCSS. 2001. Probabilistic Model Code. *Joint Committee on Structural Safety* (12th draft).

[16] Liang, Qing Quan, Yi Min Xie and Grant Prentice Steven. 2000. Topology optimization of strut-and-tie models in reinforced concrete structures using an evolutionary procedure. *ACI Structural Journal* **97**(2), pp. 322–330.

[17] Mörsch, E. 1912. *Der Eisenbetonbau, seine Theorie and Anwendung (Reinforced Concrete, Theory and Application)*. Stuttgart: Verlag Konrad Wittwer.

[18] Nakamura, H. and T. Higai. 2001. Compressive fracture energy and fracture zone length of concrete. *Modeling of inelastic behavior of RC structures under seismic loads* (November), pp. 471–487.

[19] Oviedo, Rodrigo, Sergio Gutiérrez and Hernán Santa María. 2016. Experimental evaluation of optimized strut-and-tie models for a dapped beam. *Structural Concrete* **17**(3), pp. 469–480.

[20] Rijkswaterstaat Ministry of Infrastructure and the Environment. 2012. Guidelines for Nonlinear Finite Element Analysis of Concrete Structures , p. 65URL http://www.dianausers.nl/pub/20120516GuidelinesNLFEA-final.pdf.

[21] Ritter, Karl Wilhelm. 1899. *Die Bauweise Hennebique (The Hennebique System)*, vol. 33. Schweiz Bauzeitung. URL https://www.e-rara.ch/doi/10.3931/e-rara-20036{%}0Ahttps://www.e-periodica.ch/digbib/volumes?UID=sbz-002.

[22] Roache, Patrick J. 1998. Verification of codes and calculations. *AIAA Journal* **36**(5), pp. 696–702.

[23] Rots, J.G. 1988. *Computational modeling of concrete fracture*. Ph.D. thesis, Delft University of Technology.

[24] Schlaich, J and K Schäfer. 1991. Design and detailing of structural concrete using strut-and-tie models **69**(6).

[25] Schlaich, Jorg, Kurt Schäfer and Mattias Jennewein. 1987. Toward a Consistent Design of Structural Concrete. *PCI Journal* **32**(3), pp. 74–150. arXiv:1011.1669v3, URL http://www.pci.org/pci{_}journal-1987-may-june-5/.

[26] Tjhin, Tjen N. and Daniel A. Kuchma. 2002. Computer-based tools for design by strut-and-tie method: Advances and challenges. *ACI Structural Journal* **99**(5), pp. 586–594.

[27] Tuchscherer, Robin G., David B. Birrcher and Oguzhan Bayrak. 2014. Strut-and-tie model design provisions. *PCI Journal* **56**(1), pp. 155–170.

[28] Union, The European. 2004. *Eurocode 2: Design of concrete structures - Part 1-1 : General rules and rules for buildings*, vol. 1. London: BSi.

[29] Vecchio, F. J. and M. P. Collins. 1993. Compression Response of Cracked Reinforced Concrete. *Journal of Structural Engineering* **119 (12)**, pp. 3590–3610.

[30] White, Richard N. and Mohamed A. Ali. 2001. Automatic generation of truss model for optimal design of reinforced concrete structures. *ACI Structural Journal* **98**(4), pp. 431–442.

[31] Zhang, Ruoxue and Sankaran Mahadevan. 2000. Model uncertainty and Bayesian updating in reliability-based inspection. *Structural Safety* **22**(2), pp. 145–160.